Multifocusing Seismic Imaging of Complex Geological Structures

by

Hossein Jodeiri Akbari Fam

A thesis submitted in partial fulfilment
of the requirements for the degree of

Doctor of Philosophy (PhD) in Mineral Deposits and Precambrian Geology

The Faculty of Graduate Studies
Laurentian University
Sudbury, Ontario, Canada

THESIS DEFENCE COMMITTEE/COMITÉ DE SOUTENANCE DE THÈSE
Laurentian Université/Université Laurentienne
Office of Graduate Studies/Bureau des études supérieures

Title of Thesis
Titre de la thèse Multifocusing Seismic Imaging of Complex Geological Structures

Name of Candidate
Nom du candidat Jodeiri Akbari Fam, Hossein

Degree
Diplôme Doctor of Philosophy

Department/Program
Département/Programme Mineral Deposits and Precambrian Geology

Date of Defence
Date de la soutenance April 05, 2022

APPROVED/APPROUVÉ

Thesis Examiners/Examinateurs de thèse:

Dr. Richard Smith
(Supervisor/Directeur(trice) de thèse)

Dr. Mostafa Naghizadeh
(Committee member/Membre du comité)

Dr. Öz Yilmaz
(Committee member/Membre du comité)

Dr. Charlotte M. Krawczyk
(External Examiner/Examinateur externe)

Dr. Ming Cai
(Internal Examiner/Examinateur interne)

Approved for the Office of Graduate Studies
Approuvé pour le Bureau des études supérieures
Tammy Eger, PhD
Vice-President Research (Office of Graduate Studies)
Vice-rectrice à la recherche (Bureau des études supérieures)
Laurentian University / Université Laurentienne

ACCESSIBILITY CLAUSE AND PERMISSION TO USE

I, **Hossein Jodeiri Akbari Fam**, hereby grant to Laurentian University and/or its agents the non-exclusive license to archive and make accessible my thesis, dissertation, or project report in whole or in part in all forms of media, now or for the duration of my copyright ownership. I retain all other ownership rights to the copyright of the thesis, dissertation or project report. I also reserve the right to use in future works (such as articles or books) all or part of this thesis, dissertation, or project report. I further agree that permission for copying of this thesis in any manner, in whole or in part, for scholarly purposes may be granted by the professor or professors who supervised my thesis work or, in their absence, by the Head of the Department in which my thesis work was done. It is understood that any copying or publication or use of this thesis or parts thereof for financial gain shall not be allowed without my written permission. It is also understood that this copy is being made available in this form by the authority of the copyright owner solely for the purpose of private study and research and may not be copied or reproduced except as permitted by the copyright laws without written authority from the copyright owner.

Abstract

We introduce two highly effective stacking approaches, 2.5D multifocusing (MF) and 3D generalized spherical multifocusing (GSMF) algorithms, to improve stacked seismic sections. The proposed methods can be applied to crooked-line or 3D seismic data with arbitrary recording geometry from areas with complex near-surface/subsurface to generate either a 2D crooked stacked section or a 3D stacked volume. Both methods simultaneously correct for 3D normal moveout and 3D azimuth-dependent dip moveout, and transform multi-coverage prestack seismic data into a stacked section that is equivalent to a synthesized zero-offset wavefield. In addition, the 3D GSMF approach accounts for the elevation and spatial coordinate of all source and receiver positions, so can be applied for seismic data collected in areas with irregular topography. The 2.5D MF moveout operator is accurate for quasi-hyperbolic reflections, whereas, the 3D GSMF traveltime surface is a more general higher-order moveout operator with a closed-form implicit formulation that can account for non-hyperbolic moveout. The proposed methods efficiently extract valuable 3D structural information when applied to crooked-line/3D seismic surveys. The introduced methods are data-driven algorithms and can perform automatically with a coherence-based global optimization search. We also deployed an efficient processing sequence for applying the developed methods, which mainly consists of building super common-midpoint bins, wavefield attributes analysis, multifocusing moveout correction, data enhancement/stacking, and prestack/poststack dip-independent RMS velocity analysis and migration. Our wavefield analysis uses a multidimensional differential evolution algorithm to simultaneously determine optimal wavefield parameters, which improves the efficiency and accuracy of the estimation. The performance of the proposed methods is tested using 3D synthetic data with both 3D and crooked-line surveys over various curvatures ranging from low (gently curved interface or planar layer with curvature of zero) to high (spherical reflector or point diffractor). The numerical tests demonstrate that the new approximations extract dips from seismic data accurately and are accurate for gently to highly curved interfaces beneath low (multiple homogeneous layers) to relatively high heterogeneous overburden (vertical/horizontal background velocity with a gradient of 1/s for the 2.5D MF method and vertical background velocity with a gradient of 2/s for the 3D GSMF method). Applying the 2.5D MF approach to the Larder Lake crooked-line transect with subsurface complexity, as well as a real data set collected in a thrust-belt area, focused the steeply dipping reflections more coherently and mapped new reflections that are not visible in the conventional results. Application of the 3D GSMF method on a 3D low-fold real seismic dataset, acquired over a complex thrust-belt area with rugged terrain, yielded high-resolution and an accurate stacked seismic volume with a high signal-to-noise ratio, compared to the conventional 3D stacking.

Keywords

High-resolution seismic imaging, 2.5D multifocusing, 3D generalized spherical multifocusing, Synthesized zero-offset wavefield, Azimuth-dependent dip-moveout, Global optimization, Wavefront analysis, Arbitrary recording geometry, Crooked-line survey, Three-dimensional survey, Irregular topography, Complex near-surface, Complex subsurface, Hard-rock environment

Co-Authorship Statement

The current thesis was completed by the candidate under the supervision of Dr. Richard Smith, Dr. Mostafa Naghizadeh, and Dr. Öz Yilmaz. The thesis consists of one peer-reviewed journal article published in Geophysics and two manuscripts that are intended to be submitted for peer-reviewed journal publication. The general goals and focus of the thesis were conceived by Dr. Mostafa Naghizadeh. The candidate developed the methodologies and the theoretical frameworks. The original draft of the thesis, including the published journal paper, was completed by the candidate and edited and improved by scientific guidance and constructive discussions with the co-authors. All authors provided critical feedback and helped shape the research, analysis, and manuscripts.

Chapter 2 is co-authored by Dr. Mostafa Naghizadeh and Dr. Öz Yilmaz. All authors discussed the results and contributed to the final manuscript. Dr. Yilmaz performed signal processing and statics corrections of the crooked-line real seismic data example.

Chapter 3 is co-authored by Dr. Mostafa Naghizadeh, Dr. Richard Smith, Dr. Öz Yilmaz, Dr. Saeid Cheraghi, and Dr. Kate Rubingh. All authors discussed the results and commented on the manuscript. Dr. Cheraghi performed signal processing and statics corrections of the Larder Lake transect. Also, he provided the results and description for the processing flows including 2D phase shift time migration of dip moveout corrected stack and swath 3D poststack migration. The geological interpretation for the results of the 2D phase shift and swath 3D migration methods was drafted by Dr. Cheraghi. Dr. Rubingh provided the geological description of the Larder Lake region.

Chapter 4 is co-authored by Dr. Mostafa Naghizadeh, Dr. Öz Yilmaz, and Dr. Richard Smith. The authors reviewed the manuscript, provided comments on some figures, edited the draft, and modified the terminologies. Dr. Yilmaz performed signal processing and statics corrections of the 3D real seismic data example and produced the stacking velocity field and the conventional 3D stacked volume of the real data example.

The candidate created the synthetic models, performed the numerical simulations, performed the experiments, and the analytic calculations. The programming, implementation, and testing of the code packages were executed by the candidate. All authors reviewed the results and approved the final version of the manuscripts to be published or submitted. In this thesis, for the standalone manuscripts (chapters 2 – 4), I used the term “we”, but for chapters 1 and 5, I used the term “I”, as they are related to the thesis.

Acknowledgements

I would like to express my deepest appreciation to my supervisors, Dr. Richard Smith, Dr. Mostafa Naghizadeh, and Dr. Öz Yilmaz, for their unwavering support throughout my Ph.D. study with their patience, continuous motivation, and immense knowledge. I am extremely grateful to Dr. Naghizadeh for his ingenious advice and practical suggestions, whose advice facilitated challenging problems. He provided me with a welcoming and friendly atmosphere, which flourished my talents and enabled me to show my creativity in scientific situations. I express my sincere gratitude to Dr. Smith for his unparalleled support and for providing me with valuable advice, meticulous edits, and detailed feedback. I am deeply indebted to Dr. Öz Yilmaz, who strongly supported me and provided me with precious and inspiring guidance, who have always warmed my heart and ignited my enthusiasm. I will endlessly strive to be a successful representative of your beliefs about me throughout my future career. I acknowledge the comments provided by the co-authors, for their very insightful comments on the manuscript, which pushed me to sharpen my thinking and expand my way of thinking from various perspectives. Without their support, it would not have been possible to complete this research.

This research was funded by the NSERC Canada First Research Excellence Fund. I would like to thank the Metal Earth project at Laurentian University for providing and archiving the seismic data. I acknowledge Metal Earth for funding my research. The Metal Earth project and Laurentian University are greatly thanked for providing the opportunity to attend and present our achievements in well-known conferences and to visit field operations for acquiring passive seismic data and vertical seismic profiling data. I am also grateful for all of the opportunities, I was given to further my research.

GeoThrust and Globe Claritas were used for 2D and 3D seismic data processing. I acknowledge GeoTomo for providing an academic license. Seismic Unix open-source platform was used for an efficient implementation of the proposed methods. The Seismic Unix package is originally created by the Center for Wave Phenomena at the Colorado School of Mines and maintained by Dr. Stockwell. Methodological development, numerical modeling, and visualization were carried out with *Matlab*. Three-dimensional visualization and interpretation were conducted with GOCAD. Geological maps were generated using QGIS. The SOFI3D opensource code was used to produce seismic synthetic data sets using the finite differences method. I thank Thomas

Bohlen, Denise De Nil, Daniel Köhn, and Stefan Jetschny for developing the SOFI3D package. This work was enabled in part by the facilities of the Shared Hierarchical Academic Research Computing Network (SHARCNET:www.sharcnet.ca) and Compute/Calcul Canada (www.computecanada.ca).

Absolute Imaging Inc. is thanked for conventional processing and prestack imaging of the Larder Lake seismic data. I thank Christopher Mancuso for sharing the GCDMO code package and for helpful discussions. I appreciate Dr. Benjamin Schwartz and Dr. Ivan Abakumov for constructive technical discussions. I thank Bryona Fernandes for providing the geological map in the Larder Lake area. I also had the great pleasure of working with my fellow research associate and graduate students at the Harquail School of Earth Sciences (HES). I especially thank the Metal Earth team and the HES staff.

Last, but not least, I would like to express deep appreciation to my family, who endured this long process with me from the other side of the world. I thank them from the bottom of my heart for supporting me spiritually throughout my Ph.D. study and my life in general. They offer me invaluable emotional support, consistent company, continuous motivation, and unconditional love. We shared a lot of happiness, sorrow, and stress every single day since I came to Canada. I love them unequivocally forever.

Contents

List of Figures

List of Tables

Chapter 1

Introduction to the thesis

1.1 Introduction

Imaging complex subsurface geological structures is a challenging task when using geophysical prospecting methods. The seismic reflection method provides the highest lateral and vertical resolution among deep probing geophysical remote-sensing methods and this method can maintain high precision to depths of several kilometers. Seismic studies aim to collect, process, and invert seismic wavefields to generate an interpretable image of the subsurface. A controlled pulse of energy creates a disturbance, typically on the surface of the earth, that propagates into the subsurface, and reflections from geological boundaries propagate to receivers also usually on the surface of the earth. The response of the seismic wavefield is recorded by an array of receivers, stored, processed for signal-to-noise ratio (S/N) enhancement, and finally used to produce an image of the subsurface via some type of inversion method(s). The specific choice of seismic data processing or inversion methods that are used plays an important role in constructing an accurate subsurface image from reflection seismic surveys. The final image is used as a starting point for geophysical interpretation toward the understanding of geological structures and prospecting for resources.

Depending on budget, time restrictions, and the nature of the subsurface geology of the study area, geophysicists can employ one of two fundamental types of imaging algorithms, defined by the domain in which they are applied: time migration and depth migration. The latter, depth imaging (also called prestack depth migration, PSDM) is the process that reconstructs an image of the subsurface by relocating the seismic events from the location that they were recorded at the surface into the positions in the subsurface where they were reflected. The wave equation, which describes the propagation of seismic waves, is used to move (or migrate) the seismic events. Depth migration is applied to seismic data in depth coordinates (depth domain), while time migration is applied to seismic data in time coordinates (time domain). The time migration approach requires an average apparent velocity and repositions the recorded seismic wavefield to originated specific location in the subsurface under the assumption of the straight seismic raypath. However, depth migration requires knowing the exact interval velocity, and seismic rays are allowed to bend in the model (Yilmaz, 2001).

The conventional time-domain stacking method uses hyperbolic moveout formula as a function of offset, which is only exact for a planar dipping reflector beneath a homogeneous overburden. Deviating from this assumption results in the moveout becoming nonhyperbolic with higher-order terms (Schwarz and Gajewski, 2017). In regions with significant geologic complexity and lateral velocity variations, such as hard-rock geological settings, seismic depth imaging methods are often preferred, whereas time imaging methods can only resolve low to moderate complexities. This is because depth imaging accounts for traveltime non-hyperbolic moveout and accurately approximates complicated raypaths to image steeply dipping reflectors and near-vertical faults. However, the depth-domain algorithms are computationally expensive and very sensitive to the velocity-depth model that has been estimated. Hence, depth-domain imaging methods require a very detailed and hopefully accurate interval velocity-depth model. Lack of knowledge of an accurate velocity model causes depth imaging methods to lose their convergence properties or produce wrong results. In addition, irregular distribution of sources and receivers has a further negative effect on prestack migration methods, and therefore seismic data reconstruction methods are required to regularize the locations of data before its application (Biondi, 2006). An alternative approach to the depth-domain imaging method is using the time-domain imaging methods. The stacking step plays a key role in time imaging techniques and to produce accurate zero-offset wavefield stacked sections requires accurate and generalized moveout operators instead (Hubral, 1999). The depth- and time-imaging methods are two fundamentally different approaches and do not supersede each other (Vestrum et al., 2011); their characteristics make them complementary to each other. The processing methods in the time-domain can potentially produce more coherent and clear structural stacked sections and images, detailed stacking and root-mean-square (RMS) velocity fields, and enhanced seismic gathers. They can also provide interpreted horizons for building an accurate velocity model as a function of depth. Therefore, improving the quality of time-domain stacked sections and developing accurate and generalized moveout operators is the focus of this research.

Macro-model independent time-domain methods are alternatives to the depth processing flow. They can be employed to estimate stacking velocity fields and generate stacked sections, without any prior knowledge of the subsurface model. These stacking methods can be categorized into two groups, including the methods based on common-midpoint (CMP) profiling and non-CMP-based methods. These two groups are based upon different approaches to transform prestack data into a stacked section.

The CMP-based stacking method is a standard flow used for processing 2D seismic data conventionally. This method includes sorting the data into CMP gathers (symmetrically located sources and receivers that collect traces from a point on the surface halfway between the sources and receivers called the common midpoint), correcting source-receiver offset (NMO correction), dip effects (DMO correction), and then stacking. The stacked section, commonly known as a simulated zero-offset wavefield, approximates seismic traces that could have been recorded by a coincident source and receiver at a location, but with an improved S/N (Yilmaz, 2001). If the interfaces dip, then the zero-offset section will need migration, which aims to move the seismic reflections to their correct subsurface locations.

The Metal Earth project acquired a total of 921 km regional-scale deep seismic reflection transects and 184 km of high-resolution seismic reflection profiles in the Superior Craton of Canada in 2017. The seismic traverses primarily aim to enhance the knowledge and to better understand the subsurface geology of the Abitibi Greenstone Belt within the Canadian Shield. High-quality seismic images can play an essential role in targeting mineral fluid pathways throughout the crust, and of identifying structures at deposit scales. Due to the inaccessibility of rugged terrains, logistical and environmental restrictions, the seismic surveys are conducted along existing roads, which are not straight, an acquisition geometry termed crooked-line geometry. Most of the seismic field records are collected over settings with crystalline rock and have complicated near-surface conditions, heterogeneous overburden, and irregular topography. The subsurface geology includes gently to steeply dipping and curved interfaces with low impedance contrasts, complex subsurface structures, and the common presence of diffractions and out-of-plane reflections, all of which can adversely affect the S/N of the data. Technically, irregular distribution of sources and receivers along the crooked survey line disperses the midpoint locations from the traverse line and leads to a variable fold coverage and uneven offset distribution which can result in poorly images areas. In addition, the crooked-line geometry results in considerable time- and offset-variant delay of reflections, which could defocus and deform reflections particularly from reflectors with a crossdip component (dipping perpendicular to the average trend of the traverse, or more precisely, dipping along the crossline direction). Also, the cross-profile spread of midpoints violates the assumption of a straight-line survey that is made when deriving the equations used in two-dimensional imaging methods. The intrinsic characters of the subsurface in addition to survey configuration and technical issues can give rise to potential pitfalls and artifacts, thus, resulting in difficulties in imaging and estimating the velocity-depth model.

The midpoint dispersion resulting from the crookedness of the survey geometry and the crossdip effect are linked together, and they are inseparable problems. Figure 1.1 compares the effect of survey geometry (solid yellow line) and different dip components on the reflection point dispersion (black dots) on the reflector interface and the spreading of midpoint locations (red dots) on the recording surface for a common-midpoint gather. Figures 1.1a-d show interfaces with varying dips with a crooked-line survey and Figures 1.1e-h depict the same models for each column but with a straight-line survey. The first column models have both inline and crossline dip components. The models shown in the second and third columns have only inline dip and crossline dip components, respectively, and the reflectors in the last column are horizontal. In each panel, one reflection raypath is shown using black lines generated by a source (red asterisk) and recorded by a receiver (blue triangle) along the surveys. This reflection point for this source/receiver pair is shown with the black dot at the vertex of the raypath triangle. The other black dots are for sources and receiver pairs, which their midpoints are located within the common bin on the surface. The transparent white planes are shown along the orthogonal to the traverse line across the imaging point (commonly, it is the center of the bin) and perpendicular to the reflector interface. Comparing the dispersion of the reflection points and midpoints demonstrates that the crooked-line survey results in a significant midpoint and reflection point dispersion, particularly for the reflector with a crossdip component.

Figure 1.2 shows corresponding common-midpoint gathers for each model shown in Figure 1.1. The comparison indicates that the crooked profiles could generate arrival times of seismic waves with considerable time- and offset-variant delays among reflections, particularly reflectors with the crossdip component. Also, it leads to an uneven distribution of offsets. The gap in arrival for the crooked line row (a to d) is due to the fact that the crookedness of the acquisition line dispersed the midpoints of the source-receiver pairs with the small offset, such that they are located outside of the common bin. The crookedness of the survey line does not have any effect on reflections from a horizontal interface, except the uneven distribution of data, which can be solved by correctly assigning geometry.

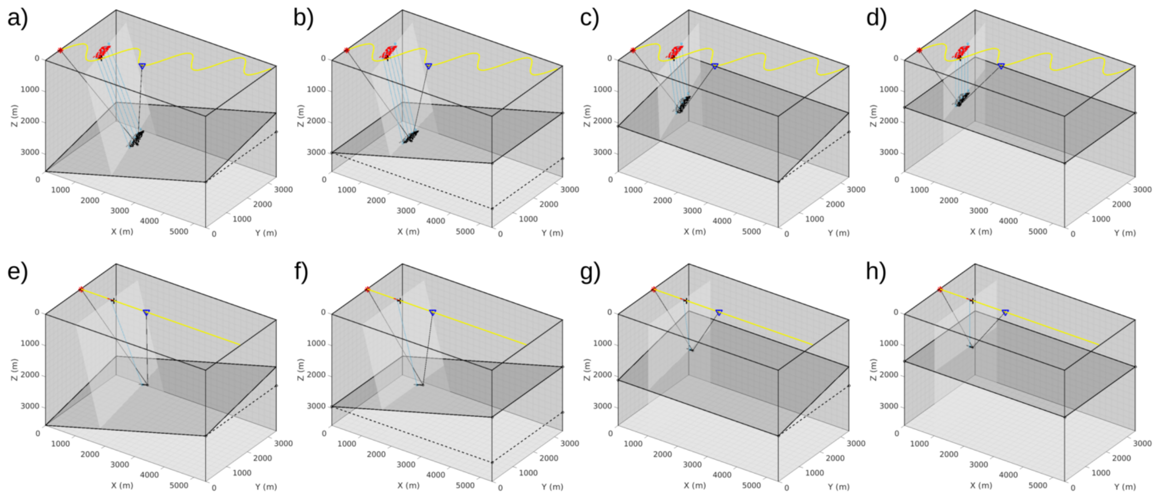

Figure 1.1: The effect of survey geometry (a-d: crooked-line survey, e-h: straight-line survey) and different dip components (a and e: both inline and crossline dips, b and f: inline dip, c and g: crossline dip, d and h: horizontal) on the reflection point dispersion and the spreading of midpoint locations for a selected common-midpoint data.

Here, I compare the model of a dipping interface along inline and crossline dip directions with straight and crooked survey lines (Figures 1.1a and 1.1e) and their corresponding CMP gathers (Figures 1.2a and 1.2e). The traveltime of reflections collected by the straight-line survey has the expected hyperbolic trajectory and does not have any unusual time delays among reflections. Since the reflection points are not dispersed broadly and midpoints almost coincide with the center of the bin. The crooked nature of the seismic line disperses the midpoint locations and reflection points broadly, which results in considerable time- and offset–variant delays among the reflections. Figure 1.3 compares the distribution of crossline shift versus offset for the straight-line survey (red) and the crooked-line survey (black). The crossline shift is the absolute value of the distance between the imaging point and the midpoints along the normal to the traverse line. A comparison of this plot with Figure 1.2a shows that the large crossline-shift values correspond to large time delays or divergence from the hyperbolic trajectory.

The CMP profiling method assumes straight-line geometry, a flat datum, and simple subsurface geological structures. Therefore, the crookedness, in addition to irregular to-

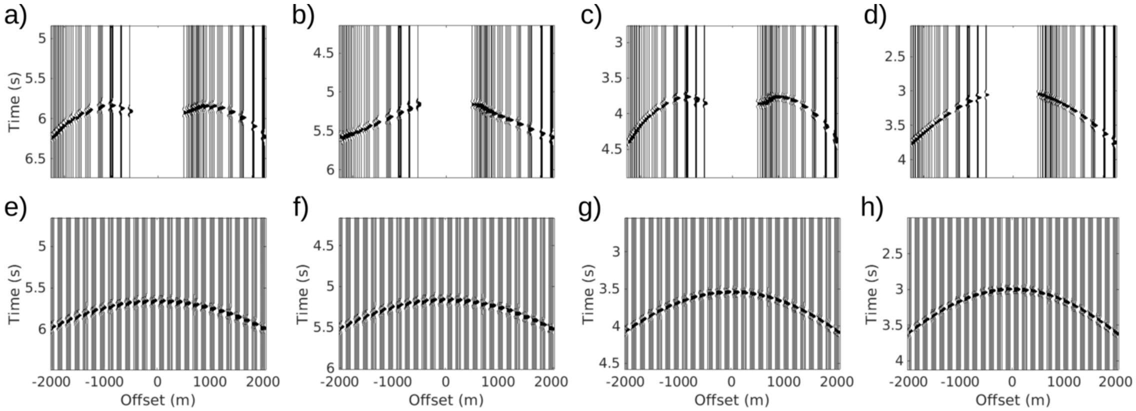

Figure 1.2: The common-midpoint data generated for the selected bin from a reflector with both inline and crossline dips (a and e), inline dip (b and f), crossline dip (c and g), and a horizontal interface (d and h) using the crooked-line survey (a-d) and the straight-line survey (e-h).

pography and complex subsurface geology hampers the application of conventional methods and limits their ability to enhance the signal-to-noise ratio. Recently, for crooked-line seismic data processing, several different crossdip analysis and correction methods have been proposed by various researchers (e.g. Nedimović and West, 2003a; Mancuso and Naghizadeh, 2021). Nedimović and West (2003a) introduced the crossdip moveout (CDMO) correction that can be carried out after removing normal-moveout and inline dip-moveout effects. Mancuso and Naghizadeh (2021) proposed the generalized croosdip moveout (GCDMO) analysis that can simultaneously correct the NMO plus CDMO effects. Hence, in conventional processing of crooked-line seismic data, a sequence of processing steps, including normal-moveout, dip-moveout, and crossdip-moveout corrections, is required to account for offset and azimuth-dependent dip effects. However, applying these steps sequentially tends to result in significant errors, especially for large offsets, and may not be successful in correcting non-hyperbolic reflections, which could lead to poor alignment and a low-resolution image. In addition, the NMO correction causes a frequency distortion, particularly for shallow events at large offsets, which is called NMO stretching (Yilmaz, 2001). Also, the accuracy of crossdip analysis is limited to a maximum of about 40°. Importantly, the imaging and preservation of diffractions are also crucial to produce a true zero-offset wavefield and for the interpretation of small-

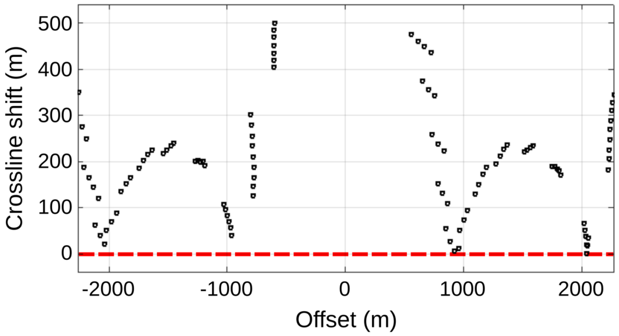

Figure 1.3: The crossline shift versus offset for the crooked-line survey (black) shown in Figures 1.1a-d and the straight-line survey (red) shown in Figures 1.1e-h.

scale structural elements and diffractor edges, especially in hard-rock imaging, mineral exploration, and fracture analysis. The conventional processing sequence could not retrieve diffractions that have non-hyperbolic traveltime moveout.

Crooked-line seismic data acquisition is a pseudo-3D (or 2.5D) survey that provides useful 3D structural information (Wu, 1996; Schmelzbach et al., 2007). One can also use a 3D processing and binning method to produce an image from 2D data collected with a crooked-line geometry; for example, Cheraghi et al. (2020) utilized 2D and 3D prestack time migration and swath 3D processing methods. Application of 3D processing techniques on 2D crooked-line seismic data might often lead to low-resolution images due to the lack of an accurate and dip-independent velocity model. Also, the low- and variable-fold coverage combined with noisy data can adversely affect the 3D processing methods (Nedimović and West, 2003a).

Recently, some attempts have been made to improve stacking procedures by utilizing non-CMP-based methods to obtain accurate zero-offset stack sections. Two-dimensional non-CMP-based multi-parameter moveout corrections and stacking strategies could also address the issues associated with CMP dispersal problems along a straight survey with arbitrary geometry (Gelchinsky et al., 1999a). However, crooked-line geometry violates the assumption of a straight survey line assumed in the 2D methods, and three-dimensional extensions are required for accurate seismic imaging purposes.

There are two major types of non-CMP-based multiparameter moveout corrections and stacking strategies. These include the multifocusing (MF) and common reflection surface (CRS) method that were originally developed by Gelchinsky et al. (1999a,b) and Müller (1999), respectively. The MF method can be more accurate than the CRS method, but it is more difficult to adapt it to 3D cases (Fomel and Kazinnik, 2013; Landa et al., 2009). This can be explained by the fact that the MF moveout operator is a double square-root expression, whereas the CRS moveout operator is essentially a quadratic expression, which is derived by a hyperbolic Taylor expansion (a series that can be used for approximating functions with high accuracy that can be difficult to compute). The CRS traveltime moveout is approximated using second-order Taylor series expansions of the squared traveltime and the higher-order terms are neglected. This approximation can be degraded if the traveltime surface is not smooth and has considerable higher-order terms, particularly for far-offsets and large midpoint separations.

During the last two decades, different MF stacking techniques based on the theory of homeomorphic imaging (Gelchinsky, 1992; Gelchinsky and Keydar, 1999) have been proposed. These include the 2D MF (Gelchinsky et al., 1999a,b), 2D irregular surface MF (IS-MF) (Gurevich et al., 2002), 2D MF with controlled reflection-point dispersal (Gurevich and Landa, 2002), common-offset MF (COMF) (Berkovitch et al., 2011, 2012b), 2D spherical MF (SMF) (Landa et al., 2009), and 2D irregular surface spherical MF (IS-SMF) (Chang et al., 2019b) methods. Also, the application of 2D multifocusing for improved time imaging is widely established in the published literature (Landa et al., 1999; Berkovitch et al., 2004; Belfer et al., 2008b; Berkovitch et al., 2008, 2009, 2012a; Curia et al., 2012; Buzlukov and Landa, 2013; Landa et al., 2013; Elhaj et al., 2014; Schoepp et al., 2014; Borghi et al., 2017; Curia et al., 2017; Chang et al., 2019a).

The MF-based methods provide simulated zero-offset wavefield sections with higher S/N by transforming multi-coverage prestack seismic data comprised traces within the limits of a certain span in the vicinity of the central point (using a much larger number of traces than in conventional CMP stacking). The MF formulation is accurate for a broad range of curvatures and heterogeneities, even for strongly curved reflectors and moderate lateral velocity variations. Also, this method accurately describes traveltime behavior for a wider class of subsurface models and does not require any knowledge of the subsurface model. Further, it can determine a dip-independent stacking velocity field and structural detail such as interface curvature and the slope of the interfaces (Landa et al., 2009). The MF methods can be considered as a method for wavefield analysis, which reliably estimates wavefront parameters of each seismic event at each observation point (Landa et al., 1999). Wavefront parameters, also called kinematic wavefield attributes, are a set of parameters that describe the propagating seismic wavefront and include the emergence angle, normal wave curvature, and normal incident point curvature (See the next section for more details). These attributes have broad applications in seismic data processing and imaging. The MF methods are time-shifted approaches and derived based on the assumption of optical imaging (auxiliary) medium for taking into account overburden heterogeneity (De Bazelaire, 1988; Gurevich and Landa, 2002; Schwarz and Gajewski, 2017). This assumption leads to a non-stretching moveout correction without distortion of the amplitude and phase, which can lead to a stacked section with higher vertical resolution.

Currently, the available MF operators do not consider the elevation and spatial coordinates of the source and receiver, the midpoint dispersion, and the azimuth-dependent dip effects for crooked-line or 3D configurations. Particularly, these MF operators do not account for the cross-offset and cross-dip components for the crooked-line configuration which is necessary for the Metal Earth data processing. The existing implementations of the MF method are technically challenging, computationally expensive, comprise several isolated steps, and lack an efficient optimization component.

In this thesis, I introduce two non-CMP-based stacking methods for crooked-line and 3D seismic data to address the problems mentioned above. First, I develop a new MF method that accounts for the cross-offset and cross-dip effects for the crooked-line configuration, which is called the 2.5D MF method. I derive the formulation for the 2.5D MF algorithm and examine the performance of the proposed method on different synthetic and real seismic data sets. Also, the computational efficiency and accuracy of the proposed method are evaluated. Second, I present the application of the 2.5D MF technique on the Metal Earth seismic data collected in the Larder Lake area with a crooked-line survey. I describe the 2.5D MF imaging workflow and how the differential evolution global optimization algorithm has been adapted to optimally search for the wavefield attributes. I compare the results of the 2.5D MF method with the 2D prestack time migration, 2D time migration of DMO stack, and swath 3D imaging. Then, I expand a 3D generalized spherical multifocusing stacking method for a crooked-line/3D seismic data set acquired over an area with irregular topography. I derive the traveltime formula and test the performance of the proposed method on synthetic and real data sets.

1.2 Research problem and thesis objectives

The main challenge regarding the application of seismic imaging methods in hard-rock geologic settings is the low quality of seismic field data due to the intrinsic characters of the subsurface. Low impedance contrasts, dispersion and scattering of seismic waves, and noisy environment all degrade the signal-to-noise ratio (S/N). In addition, crooked-line survey geometry (2D seismic surveys acquired on non-straight survey lines) is a technical issue, which exacerbates these effects and leads to coherent artifacts in resulting images. Standard seismic processing methods, such as 2D common midpoint stacking, assume a straight-line geometry and simple subsurface geological structures, so a poor S/N in addition to the crookedness of survey, irregular topography, and complex subsurface geology hampers the application of conventional methods and limits their ability to recover signals. The main goal of the current research is to improve the velocity field and to generate high-resolution images of the crooked-line seismic data from areas with complex subsurface geological structures for comprehensive geological interpretation.

The weak reflectivity, complex scattering, and noisy data are prominent characteristics of most of the Metal Earth seismic lines. High-resolution imaging of such low-quality seismic data requires an algorithm that is suited to accurately models diffractions, approximate weak reflections, distinguish out-of-plane reflections, and improve the S/N. The data condition motivates us to employ MF-type methods, which are effectively capable of generating high-resolution stack sections in noisy environments and are better suited to model the moveout of non-hyperbolic reflections and diffracted waves. Applying the MF-type methods on Metal Earth data faced two major obstacles. First, practically, there is no open-source or commercial software available for academic use. There is just one seismic processing company in the world that can provide commercial MF imaging services using their own in-house software, and this software is not available for academic or commercial use. Second, the crooked-line survey geometry is a theoretical issue that hampers utilizing MF methods. All extensions of MF methods do not consider the crossdip effects and crossline variation of source and receiver coordinates (or azimuth of each source-receiver pair) in 3D space. Therefore, those approaches cannot be applied for crooked-line seismic geometry. I extent MF-type stacking methods to adapt their applications for crooked-line seismic data. Using this theory, I build a software package that allows us to utilize the new methods for the processing of crooked-line seismic survey data.

The general objective of the research project can be broken down into the following parts:

- deriving the theoretical and mathematical concepts of novel 2.5D multifocusing (2.5D MF) and 3D generalized spherical multifocusing (3D GSMF) methods,
- incorporating numerical algorithms for wavefield analysis by adapting global optimization algorithms to improve the accuracy and resolution of generated results,
- designing an optimal sequence of signal filtering and seismic processing flows for applying the newly developed methods effectively,
- building software packages for efficient implementation of the introduced approaches,
- simulating seismic wavefields for different scenarios using the finite difference and ray-tracing methods,
- testing the performance of the methods by applying them on different synthetic and real data sets using the developed software.

1.3 Theory of the multifocusing method

A recently introduced multifocusing (MF) method is a non-CMP-based macro-velocity independent stacking algorithm that offers a more realistic simulation of the zero-offset wavefield and can considerably improve the quality of stacked sections in complex geologic areas with poor S/N. This approach proposed by Gelchinsky et al. (1999a,b) is a sophisticated alternative method for conventional stacking (normal moveout [NMO] and dip moveout [DMO]) that provides very detailed and high-resolution images based on a transformation of multi-coverage prestack data into a stacked section (Landa et al., 1999). The MF method can produce an accurate zero-offset section for seismic data with arbitrary source-receiver distribution using a new local double-square-root moveout correction formula (Berkovitch et al., 1998). In particular, the MF transformation involves stacking a larger number of source-receiver pairs with nearby common midpoints, which is called a super gather of seismic traces. Stacking large super gathers is made possible by the use of a generalized moveout correction. This moveout correction is a nonlinear multi-dimensional optimization problem and the main challenge is the determination of the MF kinematic attributes from the prestack super gather through an automatic search process. The objective function is based on a coherency measure of reflection amplitudes that is being maximized. Conventional velocity analysis aims to find and optimize a single parameter, velocity, by lining up reflection events and correcting for the offset effect. However, the MF correction involves finding more than one unknown parameter, which are termed MF kinematic attributes, and these can be determined using optimization algorithms. Thus, a manual procedure for MF is impractical and an automatic mode is necessary. This task previously is carried out by a computationally expensive iterative parameter-search algorithm. In this thesis, this problem is solved using a nonlinear global optimization method to converge to a more accurate estimation (Jodeiri Akbari Fam and Naghizadeh, 2019). In other words, the MF analysis consists of automatically calculating a panel of correlation (coherency) measures as a function of unknown parameters and finding the maximum of the panel.

Figure 1.4 summarizes the basic principle of the MF stacking method and its differences from the conventional methods. An anticline reflector is shown at the base of the panel (a). The segment R shown in red on the reflector is considered as an imaging target. The result of stacking is allocated to the zero-offset sample, here X_0 as an imaging point. The blue curve on panel (a) represents the common-midpoint reflection traveltime, collected at point X_0 for the subsurface point P. The common-offset traveltime curves are displayed in gray as a function of the midpoint for a range of constant half-offsets (half of the distance between the source and receiver). In this schematic figure, the traveltime curves are plotted for half of the offsets, since it is symmetric with respect to the offset of zero. The MF stacking surface is shown in red, which is accurately tangent to the reflection traveltimes. Note that the events are plotted here with time plotted increasing upwards. The common-midpoint stacking operator (blue) collects the reflection event (gray) only at a specific midpoint, X_0, whereas the MF stacking operator sums the data along the red surface that coincides locally with the common-offset time response of the reflector, and assigns the result to the point X_0. Figure 1.4b shows a single CMP gather on the left side of the panel (b) for the midpoint at -250 and its reflection raypaths at the right. The blue curve is the simulated common-midpoint traveltime curve. Here, this single slice of CMP gather is associated with the point X_0, which is indicated by a bold black dot at the right side. A super CMP gather which comprises 11 nearby slices of CMP gathers and its reflection raypaths are shown in Figure 1.4c. The red surface on the left side of the panel (c) is the fitted MF reflection surface. In this figure, each slice of CMP gathers corresponds to each nearby black dot in a certain span in the vicinity of the central point X_0. Overall, during the multifocusing processing sequence, we take advantage of seismic data that were acquired but are not included in the stacking step by conventional processing. In this approach, each zero-offset trace is constructed by staking traces, which does not need to belong to the same CMP gather, but their midpoints are close to X_0 (or reflection points are located in segment R). This would allow for maximally resolved data-driven reconstructions of the complex subsurface structure.

Traveltime moveout correction is one of the critical steps in the stacking procedure. An accurate moveout correction equation is required to be valid for arbitrary media and observation geometry. This implies that a correction operator needs to be independent of the subsurface geometry model and applicable for any geometric distribution of source-receiver pairs. The assumption of arbitrary acquisition geometry is violated in the normal moveout formulation since it belongs to the CMP-based method, which can be applied only when sources and receivers are located symmetrically with respect to an imaging point, X_0 in Figure 1.4. However, the MF approach is model-independent and valid for arbitrary acquisition geometry, because it can be applied to all reflection data that are reflected from a finite subsurface segment of arbitrary geometry, segment R in Figure 1.4, whose sources and receivers are in a certain vicinity of the imaging point (not a single reflection point about which the sources and receivers are located symmetrically). Therefore, both criteria can be satisfied by the MF method (Landa, 2007).

In the following subsections, I will review previously proposed MF methods. The review shows the process of extending MF-type methods for different situations and helps us to understand the advantages and weaknesses of different methods that will help us to develop new methods that aim to solve the seismic imaging problems arising with Metal Earth data.

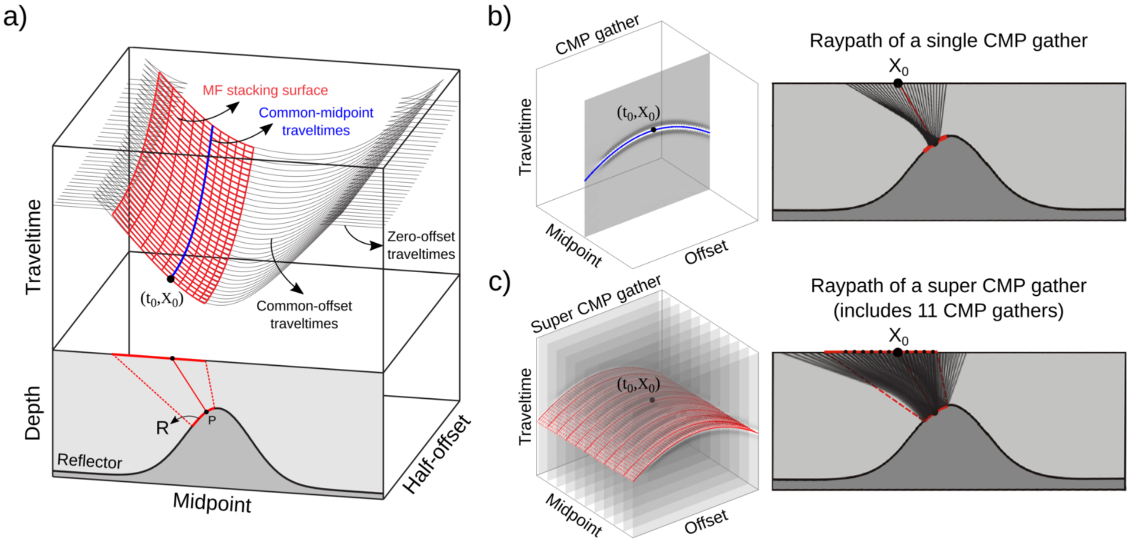

Figure 1.4: The basic principle of the multifocusing stacking method; a) The MF stacking surface for the anticlinal model (adapted from Müller, 1999; Abakumov, 2016); b) A single CMP gather for the midpoint located at X_0 and its reflection raypaths; c) A super CMP gather which comprises 11 nearby slices of CMP gathers and its reflection raypaths.

1.3.1 Standard MF method

The moveout formulation of the standard MF method is a double square-root operator. This method is also called planar MF by Landa et al. (2009), and zero-offset MF by Berkovitch et al. (2011). Figure 1.5a shows a normal ray starting at point X_0 with an angle β to the vertical line, reflects at normal-incidence-point (NIP), and returns to X_0, which is referred to as the central ray. The point X_0 represents the central point or as the image point where the stacked trace will be assigned after stacking. A paraxial ray from a randomly located source S intersects the central ray at point F, arriving back to the surface at receiver point R after reflecting off the point P. The paraxial ray refers to rays in the vicinity of the central ray, and their wavefield can be evaluated approximately from quantities determined along the central ray (Červenỳ et al., 1984; Schleicher et al., 2007). The point F in Figure 1.5a can be considered as a fictitious source of two fictitious waves with the wavefront rays $\sum^{+}$ (emitting from F upward to the surface) and $\sum^{-}$ (emitting from the point F downward, reflected at the reflector and emerging again at the point X_0). For a given source-receiver pair, in a 2D case, the MF moveout correction depends on three parameters: the emergence angle of the normal ray (β) and the curvature radii of the two fundamental wavefronts corresponding to the normal wave (R_N) and the normal incidence point wave (R_{NIP})) (Hubral, 1983; Gelchinsky et al., 1999a). Figure 1.5b shows wavefront $\sum_{NIP}$ of the NIP wave and Figure 1.5c shows the wavefront $\sum_{N}$ of the normal wave produced by a curved reflector under a homogeneous overburden with a near-surface velocity of V_0, respectively. In this context, the term overburden is all material above the reflector. The NIP wavefront ($\sum_{NIP}$) is formed by a point source located where the zero-offset ray emitted from the central point hits the reflector. The second wavefront ($\sum_{N}$) is formed by normal rays emitted by all points on the reflector (as in an exploding reflector scenario). The MF moveout equation is based on the spherical representation of wavefronts (Berkovitch et al., 1994) and expressed by

$$t(\beta, R_N, R_{NIP}) = t_0 + \triangle t_S + \triangle t_G, \tag{1.1}$$

$$\begin{aligned}
\triangle t_S &= \frac{\sqrt{\triangle X_S^2 + R_S^2 + 2.R_S.\triangle X_S.sin(\beta)} - R_S}{V_0}, \\
\triangle t_G &= \frac{\sqrt{\triangle X_G^2 + R_G^2 + 2.R_G.\triangle X_G.sin(\beta)} - R_G}{V_0}, \\
\sigma &= \frac{\triangle X_S - \triangle X_G}{\triangle X_S + \triangle X_G + \frac{2.\triangle X_S.\triangle X_G.sin(\beta)}{R_{NIP}}}, \\
R_S &= \frac{1+\sigma}{\frac{1}{R_N} + \frac{\sigma}{R_{NIP}}}, \quad R_G = \frac{1-\sigma}{\frac{1}{R_N} - \frac{\sigma}{R_{NIP}}},
\end{aligned}$$

where σ is the focusing parameter, t_0 is the traveltime of a central ray, V_0 is the near-surface velocity, and $\triangle t_S$ and $\triangle t_G$ are two moveout corrections at the source and receiver points of a paraxial ray. The variables $\triangle X_S$ and $\triangle X_G$ represent the source and the receiver offset for the given paraxial ray with respect to the central point X_0, respectively. Three parameters measured at the central point include β, R_{NIP}, and R_N. For each super-gather and each zero-offset time t_0, these parameters are obtained through a coherency analysis of the moveout-corrected super-gather (Berkovitch et al., 2008).

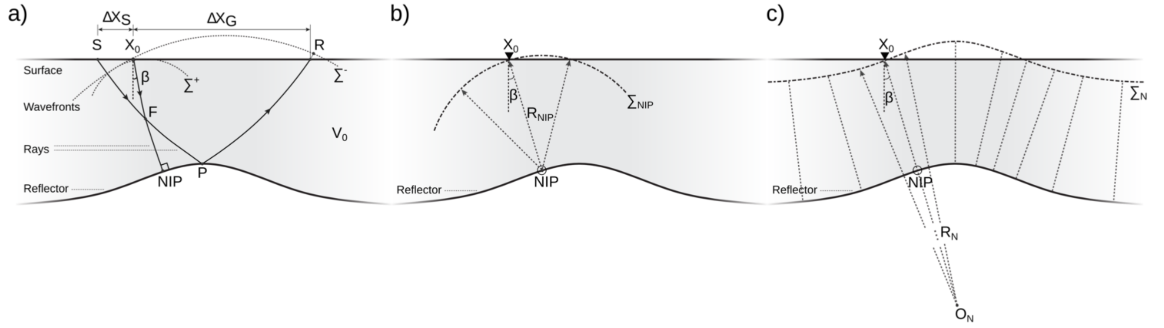

Figure 1.5: a) Ray scheme of the MF method for an arbitrary media, b) Wavefront $\sum_{NIP}$ of the NIP wave and, c) Wavefront $\sum_N$ of the normal wave produced by a curved reflector under a homogeneous overburden with a near-surface velocity of V_0 (Gelchinsky et al., 1999a; Jodeiri Akbari Fam and Naghizadeh, 2019).

1.3.2 Extensions of MF methods

Several researchers have extended MF imaging methods based on various scenarios and geometries. Here, I summarise some of the main developments in this area.

1.3.2.1 2D Irregular surface MF (IS-MF) method

Elevation statics correction is one of the processing steps, applied to seismic data to correct the difference between the source and receiver elevations. If seismic data are collected over a rugged topography, the standard elevation statics corrections might be inaccurate, since the assumption of vertical raypaths will no longer be valid. Gurevich et al. (2002) extended the standard MF method by taking into account the varying elevations of sources and receivers on an irregular surface (IS), so they termed this method the IS-MF method. They introduced this approach to apply directly to seismic data without prior elevation statics correction. This method corrects the elevation static, normal moveout, and dip moveout simultaneously. The application of the IS-MF to strongly non-hyperbolic synthetic CMP gathers that are generated over a highly variable topography indicates that, unlike, the conventional static correction and NMO that leads to residual moveouts, the IS-MF corrects the event by taking into account the rugged observation surface. This method does align the reflection event without distortions and noise and results in a better alignment of reflection events.

1.3.2.2 Common-offset MF (COMF) method

One of the main limitations of the zero-offset 2D MF method is a quasi-hyperbolic approximation for actual traveltime surfaces that limits the efficiency of its application.

The MF operator, in this case, is constructed around a zero-offset ray and, in principle, is valid for short offsets. In complex subsurface geology, strong lateral velocity variations and/or the presence of anisotropy may cause the traveltimes of seismic events to become nonhyperbolic, and the zero-offset 2D MF operator approximation starts to be inaccurate, especially for large offsets. Berkovitch et al. (2011) presented the COMF algorithm by accounting for the nonhyperbolicity of the traveltime surfaces that is a generalization of the zero-offset MF correction for the arbitrary offset case (without the spherical approach for the wavefield). The CMOF is a local MF time correction, which will accurately approximate the traveltime surface in the vicinity of an arbitrary non-zero-offset trace. The COMF operator is remarkably accurate even for strongly curved reflectors. Implementation of the COMF method requires determining five moveout parameters rather than defining three parameters as in zero-offset MF. To overcome the assumption of hyperbolic or quasi-hyperbolic approximation for traveltime curves/surfaces, this approach is applied on narrower offset ranges and does not require the full offset data in a super gather. Products of the COMF method are partially stacked common-offset images and sections of the wavefront parameters. The results can be used to generate enhanced prestack seismic records and it provides an accurate velocity model for depth imaging (Berkovitch et al., 2011, 2012b).

1.3.2.3 2D spherical MF (SMF) method

Landa et al. (2009) proposed the spherical multifocusing (SMF) method that significantly improved the accuracy of the MF method over curved reflectors. Unlike the zero-offset MF methods (MF and IS-MF) that express traveltime based on the kinematics of a central ray and the moveout correction for a paraxial reflection ray traveling in the vicinity of the central ray (Dörrie, 2013; Neumann, 1998). They derived the SMF operator based on finding the reflection traveltime for a source-receiver pair (as foci points of an ellipse) from a curved interface which is approximated by locally fitting a circle. In two dimensions, SMF needs the same triplet of parameters as the planar 2D MF method: β, R_N, R_{NIP}. They compared the application of the 2D planar and spherical MF with the CRS moveout expression for several synthetic models. The results indicated that the planar MF can be more accurate than the CRS method by increasing the curvature of the reflectors. This can be attributed to the fact that the CRS formula is based on a Taylor-series expansion, whereas the MF formulae are double-square root formulae. As a result, planar and spherical MF methods are better suited to model the moveout of diffracted waves. Landa et al. (2009) showed that SMF is more accurate than CRS and standard MF for highly curved reflectors (Fomel and Kazinnik, 2013).

1.3.2.4 2D irregular surface spherical MF (IS-SMF) method

Chang et al. (2019b) modified the SMF method (Landa et al., 2009) to apply to data acquired from irregular topography by considering non-zero elevations of sources and receivers. The new operator (IS-SMF) can correct the moveout of curved reflection directly without prior elevation static corrections and is more robust over a wide range of source and receiver elevations. Also, it performs better on strongly curved interfaces compared to the conventional method, resulting in an increased resolution in the stack and time-migration sections. Chang et al. (2019b) showed that the results obtained by the new operator also have better lateral continuity and a more focused performance compared with the results from an IS-MF operator, particularly for small-scale structural elements and curved reflection events with strong dips.

1.3.3 Limitations of the MF methods

Three-dimensional arbitrary survey geometry such as a crooked-line configuration is the theoretical issue that hampers our use of 2D MF methods. The complexity of the algebra involved in MF theory has prevented developing them into three dimensions and made it more difficult (Fomel and Kazinnik, 2013; Landa et al., 2009). Elhaj et al. (2014) proposed an application of the 3D MF method for imaging and regularization of an irregular 3D seismic data set. However, they have not further expanded on the corresponding formulations of the 3D MF method. Landa et al. (2009) proposed the spherical MF method in three dimensions by adding one more parameter to the two-dimensional spherical MF formula. Nevertheless, the 3D SMF method did not consider the variation of source and receiver elevations, and the recording surface is assumed to be flat and the formulation of 3D spherical multifocusing that can account for irregular acquisition surfaces has not yet been described in the geophysical literature. Hence, elevation statics corrections are required to compensate for the near-surface effects and to reference prestack data into a flat datum. Raypaths are typically assumed to be vertical in the conventional elevation statics correction methods. This assumption is mostly invalid and might lead to inaccurate static shifts for seismic data acquired in areas with severe irregular topography and complicated near-surface structures (Gurevich et al., 2002), particularly for high-velocity consolidated heterogeneous media in hard-rock geologic settings. Therefore, in order to use the MF methods for Metal Earth data, it is necessary to develop algorithms that take into account the azimuth-dependent dip effects, source-receiver azimuth, and coordinates variation in 3D space. To meet this need, I have developed new and generalized versions of the multifocusing moveout corrections with new strategies for crooked seismic lines and 3D surveys in an area with flat/irregular topography.

Furthermore, currently, the implementation of MF methods is technically challenging, computationally expensive, and has not been well documented. Applying the MF approaches comprises several isolated steps and lacks an efficient optimization component. This problem can be addressed by adopting a multi-dimensional nonlinear global optimization algorithm with high accuracy. Also, some global optimization strategies are required to speed up the convergence when searching for optimal parameters.

1.4 Research methodology

The current Ph.D. thesis is mainly focused on developing novel seismic imaging methods, as part of the Metal Earth initiative, to image complex subsurface geological structures of the Superior Province, Canada. Since September 2018 when I started my Ph.D. program, I began to form the framework of the thesis. I have used my mathematical background and skills to learn the fundamentals of the multifocusing method from original articles by Berkovitch et al. (1994); Gelchinsky et al. (1999a,b); Landa et al. (2009). I conducted an extensive literature review for the basics of MF from the scientific literature, which has been summarized in previous sections. The major part of my preliminary research was focused on programming of the 2D MF stacking package in *Matlab*, adapting nonlinear global optimization algorithms to implement the MF methods, and testing the scripted 2D MF code on complex synthetic data sets. In the absence of any software and code packages for academic and commercial use, I used my extensive programming skills to code the basic application of the 2D MF method on seismic data to reproduce the original implementation of this method. Next, I incorporated the global optimization algorithms into the multifocusing approach to optimize the estimation of MF parameters. I investigated the potential of using the very fast simulated annealing (VFSA) (Jodeiri Akbari Fam and Naghizadeh, 2019) and the differential evolution (DE) algorithms to optimize the estimation of MF parameters (see Appendix 1-A). Then, I examined the performance of the original 2D MF method on different complex synthetic models and real data. I successfully applied it to the well-known Marmousi synthetic complex data (Versteeg, 1994; Martin et al., 2006), which is a benchmark for testing the capability of imaging algorithms in the seismic industry. The Marmousi model involves severely curved and folded interfaces, horizontally layered horizons, and a series of nearly vertical normal faults with strong horizontal and vertical heterogeneity. The MF stacking method is a complicated algorithm, but I could reproduce the original implementation of the 2D MF method and add new optimization steps into its flow.

Then, I developed the 2.5D MF and 3D generalized spherical multifocusing (GSMF) methods to address the aforementioned seismic processing challenges and tested them by programming in *Matlab*. I also designed an efficient signal processing sequence for efficiently applying the proposed methods. I resolved how to generate 3D synthetic models and synthetic seismic data with a crooked line survey using the finite difference method and I used these synthetic data to test the newly developed algorithms. I investigated the accuracy of the new formulations by testing on synthetic data sets using the *Matlab* codes. Finally, I packaged production codes for efficient implementation of the newly developed 2.5D MF and 3D GSMF methods for crooked seismic lines and 3D surveys. These algorithms are developed in high-level but efficient languages such as C, C++, and shell scripts while using the framework of the Seismic Unix software package.

The developed software and codes have been used to image some of the seismic data acquired by the Metal Earth project, which for the most part are acquired in hard-rock environments with complex geological structures. Also, they were tested on other real seismic data sets. Further tests of the proposed algorithms in other applications and on real data examples are underway. In this thesis, my plan is to investigate both new algorithms independently to understand which approach is better suited for different situations.

1.5 Structure of the thesis

The current dissertation contains five chapters, including this introductory chapter (Chapter 1), and three journal manuscripts each in their own chapter (Chapters 2 – 4), and a concluding chapter (Chapter 5). Since chapter 2 is already published and chapters 3 – 4 are intended to be published as individual standalone manuscripts, some information is repeated in these chapters. A summary of each chapter is outlined below:

Chapter 1 (current chapter) presents background information on the project, research problems and objectives, theoretical and technical challenges associated with the crooked-line seismic surveys conducted for the Metal Earth project, and the methodologies applied to address the research problems. The chapter also includes a review of the theory behind the multifocusing algorithm, a summary of the main developments and their limitations are provided. The performance of the VFSA and DE global optimization algorithms in determining the wavefield attributes is also discussed in the Appendix 1-A.

Chapter 2, entitled "2.5D multifocusing imaging of crooked-line seismic surveys", introduces the 2.5D MF method to generate 2D zero-offset wavefields along crooked seismic surveys or a 3D zero-offset-wavefield volume for seismic data collected over an area with a flat datum and low to moderate overburden heterogeneity. The traveltime moveout formula is tailored for data collected along a crooked seismic line and it accounts for the cross-dip attributes and also the irregular distribution of sources and receivers along the acquisition line. The algorithm can be considered as a 3D extension for the planar multifocusing approach, which can explicitly correct 3D normal and azimuth-dependent dip moveouts simultaneously without any prior inline and crossline dip corrections. The method also accounts for midpoint scattering. In this chapter, the formulation for the 2.5D MF algorithm is first derived. Next, the performance of the proposed method on different synthetic and real seismic data sets is examined. Finally, the computational efficiency and accuracy of the proposed method are investigated. The 2.5D approach can approximate the 3D model of the wavefront, however, it assumes a locally spherical wavefront around the zero-offset central ray, which makes it accurate for quasi-hyperbolic reflections. This means that dipping plane reflectors can be mapped more accurately than strongly-curved interfaces. However, its capability is limited in resolving non-hyperbolic diffractions and reflections with higher-order traveltime moveout resulting from complex subsurface geology with strong lateral velocity variations and/or the presence of anisotropy. Also, the recording surface is assumed to be flat and its application is limited to seismic data acquired with a flat surface assumption. Hence, elevation statics corrections are required as a preprocessing step to compensate for the near-surface effects and to reference prestack data onto a flat datum. These weaknesses can be theoretically addressed by deriving another algorithm in three dimensions without the aforementioned assumptions, which is derived in Chapter 4.

Chapter 3, entitled "High-resolution 2.5D multifocusing imaging of a crooked seismic profile in a crystalline rock environment: results from the Larder Lake area, Ontario", is focused on the application of the novel 2.5D multifocusing method to the Metal Earth hard-rock seismic data collected in Larder Lake to exhibit its robustness compared to the conventional and other advanced processing methods. First, the technical and theoretical challenges associated with crooked-line surveys in hard-rock geological settings are discussed. Next, the theory behind the 2.5D MF algorithm is briefly reviewed, as well as its advantages and disadvantages. Afterward, the geological settings of the Larder Lake area and the specifications of the seismic data acquisition are described. Then, the workflow and results of conventional and advanced methods (2D prestack time migration, 2D time migration of DMO stack, and swath 3D imaging) are presented. The processing steps employed in the 2.5D MF imaging workflow were discussed in detail. I also developed an efficient processing workflow for applying the 2.5D MF method and utilizing its output for further imaging steps including prestack/poststack migration. Also, I describe the manner that the differential evolution global optimization algorithm has been adapted to optimally search for the wavefield attributes. To evaluate the accuracy and performance of the proposed method on a seismic data set with a real crooked-line survey geometry, I tested the 2.5D MF method on synthetic data generated using the survey configuration used in the Larder Lake area. Next, the application of the 2.5D MF technique on the Larder Lake reflection seismic data set is compared with the results of the 2D and 3D conventional standard and advanced methods, that were previously presented. Finally, a brief interpretation and discussion are provided. The 3D swath processing result clarified the necessity of processing cooked-line seismic data using a 3D approach, which included an algorithm that can generate a high-resolution true representation of the zero-offset wavefield. Assuming azimuthally isotropic constant radii of curvatures for each subsurface point allows the wavefield attributes to be estimated even with a limited number of distinct azimuth data. These capabilities enable us to produce a volumetric stack from a crooked-line survey using the 2.5D MF method. The main limitation is the assumption of a locally spherical wavefront that limits its application to the planar and gently curved reflector with mild to moderate heterogeneities. This limitation and the flat datum assumption are addressed in the next chapter.

Chapter 4, entitled “3D generalized spherical multifocusing seismic imaging”, proposes a non-hyperbolic higher-order moveout operator that is required to improve a stacked volume constructed from seismic data acquired over an area with rugged topography and strong heterogeneous overburden. A three-dimensional generalized spherical multifocusing seismic stacking method is expanded for a crooked-line/3D seismic data set acquired with an arbitrary recording geometry. The algorithm is based on a 3D extension of the spherical multifocusing method into a more general form. The extended method simultaneously corrects for elevation statics and azimuth-dependent dip-moveout effects, which results in a 3D stacked volume that is equivalent to a synthesized 3D zero-offset wavefield. In this chapter, first, the relevant background is reviewed. Then, the traveltime formula for the 3D GSMF algorithm is derived. Next, the performance of the proposed method is examined on synthetic and real data sets. Finally, the efficiency and accuracy of the method are evaluated and the results are discussed. Although, the 3D GSMF method can be more accurate than the 2.5D MF method for simulating higher-order reflections and diffractions. However, the 3D GSMF method has a high computational cost. Therefore, the size and nature of the study area, the goal of the project, and budget limitations will determine which methods would be more suited.

Chapter 5 summarizes the thesis and presents the overall conclusions of the project. Also, this chapter suggests possible future work. Additionally, this chapter outlines some of the further developments that are underway.

Appendix 1-A: Comparing the performance of the VFSA and DE algorithms

I applied the 2D MF method on the Marmousi synthetic data to reproduce the original implementation of the multifocusing, and test the performance of the VFSA and DE global optimization algorithms. Figure 1-A.1 compares the effectiveness and efficiency of the DE and VFSA algorithms in searching for the optimal solution of the 2D MF attributes. Figures 1-A.1a and 1-A.1b show the convergence graph of 10 random single execution for the VFSA and DE algorithms, respectively. I examined convergence behavior for the same common-midpoint and zero-offset time sample (CMP = 200; time = 1.788 s). The VFSA and DE algorithms reached the global maximum after approximately 400 and 550 evaluations of the objective function, respectively. Comparing these graphs demonstrates that the VFSA method is computationally cost-effective, however, the DE algorithm is more accurate and precise than the VFSA algorithm. The VFSA method can reach the global maximum faster than DE, but it is accompanied by uncertainty. In Figure 1-A.1c, we compare the computational cost of these two methods. The CPU load of the VFSA method is referenced as 100 percent, the DE algorithm has about 15% more costs than the VFSA method. In terms of computational costs, the DE algorithm spends more CPU time than VFSA, since the DE method requires a greater number of objective function evaluations to converge to the global maximum. Also, the DE algorithm itself involves several arithmetic operations for each iteration. To reduce the running time of the DE algorithm, the optimization and controlling parameters of DE algorithms can be fine-tuned. Overall, both methods are suitable for wavefield analysis and stacking, which can be chosen based on the desired accuracy or efficiency.

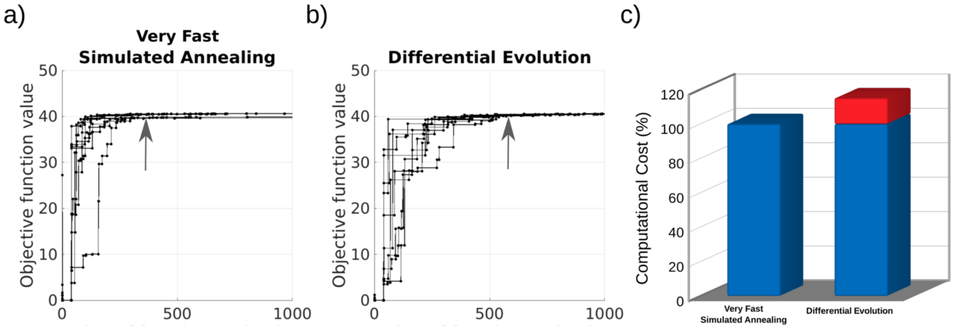

Figure 1-A.1: Convergence graphs of the global simultaneous searches of the three attributes for the 2D MF stacking operator using the a) VFSA algorithm and b) DE algorithm for 10 random single runs. c) Computational costs of the DE and VFSA methods.

Chapter 2

2.5D multifocusing imaging of crooked-line seismic surveys

Hossein Jodeiri Akbari Fam [1*], Mostafa Naghizadeh [1] and Öz Yilmaz [2]

[1] Mineral Exploration Research Centre, Harquail School of Earth Sciences, Goodman School of Mines, Laurentian University, Sudbury, Ontario, Canada.

[2] Anatolian Geophysical, Urla, Izmir, Turkey.

[*]Corresponding Author E-mail: hjodeiri@laurentian.ca

2.1 Abstract

Two-dimensional seismic surveys often are conducted along crooked line traverses due to the inaccessibility of rugged terrains, logistical and environmental restrictions, and budget limitations. The crookedness of line traverses, irregular topography, and complex subsurface geology with steeply dipping and curved interfaces could adversely affect the signal-to-noise ratio of the data. The crooked-line geometry violates the assumption of a straight-line survey that is a basic principle behind the 2D multifocusing (MF) method and leads to crossline spread of midpoints. Additionally, the crooked-line geometry can give rise to potential pitfalls and artifacts, thus, leads to difficulties in imaging and velocity-depth model estimation. We develop a novel multifocusing algorithm for crooked-line seismic data and revise the traveltime equation accordingly to achieve better signal alignment before stacking. Specifically, we present a 2.5D multifocusing reflection traveltime equation, which explicitly takes into account the midpoint dispersion and cross-dip effects. The new formulation corrects for normal, inline, and crossline dip moveouts simultaneously, which is significantly more accurate than removing these effects sequentially. Applying NMO, DMO, and CDMO separately tends to result in significant errors, especially for large offsets. The 2.5D multifocusing method can perform automatically with a coherence-based global optimization search on data. We investigated the accuracy of the new formulation by testing it on different synthetic models and a real seismic data set. Applying the proposed approach to the real data led to a high-resolution seismic image with a significant quality improvement compared to the conventional method. Numerical tests show that the new formula can accurately focus the primary reflections at their correct location, remove anomalous dip-dependent velocities, and extract true dips from seismic data for structural interpretation. The proposed method efficiently projects and extracts valuable 3D structural information when applied

to crooked-line seismic surveys.

2.2 Introduction

The ultimate goal of seismic time imaging is to generate a high-resolution seismic section with an improved signal-to-noise ratio (S/N). A seismic survey with crooked line geometry collects data with variable fold and uneven offset distribution, which, in turn, leads to seismic transparent zones (Wu, 1996). Irregular distribution of sources and receivers along a crooked profile disperses the midpoint locations from the intended straight-line traverse. The crooked nature of seismic lines could defocus and deform reflections particularly associated with reflectors with a cross-dip component. Also, the raypaths between source and receivers take shortcuts passing around the survey line (behind or in front of the desired imaging plane).

In a crooked-line seismic survey, the cross-dip not only causes defocused and smeared reflections but also results in considerable time shifts as a function of the cross-offset distribution. These time shifts can distort and duplicate out-of-plane reflections after applying cross-dip moveout (CDMO) correction using the slant stack approach. For relatively uniform cross-offset distributions, seismic events could appear twice in the stacked section: (1) at the origin zero-offset time and (2) at the shifted time corresponding to the preponderant cross-offset (Beckel and Juhlin, 2019). This problem is called reflection duplication.

Several different cross-dip analysis and correction methods have been proposed by various researchers to address the aforementioned potential pitfalls (Larner et al., 1979; Du Bois et al., 1990; Kim et al., 1992; Wu et al., 1995; Nedimović and West, 2003a; Malehmir et al., 2009; Singh et al., 2010; Kim et al., 2014). Applying a constant shift to the whole trace is the easiest and most common method for cross-dip correction (Larner et al., 1979; Wu et al., 1995; Rodriguez-Tablante et al., 2007; Lundberg and Juhlin, 2011; Ahmadi et al., 2015). However, this method generally reduces the resolution of the final image. Nedimović and West (2003a) introduce a more general form of the CDMO that can be carried out through a slant-stack transformation (Yilmaz, 2001) after removing normal moveout and inline dip effects. This approach can be done automatically by maximizing the product of semblance and a local average of the amplitudes using a grid search strategy. Kim et al. (1992) and Kim et al. (2014) use the same approach but determine the cross-dip parameter interactively. This method can partially correct cross-dip effects and generate improved images; however, it could duplicate out-of-plane reflections in the stack section. In this case, the reflection might be imaged twice in the stack section when a CDP gather has a dominant cross-offset value. Besides, using a slant-stack approach prevents to apply any further processing after the cross-dip correction because the cross-dip correction is applied for the estimated cross-dip while stacking with the slant-stack technique (see Nedimović and West, 2003a; Beckel and Juhlin, 2019). Another drawback is that the DMO operator may interpret time shift and moveout arising from cross-dip effects as an inline dip time anomaly (after NMO correction and before CDMO correction). Therefore, the estimated moveout and structural details will not be correct. Beckel and Juhlin (2019) use a shift and stack method to overcome these problems. They assume that the reflector has no dip component along the inline direction and carried out an iterative processing procedure for the implementation of the moveout corrections. They repeated the flow of NMO correction, CDMO correction, velocity analysis, DMO correction until a high-quality stacked section was obtained. Mancuso and Naghizadeh (2021) introduce the generalized CDMO (GCDMO) method that can be applied to any CMP binning geometry. This approach simultaneously corrects the NMO plus CDMO effects and can suppress the reflection duplication. The optimal attributes are manually estimated using repetitive grid search across a window, and its accuracy is limited to a maximum of 40°.

One can also use a 3D processing and binning method to produce an image from crooked-line geometry data. Crooked-line seismic data could be considered as pseudo-3D data set as the source-receiver midpoints span a surface rather than a line (Wu, 1996; Nedimović and West, 2003b). Panea and Bugheanu (2017) process crooked-line survey seismic data like a pseudo-3D survey. Cheraghi et al. (2020) use 2D and 3D prestack time migration and swath 3D processing methods. Application of 3D processing technique on 2D crooked-line seismic data often could lead to low-resolution images and could not image many reflections that are observed in 2D results. All these advanced imaging algorithms require an accurate velocity model, which needs to be dip-independent, except for macro-model-independent approaches. Besides, low fold and noisy data hamper utilizing such an advanced 3D processing method. Also, in a complex subsurface area, due to variable and low-fold coverage, crooked-line configuration with CMP binning does not provide enough information. Also, the collected data have uneven spatial distribution and are limited to a narrower azimuth and a small aperture in the cross-profile direction (Nedimović and West, 2003a).

The non-CMP-based multi-parameter moveout corrections and stacking strategies, such as multifocusing (MF) method, could also address the issues related to CMP dispersal problems (Gelchinsky et al., 1999a,b). There are two major types of non-CMP-based multiparameter moveout corrections and stacking strategies. These include the multifocusing (MF) and common reflection surface (CRS) method that were originally developed by Gelchinsky et al. (1999a,b) and Müller (1999), respectively. The MF method can be more accurate than the CRS method, but it is more difficult to extend it to 3D cases (Fomel and Kazinnik, 2013; Landa et al., 2009). Höcht (2002) and Müller (2003) present the theory and implementation of the 3D zero-offset CRS stack, which can be applied on crooked-line seismic data. During the last two decades, different MF stacking techniques based on the patented theory of homeomorphic imaging (Gelchinsky, 1992; Gelchinsky and Keydar, 1999) have been proposed. These include the 2D MF (Gelchinsky et al., 1999a,b), 2D irregular surface MF (IS-MF) (Gurevich et al., 2002), 2D MF with controlled reflection-point dispersal (Gurevich and Landa, 2002), common-offset MF (COMF) (Berkovitch et al., 2011, 2012b), 2D spherical MF (SMF) (Landa et al., 2009), and 2D irregular surface spherical MF (IS-SMF) (Chang et al., 2019b) methods. Also, the application of 2D multifocusing for improved time imaging is widely published (Landa et al., 1999; Berkovitch et al., 2004; Belfer et al., 2008b; Berkovitch et al., 2008, 2009, 2012a; Curia et al., 2012; Buzlukov and Landa, 2013; Landa et al., 2013; Elhaj et al., 2014; Schoepp et al., 2014; Borghi et al., 2017; Curia et al., 2017; Chang et al., 2019a).

The MF-based methods provide higher S/N and vertical resolution and do not require any knowledge of the subsurface model. Also, it can determine dip-independent velocities and structural detail such as interface curvature and slope of the events (Landa et al., 2009). The MF methods are time-shifted approaches and derived based on the assumption of optical imaging (auxiliary) medium for taking into account overburden heterogeneity (De Bazelaire, 1988; Gurevich and Landa, 2002; Schwarz and Gajewski, 2017). This assumption leads to a non-stretching moveout correction without distortion of the amplitude and phase, which can be one of the MF operators' key advantages. However, currently, the available MF operators do not consider the cross-offset and cross-dip components for the crooked-line configuration. In this paper, we develop a non-CMP-based stacking method for crooked-line seismic data imaging to address the above issues.

In the following sections, we first derive the formulation for the 2.5D MF algorithm. Next, we examine the performance of the proposed method on appropriate synthetic and real seismic data sets. Finally, the computational efficiency and accuracy of the proposed method are investigated.

2.3 Theory

We develop an MF traveltime correction formula tailored for data collected along a crooked seismic line (Jodeiri Akbari Fam and Naghizadeh, 2020). The formula includes an ability to take into account the cross-dip attributes and also the irregular distribution of sources and receivers along the acquisition line. The main advantage of the new formulation is its ability to correct the moveout of 3D dipping events directly without any prior inline and crossline dip corrections. The case of a dipping plane reflector can be imaged more accurately than spherical bodies using this method. Our proposed method can be considered a 3D planar multifocusing approach; however, we will use the term 2.5D multifocusing in this article for convenience. The new 2.5D moveout formula is exact for 3D plane-dipping reflectors of arbitrary inline and crossline dips in a constant velocity model, and also limiting cases such as point scatterers. However, the method does not account for variable topography.

After signal processing and elevation statics corrections, first, we bin the seismic data on a slalom/straight processing line that best fits the distribution of midpoints. The optimal size of bins is calculated using the Fresnel zone analysis (Hubral, 1983; Gurevich et al., 2002; Berkovitch et al., 2009). We build CMP super gathers by comprising several nearby common midpoint gathers in order to achieve a high fold reflection gather. This will result in a high S/N stack section by constructively stacking the reflection data.

Next, we remove the normal, inline, and crossline dip moveouts using dynamic (time- and offset-variant) time shifts. Such time shifts are especially important for correcting the far-offset data. In this regard, we extended 2D multifocusing to 2.5D by modifying the emergence angle and the curvature radius of the normal-incident-point wave (R_{NIP}). The proposed formulation also includes an extra term that corrects for the zero-offset time shift in order to avoid the reflection distortion and duplication problems (see Beckel and Juhlin, 2019).

Snell's law states that the incident and reflected rays from a reflection point should reside in the same plane with the reflector normal. Therefore, we can treat each source-receiver pair as a 2D seismic survey acquired in a specific direction. By taking into account the azimuthal variation of each source and receiver pair, we derive functions that connect the emergence angle and R_{NIP} to the apparent dip. Finally, we will decompose the derived apparent dips to inline and crossline dip components. Also, spherical bodies can accurately approximate locally 3D curved reflectors (Landa et al., 2009). Therefore, It can be assumed that we can recognize curved events and model their geometry (shape or form) with only one curvature. Here, for simplicity, we consider a dipping locally planar reflector embedded in a constant velocity (V_0) half-space (Figure 2.1).

Figure 2.1 shows the ray geometry for a crooked-line survey configuration above a 3D dipping reflector with inline dip θ_x and crossline dip θ_y components. Here, the inline and crossline directions are assumed to be along the $x-$ and $y-$axes, respectively. The black solid and dashed lines are the survey and processing lines, respectively. In order to mitigate the effect of spreading source-receiver over the cross profile, the slalom processing line (black dashed line) has been chosen that is best fitted to the midpoints. Projecting the midpoint locations onto a slalom line by applying a crooked-line binning method suppresses acquisition geometry artifacts and optimally regularizes the trace fold amongst bins (Du Bois et al., 1990; Rodriguez-Tablante et al., 2007; Juhlin and Lund, 2011). An optimal processing line can be created using two approaches, including (1) low-order polynomial regression and (2) smoothing the receiver line. The first method fits a low-order polynomial curve to the midpoints by minimizing the orthogonal distance between the imaging point and midpoints. In the second approach, a smoothed curve can be generated by repeatedly applying a mean filter to the receiver line until its vertices approach the centers of the maximum accumulation of midpoints. To calculate imaging point coordinates, the arc length of the processing line can be approximated by linear segmentation. Then, we divide it up into equal-length space. The center of each interval is the imaging point. $M_0 = [X_{M_0}, Y_{M_0}]$ is an arbitrarily chosen imaging point on the processing line, and M'_0 is the intersection between the orthogonal to the processing line and a line that connects the source and receiver ($S - R$). The distance between M_0 and M'_0 is defined as a crossline shift. In this configuration, instead of a normal ray used in the 2D multifocusing (Berkovitch et al., 2008) method, we consider a normal plane, which is indicated by the transparent gray-colour plane. This plane has an inclination of β with respect to the vertical axis along the true dip direction, which is called the central plane. The central plane contains the orthogonal (normal) to the processing line ($M_0M'_0$), and its direction has the angle of ϕ'' with respect to the inline direction. A normal ray starts at M_0, hits the reflector at point M_c, and returns back to M_0—referred to as the central ray for the imaging point. Also, another normal ray starts at M'_0 and is reflected back from point M'_c. These two normal rays M_0M_c and $M'_0M'_c$ are coplanar, and the central plane includes them both. A paraxial reflection ray (solid blue ray) is generated by a randomly located source $S = [X_S, Y_S]$ on the crooked profile that intersects the central plane at point F, reflects off the dipping reflector at point O, arriving back to the surface, and is recorded by the receiver $R = [X_G, Y_G]$. The source and receiver $S - R$ surface line (connected with a blue dashed line) makes an angle ϕ' with respect to the inline direction. The reflector has the apparent dip of β' and β'' along the source and receiver $S - R$ line and the orthogonal to the processing line M_0M_0', respectively.

In this case, the differences in zero-offset time, caused by the difference between R_{NIP} and R'_{NIP} shown in Figure 2.1, could lead to vertical shifts, distortion, and event duplication after stacking. Employing a slalom processing line (curved crooked-line binning) suppresses artifacts of the cross-dip component and prevents reflection duplication partly but cannot completely mitigate them (Mancuso and Naghizadeh, 2021). In order to overcome these issues, we add an extra term that corrects for the zero-offset time shift. Table 2.1 summarizes the description of the parameters used in our paper. The 2.5D multifocusing traveltime (t) is derived in Appendix 2-A and expressed as follows:

$$t(\theta_x, \theta_y, R_N, R_{NIP}) = t_0 + \frac{2\ D\ \sin(\delta)}{V_0} + \triangle t_S + \triangle t_G, \tag{2.1}$$

where

$$\triangle t_S = \frac{\sqrt{\triangle X_S^2 + R_S^2 + 2\ R_S\ \triangle X_S\ \sin(\beta')} - R_S}{V_0}, \qquad \triangle X_S = \sqrt{(X_S - X_{M_0'})^2 + (Y_S - Y_{M_0'})^2},$$

$$\triangle t_G = \frac{\sqrt{\triangle X_G^2 + R_G^2 + 2\ R_G\ \triangle X_G\ \sin(\beta')} - R_G}{V_0}, \qquad \triangle X_G = \sqrt{(X_G - X_{M_0'})^2 + (Y_G - Y_{M_0'})^2},$$

$$\sigma = \frac{\triangle X_S - \triangle X_G}{\triangle X_S + \triangle X_G + \frac{2\ \triangle X_S\ \triangle X_G\ \sin(\beta')}{R'_{NIP}}}, \qquad R_S = \frac{1+\sigma}{\frac{1}{R_N} + \frac{\sigma}{R'_{NIP}}}, \quad R_G = \frac{1-\sigma}{\frac{1}{R_N} - \frac{\sigma}{R'_{NIP}}},$$

$$\tan(\beta') = \tan(\theta_x)\ \cos(\phi') + \tan(\theta_y)\ \sin(\phi'), \qquad \sin(\delta) = \tan(\beta'')\ \cos(\beta),$$

$$\tan(\beta'') = \tan(\theta_x)\ \cos(\phi'') + \tan(\theta_y)\ \sin(\phi''), \qquad \tan(\beta) = \sqrt{\tan^2(\theta_x) + \tan^2(\theta_y)},$$

$$R'_{NIP} = R_{NIP} + (D\ \sin(\delta)),$$

and t depends on four unknown parameters $(\theta_x, \theta_y, R_N, R_{NIP})$. The second term $(\frac{2\ D\ \sin(\delta)}{V_0})$ avoids reflection duplication by taking into account the zero-offset time shift along the normal incident ray from the point M_0' to the reflector. In fact, this term shifts back reflections' arrival time to their origin time by projecting them into the imaging plane.

The analysis is performed for a homogeneous overburden; however, this can be extended to the inhomogeneous case using the theory of an auxiliary medium (Gurevich and Landa, 2002; Schwarz and Gajewski, 2017). The auxiliary medium can be defined as a homogeneous medium with the velocity equal to the near-surface velocity (V_0), where both the central and paraxial rays are represented with combinations of straight-line segments (Perroud et al., 1999). Therefore, for a heterogeneous overburden, the proposed derivation corresponds to the moveout approximation in the auxiliary medium.

The application of the 2.5D MF method to generate the zero-offset wavefield reduces to the conventional transformations NMO+DMO+CDMO+stack for the case of a super gather with only one CMP. We tested the 2.5D MF method on a CMP gather, and the results indicate that the MF method and conventional transformation have almost the same results, but MF corrected gather is stretch-free and has a better alignment for the case of a curved reflector with low to moderate overburden heterogeneity. This can be

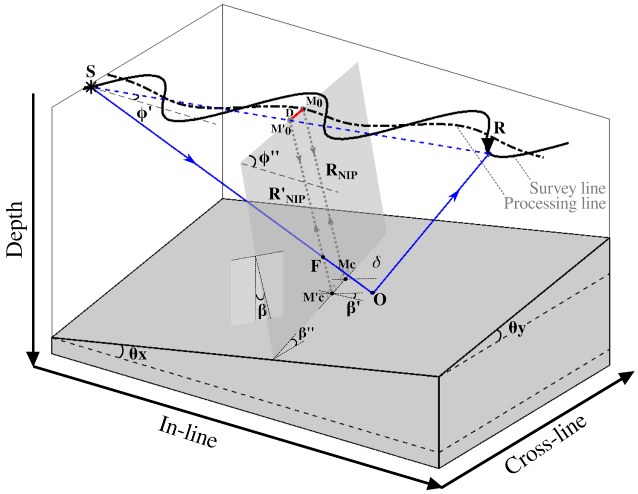

Figure 2.1: 3D Ray scheme of the 2.5D multifocusing method for a dipping plane reflector with constant velocity for a 2D crooked-line survey.

Table 2.1: Nomenclature

Parameters	**Parameter description**	**Parameters**	**Parameter description**
t_0	Zero-offset time	V_0	Near surface velocity (m/s)
θ_x	Inline dip	θ_y	Crossline dip
ϕ'	Angle between Inline and SR	ϕ''	Angle between Inline and M_0M_0'
R_{NIP}	NIP wave radius at M_0	R'_{NIP}	NIP wave radius at M_0'
R_N	Normal wave radius at M_0	β	Emergence angle of the central ray M_0M_c with respect to the vertical axis along with the true dip
σ	Focusing ratio	D	Crossline shift
β'	Apparent dip along SR (or emitting angle of $M_0'M_c'$ with respect to the projected vertical axis in the plane contains S-O-R)	β''	Apparent dip along M_0M_0'
δ	β'' projection on the central plane		
$\triangle t_S$	Moveout at source	$\triangle t_G$	Moveout at receiver
$\triangle X_S$	Offset between source and M_0'	$\triangle X_G$	Offset between receiver and M_0'
R_S	Radius of fictitious wavefront (F to S)	R_G	Radius of fictitious wavefront (F-O-R)
$[X_S, Y_S]$	Source coordinate	$[X_G, Y_G]$	Receiver coordinate
$[X_{M_0}, Y_{M_0}]$	Image point coordinate	$[X_{M_0'}, Y_{M_0'}]$	Coordinate of the intersects between an orthogonal line to the processing line and a line that connects $S-R$

attributed to the fact that the MF formulae are double-square root formulae, and it is not based on Taylor expansion.

By substituting crossline shift with zero ($D = 0$), the proposed MF equation exactly is simplified into standard 2D MF. Therefore, the straight-line 2D MF formula is a special case of the crooked-line 2.5D MF equations. In this case, the number of unknown parameters drops from four to three. Also, the practical implementation of diffraction stacking is a special case of multifocusing implementation (Berkovitch et al., 2009). The 2.5D MF operator is equally valid for two limiting cases: the planar reflector $R_N = \infty$ and the point diffractor $R_N = R_{NIP}$ (Landa et al., 2009; Fomel and Kazinnik, 2013). Therefore, by using ($R_N = R_{NIP}$) assumption and converting apparent dips to the emergence angles in 2.5D MF formulation, we could generate a diffraction stack. Such sections contain important information for identifying local heterogeneities and discontinuities in the subsurface. The specular and diffraction stack can be summed up to generate a true zero-offset wavefield.

2.4 Model experiments

We examined the performance of the proposed 2.5D MF operator on different numerically modeled synthetic data sets. The optimization step for determining the unknown parameters of the method was carried out with nonlinear global optimization algorithms such as differential evolution (DE) or very fast simulated annealing (VFSA) (Jodeiri Akbari Fam and Naghizadeh, 2019). These algorithms can perform automatically using a data-driven global optimization approach based on a coherency objective function. Here, performing automatically means a non-interactive process, which requires only quality control of the convergence behavior. For example, velocity picking is a time-consuming interactive task that is labor-intensive in order to build an accurate velocity model. However, in the global optimization method, we just need to adjust the parameters of the optimization algorithm. The coherency function is defined using the correlation of reflection amplitudes.

2.4.1 Single planar reflectors

Figure 2.2a depicts a super gather acquired above a single dipping layer that has both inline and crossline dip components. The model ($V_{P1,2} = 1000, 2000$ m/s and $\theta_{x,y} = 15, 10°$), acquisition, and processing lines are shown in Figure 2.1. This super gather, located in the middle of the survey, comprises five nearby CMP gathers; as such, the fold is increased by a factor of five. Figure 2.2a shows that the reflection includes considerable time shifts and breaks. These are the result of the crooked-line acquisition and the presence of a cross-dip component in the data. Figure 2.2b shows the super gather after applying the 2.5D MF moveout correction. The reflection has almost perfectly aligned across all of the near- and far-offsets. This shows that the proposed 2.5D MF method is accurate in a large range of offsets and midpoints. The 2.5D moveout correction yields flattening of the reflection event on the super gather. Combined with the high fold of the super gather, the resulting stacked section is equivalent to a zero-offset wavefield with high S/N.

Figure 2.3 shows three simple models (top row) and their typical super gathers before (middle row) and after (bottom row) applying the 2.5D MF moveout correction. The V_{P1} and V_{P2} are 1000 and 2000 m/s, respectively. The super gather location, survey layout, and processing line are the same as in the previous example shown in Figure 2.2. Figure 2.3a shows an inline dipping interface model ($\theta_x = 15°$). This reflection contains normal moveout, dip moveout, and midpoint dispersion effects. In Figure 2.3b, the cross-dipping model ($\theta_y = 10°$), time anomalies are the result of normal moveout, cross-dip moveout, and cross-offset variation. Figure 2.3c shows the application of the proposed method on a horizontal interface. Overall, the cross-dip component contributes more than other factors to an uneven distribution of data with considerable time shifts on the reflection events. The proposed 2.5D MF method was able to correct all of the moveout effects in different models. Therefore, this method can be an alternative method for cascaded application of normal, inline dip, and cross-dip moveout correction in crooked-line surveys. Also, it can handle situations with irregularly distributed sources and receivers across the acquisition lines.

2.4.2 Curved and multiple reflectors

We also generated several 3D curved and multi-layer synthetic models to investigate the accuracy of the proposed 2.5D MF method and to compare its results with other algorithms, such as the GCDMO and 2D MF methods. The synthetic seismic data for these models were generated using the finite-difference method (Bohlen, 2002). Figure 2.4

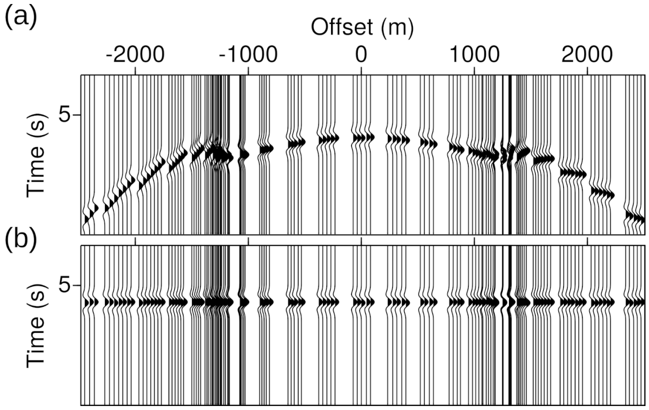

Figure 2.2: A super gather synthetized in the middle of the survey and model shown in Figure 2.1 a) before and b) after applying the proposed 2.5D MF method.

shows six different synthetic velocity models, including a single strongly curved sphere reflector with a constant curvature (Figure 2.4a), a single gently curved layer with positive curvatures and vertical heterogeneity (Figure 2.4b), a single gently curved anti/synform layer with positive and negative curvatures and lateral heterogeneity (Figure 2.4c), conflicting dip planar reflectors (see Yilmaz, 2001) (Figure 2.4d), multiple planar dipping reflectors (Figure 2.4e), and multiple gently curved reflectors (Figure 2.4f). Figure 2.5a shows the crooked-line seismic survey geometry that we used to generate the synthetic data sets for the aforementioned models. In this Figure, red and blue dots are the source and receivers, respectively, and the solid black line is the processing line. The processing line is a slalom line and has been generated based on the midpoint locations. This line was fit to midpoints by applying a mean filter to the receiver line. We then divided the processing line into equal-length intervals with constant radius (prism-like bins). The midpoints were binned every 10 m along this line at a maximum radius of 500 m. We selected four different imaging point locations (#100, #200, #300, and #400) as repre-

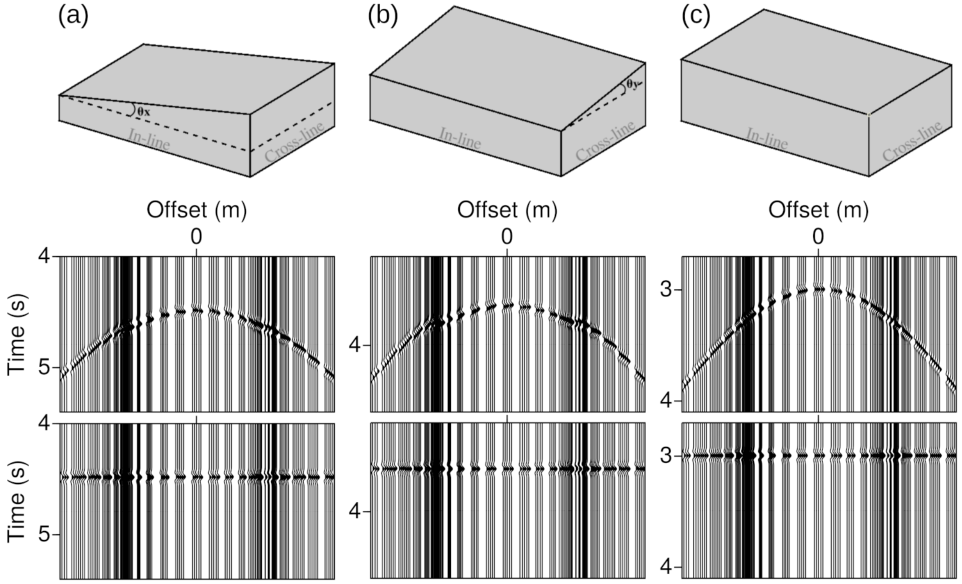

Figure 2.3: 3D toy models and their super gathers before and after applying the proposed 2.5D MF method. Dipping interface along a) inline and b) crossline directions. c) Horizontal interface.

sentative of the entire data to illustrate the results. These are shown with black squares that are labeled with their common midpoint location number in gray.

Figure 2.5b depicts crooked-line seismic binning (with constant CMP intervals) for building super gathers. In this figure, the processing line is coloured with fold numbers, which indicate the number of traces that belong to a super gather in the MF method. Here, midpoint locations are shown with gray map coloured dots that are distributed around the acquisition line. The green dots show seismic traces (midpoint locations) that belong to each of the selected super gathers (#100, #200, #300, and #400). These super gathers comprise nine nearby CMP gathers that increase the fold by a factor of nine.

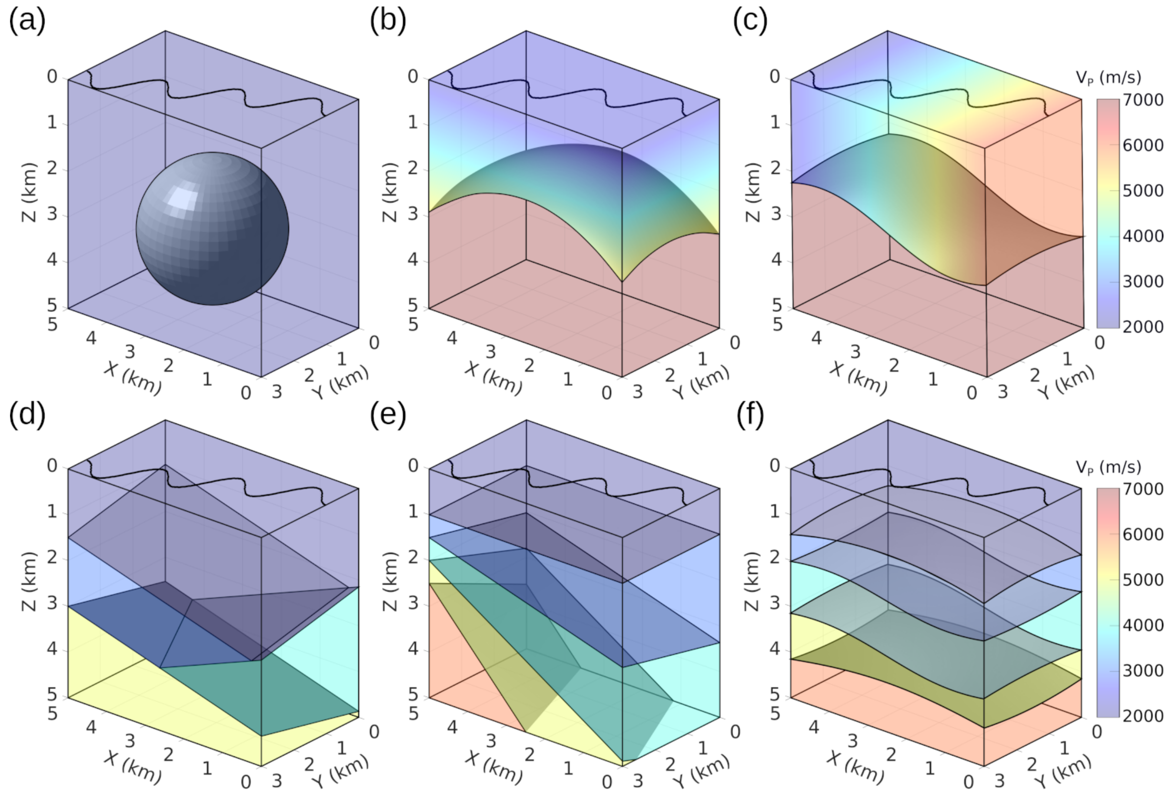

Figure 2.4: 3D synthetic velocity models that include a) single sphere reflector, b) single curved reflector with inhomogeneous background velocity (vertical velocity variation), c) single curved antiform-synform reflector with heterogeneous overburden (lateral velocity variation), d) multi conflicting reflectors, e) multi flat reflectors, and d) multi curved reflectors.

The intensity of the crossline shift effect on the reflection seismic data can be demonstrated with the distribution of these green dots along the direction perpendicular to the processing line. For instance, super gather #300 has the largest crossline shift effect among these four super gathers since the midpoint of this super gather distributed farther from the processing line compared to the others. The main goal is to collapse all of the recorded energies in a specific super gather (green dots located in a specific super bin) to the corresponding imaging point on the processing line (black squares).

Figures 2.6 and 2.7 compare the results of applying the 2.5D MF operator on the synthetic super gathers for the single sphere reflector (Figure 2.4a) and single curved reflector (Figure 2.4b) with NMO and GCDMO corrections, respectively. Figures 2.8 and 2.9 de-

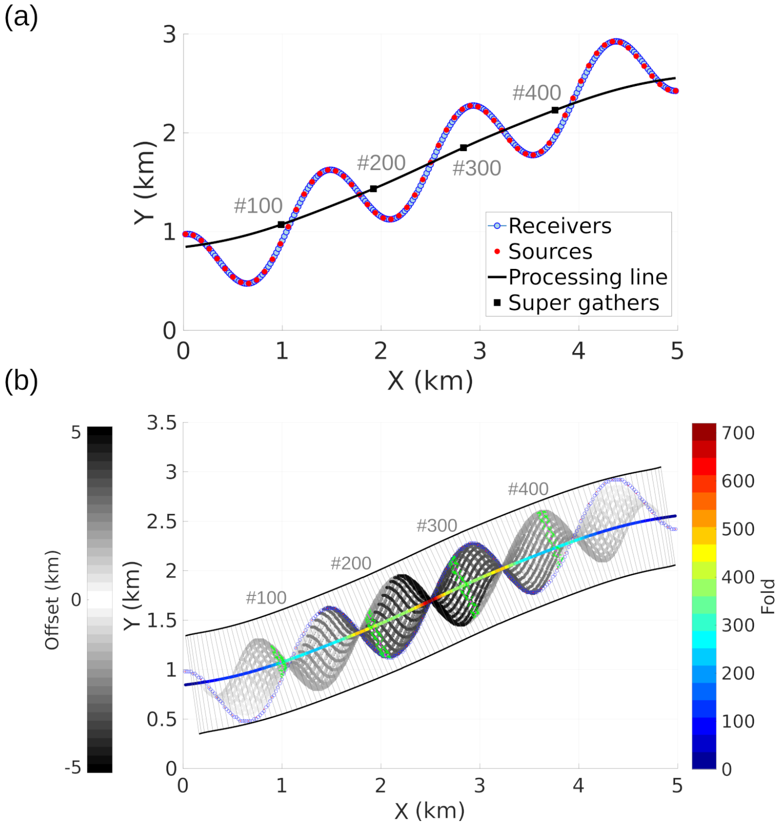

Figure 2.5: Survey geometry, crooked-line seismic bins, common midpoint distribution (coloured by offset), and the processing line (coloured by fold) for the multifocusing method.

pict the results of correcting synthetic super gathers for the single anti/synform curved reflector (Figure 2.4c) and multiple conflicting flat reflectors (Figure 2.4d), respectively, using 2D and 2.5D MF approaches. We incorporated the DE global optimization algorithm into the GCDMO and 2D MF methods to estimate optimal parameters. Also, this optimization algorithm is used to estimate the four 2.5D MF unknown attributes. For NMO correction, we used the NMO velocity calculated from the exact synthetic velocity model. Each row in the figures from top to bottom corresponds to common midpoint locations of #100, #200, #300, and #400, respectively. The first column shows the original super gathers that were sorted based on the trace number with visible undulations along reflection caused by the crooked nature of the acquisition line. The remaining four columns are the X-corrected super gathers, stack after X correction, 2.5D MF-corrected gathers, and stack after 2.5D MF correction, respectively. Here, X is NMO and GCDMO for Figures 2.6 and 2.7, and 2D MF for Figures 2.8 and 2.9, respectively. The amplitudes of stack trace in columns (c and e of Figures 2.6-2.9) are preserved and are comparable in each row. The main goal of showing NMO-corrected gathers in Figure 2.6 is revealing the intensity of nonhyperbolicity of reflections imposed by different factors, such as the reflector curvature. The 2.5D MF correction performs superior to other operators in all four models and selected four imaging mid-points, even in the presence of overburden heterogeneity. The final stacks after 2.5D MF correction (column [e] in Figures 2.6-2.9) show higher S/N and sharper wavelet compared to the final stacks after other operators correction (column [c] in Figures 2.6-2.9).

Figures 2.10 and 2.11 show the 2D and 2.5D MF stack images for the synthetic data with multiple dipping planar (Figure 2.4e) and multiple curved (Figure 2.4f) reflectors, respectively. The reflectors and interval velocity models are transformed from migrated depth domain into the stacked time domain to utilize them as reference images. The columns (a-d of Figures 2.10 and 2.11) show the projected layer interfaces, 2D MF and

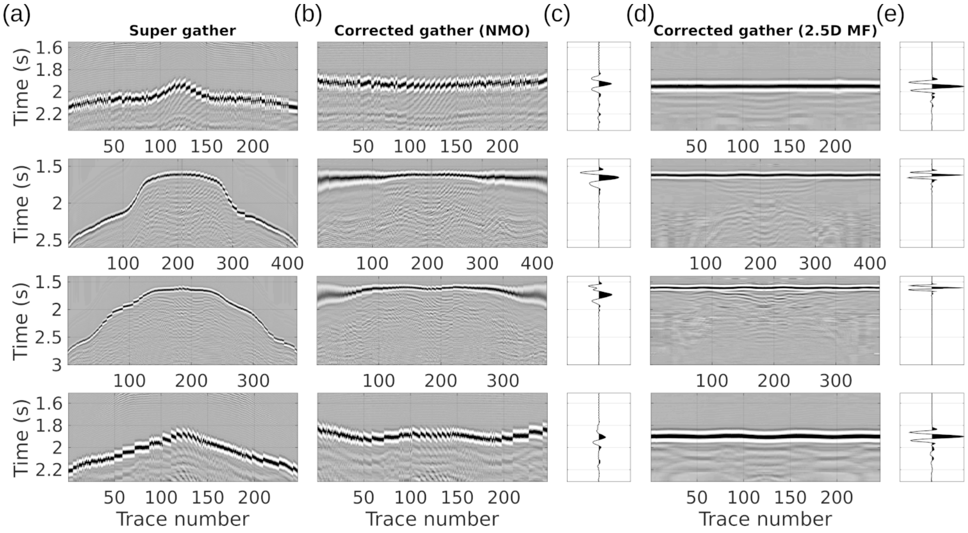

Figure 2.6: Results of applying NMO and 2.5D MF on the synthetic data with the single sphere reflector (Figure 2.4a). Each row corresponds to different image point locations on the processing line (First, second, third, and fourth rows are for common midpoint locations of #100, #200, #300, and #400, respectively.). a) Super gathers, b) NMO corrected gathers, c) Stacked traces of NMO corrected gathers, d) 2.5D MF corrected gathers, and e) Stacked traces of 2.5D MF corrected gathers.

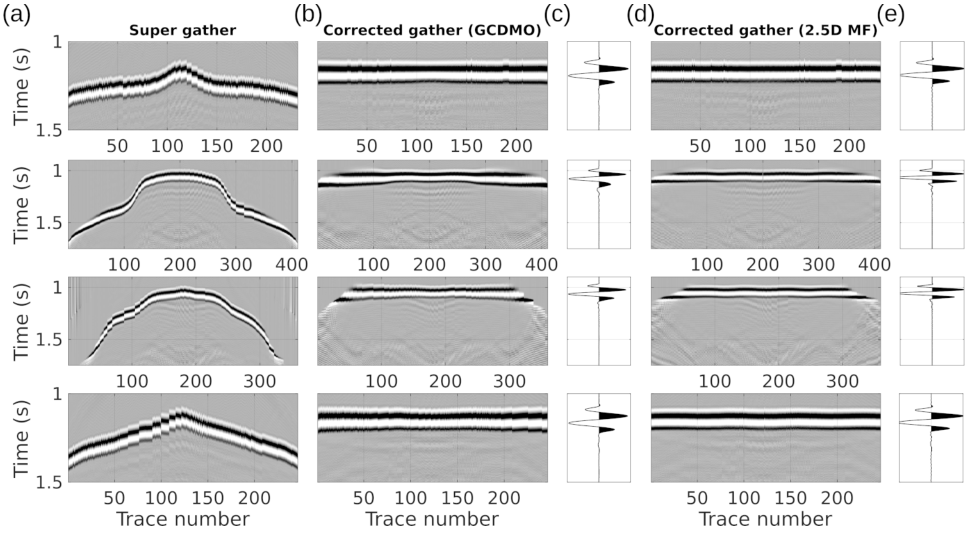

Figure 2.7: Results of applying GCDMO and 2.5D MF on the synthetic data with the single curved reflector (Figure 2.4b). Each row corresponds to different image point locations on the processing line (First, second, third, and fourth rows are for common midpoint locations of #100, #200, #300, and #400, respectively.). a) Super gathers, b) GCDMO corrected gathers, c) Stacked traces of GCDMO corrected gathers, d) 2.5D MF corrected gathers, and e) Stacked traces of 2.5D MF corrected gathers.

2.5D MF stack sections, and the projected exact interval velocity model overlayed with 2.5D MF stack image, respectively. Comparing 2D MF stack images (Figures 2.10b and 2.11b) with reference images of reflectors (Figures 2.10a and 2.11a) disclose that the 2D MF method could not correct cross-dip effects, and imaged reflections contain considerable undulations and time shifts. The mismatches between the 2D MF stack and reference images are indicated with red arrows. These arrows show that the 2D MF approach was not able to focus reflection at the correct location. Figures 2.10d and 2.11d confirm that the 2.5D MF method imaged reflections accurately, which are well-matched with projected interval velocities.

Overall the results in Figures 2.6-2.11 reveal that the proposed 2.5D MF method accurately corrected all of the normal, inline dip, and crossline dip moveout effects simultaneously (not sequentially) in different models, even in the presence of heterogeneity.

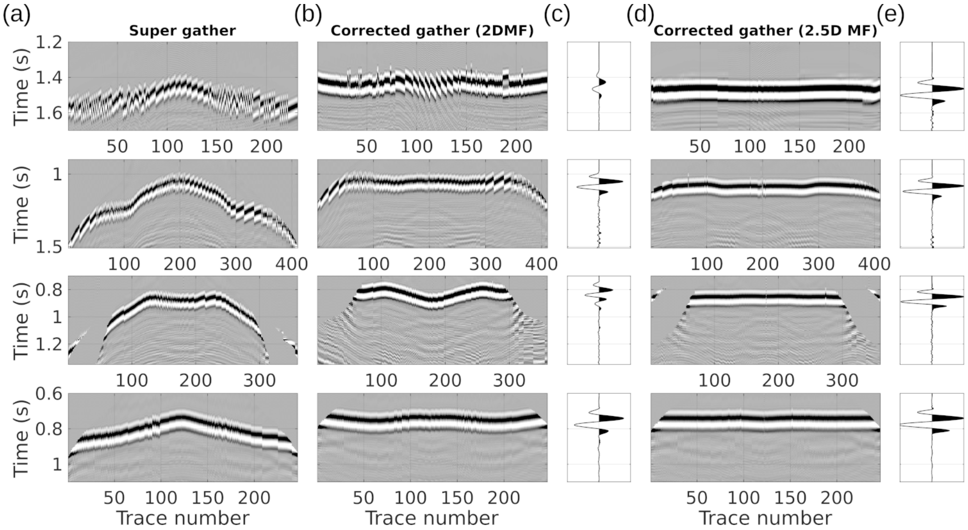

Figure 2.8: Results of applying 2D MF and 2.5D MF on the synthetic data with the single curved antiform-synform reflector (Figure 2.4c). Each row corresponds to different image point locations on the processing line (First, second, third, and fourth rows are for common midpoint locations of #100, #200, #300, and #400, respectively.). a) Super gathers, b) 2D MF corrected gathers, c) Stacked traces of 2D MF corrected gathers, d) 2.5D MF corrected gathers, and e) Stacked traces of 2.5D MF corrected gathers.

Meanwhile, the 2D MF correction is unable to correct the crossline dip moveout effect, and it requires to follow by applying CDMO correction. Also, the 2.5D MF method prevents the stretching problem allowing to use of full-offset data, leading to an increased vertical resolution in stacked sections. However, the NMO and GCDMO corrections cause wavelet stretching for shallow and long-offset reflections that cannot be mitigated by any of the subsequent corrections and need to be muted. The stacked traces of 2.5D MF corrected gathers show that the 2.5D MF method accurately places the reflection event at the correct location and produces stacked reflection data with higher vertical resolution and S/N than the other methods.

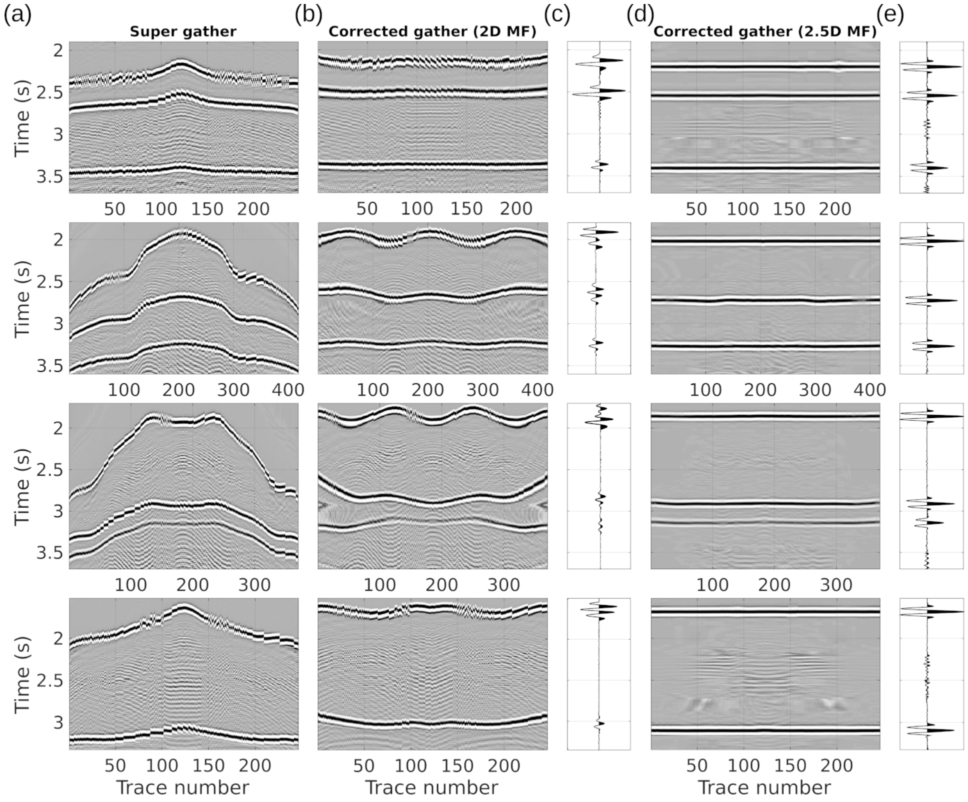

Figure 2.9: Results of applying 2D MF and 2.5D MF on the synthetic data with multi conflicting reflectors (Figure 2.4d). Each row corresponds to different image point locations on the processing line (First, second, third, and fourth rows are for common midpoint locations of #100, #200, #300, and #400, respectively.). a) Super gathers, b) 2D MF corrected gathers, c) Stacked traces of 2D MF corrected gathers, d) 2.5D MF corrected gathers, and e) Stacked traces of 2.5D MF corrected gathers.

The corrected super gathers with 2.5D MF method for sphere model in Figure 2.6d show minor oscillations and misalignments. This is due to the fact that 2.5D MF assumes a locally planar reflector. Therefore, the proposed approach is well-suited for planar and gently curved reflectors. Proper implementation of the MF method on strongly curved reflectors requires a 3D MF algorithm without any assumption about the subsurface reflector model. In Figures 2.7 and 2.8, the effects of heterogeneity and different curvatures

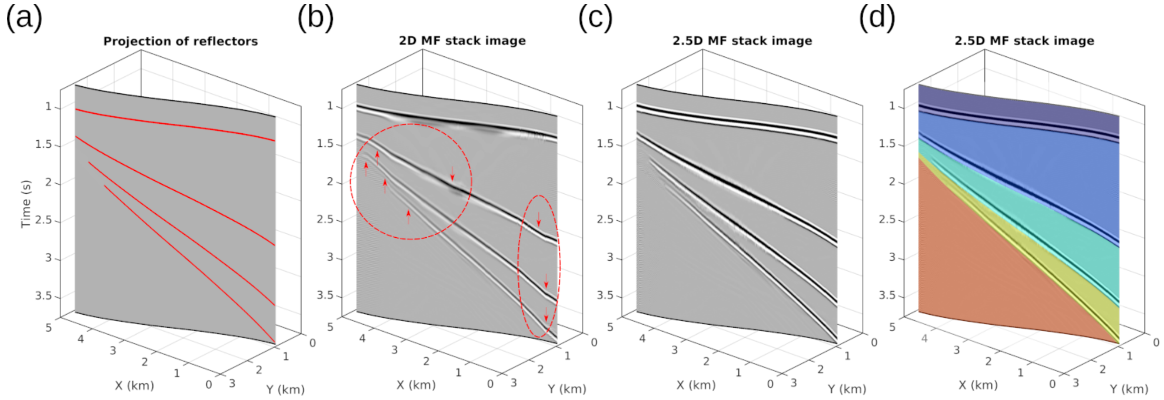

Figure 2.10: Results of applying 2D MF and 2.5D MF on the synthetic data with multiple dipping planar reflectors (Figure 2.4e). a) Projection of reflectors' interfaces into the time stack domain, b) 2D MF stack section, c) 2.5D MF stack section, d) Projected exact interval velocity model into the time stack domain overlayed with 2.5D MF stack image.

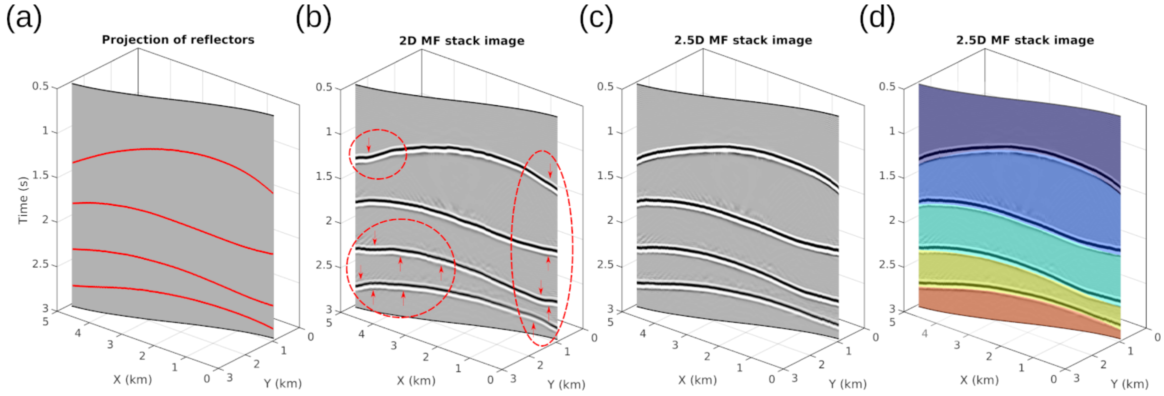

Figure 2.11: Results of applying 2D MF and 2.5D MF on the synthetic data with multiple curved reflectors (Figure 2.4f). a) Projection of reflectors' interfaces into the time stack domain, b) 2D MF stack section – the labeled features are discussed in the text, c) 2.5D MF stack section, d) Projected exact interval velocity model into the time stack domain overlayed with 2.5D MF stack image.

have been investigated. The 2.5D MF method is derived based on an auxiliary medium with constant velocity, and the effects of heterogeneity are accounted for by shifting the reference time. The effect of vertical heterogeneity was resolved (Figure 2.7d) by precisely determining the near-surface constant velocity. However, the presence of strong lateral velocity variation causes misalignments (second row in Figure 2.8d) that can be solved by transforming the 2.5D MF formulation from the optical domain into the velocity-shifted effective medium (Schwarz and Gajewski, 2017). Note that the velocity-shifted moveouts may suffer from wavelet stretching. The GCDMO method is formulated for planer reflectors in the velocity-shifted domain (Mancuso and Naghizadeh, 2021), and it was able to correct the heterogeneity effects; however, it could not address the effect of reflectors' curvature, which causes minor misalignments (Figure 2.7b).

2.4.3 Computational and Convergence Analyses

Figure 2.12 shows the application of the 2D MF and 2.5D MF methods on the single sphere reflector model (Figure 2.4a) at midpoint location of #100. Figure 2.12a shows the exact traveltime reflection surface generated by a ray-tracing algorithm. The 2D MF and 2.5D MF moveout surfaces are shown in Figure 2.12b and 2.12c, respectively. The moveout error—the difference between the moveout surface and the exact traveltime reflection surface—for 2D MF and 2.5D MF methods are shown in Figures 2.12d and 2.12e, respectively. The root-mean-square error for the 2D MF and 2.5D MF methods are 5.37 and 1.97 ms, respectively. This shows that the 2.5D MF method can generate more accurate results than the 2D MF method when applied to crooked seismic surveys. The irregular surface mesh in Figure 2.12 indicates that the data were acquired with a crooked-line survey, and midpoint locations were distributed irregularly around the processing line.

We examined the convergence behavior of the 2.5D MF method for the single strongly curved sphere reflection synthetic data set at the common midpoint location of #100. Figure 2.13 displays the convergence graph for ten single independent runs of the DE algorithm to find the optimal values of 2.5D MF unknown parameters. The DE optimization algorithm maximizes the coherency function that is defined using the 2.5D MF traveltime operator. The maximum coherence value achieved by the DE algorithm was 6.15×10^4 after approximately 1000 evaluations of the objective function. We have carried out similar convergence and computational cost analyses for all of the simulated data over the other models shown in Figure 2.4. Overall, in all of our synthetic examples, the 2.5D MF method performed computationally efficient and estimated wavefield

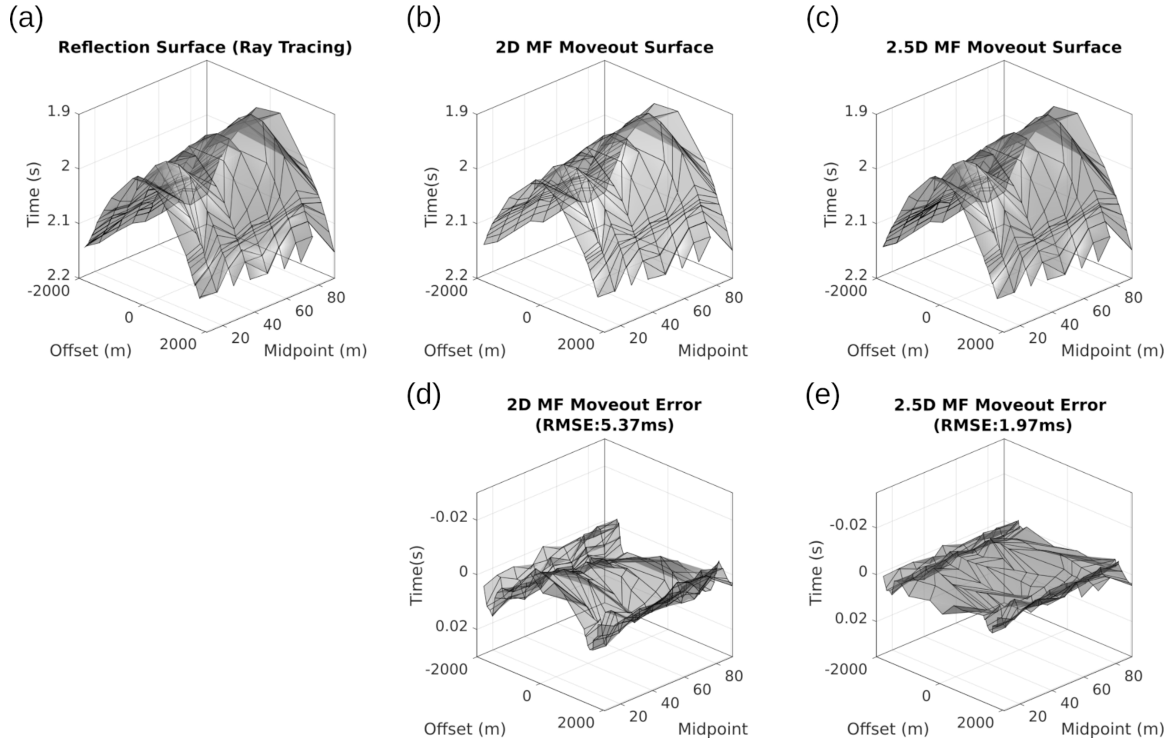

Figure 2.12: Comparing of applying 2D MF and 2.5D MF methods on the single sphere reflector model (Figure 2.4a) at midpoint location of #100. a) Reflection surface (Ray Tracing), b) 2D MF moveout surface, c) 2.5D MF moveout surface, d) 2D MF moveout error (differences between b and a), and e) 2.5D MF moveout error (difference between c and a).

parameters accurately.

2.5 Real data example

We applied conventional NMO, GCDMO, and 2.5D MF stacking methods to a real land crooked-line data set collected in a thrust-belt area with subsurface complexity. The length of the profile is approximately 10 km with a line traverse in the N-NE direction. Figure 2.14 shows the map view of the line traverse that was rotated and transformed to the origin. The crossline spread of the shot and receiver locations varies between -220 m and 210 m with respect to the intended line traverse indicated by the black line representing the receiver locations in Figure 2.14. Shot and receiver intervals are both 20 m, and their elevations vary between 697 m and 1355 m. The seismic source is explosive with a charge depth of 15 m at shot locations inaccessible for vibroseis vehicles

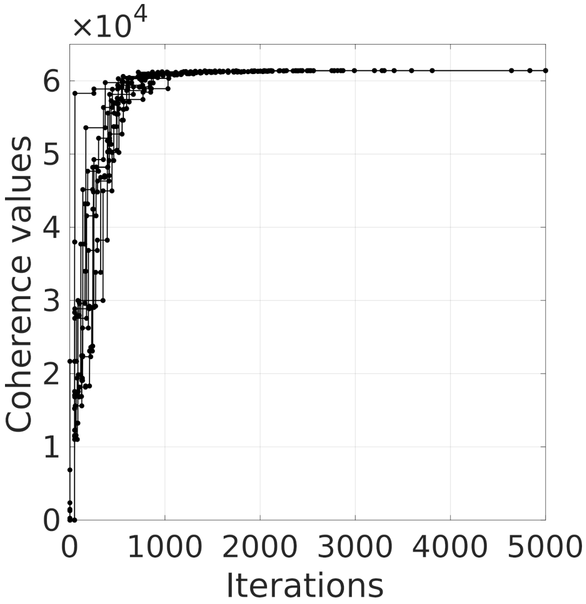

Figure 2.13: Convergence graph of the simultaneous global searches of the wavefront attributes for the 2.5D MF stacking operator using the DE algorithm for ten single random runs.

Table 2.2: The processing sequence of the real seismic data set

Process	**Parameter**
Trace balancing	
Shot-Receiver Tomostatics Corrections	
Refraction Residual Statics Corrections	
Geometric Spreading Correction	
Time-Variant Spectral Whitening	signal passband of 4-48 Hz
Binning	
Partial Stacking	50 m offset
Window	CMP from 375 to 775
Window	time 0.3 to 1.3 s
Stacking Velocity Analysis/Attributes Search	
NMO/GCDMO/2.5D MF Correction	
Stacking	
Bandpass Filter	4-48 Hz
Automatic Gain Control	250 sample window

and vibroseis with a sweep band of 8-72 Hz. The data were acquired by split-spread recording geometry with 501 channels and a maximum offset of 6,010 m. The fold is variable along the line traverse, as shown in Figure 2.14. The recoverable signal band in the shot gathers is 4-42 Hz. Table 2.2 summarises the processing sequence applied to the field data. Figure 2.15 shows an example of a field record before and after single-channel signal processing. After the application of signal processing, the recovered reflections are highly segmented and mostly confined to large offsets (indicated with yellow circles).

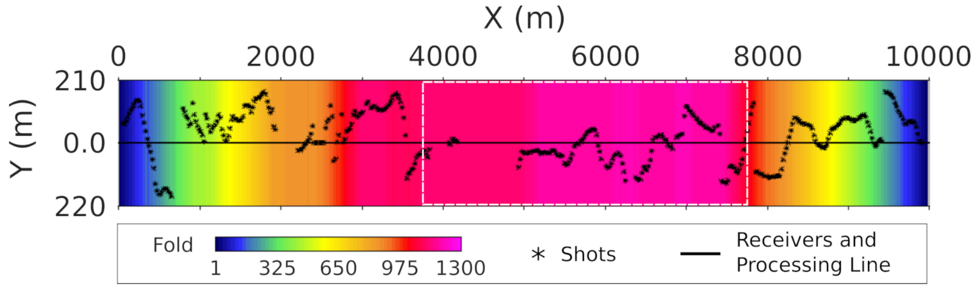

Figure 2.14: Survey geometry and super bin fold map

We used the same preprocessed data to all of the examined methods in order to generate comparable results. The preprocessed data were binned every 10 m along the processing line at a maximum radius of 220 m. We built the super gathers by comprising five nearby CMP gathers. We tested proposed methods on data with the CMP number range from 375 to 775 (shown with a white dashed box in Figure 2.14) and time window 0.3 to 1.3 s. The CMP and super gathers are used in NMO/GCDMO and 2.5D MF approaches, respectively. The signal processing and conventional NMO stacking were performed in GeoThrust. We developed the 2.5D MF algorithm package code in C using the Seismic Unix framework (Stockwell Jr, 1999). For efficient implementation of the proposed algorithm, the produced C code package was parallelized using a serial farming technique with Shell scripting. We estimated the GCDMO's three unknown parameters and the 2.5D MF's four wavefield attributes using DE global optimization

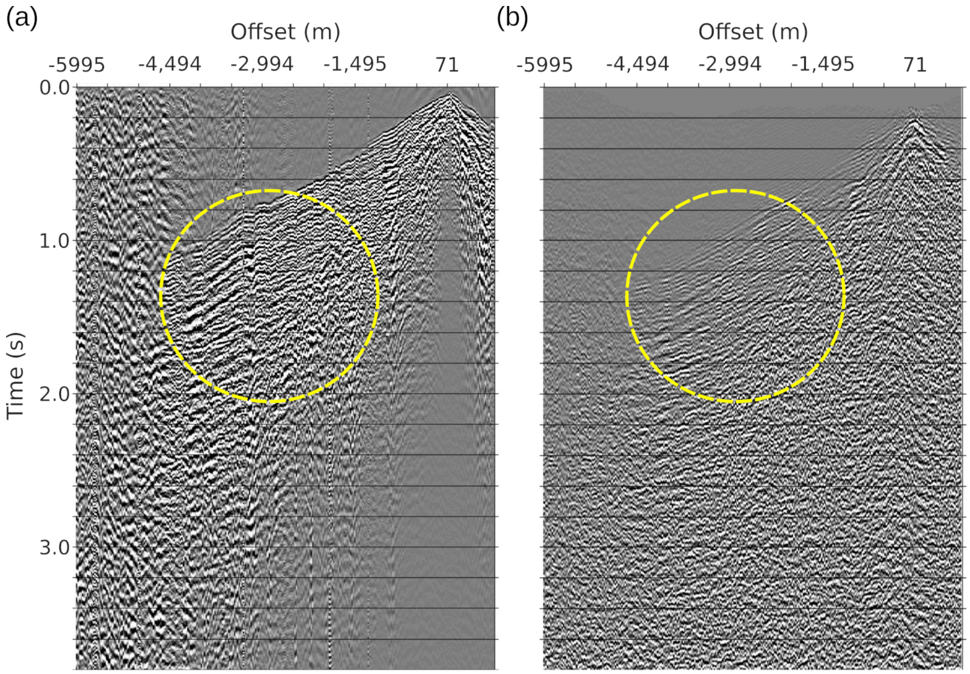

Figure 2.15: Field record before (a) and after (b) single-channel signal processing, including shot-receiver and residual statics corrections, geometric spreading correction, and time-variant spectral whitening

Table 2.3: The DE optimization algorithm input parameters and lower and upper bound constrain for the GCDMO and 2.5D MF methods.

Parameter	**2.5D MF**	**GCDMO**
Window Length of Coherence Function	50 samples	50 samples
Maximum Number of Generations	30	30
Population Size	50	30
Crossing Over Factor	0.5	0.5
Weighting Factor	0.5	0.5
θ_x	$-45° < \theta_x < 45°$	$-45° < \theta_x < 45°$
θ_y	$-25° < \theta_y < 25°$	$-25° < \theta_y < 25°$
$V_{min,max}$	1500-6500 m/s	1500-6500 m/s
V_0	2500 m/s	
R_N	$-1000km < R_N < 1000km$	
R_{NIP}	$V_{min}^2(t/2V_0)\cos^2(max(\lvert\beta\rvert)) < R_{NIP} < V_{max}^2(t/2V_0)$	

algorithm. Unnormalized cross-correlation summation is used as the coherence function. The optimization algorithm input parameters, lower and upper bound constrain for the GCDMO and 2.5D MF methods are outlined in Table 2.3. Figures 2.16a-2.16c show the conventional NMO, GCDMO, and 2.5D MF stack sections, respectively. Comparing the result of the 2.5D MF method with the stack sections obtained using other methods reveal that the 2.5D MF improved the quality of the stack image and was able to focus the reflections, which conventional flow could not. The 2.5D MF enhanced the vertical resolution and S/N of the stack section compared to the GCDMO image. The lateral continuity of reflections in stack images obtained by GCDMO and 2.5D MF methods can be improved by imposing smoothness constraints across nearby CMP super gathers.

2.6 Discussion

The zero-offset 2.5D MF methods express traveltime based on the kinematics of a central ray (as a function of apparent inline and crossline dip angles of the reflector) and the moveout correction for a paraxial trace in the vicinity of the central point. The main limitation of the zero-offset 2.5D MF method is its construction around a zero-offset central ray (M_0M_c in Figure 2.1) and the spherical wavefront assumption. In other words, similar to the 2D case, the 2.5D MF expression approximates moveouts for a constant near-surface velocity V_0 and locally spherical wavefronts around the zero-offset central ray. The planar interface ($R_N = \infty$) is only assumed to derive the focusing parameter σ and relation between R_S and R_G (Landa et al., 2009). However, equation 1 can also be used for curved reflectors ($R_N < \infty$). The 2.5D MF approach is exact for a

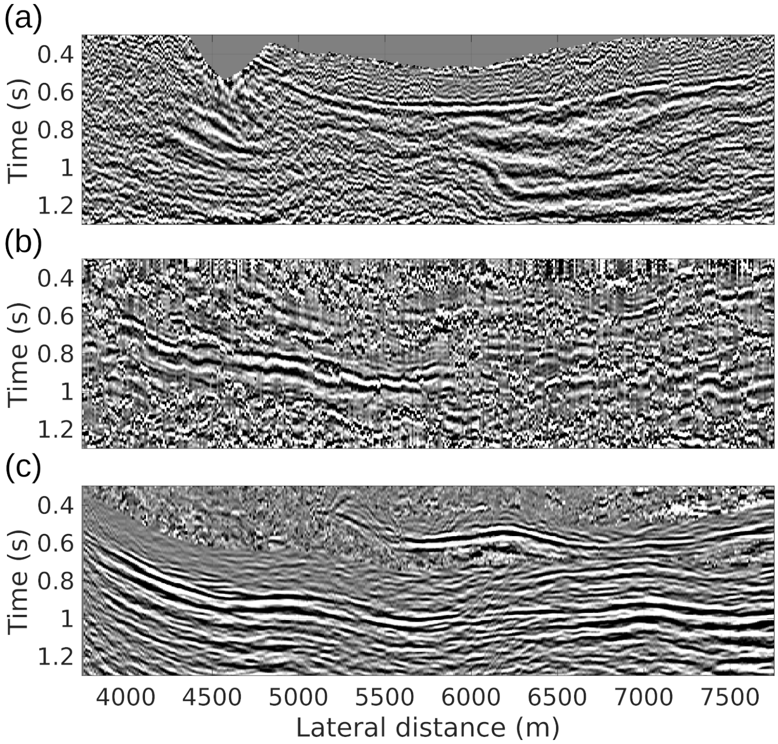

Figure 2.16: Comparing stack sections obtained by the a) conventional NMO, b) GCDMO, and c) 2.5D MF methods.

dipping planar interface with constant overburden and approximate for all other cases, for instance, an arbitrary velocity model with curved reflectors. The results from synthetic data sets showed it could also handle strongly curved reflectors with reasonable accuracy. In complex subsurface geology, strong lateral velocity variations and/or the presence of anisotropy can violate the zero-offset ray approximation and reduce the accuracy of this method for large offsets (Berkovitch et al., 2011). In order to overcome this issue, this approach can be applied on a finite offset around the central ray and does not require full offset data in a super gather (Gelchinsky et al., 1999a; Landa et al., 2009). Also, the extended MF and CRS stacking methods, including spherical MF (Landa et al., 2009), implicit CRS (Schwarz et al., 2014b), and non-hyperbolic CRS (Fomel and Kazinnik, 2013), are expected to achieve better results in the scenarios mentioned above. However, these approaches still need to be generalized to crooked seismic line scenarios. This issue can be theoretically addressed by developing a 3D MF/CRS algorithm without any assumptions. However, such an algorithm will depend on more unknown wavefield parameters (eight parameters compared to four parameters of the 2.5D MF method), consequently increasing the computational cost.

The proposed 2.5D MF method does not require a slant-stack step for removing cross-dip effects allowing more flexibility for applying other data processing steps before stacking. By correcting all moveouts (NMO, DMO, and CDMO) simultaneously, we also avoid the issues of residual moveout effects associated with each individual correction. Also, this method can be employed to process 3D seismic data. The 3D seismic image volume and structural information can be extracted from 2D crooked-line seismic data. However, the lack of an accurate dip-independent velocity model, variable and low-fold coverage, and noisy data put constraints on the application of conventional 3D processing techniques, which often leads to low-resolution images on 2D crooked-line seismic data. These issues can be addressed by the proposed method using a 3D super binning instead of a 2.5D

Table 2.4: Comparing estimated inline and crossline dips for the multi flat layers model (Figure 2.4e) at midpoint location of #200.

	Exact Values		**GCDMO**		**2.5D MF**	
Parameters	$\theta_x(^\circ)$	$\theta_y(^\circ)$	$\theta_x(^\circ)$	$\theta_y(^\circ)$	$\theta_x(^\circ)$	$\theta_y(^\circ)$
Reflector #1	0.000	0.000	-0.750	-0.582	-0.420	-0.663
Reflector #2	15.000	10.000	12.600	8.119	14.394	10.976
Reflector #3	30.000	15.000	24.634	13.135	30.957	16.560
Reflector #4	45.000	20.000	36.238	16.895	40.449	19.139

super binning along a slalom processing line. This means the super gather traces will be located inside a 2D polygon (rectangular, square, or hexagonal bins), which can be significantly larger than the bin sizes in conventional 3D processing leading to a very high fold gather. Nevertheless, the proposed 2.5D MF method could still focus the energy from all midpoints to the imaging point without any change in the formula. Note that a conventional 3D processing approach assumes that the distance between imaging point and midpoint locations within the bin are insignificant. However, our proposed method takes into account these distances as they can be significant for a large bin size.

Table 2.4 summarizes the exact and estimated inline and crossline dips using the GCDMO and 2.5D MF methods for the multi flat layers model (Figure 2.4e) at the midpoint location of #200. Comparing exact and estimated values demonstrates that the 2.5D MF method can extract structural information with good accuracy even for layers with dips over 40°.

2.7 Conclusions

We proposed a theoretical framework for generating 2D seismic images by collapsing 3D seismic volumes into a 2.5D plane. We developed a new kinematic expression for the multifocusing stacking surface, which depends on four unknown parameters. The derived 2.5D MF formula explicitly takes into account the midpoint dispersion and cross-dip effects and corrects normal, inline, and crossline dip moveouts simultaneously. This algorithm can perform automatically using a nonlinear global optimization method based on a coherency objective function. We examined the performance of the new formula on different synthetic models with various 3D dipping and curved interfaces and heterogeneous overburdens. The results indicate that the 2.5D MF method is computationally efficient and accurate for 3D dipping planar or gently curved reflectors with low to moderate overburden heterogeneity. The 2.5D MF can accurately simulate reflection traveltime even for strongly curved 3D models with high reflector curvatures in the presence of moderate inhomogeneities of the overburden. The new MF traveltime formula yields more accurate time shifts and better-flatten reflection events. The proposed method avoids the duplication of reflections and leads to a more reliable image with a high S/N. The introduced approach could lead to high-resolution seismic images by extracting 3D structural information from 2D crooked-line seismic surveys. Applying the proposed method to real data improved the quality of the stack image significantly, focused steeply dipping reflections at their correct locations, and imaged them with high clarity compared to the conventional method. Also, this algorithm brought new reflections to focus that did not appear in the conventional result.

2.8 Acknowledgements

This research was funded by the NSERC Canada First Research Excellence Fund (MERC-ME-2021-54). GeoThrust software was used for 2D and 3D seismic data processing. We acknowledge GeoTomo for providing an academic license. SOFI3D open-source software was used to produce seismic synthetic data sets using the finite differences method. We thank Thomas Bohlen, Denise De Nil, Daniel Köhn, and Stefan Jetschny for developing the SOFI3D code. We thank Christopher Mancuso for sharing the GCDMO code package. The authors would like to acknowledge the comments provided by Prof. Richard Smith and all editors, for their very insightful and constructive comments on the manuscript.

Appendix 2-A: Derivation of the 2.5D multifocusing traveltime

The derivation of the 2.5D multifocusing operator is given below. Based on Snell's law, the incident and reflected rays reside in the same plane with the reflector normal. The source S and the receiver R are coplanar with the reflection point O in a plane (the transparent blue plane in Figure 2-A.1) with an inclination angle of γ with respect to the vertical axis (i.e., γ is an apparent dip of the reflector along $\phi' + 90^\circ$ direction.). Therefore, to derive a 2D multifocusing formulation for a crooked-line survey, we can treat each pair of source and receiver as 2D seismic data acquired in a specific direction. Overall, the structural parameters, such as dip, define the shape of reflectors in a 3D space and they are directly related to the wavefront parameters, such as the emergence angle. Therefore, the problem reduces to connecting the wavefront parameters in 2D multifocusing to the 3D structural parameters by taking into account the effect of cross-dip. In a 3D space, a dipping layer can be defined using its true dip and strike or two apparent dips and the angle between their directions. In this study, we chose the latter configuration.

For each pair of source and receiver in a specific direction (Figure 2-A.1), we rewrite the 2D MF traveltime with the modified emergence angle β' and the modified radius of curvature of normal incident point wave R'_{NIP} as follows

$$
\begin{aligned}
t(\beta', R_N, R'_{NIP}) = t_0 &+ \frac{\sqrt{\triangle X_S^2 + R_S^2 + 2\ R_S\ \triangle X_S\ \sin(\beta')} - R_S}{V_0} \\
&+ \frac{\sqrt{\triangle X_G^2 + R_G^2 + 2\ R_G\ \triangle X_G\ \sin(\beta')} - R_G}{V_0},
\end{aligned}
\qquad (2\text{-A.1})
$$

$$
\begin{aligned}
\sigma &= \frac{\triangle X_S - \triangle X_G}{\triangle X_S + \triangle X_G + \frac{2\ \triangle X_S\ \triangle X_G\ \sin(\beta')}{R'_{NIP}}}, \\
R_S &= \frac{1+\sigma}{\frac{1}{R_N} + \frac{\sigma}{R'_{NIP}}}, \quad R_G = \frac{1-\sigma}{\frac{1}{R_N} - \frac{\sigma}{R'_{NIP}}}.
\end{aligned}
$$

To derive the 2.5D MF formulation, we do not need to modify (alter) the R_N because

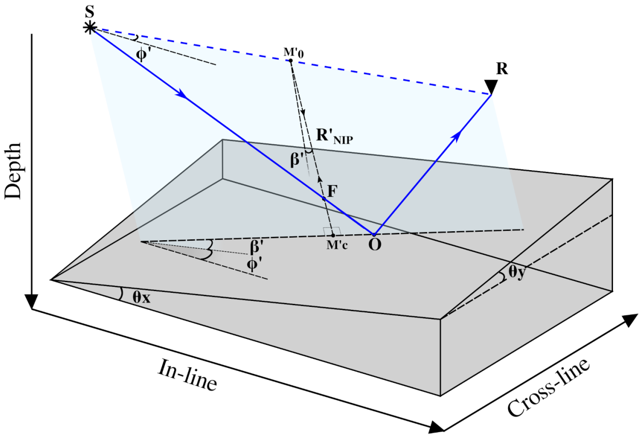

Figure 2-A.1: 3D Schematic diagram of the modified 2D multifocusing method along the transparent blue plane that contains the reflection ray $S-O-R$ and normal ray $M'_0 M'_c$.

the radius of the curvature for a curved subsurface structure can be accurately estimated by locally fitting a sphere (with constant radius) at the reflection point (Landa et al., 2009). Also, the R_N is constant for different incident angles at a specific reflection segment. Meanwhile, this parameter is ∞ for flat layers. However, parameters β' and R'_{NIP} vary for each source-receiver pair. Thus, we need to find functions that connect these parameters to the inline θ_x and crossline θ_y dips. First, we derive a function of the apparent dip along the source-receiver direction based on the inline θ_x and crossline θ_y dips. This allows us to take into account the distribution of the source and receiver across the profile (direction variations for each pair of source-receiver) and the cross-dip effect. Figure 2-A.2 shows the relationship between an apparent dip in a specific direction with the inline and crossline dips. According to the Figure 2-A.2, the inline θ_x and crossline θ_y dips can be expressed by

$$\tan\theta_x = \frac{h_1}{x} = \frac{h_1}{l\ \cos\phi'} \longrightarrow \tan\theta_x\ \cos\phi' = \frac{h_1}{l}, \tag{2-A.2}$$

$$\tan\theta_y = \frac{h_2 - h_1}{y} = \frac{h_2 - h_1}{l\ \sin\phi'} \longrightarrow \tan\theta_y\ \sin\phi' = \frac{h_2 - h_1}{l}, \tag{2-A.3}$$

where ϕ' is the angle between the inline and the line that connects source and receiver, and l is the distance between source and receiver. By summing both sides, we have (Marfurt and Kirlin, 2000; Gao and Di, 2015)

$$\tan\theta_x\ \cos\phi' + \tan\theta_y\ \sin\phi' = \frac{h_2}{l} = \tan\beta', \tag{2-A.4}$$

where β' is the apparent dip along SR direction. In the same way, the apparent dip β'' along the orthogonal to the processing line can be given by

$$\tan\beta'' = \tan\theta_x\ \cos\phi'' + \tan\theta_y\ \sin\phi'', \tag{2-A.5}$$

where ϕ'' is the angle between the inline and the orthogonal direction to the processing line.

In the 2D multifocusing method, the derived stacked image is assigned to the imaging point known as the central point. For the modified 2D multifocusing algorithm along the source-receiver pair SR in Figure 2-A.1, the final stacked trace has been assigned to the central point M'_0. The distance D between the main imaging point M_0 and the central point M'_0 leads to a considerable time shift. Figure 2-A.2 shows how we can project apparent dip β'' along the central plane to calculate the time shift. By considering the tetrahedron $PM_cM'_cQ$ in Figure 2-A.2, the time shift for each source-receiver pair can be expressed as

$$\Delta t = \frac{2\ \Delta R_{NIP}}{V_0}, \tag{2-A.6}$$

where $\Delta R_{NIP} = R'_{NIP} - R_{NIP}$, and

$$\Delta R_{NIP} = D\ \sin\delta. \tag{2-A.7}$$

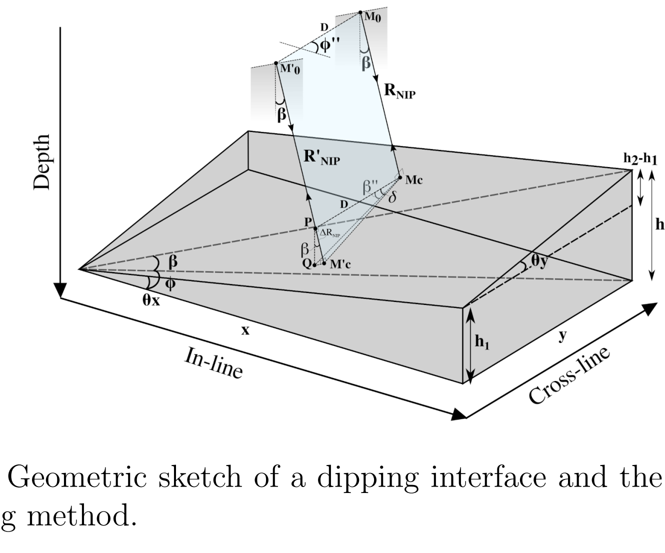

Figure 2-A.2: 3D Geometric sketch of a dipping interface and the central plane for the 2.5D multifocusing method.

Hence, the modified R'_{NIP} can be written as

$$R'_{NIP} = R_{NIP} + D\ \mathrm{sin}\delta. \tag{2-A.8}$$

Also, we can determine δ based on the previously defined parameters. In Figure 2-A.2, for the tetrahedron $PM_cM'_cQ$, we have

$$\frac{\Delta R_{NIP}}{\mathrm{sin}\delta} = \frac{PQ}{\mathrm{tan}\beta''}, \tag{2-A.9}$$

and

$$\mathrm{cos}\beta' = \frac{\Delta R_{NIP}}{PQ}. \tag{2-A.10}$$

which lead to

$$\mathrm{sin}\delta = \mathrm{tan}\beta''\ \mathrm{cos}\beta, \tag{2-A.11}$$

where β'' and β are function of $(\theta_x,\ \theta_y)$. β is the inclination of the central plane to the vertical axis, measured along the true dip direction, and is equal to the true dip θ. For determining the direction of true dip ϕ based on two apparent dips (θ_x, θ_y) with the angle of ψ ($= 90°$) between them, we use (Fossen, 2016)

$$\mathrm{tan}\phi = \frac{1}{\mathrm{sin}\psi}[\frac{\mathrm{tan}\theta_y}{\mathrm{tan}\theta_x} - \mathrm{cos}\psi] = \frac{\mathrm{tan}\theta_y}{\mathrm{tan}\theta_x}. \tag{2-A.12}$$

The strike $\varphi = \phi \pm 90°$ is determined with respect to the inline direction. Finally, for finding the true dip, we use $\mathrm{tan}\theta_x = \mathrm{tan}\theta\ \mathrm{cos}\phi$, then by substituting ϕ in this equation and using $\mathrm{cos}(\mathrm{atan}(x)) = \frac{1}{\sqrt{x^2+1}}$, the true dip θ can be determined as

$$\mathrm{tan}\theta = \sqrt{\mathrm{tan}^2\theta_x + \mathrm{tan}^2\theta_y}. \tag{2-A.13}$$

Therefore, we can calculate sinδ by substituting equations 2-A.5 and 2-A.13 into 2-A.11. Finally, Δt and R'_{NIP} are defined based on θ_x and θ_y. By adding the time shift term (equation 2-A.6) to the 2D MF traveltime (equation 2-A.1) and replacing the modified emergence angle β' with equation 2-A.4 and the modified radius of curvature of normal incident point wave R'_{NIP} with equation 2-A.8, the equation 2.1 can be derived as follows:

$$t(\theta_x, \theta_y, R_N, R_{NIP}) = t_0 + \frac{2\ D\ \sin(\delta)}{V_0} + \triangle t_S + \triangle t_G, \tag{2-A.14}$$

where

$$\triangle t_S = \frac{\sqrt{\triangle X_S^2 + R_S^2 + 2\ R_S\ \triangle X_S\ \sin(\beta')} - R_S}{V_0}, \qquad \triangle X_S = \sqrt{(X_S - X_{M'_0})^2 + (Y_S - Y_{M'_0})^2},$$

$$\triangle t_G = \frac{\sqrt{\triangle X_G^2 + R_G^2 + 2\ R_G\ \triangle X_G\ \sin(\beta')} - R_G}{V_0}, \qquad \triangle X_G = \sqrt{(X_G - X_{M'_0})^2 + (Y_G - Y_{M'_0})^2},$$

$$\sigma = \frac{\triangle X_S - \triangle X_G}{\triangle X_S + \triangle X_G + \frac{2\ \triangle X_S\ \triangle X_G\ \sin(\beta')}{R'_{NIP}}}, \qquad R_S = \frac{1+\sigma}{\frac{1}{R_N} + \frac{\sigma}{R'_{NIP}}}, \quad R_G = \frac{1-\sigma}{\frac{1}{R_N} - \frac{\sigma}{R'_{NIP}}},$$

$$\tan(\beta') = \tan(\theta_x)\ \cos(\phi') + \tan(\theta_y)\ \sin(\phi'), \qquad \sin(\delta) = \tan(\beta'')\ \cos(\beta),$$

$$\tan(\beta'') = \tan(\theta_x)\ \cos(\phi'') + \tan(\theta_y)\ \sin(\phi''), \qquad \tan(\beta) = \sqrt{\tan^2(\theta_x) + \tan^2(\theta_y)},$$

$$R'_{NIP} = R_{NIP} + (D\ \sin(\delta)).$$

The direction cosines of the central ray (M_0M_c) are commonly used for determining wavefront parameters (Figure 2-A.3). These are the cosines of the angles between the normal to the interface and the three coordinate axes (here, we assumed x,y, and z coordinate axes are along the inline, crossline, and depth [vertical] directions, respectively.) and can be found as

$$\cos\beta_z = \cos\theta, \tag{2-A.15}$$

$$\cos\beta_y = \cos\beta_z \; \tan\theta_y, \tag{2-A.16}$$

$$\cos\beta_x = \cos\beta_z \; \tan\theta_x. \tag{2-A.17}$$

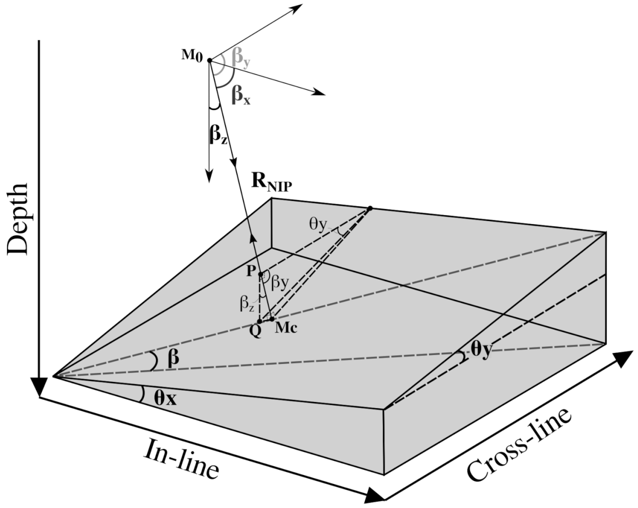

Figure 2-A.3: 3D Geometric diagram of a dipping interface and a normal ray (as the central ray) for the 2.5D multifocusing method.

Chapter 3

High-resolution 2.5D multifocusing imaging of a crooked seismic profile in a crystalline rock environment: results from the Larder Lake area, Ontario, Canada

Hossein Jodeiri Akbari Fam [1*], Mostafa Naghizadeh [1], Richard Smith [1], Öz Yilmaz [2], Saeid Cheraghi [1], Kate Rubingh [1]

[1] Mineral Exploration Research Centre, Harquail School of Earth Sciences, Goodman School of Mines, Laurentian University, Sudbury, Ontario, Canada.

[2] Anatolian Geophysical, Urla, Izmir, Turkey.

[*]Corresponding Author E-mail: hjodeiri@laurentian.ca

3.1 Abstract

A high-resolution seismic reflection transect was acquired over a hard-rock geological setting along an existing roadway in the Larder Lake area of the Superior Craton of Canada for the Metal Earth project in 2017. This profile, as well as other Metal earth transects, primarily aims to enhance the knowledge and to better understand the subsurface geology of the Abitibi Greenstone Belt within the Canadian Shield. Low impedance contrast and signal-to-noise ratio (S/N) and the presence of steeply dipping interfaces and out-of-plane reflections make the imaging and estimation of the velocity-depth model a challenging task. The irregular distribution of sources and receivers along the crooked survey line disperses the midpoint locations from the traverse line, leads to variable fold coverage, and degrades the ability to image in a zone of very low reflectivity. In addition, the crooked-line geometry results in considerable time- and offset-variant delay among reflections, which could defocus and deform reflections particularly from reflectors with a cross-dip component. Also, the crossline spread of midpoints violates the assumption of a straight-line survey inherent in the derivation of two-dimensional imaging methods. A recently introduced 2.5D multifocusing (MF) time imaging method is one potential solution for addressing these long-standing imaging challenges. The 2.5D MF approach offers more realistic modeling of the zero-offset wavefield by explicitly accounting for the midpoint dispersion and cross-dip effects. The main practical problem of the 2.5D MF implementation is the simultaneous determination of the optimal wavefield parameters for each image point and time location. We address this optimization problem using a multidimensional constrained differential evolution global optimization algorithm, as this improves the efficiency and accuracy of the estimation. We have also designed an efficient processing sequence for MF seismic imaging. The performance of the 2.5D MF procedure has been examined on a synthetic model, generated using the same real acqui-

sition geometry. Numerical tests demonstrate that the 2.5D MF technique can produce a more focused stack with the primary reflections appearing at their poststack correct locations and the procedure can also provide reliable estimates of interface dips. Due to the importance and difficulty of imaging the data, several conventional and advanced processing strategies have been attempted on the transect, specifically: 2D phase-shift time-migration of a dip moveout corrected stack; 2D prestack Kirchhoff time migration; swath 3D poststack migration; and our 2.5D MF imaging algorithm. We found that applying the 2.5D MF stacking algorithm followed by a poststack time migration approach improved the resolution of the image significantly compared to all the conventional and advanced methods and identified new reflections. The 2.5D MF method also focused the steeply dipping reflections more coherently, which resolved ambiguities in geological architecture by understanding the location and continuity of structures. The method also accurately extracts 3D structural information and results in an improved S/N.

3.2 Introduction

The Metal Earth project is focused on understanding the processes that control the differential metal concentration in Archean greenstone provinces at a full crust-mantle scale (Naghizadeh et al., 2019). A total of 921 km regional-scale deep seismic reflection transects and 184 km of high-resolution seismic reflection profiles were acquired in the Superior province of Canada in 2017. The surveys include fifteen regional (termed R1) and fourteen high-resolution (R2) surveys. The Larder Lake high-resolution survey was used to evaluate the imaging capability of the surveys with crooked geometry, a prominent attribute of most of the Metal Earth seismic lines.

The seismic reflection method is considered to be the most accurate and intuitive geophysical prospecting method to image subsurface architecture. It can provide the highest lateral and vertical resolution (Mooney, 2021) among deep probing geophysical remote-sensing methods and can maintain high precision to depths of several kilometers. However, the application of seismic methods in hard-rock settings encounters difficulties due to the complex geologic structures, complicated near-surface conditions, low and variable fold coverage, noisy environment, and the presence of steeply dipping interfaces and strong heterogeneities (faults, fracture zones, etc). In addition, interfaces can have low impedance contrasts, sharp discontinuities can result in numerous diffractions and there can be interfering out-of-plane reflections. All these factors make the imaging of crooked-line seismic data from hard-rock settings challenging compared to data from sedimentary basins (Milkereit et al., 2000; Malehmir et al., 2012). Application of standard 2D processing methods often results in poor images in these circumstances (see Nedimović and West, 2003a; Jodeiri Akbari Fam et al., 2021a) since they are unable to approximate wavefields accurately and use relatively low-fold data and simplified velocity fields that limit the S/N improvement (for example Bécel et al., 2015).

In regions with significant geologic complexity and lateral velocity variations, such as hard-rock geological environments, seismic depth imaging methods are often preferred to time imaging methods (Yilmaz, 2001; Bräunig et al., 2020; Hloušek et al., 2021). However, the depth-domain algorithms are computationally expensive and very sensitive to velocity-depth models. Lack of knowledge of a detailed and accurate velocity model causes depth imaging methods to lose their convergence properties or produce incorrect results. An alternative approach to the depth-domain imaging methods is to improve the time-domain imaging methods. The stacking step plays a key role in the time imaging techniques, which required a generalized moveout operator that can accurately account for the source-receiver geometry and correct azimuth-dependent dip-moveouts (Landa et al., 2009; Schwarz et al., 2014b). Therefore, improving the quality of stack sections is an essential research topic that can be achieved by revising the moveout formulation (Taner and Koehler, 1969; May and Straley, 1979; De Bazelaire, 1988; Castle, 1994; Alkhalifah and Tsvankin, 1995; Causse et al., 2001; Causse, 2002; Taner et al., 2007; Schwarz and Gajewski, 2017). These operators, which include normal/dip/cross-dip moveout (NMO/DMO/CDMO) (Mayne, 1962; Hale, 1984; Nedimović and West, 2003a), multifocusing (MF) (Gelchinsky et al., 1999a,b), and common reflection surface (CRS) (Müller, 1999), are based upon a transformation of multicoverage prestack data into a simulated zero-offset stack section that provides an alternative to the depth-processing sequence.

The crooked geometry predominately images structures dipping in the plane of the stacking line; the structures dipping off the plane of the stacking line generate reflections that stack out of phase (Wu et al., 1995; Lundberg and Juhlin, 2011; Hedin et al., 2016). An irregular spatial geometry of sources and receivers along the survey line with variable crookedness results in subsurface reflection points dispersal and an uneven fold coverage, and distributions of offset and azimuth. Problems arising from the variable crookedness of the survey line are often addressed with patch by patch analysis in the conventional processing method. In this case, the processor divides the survey line into straight line segments and then processes each segment independently. Finally, the obtained results for each segment are integrated to produce the final results. Applying the 2D standard common-midpoint processing even to a small patch of straight traverse lines could not resolve the issues associated with the midpoint dispersion along with the crooked survey. In addition, this strategy might lead to misfits between patches and add numerous processing and imaging artifacts.

Also, the crooked geometry of seismic lines can result in considerable undulation artifacts of the imaged reflections, particularly reflectors that are cross-dipped. Various cross-dip analysis and correction methods have been proposed for crooked-line seismic data processing – including a constant shift (Larner et al., 1979), cross-dip moveout (Nedimović and West, 2003a), iterative cross-dip analysis in the absence of an inline-dip component (Beckel and Juhlin, 2019), and generalized cross-dip moveout (GCDMO) (Mancuso and Naghizadeh, 2021). Applying a constant shift trace by trace has been a commonly used method (Larner et al., 1979) that generally reduces the resolution of the resulting images. The CDMO method (Nedimović and West, 2003a) can be applied through a slant-stack transformation after correcting normal and inline dip moveouts. The cross-dip parameter can be determined using a grid search strategy interactively (Kim et al., 2014) or automatically. Even though, applying the CDMO method can partially correct cross-dip effects and improve the stacked sections; the main drawback is imaging out-of-plane reflections twice in the stack section, called the duplication problem. The sequential application of the NMO, DMO, and CDMO corrections might cause interfering of those effects, which results in inaccurate estimates of seismic attributes and the stacking-velocity field. For instance, the DMO operator may interpret moveout arising from cross-dip effects as an inline-dip time anomaly, and using these inline- and crossline-dips would lead to an incorrect velocity field. Furthermore, the slant-stack transformation prevents applying any further processing after the cross-dip correction and before stacking (see Nedimović and West, 2003a; Beckel and Juhlin, 2019). An iterative approach (Beckel and Juhlin, 2019) is used to overcome these problems; however, it has been assumed by Beckel and Juhlin (2019) that the reflector has no inline-dip component. In this method, the repetitive flow consists of NMO correction, CDMO correction, velocity analysis, and DMO correction. This sequence is applied until a high-quality stack section was achieved. The GCDMO approach can be used for any binning geometry and simultaneously corrects the NMO and CDMO effects. The optimal parameters – including dip-independent velocity, inline dip, and crossline dip – are interactively estimated using a repetitive grid search within a defined window. This method can suppress the reflection duplication, however, its accuracy is limited to a maximum of 40° and the interactive aspect makes the method laborious.

The quasi-3D nature of crooked seismic lines enabels us to image 3D complex structures when the line track is severely deviated. 3D binning and processing methods can be used to produce a volumetric image from 2D crooked-line seismic data. Application of the 3D conventional swath processing sequence on 2D crooked seismic data typically focuses prominent features with more accuracy but usually leads to low-resolution images. Cheraghi et al. (2020) utilized 2D and 3D prestack time migration and swath 3D processing methods for imaging another Metal Earths transect. Uneven spatial distribution of midpoints along the survey line, a narrow azimuth source-receiver geometry with a small aperture in the cross-profile direction are the main obstacles to achieving a high-quality image cube from a crooked-line seismic traverse (Cheraghi et al., 2020). Malehmir and Bellefleur (2016) applied 3D swath processing for a 2D crooked-line and 3D seismic data for deep mineral exploration. They showed that 3D data would lead to better subsurface images than 2D data. Also, they showed that diffractions can be collapsed at their correct locations with clearer signatures in 3D data.

The weak reflectivities, complex scattering, and noisy data are the main characteristics of the Larder Lake seismic data (Naghizadeh et al., 2021). The MF methods are capable of generating high-resolution stack sections in this type of noisy environment and are better suited to model the moveout of diffracted waves. However, a crooked-line survey geometry can hamper utilizing MF methods (Jodeiri Akbari Fam et al., 2021a). The early implementations of MF methods did not consider cross dip effects and horizontal variation of source and receiver coordinates (or variations in the azimuth of each source-receiver pair) in 3D space. Therefore, those early approaches cannot be applied for crooked-line seismic geometry (Landa et al., 1999; Gurevich et al., 2002; Berkovitch et al., 2008). For this reason, we developed an algorithm that takes into account the cross-dip effects, source-receiver azimuth, and coordinates variation in 3D space, called 2.5D MF (Jodeiri Akbari Fam et al., 2021a).

The main purpose of this paper is to apply the novel 2.5D multifocusing method to the Metal Earth hard-rock seismic data collected in Larder Lake to investigate its robustness and to compare its results to the conventional and advanced processing methods. We first discuss the technical and theoretical challenges associated with crooked-line surveying. The paper will review the theory behind the 2.5D MF algorithm, as well as its advantages and disadvantages; give a brief explanation of the geological settings over the Larder Lake area and the acquisition of the seismic data; present the workflow and results of the 2D prestack time migration, 2D time migration of DMO stack, and swath 3D imaging; describe the 2.5D MF imaging workflow and how the Differential Evolution (DE) global optimization algorithm has been adapted to optimally search the wavefield attributes. The latter step required evaluating the performance of the proposed method on synthetic data. Finally, a brief interpretation and discussion will be provided.

3.2.1 Technical and theoretical challenges associated with crooked-line surveying

In this section, we review the theoretical and technical challenges imposed by crooked-line survey geometries. Crooked lines following existing roads are often employed in 2D seismic surveys to reduce environmental impacts and cost (Malehmir and Bellefleur, 2016). The crooked-line seismic data acquisition can be considered as a pseudo-3D or 2.5D survey that provides useful 3D structural information (Wu, 1996; Schmelzbach et al., 2007). However, crooked-line geometry violates the fundamental assumption of 2D imaging algorithms – a straight-line survey with uniform fold coverage and even offset distribution. Irregular distribution of sources and receivers along a crooked profile disperses the reflection point locations from directly below the traverse line and results in considerable time and offset variant delay among reflections. Variable fold and uneven offset distribution in crooked-line geometry hamper utilizing 2D conventional common midpoint and advanced imaging techniques (Wu, 1996). Application of the 2D imaging approaches without an accurate cross-dip analysis not only fails to provide correct 3D structural information but also could lead to unreliable seismic images displaying transparent zones and defocused reflections, particularly from reflectors with a cross-dip component. Despite all challenges and pitfalls caused by the crookedness of the survey line, unlike the straight-line survey, crooked-line profiling can provide crossdip information, which plays a key role in structural interpretation (Wu et al., 1995). Therefore, useful information about 3D geological structures can be extracted from 2D crooked seismic data. However, it should be considered that the crooked-line survey cannot be a replacement for a properly designed 3D seismic survey (Malehmir and Bellefleur, 2016).

The 3D schematic diagrams shown in Figure 3.1 illustrate the problems posed by a crooked-line survey. Figure 3.1a and 3.1c show a crooked-line and a straight-line seismic surveys. Figure 3.1b shows the correct migrated image for the crooked-line seismic data along the black slalom traverse line (which is a smooth line fit to the crooked survey line). The survey lines are shown in blue. The green and magenta dots represent midpoint locations and reflection points for the entire survey, respectively. The transparent white plane is the desired imaging plane in the conventional processing method, which is a vertical plane extending along a straight traverse fit to the survey line. The black raypaths are shown for specific common-midpoint bins and their common-midpoint gathers are displayed in Figure 3.1d. The black points on the surface are the corresponding midpoint locations that belong to the selected common-midpoint bin. The reflections recorded in the common-midpoint gather by the crooked-line survey (Figure 3.1a) are shown with red wiggles. For comparison purposes, the black reflections collected by the straight survey line (Figure 3.1c) are superimposed in Figure 3.1d for the same imaging point location. Comparing the red and black reflections demonstrates how the crooked line geometry can affect recorded data by adding considerable time and offset variation among reflections. In this case, the red reflection arrivals are similar to the black at either side of the plot, as the location of the source-receiver pairs with far-offsets along the crooked-line survey are close to their locations in the straight survey line. For intermediate offsets, the red arrivals are earlier than the black, because, the path is shorter due to reflecting from part of the dipping reflector with smaller depth. In the center of the gather, there are no red reflections because the crookedness of the acquisition line shifted the midpoints off the selected common bin for the source-receiver pairs with near-offsets. Rather than imaging a single reflection point all the red reflections contribute to image the small part of the reflector marked with a dashed yellow circle in Figure 3.1a. A traveltime moveout operator is required that is able to correct the effects of offset, inline dip, and crossline dip accurately to focus all the reflections at the correct location with the least deformation. Comparing the crooked- (Figure 3.1a) and straight-line (Figure 3.1c) surveys shows how crooked geometry can spread the midpoint locations (green) and reflection points (magenta), which are passing around – behind or in front of the desired 2D vertical imaging plane. Moreover, the comparison of the reflection raypaths shown for the same location along the survey lines indicates that the crooked configuration significantly causes out-of-plane reflections. The midpoints for the selected example bin are shown in black, which spread out in the cross-dip direction in Figure 3.1a, while they are inherently centered in Figure 3.1c. Collapsing seismic energies associated with spread midpoints can be challenging for the crooked-line surveys, and it requires an imaging method that considers the displacement among the midpoints and the imaging point located on the traverse line.

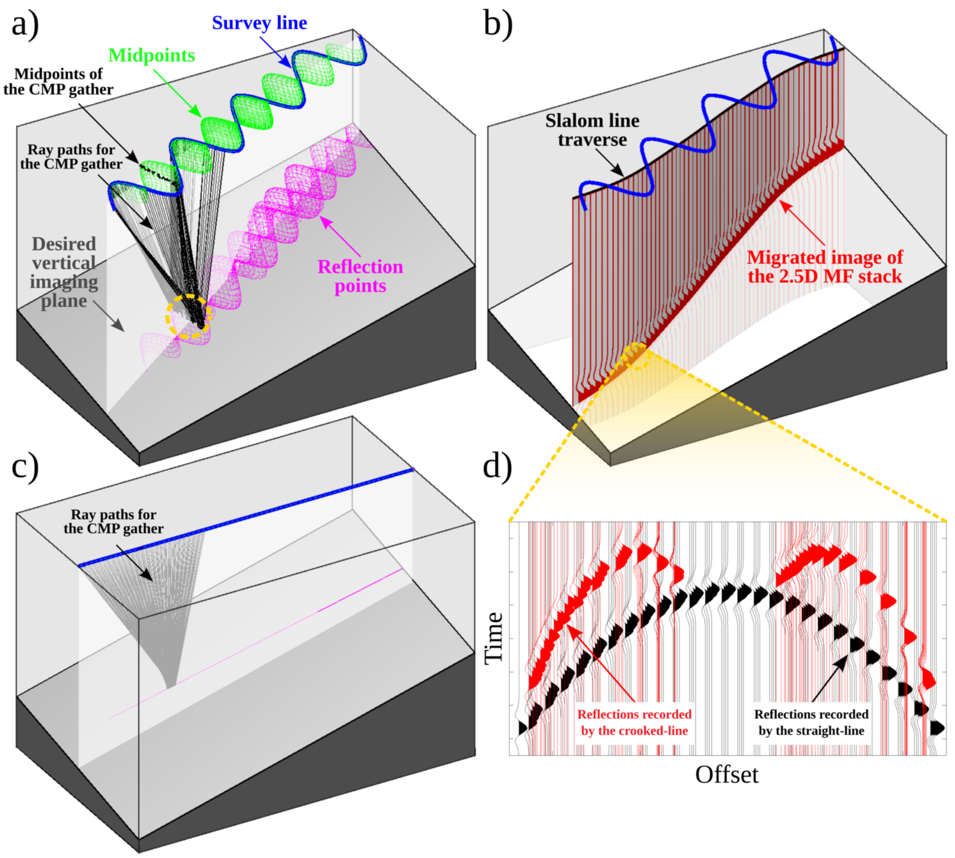

Figure 3.1: 3D schematic diagram of a) a crooked-line and c) a straight-line seismic survey. b) The correct migrated image for the crooked-line seismic data along the black traverse line. d) The examples of reflections recorded in the common-midpoint gathers by the crooked-line survey (red reflections) shown in (a) and the straight-line survey (black reflections) shown in (c). The survey lines are shown in blue. The green and magenta dots represent midpoint locations and reflection points for the entire crooked-line survey, respectively. The transparent white plane is the desired imaging plane in the conventional processing method. The black raypaths are shown for the common-midpoint gathers displayed in (d).

3.3 Review of multifocusing method

The MF approach is originally proposed by Gelchinsky et al. (1999a) based on the homeomorphic imaging theory and classified as a non-CMP-based stacking strategy. The MF algorithm is a highly-effective stacking method that simulates the zero-offset stack section by transferring multicoverage prestack seismic data into poststack domain. This method is a macro-model independent technique and does not require any knowledge of the subsurface model except the near-surface velocity.

The MF moveout operator is a multiparameter double-square-root approximation of wavefield traveltime, which depends on wavefield kinematic parameters. The MF formulation offers a more realistic simulation of reflections and diffractions traveltimes compared to the hyperbolic approximations, and MF can improve the resolution of seismic images and provide higher S/N. Also, this method accurately describes traveltime behavior for a wider class of subsurface models, even for strongly curved reflectors and moderate velocity variations. Shifting in time is the mechanism used in MF methods to account for overburden heterogeneity in an optical imaging auxiliary medium (De Bazelaire, 1988; Gurevich and Landa, 2002; Schwarz and Gajewski, 2017). This mechanism makes MF moveout non-stretching, which helps to avoid distortion or deformation of the amplitude and phase, particularly important for shallow events at large offsets.

Also, MF can be considered as a method for wavefield analysis, which reliably estimates wavefront parameters of each seismic event at each imaging point (Landa et al., 1999). Wavefront parameters, also called kinematic wavefield attributes, are a set of parameters that describe the propagating seismic wavefront and include emergence angle, radii of the normal-wave and normal-incident-point curvatures (Hubral, 1983). These unknown parameters can be estimated automatically using global optimization algorithms. These attributes have broad applications in seismic imaging and interpretation. Importantly, they can be used to determine dip-independent velocities and structural detail such as interface curvature and slope of the events (Landa et al., 2009). In addition, distinguishing diffractions and multiples are the other notable applications of MF methods.

During the last two decades, different extensions of the MF method have been introduced and employed in a wide range of applications, but mainly utilized to generate very detailed and high-resolution images in geologically complex areas (Landa et al., 1999; Gurevich et al., 2002; Berkovitch et al., 2004; Belfer et al., 2008b; Berkovitch et al., 2008, 2011, 2012b; Borghi et al., 2017; Curia et al., 2017; Chang et al., 2019b). In addition, other applications include mapping fracture corridors (Landa et al., 2013; Schoepp et al., 2015), multiple attenuations (Berkovitch et al., 2012a; Chang et al., 2019a), prestack seismic data enhancement and regularization (Buzlukov and Landa, 2013; Elhaj et al., 2014), diffraction imaging (Berkovitch et al., 2009), etc. The imaging and preservation of diffractions are crucial for the interpretation of small-scale structural elements, particularly in hard-rock imaging.

High-fold seismic data set is required to achieve an interpretable image in a hard-rock setting. Logistic and budget limitations restrict the number of sources and receivers used in 2D crooked lined profiling. The super bin data gathering can compensate for the effect of low fold geometry on the quality of the resulting images (Malehmir and Bellefleur, 2016). In fact, the MF approach constructs a zero-offset stack trace computed not only from the prestack traces belonging to the selected common-midpoint bin but also the prestack traces which are arbitrarily located around the imaging position within neighbouring bins. The accuracy of MF traveltime formulation in simulating far-offset data makes this strategy possible, which will enhance the S/N of stacked sections through stacking a much larger number of traces than in conventional CMP stacking.

The 2D MF methods can be applied for seismic data collected by surveys with arbitrary source and receiver distributions along the straight profile. However, the early MF operators did not consider the cross-offset and cross-dip components for crooked-line configurations, which is necessary for processing seismic data acquired by the Metal Earth project. Hence the motivation is for testing our new method (Jodeiri Akbari Fam et al., 2021a), which preserves the azimuth and accounts for the spatial distribution of the sources and receivers to address CMP dispersal problems.

The 2.5D MF method corrects normal, inline, and crossline dip moveouts simultaneously, which leads to more accurate time shifts and alignment of reflections. Its formulation depends on four unknown parameters including the inline dip (θ_x), crossline dip (θ_y), radius of curvature of normal wave (R_N), and radius of curvature of normal-incident-point wave (R_{NIP}). The proposed method avoids the duplication of reflections, an artifact produced by the CDMO operator when applied in crossdip analysis, and results in a more reliable stack section. Removing offset, inline, and crossline dip moveout effects sequentially will result in interference of these effects and lead to a cumulative error in the estimation of inline and crossline dips. Consequently, this will lead to inaccurate velocity fields. For instance, the CDMO operator interprets the residual moveout effects of normal and inline dip moveouts as a crossline dip moveout or vice versa. However, the 2.5D MF operator avoids the issues of residual moveout effects by correcting them simultaneously. As a result, the proposed method can extract true dips from seismic data, which can be used for structural interpretation and generating dip-independent stacking velocity fields.

The 2.5D MF method can be applied for 2D, 3D, and crooked-line seismic data with a flat datum. Therefore, the application of this method on a dataset collected over rough terrains requires prior source and receiver elevation statics corrections. The diffraction volume can be generated by substituting $R_N = R_{NIP}$ and converting apparent dips to the emergence angles in 2.5D MF formulation. Similar to the 2D MF, the 2.5D MF expression is derived for a constant near-surface velocity by assuming locally spherical wavefronts. The spherical wavefront assumption limits its accuracy for far offset data from strongly curved reflectors. Aside from this limitation, the 2.5D MF method can be considered as a comprehensive solution for stacking crooked-line seismic data, which can generate high-resolution sections of complex geologic structures in hard-rock settings and estimate structural attributes (see Jodeiri Akbari Fam et al., 2021a).

3.4 Geological setting of the Larder Lake area, Abitibi Greenstone Belt

The Larder Lake area, located within the southern Abitibi greenstone belt of the Superior Province (Figure 3.2), is a greenschist facies metavolcanic belt composed of six major volcanic successions that range in age from 2750 to 2696 Ma (Ayer et al., 2005). A series of calc-alkaline to alkaline composite stocks intruded these volcanic successions, coeval with the deposition of two sedimentary basins: the coarse clastic Timiskaming-type basin (2679–2669 Ma) (Ayer et al., 2005) and the fine turbidite dominated Porcupine-type basin (2690–2685 Ma). On a regional scale, these basins are spatially associated with major crustal-scale structures such as the Cadillac-Larder-Lake deformation zone (CLLDZ) (Figure 3.3) and the Porcupine-Destor deformation zone (PDDZ) (Frieman et al., 2017). In the Larder Lake area, the regional R1 seismic survey (Figure 3.3) strikes N-S for 42 km (49 km on roads) and at its northern end transects the Ben Nevis volcanic complex, part of the Blake River Group (2701 ± 3 –2698.5 ± 2 Ma) (Peloquin et al., 2008). These rocks are unconformably overlain by conglomerates, arkosic sandstones, and trachytic volcanics of the Timiskaming assemblage, (2679 – 2669 Ma) (Ayer et al., 2005). A sequence of mafic-ultramafic volcanic rocks of the Larder Lake group (circa 2705 Ma; 2710–2704 Ma) (Ayer et al., 2005) lies within the Timiskaming assemblage and the contact is associated locally with the CLLDZ. This major crustal-scale structure strikes E-W for approximately 250 km and steepens to near-vertical in the Larder Lake area (Figure 3.3) (Poulsen, 2017). The high-resolution seismic survey transects 11 km of a complexly folded, sedimentary basin composed of volcanic and sedimentary rocks and a series of felsic intrusions, which is fault-bounded in the north by the CLLDZ and in the south by the Lincoln Nipissing shear zone (LNSZ) (Figure 3.3).

Previous regional mapping in the area of the high-resolution survey (Figure 3.3) has defined volcanic rocks of felsic, mafic and ultramafic composition, assigned to the Larder Lake group, that are unconformably overlain by younger clastic sedimentary successions of the Hearst or possibly Timiskaming assemblage (Thomson, 1943, 1946; Hewitt, 1949, 1951, 1963; Jackson et al., 1991, 1994). The Hearst assemblage (circa 2700 Ma) (Ayer et al., 2002) comprises greywackes, arenites and local conglomerates, that are considered part of the Porcupine assemblage (Ayer et al., 2005). Intruded into all these units are mafic diorite, gabbro and a suite of felsic intrusive rocks, which range from syenite to granodiorite in composition (Figure 3.3).

3.5 Seismic data acquisition of the Larder Lake R2 records

In the Larder Lake transect area, the R2 seismic profile is located primarily in the southern half (Figure 3.3). The surveys are designed to cross complex geological structures mapped in the Larder Lake study area (Figure 3.3). The regional R1 survey of Larder Lake extends further to the north (and south) along the same traverse line (Figure 3.3). Figure 3.4 summarizes the geometry of the survey.

Table 3.1 summarizes the acquisition geometry of the Larder Lake R2 seismic line. The survey was acquired along a crooked line geometry due to logistical reasons and environmental restrictions, which led to the midpoints distribution in both inline and crossline directions of the survey (Figure 3.4). The profile length is about 12.5 km and the nominal

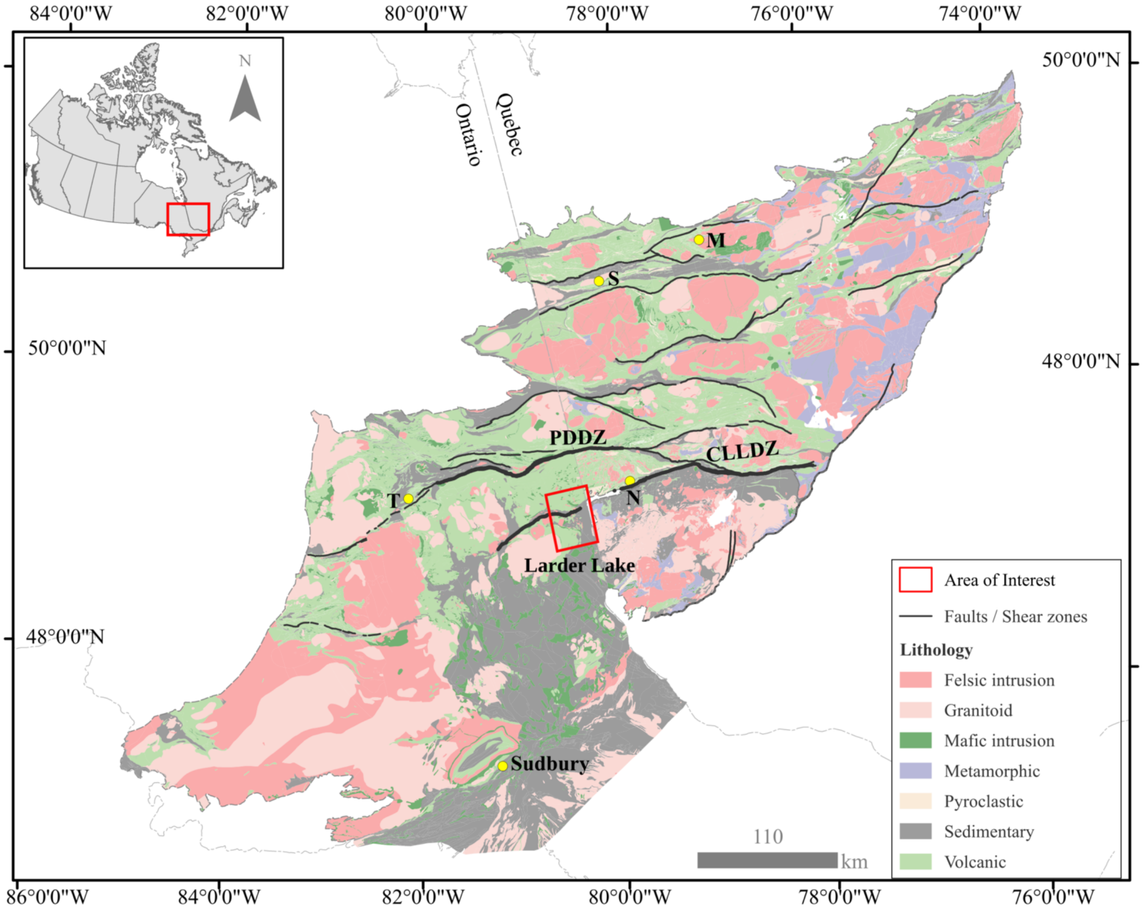

Figure 3.2: Location of the Larder Lake study area on the geological map of the Abitibi subprovince (Ayer et al. 2002). Inset shows the location of the Abitibi subprovince on a Canada map; rectangle marks the area of Figure 3. CLLDZ is the Cadillac–Larder Lake deformation zone. M, N, S, T locate the Matagami, Noranda, Selbaie, and Timmins mining centers, respectively.

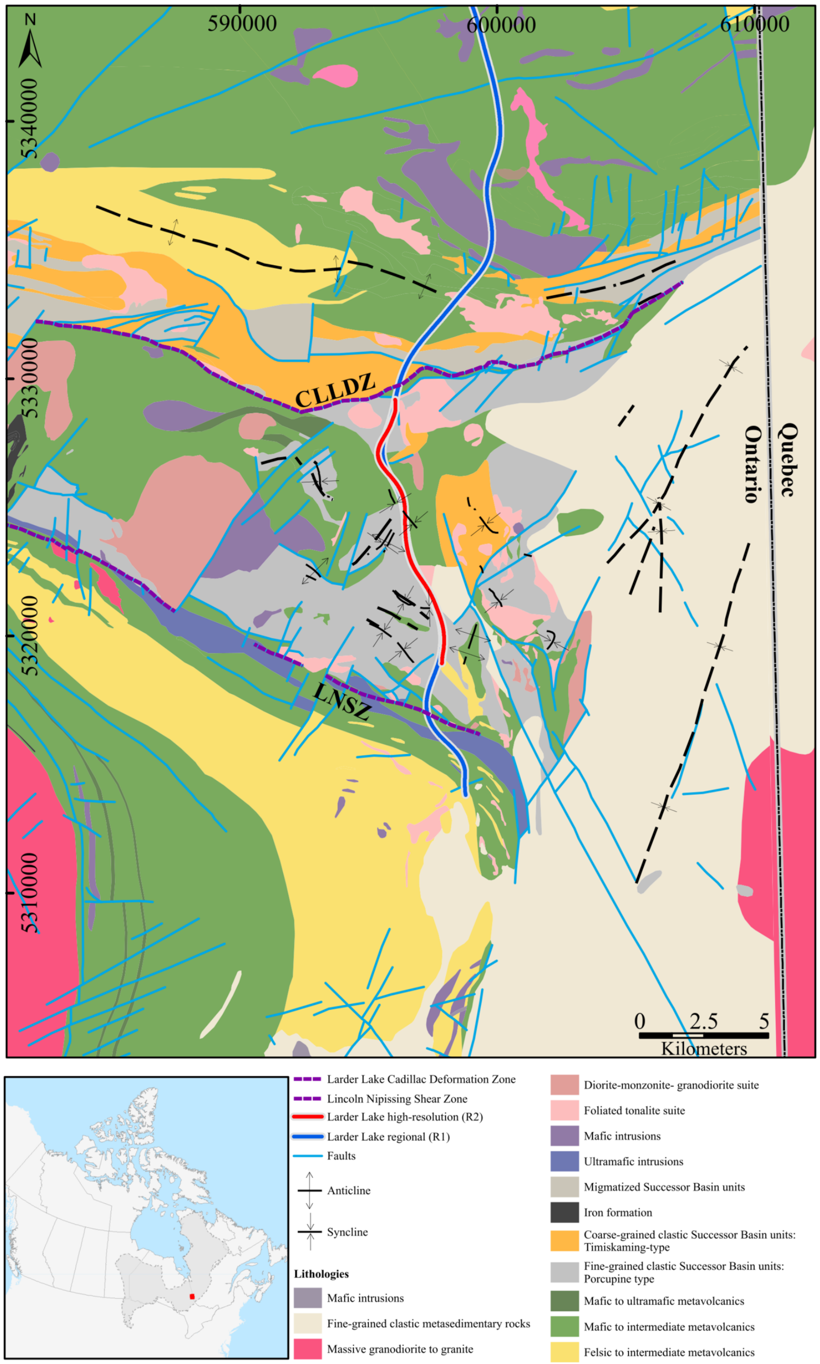

Figure 3.3: Geological map of the Larder Lake area. The route of the regional seismic survey (R1) is shown in blue, and overlaying this in red is the location of the high-resolution survey (R2). The location of the study area is shown in the inset.

maximum offset for processing is 10 km. The sources and receivers are placed with the split spread geometry along the crooked survey line (the solid thick black line in Figure 3.4) with intervals of 6.25 and 12.5 m, respectively. The vibroseis trucks were employed to generate four 28-second sweeps with the frequency bands of 2 to 120 Hz and for shot spacing of 25 m. An array of wireless single-vertical-component geophones were used to record seismic data for 12 s with a sampling rate of 2 ms. However, since the R2 survey focused on the upper crust, only 4 s of data was utiused in the processing.

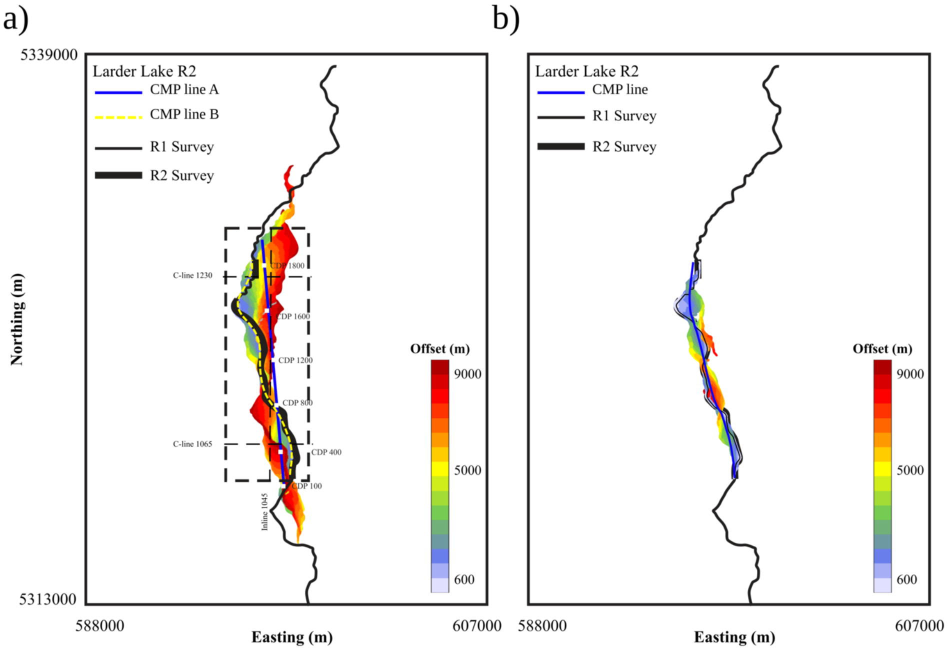

Figure 3.4: Distribution of midpoints (coloured by the offset in meters) along the R2 survey acquired in the Larder Lake area, used for the a) conventional and b) 2.5D MF processing flows. In figure (a), the midpoints are shown for the sources deployed along the R2 line and receivers activated on R1+R2 surveys. The solid blue straight (labeled A) and dashed yellow slalom (labeled B) lines are the traverse lines used for the 2D conventional seismic imaging and 2D prestack Kirchhoff time migration, respectively. Some CMP bins are numbered on the straight CMP line. The dashed rectangle marks the area considered for the swath 3D processing. The inline 1045 and crossline 1065 and 1230 from the 3D processing cube are explained in the text. In figure (b), the midpoints are shown for the sources and receivers planted only along the R2 line. The solid blue slalom line is the traverse line used for 2.5D MF processing flow.

Table 3.1: The survey geometry of the Larder Lake R2 seismic line.

Parameter	**Specifications**
R2 profile length	12.5 km
Spread type	Split spread
Recording instrument	Geospace GSX Node
Geophone type	5 Hz, single vertical component
Source type	Vibroseis
Number of sources in an array	3
Sweep length	28 s
Number of sweeps	1, For shot spacing of 25 m, four sweeps are acquired.
Source starting/ending frequency	2 / 120 Hz
Field low/high cut recording filter	2 / 207 Hz
Recording length	12 s
Sampling rate	2 ms
Source interval	6.25 m
Receiver interval	12.5 m
Nominal maximum offset for processing	10 km

Figure 3.4 shows the distribution of midpoints (coloured by the offset in meters) along the survey acquired in the Larder Lake area and the fitted traverse lines (also called CMP lines), used for the conventional (a) and 2.5D MF (b) processing flows. In Figure 3.4a, the midpoints are shown for the sources deployed along the R2 line and the receivers that were activated (these were identical for the R1+R2 surveys). The blue straight line (labeled A) was used for the 2D DMO processing, with some CMP bin numbers being labeled. The dashed yellow slalom line (labeled B) was generated by repeatedly applying a mean filter to the R2 receiver line. This line was used for the 2D DMO processing and 2D prestack Kirchhoff time migration. The dashed rectangle marks the area considered for the swath 3D processing. In Figure 3.4b, the midpoints are shown for the sources and receivers planted along the R2 line only. The solid blue slalom line represents the processing line used for 2.5D MF processing flow. This traverse line was generated based on the midpoint locations using a low-order polynomial regression approach, which can

reduce the midpoint dispersion effects and imaging artifacts by minimizing cross-shifts (see Table 1 provided by Jodeiri Akbari Fam et al. (2021a)) optimally for most of the midpoints.

3.6 Imaging of the Larder Lake R2 seismic survey

The Larder Lake area has been one of the main interests of the Metal Earth project. Due to the importance and difficulty of the study area, various conventional and advanced processing strategies have been employed by different processors to image the Larder Lake transect with high resolution. In this section, we will present the results.

3.6.1 2D conventional seismic imaging

The seismic processing sequences used in the 2D conventional and 2.5D MF imaging flows are outlined in Table 3.2. Prior to setting up the geometry, the field records were first converted from SEGD to SEGY format, and then the recording quality was checked. In most field records, first arrivals are clearly visible in far-offsets, which demonstrates solid coupling of geophones to the ground and sufficient source strength to propagate waves to distant locations. A complicated basin over a complex subsurface hard-rock setting with low-impedance contrasts led to field-shot records that showed only a limited number of reflections, with poor S/N. The reflections are from subhorizontal and steeply dipping interfaces with both inline and crossline dip components. Also, numerous out-of-plane reflections were believed to have been recorded by the survey. Figure 3.5 depicts an example of the field record before and after signal processing and static corrections. This figure demonstrates how challenging it can be to extract signals from this field data with weak reflectivity and low S/N. In some of the shot gathers, reflections were captured and can be observed in processed data, for instance, see the retrieved reflection indicated with black arrows in Figure 3.5b. In this example, a high level of random and coherent noises would not allow the recorded reflection to be seen coherently in the data prior to signal processing (Figure 3.5). Spectral analysis was also performed and showed that the raw field data contain information within the expected frequency range from 5 to 130 Hz.

After inspection and editing the traces manually, we picked the first arrivals with offset up to 10 km using an automatic algorithm followed by a manual modification. Next, we performed refraction static analysis to calculate time delays necessary to correct the

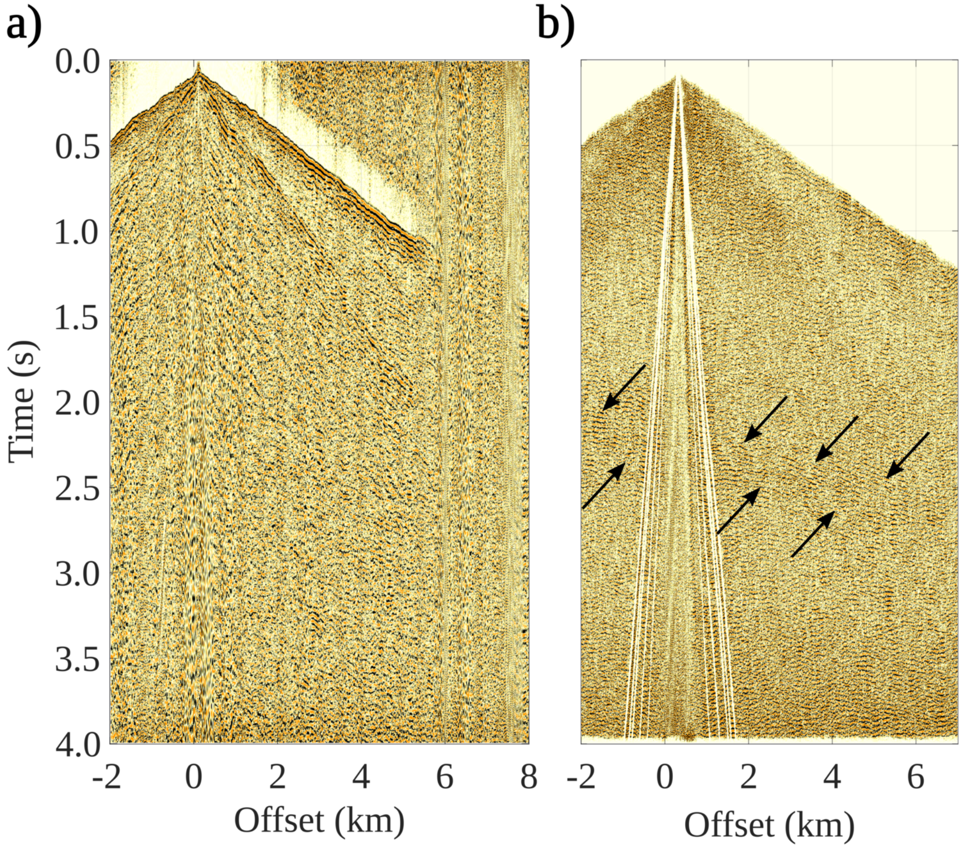

Figure 3.5: An example of the field record before (a) and after (b) signal processing and static corrections.

effect of low velocity overburden in wave propagation (Juhlin, 1995). The initial near-surface velocity model consisted of a layer with a velocity of 1000 m/s and a replacement velocity of 5200 m/s. The time delays were calculated with a maximum offset of 3000 m, and then the elevation and refraction statics corrections were applied. In order to recover signal amplitudes attenuated with depth, a spherical divergence was used. Next, we designed a median velocity filter to attenuate some seismic events with velocities of 1400, 2500, and 3000 m/s. Also, by considering the frequency content of the raw data (i.e., 5-130 Hz), a band-pass filter was used to preserve wave energy within a range of 35-120 Hz. This frequencies range would allow imaging potential reflections and attenuate low-frequency random and coherent noise such as ground roll (Yilmaz, 2001). A median filter was also applied to attenuate ground roll and shear waves. Then, a notch filter was used to remove 60 Hz data associated with noise with constant frequency. The low-frequency and low-velocity coherent noise, possibly surface waves, which were remained and had not been attenuated, were muted. We used the same signal processing and static corrections mentioned above for the 2.5D MF imaging. We applied a surface consistent deconvolution filter (length of 100 ms and gap of 17 ms) to increase vertical resolution by reducing the effect of the source wavelet. Trace balancing and automatic gain control were applied to recover the amplitude of attenuated signals. Then, the first arrivals were muted using a cosine-taper.

To image crooked-line seismic data, determining a proper traverse line (CMP line) is a crucial step prior to binning and stacking, particularly for a survey with a broad spread of midpoints in the crossline direction. A CMP line needs to be fitted to midpoint distribution such that it minimizes the cross-offset effects and partly address the problems of and uneven distribution of offsets and fold coverage. Based on the capability of each imaging methods, we examined both straight and slalom traverse lines. For applying 2D conventional stacking, we selected a straight traverse line (CMP line A) with a

Table 3.2: The processing sequences applied in the conventinal and multifocusing flows.

2D/3D conventinal flows	**2.5D multifocusing flow**
Reading data in SEGD format and converting them to SEGY format	
Setup geometry	
Trace editing (manual)	
First arrival picking (near and far offsets)	
Elevation and refraction static corrections [a]	
Spherical divergence compensation (V^2t)	
Median velocity filter (1400, 2500, and 3000 m/s)	
Band pass filter (20-35-100-125 Hz)	
1D median filter to remove the ground roll and shear waves (Airwave filter)	
Notch filter to remove 60 Hz frequency	
1D linear filtering to remove remaining low-velocity noise	
Surface-consistent r deconvolution	
Trace balancing	Trace balancing
Automatic gain control (window of 150 ms)	Down sampling to 4 ms
Top-muting to remove first arrivals	Top-muting to remove first arrivals
Common-midpoint bining [b]	Super common-midpoint bining [c]
Velocity analysis	Wavefield attributes analysis
Smoothing velocity field	Smoothing attributes along reflections
NMO+DMO corrections	2.5D MF correction
Residual static correction	Residual static correction
Top-muting to remove first arrivals	
Stacking	Stacking
Coherency filter (F-X deconvolution, filter length of 19 traces)	
Trace balancing	Trace balancing
Phase shift time migration (5000 m/s)	Kirchhoff time migration

[a] Replacement velocity: 5200 m/s, floating datum level: 340 m, V_0: 1000 m/s

[b] CMP spacing for 2D bining: 6.5 m, cell size for 3D bining: 50 m by 50 m

[c] Compromises of 5 nearby CMP gathers and CMP spacing of 10 m

CMP interval of 6.2 m, which is along the longest axis of the midpoint cloud (Figures 3.4a). After binning data along the straight CMP line, we performed velocity analysis to generate a velocity field for DMO corrections. We then calculated and applied residual static corrections to enhance the coherency of the reflections by reducing the effects of the short-wavelength near-surface velocity variations.

In the conventional processing sequence, dip moveout analysis is required to estimate dip independent velocity, particularly for imaging shallow/deep steeply-dipping reflections (Schmelzbach et al., 2007). For 2D conventional imaging of the Larder Lake data, the sequence of DMO stacking followed by phase-shift time migration was used, the same as the processing steps proposed by Schmelzbach et al. (2007). The DMO velocity analysis consists of three steps including 1) generating DMO stack panels for a range of constant velocities to construct a stacked volume, 2) picking velocity functions from the semblance spectra that generate more coherent reflections, and 3) constructing a stacking velocity field by interpolation and then smoothing of the velocity functions. The resulting velocity field ranges from 5500 to 6500 m/s. We did not have access to petrophysical measurements from the Larder Lake area to use as constraints in velocity field building. Overall, the estimated velocities are typical for crystalline environments (Salisbury et al., 2003). The crossdip events significantly affected velocity analysis and the performance of the DMO correction. Therefore, the crossline illumination components needed to be considered in the moveout correction. Crossdip moveout analysis was then applied, but could not enhance the quality of the section due to the complexity of the subsurface. After stacking, a coherency filter (F-X deconvolution) was also applied to enhance the quality of the stack section. We tested various algorithms to perform poststack migration including Stolt, finite difference, and phase-shift migration methods (see Yilmaz, 2001 for detailed information about the methods). We observed that the phase-shift migration with constant velocity resulted in the most coherent images with fewer migration artifacts compared.

The final DMO stacked and the migrated seismic sections along the Larder Lake R2 line are shown in Figure 3.6 (see Figures 3.3 and 3.4a for the location). A time to depth conversion using the estimated velocity field gives a maximum depth of approximately 12 km. The northern end of the R2 survey (Figure 3.3) is located at the LLCDZ (Larder-Cadillac deformation zone), but structures directly associated with the local LLCDZ were apparently not imaged due to its assumed near-vertical structure. The R2 survey terminates at its southern end approximately 1 km north of the LNSZ (the Lincoln-Nipissing shear zone, Figure 3.3). This structure, which is poorly understood, dips steeply to the north and, depending on the geometry of this structure at depth, may project onto and be expressed on the seismic survey despite the apparent distance away from this structure on surface (Figure 3.3). The sharp, vertical truncation of prominent reflections at 0.6 s and CMP 200 (most evident on the migrated section) suggests a near-vertical fault splay perhaps related to the LNSZ.

The structural basin through which the Larder Lake R2 survey traverses is poorly understood due to the structural complexity of this basin and the lack of detailed structural analysis. This is owing to a lack of accessibility into the area, limited surface exposure of the rocks, and no available borehole data. The migrated seismic section of the Larder Lake R2 line imaged a package of shallowly north-dipping reflections at times of 1.8-2.5 s over $\sim$ 5 km of the section at CMPs 100-900 (see Figure 3.6). These reflections may mark the base of the metavolcanic and successor basin rocks of the Hearst assemblage. A series of tight antiforms, apparently stacked vertically along the northern limit of the seismic section (at times of 0.1-0.6 s and CMP 1400-2000 on the migrated section), may represent deformation associated with the nearby LLCDZ.

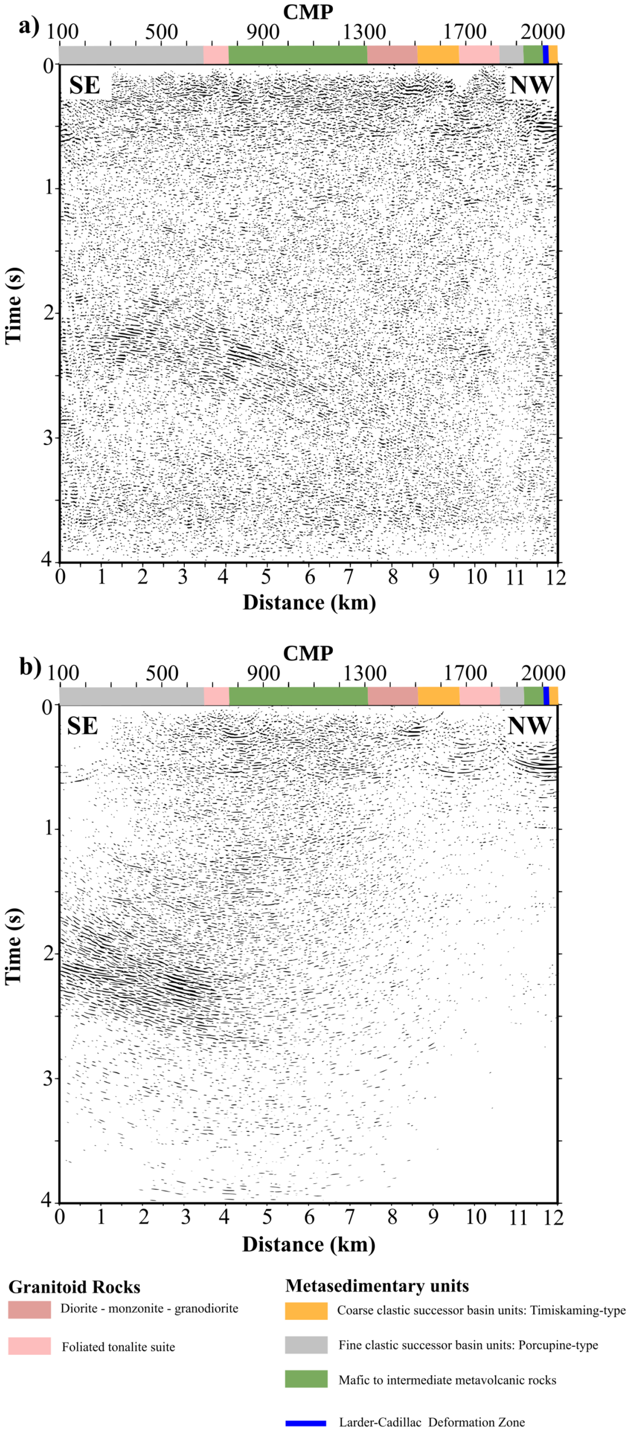

Figure 3.6: a) DMO stack and b) migrated stack time sections along the CMP line A in which one prominent package of subhorizontal reflections is observed at 2 s. See text for its interpretation. Rock types mapped or inferred at the surface of the survey path are shown at the top of each section with no dips of contacts implied.

3.6.2 2D prestack Kirchhoff time migration

The crossdip analysis (Nedimović and West, 2003a) failed to enhance the resulting images in the Larder Lake area with complex subsurface geology. In such scenarios, applying the 3D prestack time migration (PSTM) method for processing crooked surveys can be considered as a suitable solution (Nedimović and West, 2003b). However, the 3D PSTM method is computationally expensive and requires an accurate dip-independent RMS velocity field. Also, for applying the 3D PSTM method, an additional step, seismic data reconstruction, is required to regularize the midpoint locations of data for reducing the negative effects posed by the midpoint dispersion problem (Biondi, 2006). Compared to the 3D PSTM method, the 2D PSTM method is computationally less expensive but still suffers from the midpoint dispersion problem. In this section, we will test the application of the 2D prestack Kirchhoff time migration method for the Larder Lake survey.

Table 3.3 listed the processing flow used for applying the 2D PSTM method, which was developed and executed commercially by a seismic processing company. This processing flow was designed to have a final shot point spacing of 25 m and a receiver spacing of 12.5 m. Therefore, every four field records were stacked such that a nominal shot point interval of 25 m was achieved before the final geometry assignment and start of the processing flow. Note that only shot stations were stacked, receiver stations were recorded at their desired intervals.

The quality of field records was controlled, reversed traces were edited manually, and bad records were discarded. The first breaks were then interactively picked and used for analyzing the geometry errors using a geometry predictor. After correcting the geometry, the data was sorted and binned along the traverse line (the dashed yellow line in Figure 3.4a). The CMP line was generated by applying a smoothing filter to the receiver line, such that did not deviate much from the survey path and followed the midpoints distribution aisle. This proved to be one of the challenging steps and required several iterations to achieve an effective plausible solution described above. A minimum phase filter was created and applied using the recorded sweep trace to remove the effect of the sweep and to convert the vibroseis data to the minimum phase before deconvolution. Then, an ensemble balance (a single scalar for each input of ensembles) was applied to minimize the variation in amplitudes between shot records within a given dataset. A time-frequency domain random- and linear-noise suppression technique was employed to attenuate high amplitude noise presents in the field records. Time and offset variant gain functions were applied to recover the amplitude and compensate for the amplitude attenuation due to wavefront spreading and attenuation. A spectral analysis was performed on the raw field data to identify harmonic noise. In this region, the main source of harmonic interference was considered possibly to be due to high voltage power transmission lines. A strong 60 Hz noise train was present throughout the data, which was rejected using a notch filter.

After some initial testing, a surface consistent deconvolution filter with an operator length of 160 ms and pre-whitening of 0.1 percent was designed within windows where noise (such as ground roll, air blast, and first break reverberations) had been excluded. As such, the design gate was optimized by interactively picking and reviewing the window along the line. An anomalous frequency suppression was applied in the frequency domain. Also, a single-window trace by trace amplitude balancing function was applied for trace equalization. The first break picks were used to build an initial near-surface velocity field, and then tomography was executed to calculate the near-surface velocity field. A replacement velocity of 5600 m/s and a flat datum of 500 m were used in the final static calculations. After statics corrections, a sequence of velociy analysis and surface consistent residual static calculation were performed iteratively on super common-midpoint gathers (a specified number of nearby CMPs) (see Table 3.3 for more details). For comparison with the results of other processing flows, the NMO correction and stacking was applied to produce a stack section along the traverse line. The stacking operator excluded 10% of the highest and lowest sample values contributing to each CMP. The resulting stack section is shown in Figure 3.7a.

After signal processing and long/short wavelength statics corrections, prestack velocity analysis was carried out with incremental velocity changes of 2%. The migrated stack panels and gathers (70-130 every 2%), were created and used for prestack migration velocity analysis. Such precision in prestack velocity analysis (only 2% incremental velocity changes compared to coarse changes in velocity analysis for stacking and poststack migration) often result in an accurate RMS velocity field, which is crucial in prestack migration. Afterward, the prestack time migration was applied with a migration angle of 65 degrees and a maximum aperture of 10 km. The PSTM operator migrates each trace to the corresponding output CMP bin center by accounting exactly for its spatial coordinates of source and receivers and for any variations in elevation. The severe crookedness of the survey line dispersed the midpoints and resulted in very large CMP-CDP distances, particularly for reflectors with the crossdip component. These large distances would prevent the cancellation of off-line energy during the prestack migration process leading to a less than optimal result. Therefore, the PSTM method was applied for traces with a CMP-CDP distance of up to 500 m. After CDP stacking, a limited aperture $\tau - p$ transform was applied to the final sections to enhance the coherent seismic events. A zero phase, bandpass filter of 6-12-25-40 Hz was determined most suitable for the final displays. In addition, to achieve a well-balanced section, a trace-by-trace multi-gate scalar was used with a rolling gate of 1000 ms and a 500 ms overlap. The final PSTM image is shown in Figure 3.7b. The poststack Kirchhoff time migration was also applied on the stack section (Figure 3.7a). The result was almost similar to the PSTM

Table 3.3: The processing sequence used for applying the 2D prestack Kirchhoff time migration, designed by a commercial seismic-processing company.

Process	**Parameter/Explanation**
Field data reformat	
Stacking of shot stations	
Geometry (crooked line binning)	
Trace kills and reversals	
Minimum phase conversion	to convert the vibroseis data to minimum phase
Ensemble balance	to minimize the variation in amplitudes between shot records
Linear and erratic noise suppression	
Amplitude recovery	time and offset variant gain functions + gain correction ($g(t) = t^{1.5}$)
Harmonic noise suppression	60 Hz
Surface consistent deconvolution	an operator length of 160 ms and pre-whitening of 0.1 percent
Anomalous frequency suppression	output band of 5-100 Hz
Trace equalization	trace by trace amplitude balancing function
Refraction analysis [a]	replacement velocity of 5600 m/s and floating datum level of 500 m
Velocity analysis [b]	
Surface consistent residual statics	correlation window 2000-9000 ms, static shift $+/-$ 68 ms, correlations per trace 15, number of iterations 3
Velocity analysis [b]	
Surface consistent residual statics	correlation window 1000-9000 ms, static shift $+/-$ 48 ms, correlations per trace 15, number of iterations 3
Velocity analysis [b]	
Normal moveout and mute	
CMP stack	
Prestack velocity analysis	
Prestack time migration (PSTM)	a migration angle of 65 degrees and a maximum aperture of 10 km, Limit the CMP-CDP distance to 500 m for the prestack time migration
CDP stack	
Noise attenuation	a limited aperture $\tau - p$ transformation
Filter/trace equalization [c]	a zero phase, band pass filter of 6-12-25-40 Hz

[a] Offsets up to 5 km were used to generate the refraction model and statics. Offsets up to 15 km were used to obtain an initial near surface model and then tomography was run to calculate the near-surface velocity field.

[b] performed on super common-midpoint gathers.

[c] a trace-by-trace multi-gate scalar with rolling gate of 1000 ms and a 500 ms overlap

section shown in 3.7b, which indicates that the PSTM method was unable to improve the resolution of the crooked-line seismic data. Two factors prevented us benefitting from the potential of the 2D prestack time migration to produce a high-quality image. The first reason was the 3D nature of crooked-line seismic data, and the second was that the dip-independency requirement of the RMS velocity field was not fulfilled.

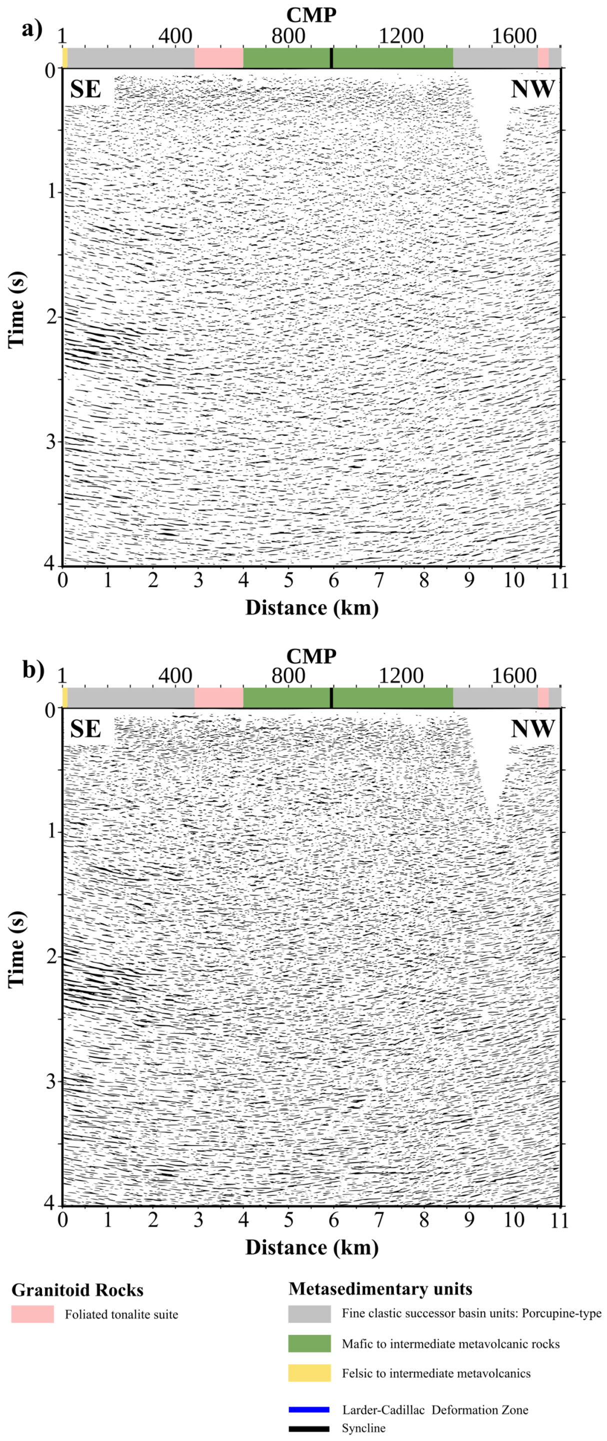

Figure 3.7: a) NMO stack and b) prestack time migrated sections (commercially processed seismic imaging results) along the CMP line B in which one prominent package of subhorizontal reflections is observed at 2 s in the southeast. Rock types mapped or inferred at the surface of the survey path are shown at the top of each section with no dips of contacts implied.

3.6.3 Swath 3D seismic imaging

A significant number of trace midpoints are placed off the fitted traverse line, prominently in the crossline direction (see Figure 3.4). Therefore, accounting for the cross-offset and cross-dip effects are required to accurately image reflectors dipping in the crossline direction. One can consider the effect of off-line midpoints using 3D binning and processing flow, which allows generally resolved data-driven reconstructions of the subsurface (Nedimović and West, 2003a,b; Malehmir et al., 2012; Malehmir and Bellefleur, 2016). Note that the 3D wave sampling criteria cannot be completely fulfilled by swath 3D surveys, which leads to imaging with less capability than by conventional 3D surveys (Vermeer, 1998).

We utilized the processing workflow provided by Hedin et al. (2016) and Malehmir et al. (2011) to apply the swath 3D imaging algorithm in the Larder Lake R2 survey. The 2D preprocessed field records were input into the proposed flow. Then, the midpoints were sorted into regular common bins. We conducted bin size analysis with sizes ranging from 20 to 50 m to investigate which can result in a 3D stack volume with high quality. The dashed black rectangle in Figure 3.4a shows the surface projection of the selected 3D processing area. The best result was achieved with square bins with a size of 50 m by 50 m. Next, we iteratively performed velocity analysis to build a reliable 3D velocity field. Finally, the phase-shift migration was applied in both inline and crossline directions of swath 3D surveys to generate a volumetric image from crooked-line seismic data. A coherency filter (F-X deconvolution) was also applied in both directions to enhance the quality of the images. After each step of inline and crossline migrations, the bins without midpoints are muted. This would help to reduce the artifacts generated by the migration process and the coherency filter, which could smear noise to empty bins.

The 2D section from the Larder Lake area showed one package of reflections at times of 1.8-2.5 s. Two 3D views along inline 1045 are shown in Figures 3.8 and 3.9. Inline 1045 (shown with the dashed black line on Figure 3.4a) roughly coincides with the straight and slalom 2D processing lines shown in Figure 3.4a. Figures 3.8 and 3.9 imaged subhorizontal reflections at times of 0.5-1 s and also at the time of ~ 2.5 s in the south and north of the area. Both sets of subhorizontal reflections in the south continue towards the north and east along inline 1045 and crossline 1065, respectively (Figure 3.8). The prominent reflections along the 2D section of the Larder Lake area shown in Figure 3.6 are also imaged in 3D as a package of subhorizontal reflections at the time of ~ 2.5 s.

The swath 3D processing imaged some reflections in the area close to the LNSZ and LLCDZ (Figures 3.8 and 3.9), which are a poorly understood structure and can be confirmed using the coincident regional line (Naghizadeh et al., 2019). The reflections observed in the southern part (Figure 3.8) can be correlated tentatively as part of the LNSZ (Figure 3.3) and most likely represent its expression along a possible linked detachment fault at depth. The reflections at the northern part of the area (Figure 3.9) continue in the south and east directions near the location where inline 1045 and crossline 1230 intersect (see Figure 3.4a for the location). This set of reflections could be related to tight folding in the vicinity of the LLCDZ (Figure 3.3).

3.7 2.5D multifocusing method

3.7.1 Processing workflow

Figure 3.10 summarizes the processing workflow designed for applying the 2.5D MF algorithm to produce high-resolution stack and prestack/poststack time migrated images.

After signal processing, the near-surface velocity-depth model is estimated, and source-receiver tomo-statics corrections are calculated and applied. Next, the data is sorted into common-midpoint bins. The conventional velocity analysis is performed to build an initial stacking velocity field. This stacking velocity field will be used to determine constraints on the search range for R_{NIP} in the wavefront attributes estimation. Next, the Fresnel zone is analyzed to define an optimal aperture for building super common-midpoint bins (see next section for details). Practically, one can try several candidates for the midpoint aperture until good results are achieved, similar to the estimation of the offset aperture. Then, the processed field records are sorted into multi-coverage super common-midpoint gathers. The next step involved adjusting the parameters of the global optimization algorithm and determining the constraints for unknown parameters, which controls the search operator. The adjustment can be performed based on prior geological knowledge and legacy data. The globally optimal wavefield attributes are estimated (see section 6.1.2 for details) using global optimization algorithms such as the

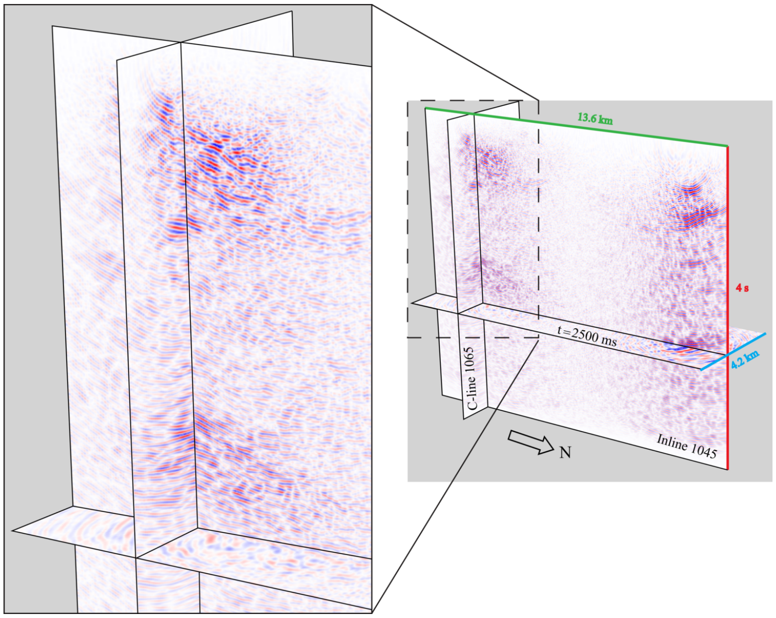

Figure 3.8: Three-dimensional perspective view of Larder Lake survey using Inline 1045, crossline 1065, and time slice 2500 ms. See text for interpretation.

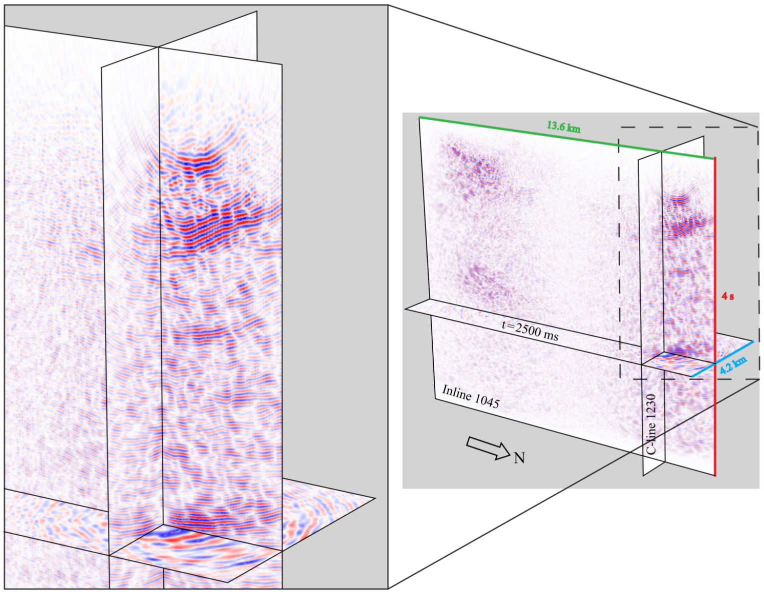

Figure 3.9: Three-dimensional perspective view of Larder Lake survey along Inline 1045, crossline 1230 and time slice 2500 ms. See text for interpretation.

differential evolution method (see Appendix 3-A) or the very-fast simulated annealing method (Jodeiri Akbari Fam and Naghizadeh, 2019). This step requires several iterations to adjust the constraints and fine-tune searching parameters to achieve accurate solutions effectively. Next, the 2.5D MF moveout correction is applied using estimated optimal attributes. The alignment of reflections can be improved by residual static corrections. Partial stacking also can enhance the S/N and would yield more coherent reflections. The enhanced 2.5D MF corrected super gathers are stacked to produce an accurate representation of the zero-offset wavefield. Finally, migration velocity analysis can be performed to build dip-independent velocity fields for prestack/poststack migration using standard methods.

3.7.1.1 Fresnel zone analysis and super common-midpoint binning

Determining the optimum aperture in the super common-midpoint binning procedure, (a) optimizes the computational cost, (b) improves the S/N, and (c) produces sharper and high-resolution stack sections (Schleicher et al., 1997). Due to the limited bandwidth of seismic waves, reflections do not have an infinitesimally small common reflection point but also reflect from adjacent points on the reflector located within a finite area around the reflection point which is called a Fresnel zone (Heilmann, 2007; Mann, 2002). In other words, the Fresnel zone is a measure of lateral resolution which indicates the smallest horizontal size of a subsurface segment that can be imaged (Hubral et al., 1993).

In the MF methods, each zero-offset trace is constructed by stacking traces that belong

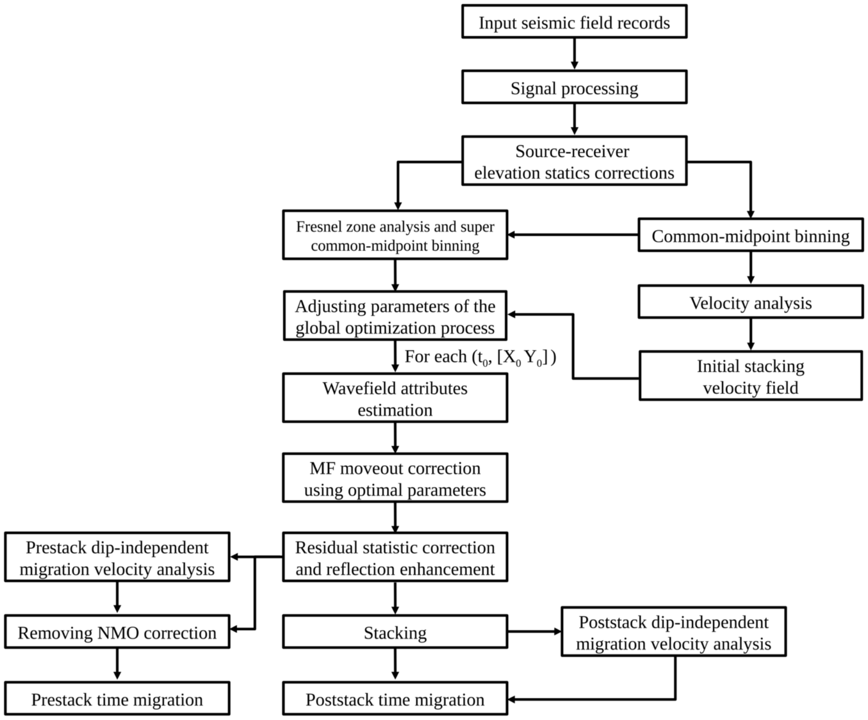

Figure 3.10: The processing workflow designed for the 2.5D MF algorithm.

to a super gather. Each super gather comprises several nearby CMP gathers within the limits of a certain span in the vicinity of the central (imaging) point on the recording surface. The MF moveout correction is based on the spherical approximation of wavefronts and the correction is exact for a single dipping planar reflector under a homogeneous overburden. Also, the MF correction is accurate for any curved reflector that can be adequately approximated by an arc of constant curvature at the reflection points (Gurevich and Landa, 2002). However, if these conditions are violated, the spherical approximation of wavefronts is no longer valid (such as the presence of a fault and sharp changes in the overburden). Therefore, MF stacking may smear any sharp reflection discontinuities.

For maintaining a good spatial resolution of generated sections and true-amplitude imaging, there are two criteria that have to be taken into account to control the size of the super binning aperture: 1) the size of the Fresnel zone and 2) the size of the paraxial vicinity. The first criterion defines the maximum aperture which contains rays with wavefronts that interfere constructively at the receiver and can be used for imaging without loss of lateral resolution (Heilmann, 2007; Mann, 2002). The size of the Fresnel zone depends on the frequency content of the data, which, in turn, controls the maximum achievable resolution. In principle, defining these apertures in a data-driven way can be estimated using Fresnel zone analysis. But in practice, it is not easy to estimate the size for arbitrary inhomogeneous media with curved interfaces (if at all possible) (Berkovitch et al., 2012b). The second criterion defines the aperture for which a maximum S/N can be achieved by constructive stacking while the MF traveltime approximation is sufficiently valid. The latest criterion implicitly depends on the complexity of the unknown subsurface structure and is difficult to evaluate. The aperture can be estimated in two ways: 1) estimating the size of the projected first Fresnel zone, which addresses the first criterion (Berkovitch et al., 2009; Heilmann, 2007; Mann, 2002) and 2) subsurface aperture analysis, which can account for both criteria (Gurevich and Landa, 2002).

In the first method, the aperture area is determined by the size of the first projected Fresnel zone (Berkovitch et al., 2008). Hubral et al. (1993) demonstrated how the projected Fresnel zone for zero-offset rays can be estimated from properties of the central ray. Later, Schleicher et al. (1997) published a generalized form for arbitrary acquisition geometries. The first interface Fresnel zone is the intersection of the first Fresnel volume with a reflector in the depth domain, which defines the maximum achievable resolution in terms of reflector properties. This parameter corresponds to the projected first Fresnel zone in the time domain. The size of the time-variant aperture around the central point $[X_0, Y_0]$ for reflected waves is defined by (Hubral, 1983; Berkovitch et al., 2009)

$$W = |d_0 - d_m| = \frac{2}{cos\beta}\sqrt{\frac{V_0 T}{2|\frac{1}{R_N} - \frac{1}{R_{NIP}}|}}, \tag{3.1}$$

where $|d_0 - d_m|$ is the absolute value of midpoint displacement along the azimuth of the true dip, β is the true dip ($tan\beta = \sqrt{tan^2\theta_x + tan^2\theta_y}$), and T is the period of the signal ($T = 1/f$, with f the dominant frequency). The midpoint displacement can be decomposed along the inline and crossline direction. At an early stage in the algorithm, the MF parameters are not yet available and initial attribute search requires user-defined apertures. We solve this issue using approximate time-invariant apertures which can be estimated using the following expression (Mann, 2002)

$$W = min[W_{f,max}, \frac{V_0 + (V_{max} - V_0)\frac{t_0}{t_{max}}}{2}\sqrt{2Tt_0} + W_{f,min}], \tag{3.2}$$

where $W_{f,min}$ and $W_{f,max}$ are user-given constant minimum and maximum widths, V_0 is the near-surface velocity at zero-offset traveltime (t_0), and $V_{max} = V_{RMS}(t_0 = t_{max})$. Afterward, we could improve the attribute estimation using the obtained initial attributes and updated searching aperture with equation 3.1. But for the stacking process, it is always possible to use the attributes to limit the stacking aperture. However, the search and stacking apertures should not differ significantly. Otherwise it cannot be guaranteed that the determined attributes define the best-fitting stacking operator.

The second approach aims to control the extent of the area of reflection points on a given reflector (subsurface aperture or reflection point dispersal d) rather than limiting the range of nearby CMPs (surface aperture). This approach requires a relation between the MF attributes and the range of validity of the associated MF traveltime approximation for mapping a specific subsurface segment with high S/N. This condition can be evaluated through maximizing the coherence criterion computed over the super gather. To restrict the reflection point dispersal by a user-defined threshold value d, for a specific sample and a given combination of moveout parameters, coherence calculations should only use the traces that satisfy this condition (Gurevich and Landa, 2002):

$$|\frac{\Delta d_G + \Delta d_S + \frac{2\Delta d_G \Delta d_S}{R_{NIP}} sin\beta}{2R_{NIP} + (\Delta d_S + \Delta d_G) sin\beta}| R_{NIP} < d. \tag{3.3}$$

Here, d is the subsurface aperture, and the left expression represents the normal projection of reflection point dispersal δ (distance between the reflection point and normal incident point) onto the surface along the azimuth of the true dip. The parameter Δd_S (or Δd_G) is the projected offset between source (or receiver) and M_0' along the azimuth of the true dip. The point $M_0' = [X_{M_0'}, Y_{M_0'}]$ is the intersection between an orthogonal line to the traverse line at the image point $[X_0, Y_0]$ and a line that connects the source and receiver (see Appendix 2-A).

In the coherence analysis of a super gather, only those traces will be considered that are reflected from a certain distance *delta* in the vicinity of the normal incident point. The parameter d can be chosen within the interval $0 \leq d \leq n \triangle x$; where $\triangle x$ is the interval between adjacent CMPs and n is the number of CMP gathers that form a super gather.

The optimal subsurface aperture depends on the spatial resolution of the seismic data, which can be defined using the size of the Fresnel zone and the S/N in the data. To increase the stacking power despite reducing the resolution, if the noise level in prestack data is high, one can use a wider subsurface aperture, up to $d = n \bigtriangleup x$. On the other hand, if the S/N is sufficiently high, smaller values of d that is close to the size of the Fresnel zone can be used to achieve the highest resolution (Gurevich and Landa, 2002). The subsurface aperture analysis has two potential advantages in controlling the reflection-point dispersal. First, if d is set to be appropriately small, the effect of reflector curvature can be neglected and the MF moveout correction can be accurately approximated by taking the normal-wave radius to be infinite, i.e., $R_N = \infty$. Secondly, the subsurface aperture analysis prevents unwanted smearing of the reflection events on the stacked section (Gurevich and Landa, 2002).

3.7.1.2 Wavefront parameter analysis

The practical implementation of the 2.5D MF method requires the simultaneous determination of wavefield parameters (θ_x, θ_y, R_{NIP}, and R_N) at each $(t_0, [X_0, Y_0])$. Searching unknown wavefield attributes for each $(t_0, [X_0, Y_0])$ coordinates, is a global optimization problem, which is technically challenging and computationally expensive. This technical problem can be addressed by adopting a global optimization approach, which determines the wavefield parameters automatically – rather than using an interactive procedure for parameter estimation like conventional velocity analysis. The main challenge is the simultaneous determination of the parameters optimally and efficiently.

Determining globally optimal parameters is a crucial step of 2.5D MF stacking, especially for complex structures and low-fold data. All subsequent processes rely on the estimated wavefield attributes. Poor data quality in hard-rock settings compromises the accuracy of determination of wavefield parameters and might make the optimization process unstable (Ahmed et al., 2015). Therefore, determining search range and fine-tuning search parameters are more critical for hard-rock seismic data. Additionally, hard-rock seismic data is mainly dominated by diffractions and out-of-plane reflections, which makes it necessary to apply conflicting dip analysis during wavefield parameter estimation (Xie and Gajewski, 2018).

In this research, we optimize the estimation of MF parameters using the multidimensional constrained differential evolution (DE) global optimization algorithm (Garabito and Cruz, 2019; Jodeiri Akbari Fam et al., 2021b). This algorithm is a data-driven global optimization approach. The objective function that is maximized is coherence, which measures the local similarity of signals in a defined time window. Searching over all data provides kinematic wavefield attributes and a coherence section. The stacking velocity field derived from conventional velocity analysis is used to determine the lower and upper bound constraints of the search range for the radius of curvature of normal-incidence-point wave (R_{NIP}). This strategy improves the convergence behavior and estimation accuracy of the wavefield attributes.

The coherence section can be considered as a valuable by-product, which provides an attribute for interpreters (Ahmed et al., 2015). The coherence indicates which reflections are mapped more coherently and can be interpreted with high confidence. Or in other words, this helps us to determine the part of the derived stack section that is more reliable than others. Also, the coherence values can be used for weighting the stack section – multiplying the coherence with the stacked amplitudes for each $(t_0, [X_0, Y_0])$ – to further improves the S/N leading to more reliable interpretations. A coherence-weighted stack section is a helpful tool for hard-rock structural interpretation that can be used in addition to the other commonly-used seismic sections.

3.7.2 Synthetic model experiment

We examined the accuracy of the proposed 2.5D MF stacking operator on a synthetic data set generated using the finite-difference method (Bohlen, 2002) with the same survey geometry utilized in the Larder Lake R2 seismic profile. Figure 3.11a shows the synthetic velocity model, which includes three planar interfaces with different inline and crossline dip components outlined in Table 3.4. The velocity range was assigned based on prior geological knowledge and legacy data from the Larder Lake area. Differential Evolution (DE) optimization algorithm was employed to automatically determine the unknown parameters of the method. This algorithm uses a data-driven global optimization approach based on maximizing a coherency objective function. In Figure 3.11, the acquisition and the slalom processing lines are shown on the datum surface using the solid red and black lines, respectively. Figure 3.11b shows the result of applying the 2.5D MF method on the synthetic seismic data to produce a stack section along the traverse line.

The interval velocity model along the traverse line is transformed from the migrated depth domain into the stacked time domain, which can be considered as the reference section. Figure 3.11c depicts the reference section overlaid on the 2.5D MF stack. This figure confirms that the 2.5D MF method images reflections accurately, which are well-matched with the projected interval velocity section. The result in Figure 3.11c reveals that the 2.5D MF method was able to accurately correct all of the normal, inline dip, and crossline dip moveout effects simultaneously. Also, the proposed method accurately focused the reflections at the correct location and produced stacked reflection data with

Table 3.4: Comparing the estimated inline and crossline dips for the synthetic model

	Exact Values		**2.5D MF**	
Parameters	$\theta_x(^\circ)$	$\theta_y(^\circ)$	$\theta_x(^\circ)$	$\theta_y(^\circ)$
Reflector #1	0.000	-15.000	-0.312	-14.785
Reflector #2	-10.000	0.000	-9.906	-1.392
Reflector #3	-15.000	-10.000	-14.257	-10.052

a high vertical resolution.

The exact and estimated inline and crossline dips for the synthetic model (Figure 3.11a) are summarized in Table 3.4. Comparing the exact and estimated values demonstrates that the 2.5D MF method can extract the structural information with good accuracy using the DE global optimization algorithm.

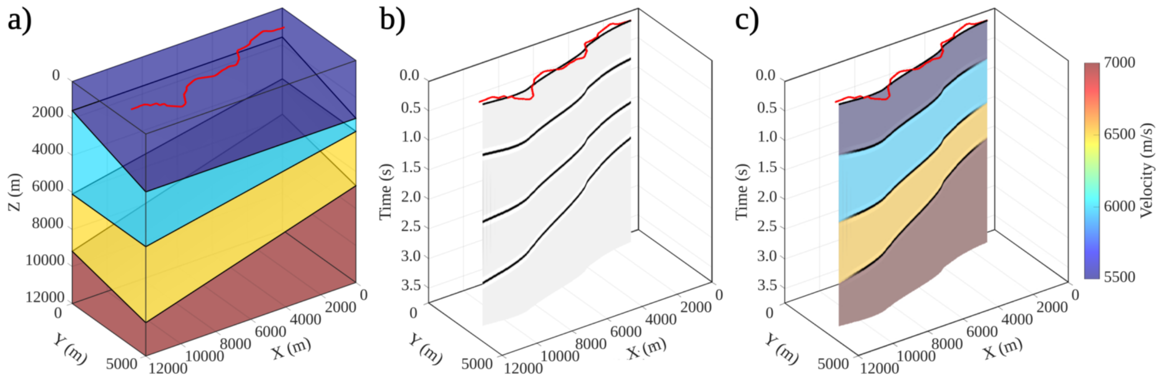

Figure 3.11: a) 3D synthetic velocity model and the acquisition line (solid red), b) 2.5D MF stack section along the solid black slalom processing line, and c) projected interval velocity model (reference section) from the migrated depth domain into the time stack domain overlaid with the 2.5D MF stack section shown in (b).

3.7.3 Application of the 2.5D multifocusing method on Larder Lake R2 data

The processing sequence used in the 2.5D MF imaging is summarized in Table 3.2. The signal processing and statics corrections were applied in a manner comparable to the flow used in conventional processing, which was discussed in the previous section. For applying the proposed method, we only used the seismic data recorded by receivers placed for the R2 survey and excluded the traces genrated by R2 sources and captured by active R1 receivers that are beyond the R2 line (see Figure 3.4b). This was done to exclude traces with far offsets where the reflections become nonhyperbolic. This also reduces the fold coverage and the data volume, which challenge the proposed method to retrieve signals from a dataset with a lower fold than the fold coverage of data used in the other processing flows. After trace balancing, the preprocessed data were downsampled from 2 ms to 4 ms to reduce the computational cost of the optimal MF parameters search. Then, the midpoints were binned with constant CMP intervals (every 10 m) along the solid blue slalom line (Figure 3.4b) at a maximum radius of 750 m. Then, the data was sorted into CMP gathers. Based on Fresnel zone analysis, five nearby CMP gathers were combined to contribute to a super CMP gather to achieve a high fold coverage. Super binning increased the fold, the number of traces belonging to each super CMP gather, by a factor of 5. This should significantly improve the S/N of the resulting stack section if the moveout of reflections is optimally approximated.

Next, wavefield analysis was carried out to estimate the wavefield attributes. We developed the 2.5D MF algorithm package code in C using the Seismic Unix software package (Stockwell Jr, 1999). For efficient implementation of the proposed algorithm, the parallel processing of the packaged C code was achieved using a serial farming technique by

Table 3.5: The adjustments of the DE optimization algorithm and the constraints used for wavefield parameter searching.

Parameter	**Adjustments/Constraints**
Window Length of Coherence Function	15 samples
Maximum Number of Generations (G)	30
Population Size (NP)	50
Crossing Over Factor (CR)	0.5
Scale Factor (F)	0.5
Problem Size (D)	4
θ_x	$-85° < \theta_x < 85°$
θ_y	$-55° < \theta_y < 55°$
$V_{min,max}$	4500 - 7500 m/s
V_0	5500 m/s
R_N	Constant (1000 km)
R_{NIP}	$0 < \theta_y < 15$ km [a]

[a] $V_{min}^2(t/2V_0)\cos^2(max(|\beta|)) < R_{NIP} < V_{max}^2(t/2V_0)$

Shell scripting. Building a software package allows us to utilize the proposed method as a comprehensive solution for the imaging of crooked-line seismic records and maximizing the data-driven extraction of structural information. Several runs of the DE search were conducted to adjust the constraints and fine-tune the searching parameters to achieve an accurate solution effectively. Based on prior geological information and conventional images, we adjusted the near-surface velocity to 5500 m/s and the normal wavefront curvature to zero. This strategy decreased the number of unknowns from four to three resulting in faster convergence to the global maxima. The parameters of the DE optimization algorithm and the constraints used for wavefield parameter searching are summarized in Table 3.5. After optimizing the required parameters, we applied an event-consistent smoothing filter (Mann and Duveneck, 2004) on the estimated attributes along the reflections.

Figure 3.12 shows the 2.5D MF parameters and coherence function (in colour) estimated using the differential evolution global optimization algorithm. All the sections are superimposed on the 2.5D MF stack section shown in black and white. Figure 3.12a is the inline dip (θ_x), the apparent dip along the north-south direction, on which red and blue colours correspond to positive and negative dips towards the south and north, respectively. Figure 3.12b is the crossline dip (θ_y), the apparent dip along the east-west direction, where red and blue colours correspond to positive and negative dips towards east and west, respectively. The prominent reflection package at about 2.5 s has a 15 degrees dip to the north and about 10 degrees to the east. Using these two apparent dips, true dip and strike can be estimated, which are valuable information for the structural interpretation of the geological units. Figure 3.12c displays the radius of the normal-incident-point wave curvature R_{NIP}, which generally increases with depth and is not reliable on the edges of the section. The coherency function in Figure 3.12d shows that the prominent reflection package at ~ 2.5 s and the near-surface futures were imaged reliably and can be interpreted with more confidence compared to other events. The attribute images have been smoothed using a moving average filter along the reflections.

We utilized these optimal attributes to apply 2.5D MF correction to the traces in each super CMP gather. The residual static correction was then calculated and applied to address the effects of any short-wavelength near-surface velocity variations. Next, the corrected super CMP gathers were stacked and plotted along the slalom traverse line. The balanced 2.5D stack section is shown in Figure 3.13a. To migrate the 2.5D MF stacked section, we estimated a velocity field by applying poststack migration velocity analysis on the 2.5D MF corrected data. Finally, we applied the poststack Kirchhoff time migration using the smoothed dip-independent velocity field. Zero padding was used to reduce the migration artifacts on the final image. Figure 3.13b shows the final migrated image of the 2.5D MF stack section (Figure 3.13a). The Larder Lake transect exhibits several subsurface conflicting dip layers (see L5-L6 and L7-L8 in Figure 3.13b). In comparison to the conventional image, the proposed 2.5D MF method made noticeable improvements (see L5 in Figure 3.13b) to the quality of seismic imaging and alignment of reflection events (indicated by the red arrows in Figure 3.13a). The results also show that the 2.5D MF method mapped new reflections, including dipping and sub-horizontal features at the time gate of 1.5-4 seconds labeled by L6, L7, and L8 (Figure 3.13b). Also, several new near-surface reflections were imaged by the 2.5D MF method at top 0.75 s and CMPs 1-250 and 0.25-1 s and CMPs 250-750, which are not visible in the other

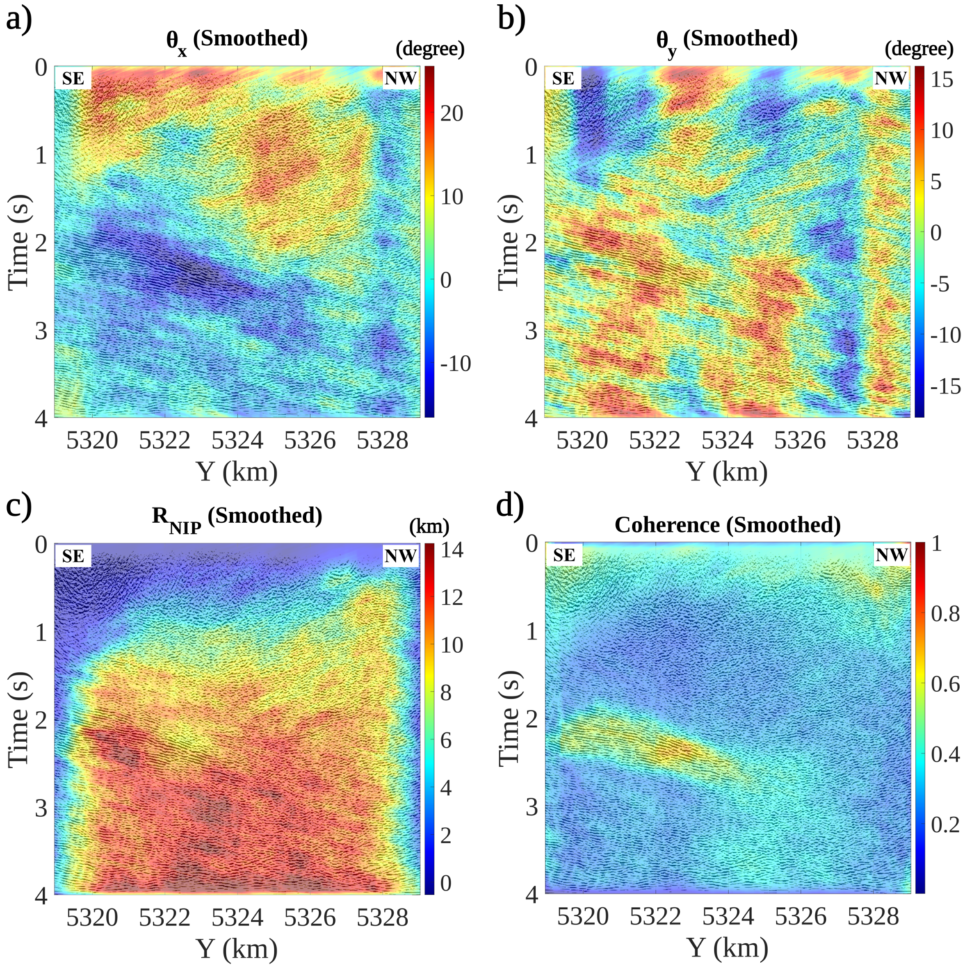

Figure 3.12: The estimated 2.5D MF parameters and coherence function using a nonlinear global optimization algorithm. a) The apparent dip along the north-south direction, b) The apparent dip along the east-west direction, c) The radius of normal-incident-point wave curvature, and d) The coherence section. All sections are shown in colour superimposed on the 2.5D MF stack section (black and white).

processed 2D seismic sections. Overall, the 2.5D MF method provided more clear and coherent sections with a higher S/N and vertical resolution than the 2D conventional and PSTM methods.

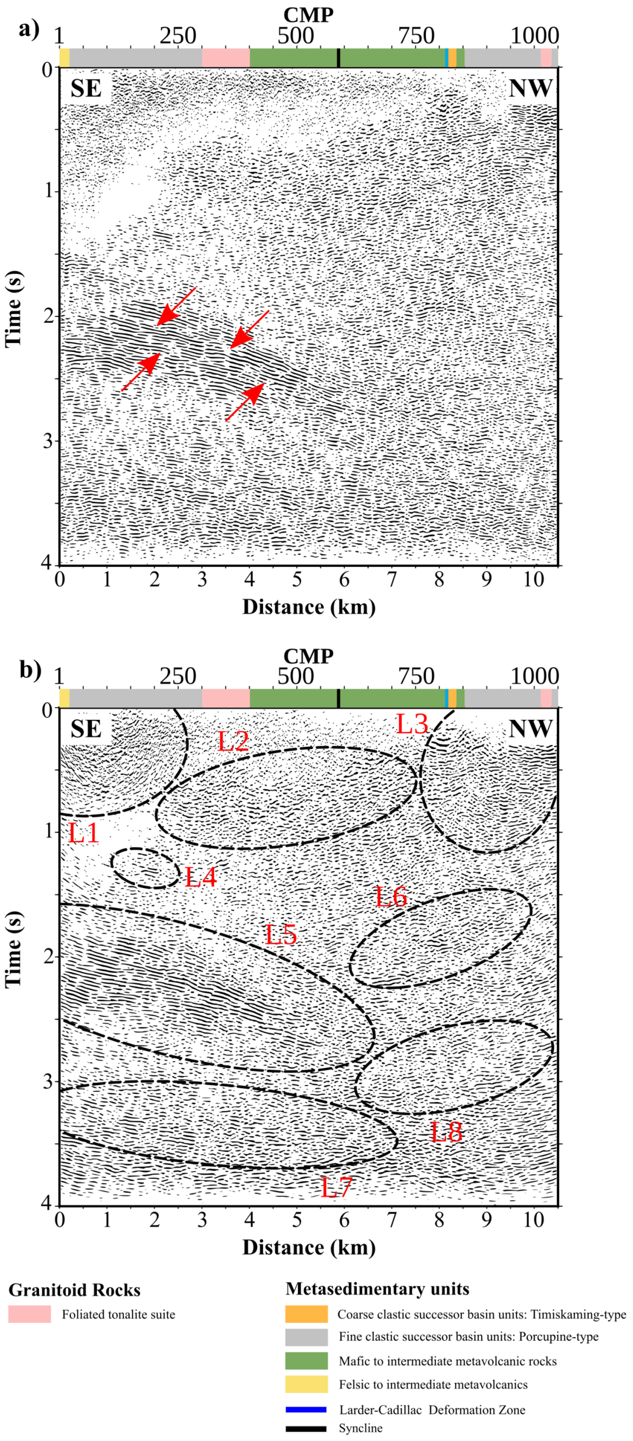

Figure 3.13: a) 2.5D MF stack and b) poststack Kirchhoff migrated stack sections. See text for its interpretation. Rock types mapped or inferred at the surface of the survey path are shown at the top of each section with no dips of contacts implied.

3.8 Discussion and interpretations

Figures 3.4a and 3.4b shows the data points used in the different processing methods. The field recordings used in the 2.5D MF method were limited to the traces recorded by only the R2 survey, while in the 2D prestack time migration and 2D postack migration of DMO stack, we used traces generated by the sources shot along the R2 line and receivers activated on R1+R2 surveys. Using the traces recorded in R1 receivers provided more far-offset seismic data for both 2D methods. Also, in the processing flow of the 2D prestack time migration, every four field records were stacked such that a nominal shot point spacing of 25 m was achieved before final geometry and processing commenced.

The sections shown in Figures 3.14 and 3.16 are plotted with the same Northing coordinate for comparison purposes. Figures 3.14a and 3.14b are the conventional NMO stack and the prestack Kirchhoff time migration along the CMP line B, respectively. The conventional NMO+DMO stack and its poststack phase-shift time migration along the CMP line A are shown in Figures 3.14c and 3.14d, respectively. Figures 3.14e and 3.14f display the 2.5D MF stack and its poststack Kirchhoff time migration image, respectively.

The main reflector package includes a group of steeply dipping interfaces located at about 1.5-3 s, which are indicated by a black dashed ellipse (L5) in the migrated images shown in Figures 3.14b, 3.14d, and 3.14f. Comparing L5s shows that the migrated section of the 2.5D MF stack imaged this zone more coherently and continuously over a larger area. The near-surface in the northwest of the section was imaged in the migrated 2D DMO stack (weakly) and 2.5D MF stack (more coherently), while the prestack migration resulted in a gap zone that was indicated by a question mark. The near-surface in the southeast was imaged in the migrated 2.5D MF stack, while it was not evident in the other two. The near-surface in the middle of the survey was imaged only in the migrated 2D DMO stack (labeled L0). The 2.5D MF method mapped some subhorizontal reflectors at about 3.5 s and some dipping interfaces at 2 and 3 s in the NW (labeled L6 and L8) were imaged in the migrated 2.5D MF stack. The evidence of the presence of subhorizontal reflectors can be also seen in the prestack migration result at 3.5 s on Figure 3.14b, label L7. A package of subhorizontal reflectors was imaged in the migrated 2.5D MF stack, in the middle of the profile at about 0.75 s (labeled L2) that can be interpreted as the base of the Larder Lake basin.

In the shallow basin above ~ 2 s, there are few coherent reflectors. With some imagination, the NMO stack (Figure 3.14a) shows a shallow dip to the NW that flattens at the NW end of the section. The conventional DMO stack shows some short isolated reflections scattered throughout the top 2 s of the section, with a few more coherent reflections on the top 0.2 s to the NW (Figure 3.14c). The 2.5D MF stack section also shows the short flat reflections in the top 2 s. The migrated sections show little improvement in the part of the section below 2 s, except the 2.5D MF section, where the short flat-lying reflections are stronger in features that dip to the SE (labeled L6, L7, and L8). Little confidence might be placed in these, except that the seismic attribute maps show similar trends and θ_x on Figure 3.12a also suggest that the interfaces are dipping to the SE. South-dipping interfaces are also evident on the 3D swath processing (Figure 3.16a), but only at the extreme north of the section (labeled L3 and L8 in Figure 3.16a). The 2.5D MF processing, therefore, provides new and useful regional-scale information about the structural basin between the LNDZ and the CLLDZ. The lack of coherence in this basin might be due to tight folding on scales comparable to the Fresnel zone.

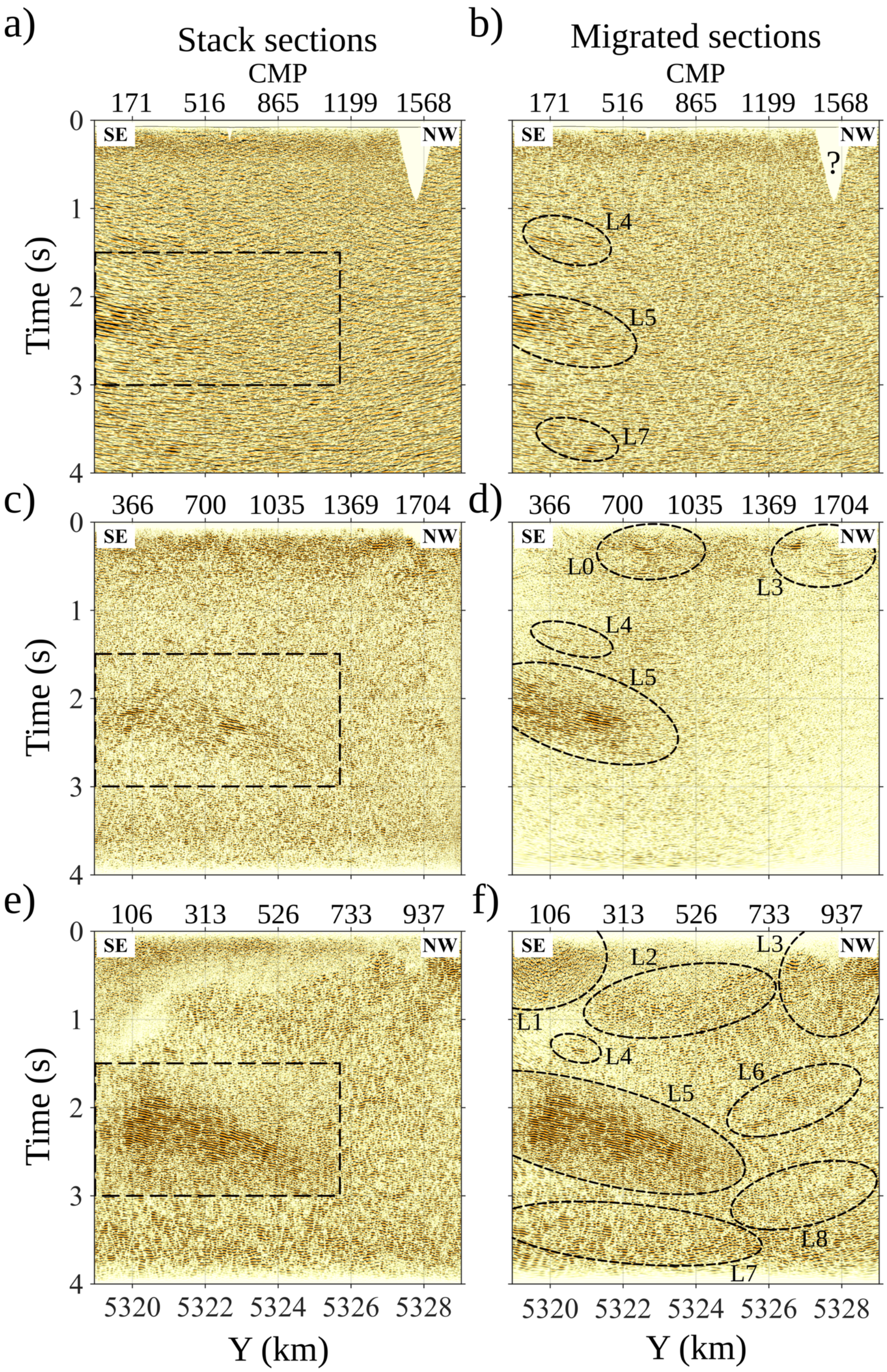

Figure 3.14: Comparing the stack sections and migrated images obtained by different flows including a) conventional NMO stack and b) prestack Kirchhoff time migration along the CMP line B, c) conventional NMO+DMO stack and d) poststack phase-shift time migration of the stack section along the CMP line A, e) 2.5D MF stack and f) poststack Kirchhoff time migration of 2.5D MF stack section. All sections are plotted within the same Northing coordinate.

Overall, the poor result obtained by the 2D prestack time migration and the migrated 2D DMO stack can be attributed to the fact that they do not account for midpoint dispersion and crossdip effects. A significant number of trace midpoints are placed off the fitted traverse line, prominently in the crossline direction (see Figure 3.4a). Therefore, accounting for the cross-offset and cross-dip effects are required to accurately image reflectors dipping in the crossline direction.

Figure 3.15 compares the prominent package of steeply dipping reflections (marked with a black dashed rectangle at ~ 2.5 s in corresponding sections in Figures 3.14a, 3.14c, and 3.14e) mapped on stack sections obtained by the NMO stack (Figure 3.15a), NMO+DMO stack (Figure 3.15b), and 2.5D MF stacking (Figure 3.15c) methods. This figure clearly depicts the robustness of the 2.5D MF method in improving the resolution of the stack section. The 2.5D MF approach generated a more clear and coherent stack with a higher S/N than the conventional methods, which can be considered as a more accurate representation of the zero-offset wavefield. The proposed method was able to resolve the ambiguity involved in geological structure by understanding the location and continuity of reflections.

Seismic surveys acquired along severely crooked transects can image complex 3D structures in the subsurface if a proper 3D imaging algorithm is deployed (Wu, 1996; Malehmir and Bellefleur, 2016). Comparing Figures 3.16a and 3.16b shows that the 3D swath processing of our 2D data did not image steeply-dipping reflectors properly (compare L5s on both sections) but it delineated the extension of some of the subhorizontal reflectors with low resolution. The 3D processing was able to image the reflectors in the Larder Lake structural basin which are connected with complex folded structures to the extreme south and north of the area (labeled L1 and L3 in Figure 3.16a). The 2.5D MF workflow imaged the steeply-dipping reflector (L5 in Figure 3.16b) coherently and focused new reflectors (L4 and L6 in Figure 3.16b) with low S/N, while could not delineate the reflector L0 (Figure 3.16a). Also, the 2.5D MF approach partly mapped the folded structures in the shallower part (L1 and L3). Overall, the 2.5D MF workflow generated an image with higher resolution than the swath 3D method, but its application along a 2D traverse line could not fully resolve the complexity associated with the folded structures in the basin

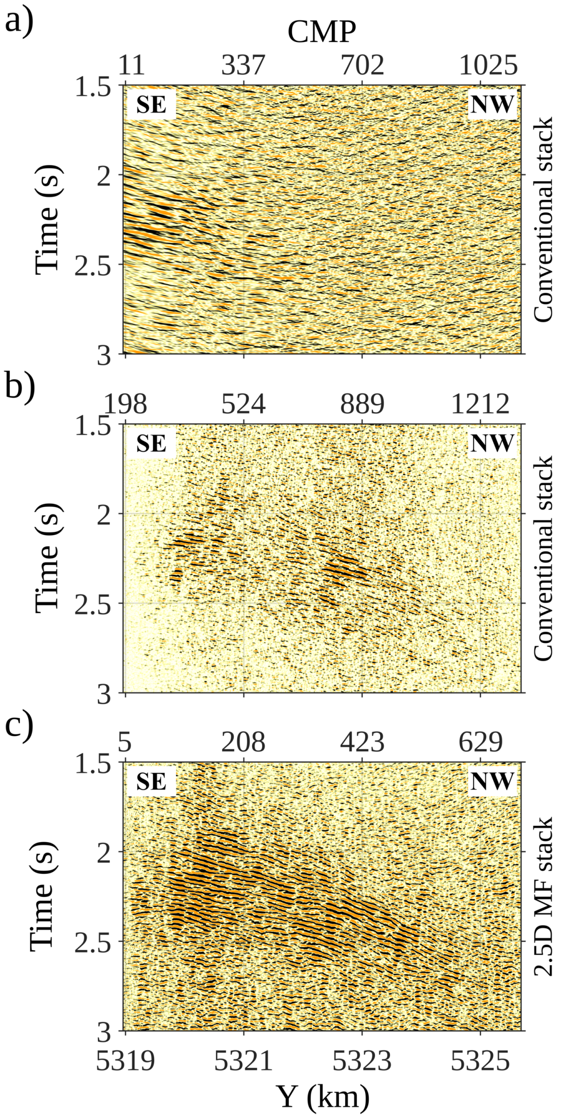

Figure 3.15: Comparing the prominent package of steeply dipping reflections mapped on stack sections obtained by the a) conventional (NMO stack), b) conventional (NMO+DMO stack), and c) 2.5D MF methods.

to the extreme south and north of the area.

This study clarified the necessity of processing cooked-line seismic data using a 3D approach but with an algorithm that can generate a high-resolution true representation of zero-offset wavefield and/or image volume. Swath 3D imaging result convinced us to test the 2.5D MF approach to produce a volumetric stack in future research. Assuming azimuthally isotropic constant radii of curvatures for each subsurface point allows the wavefield attributes to be estimated even with a limited number of distinct azimuth data. These capabilities enable us to produce a volumetric stack from a crooked-line survey using the 2.5D MF method.

The main limitation is the assumption of the locally spherical wavefront that limits its application to the planar and gently curved reflector with mild to moderate heterogeneities. To address this limitation, the spherical multifocusing method can be extended to three dimensions.

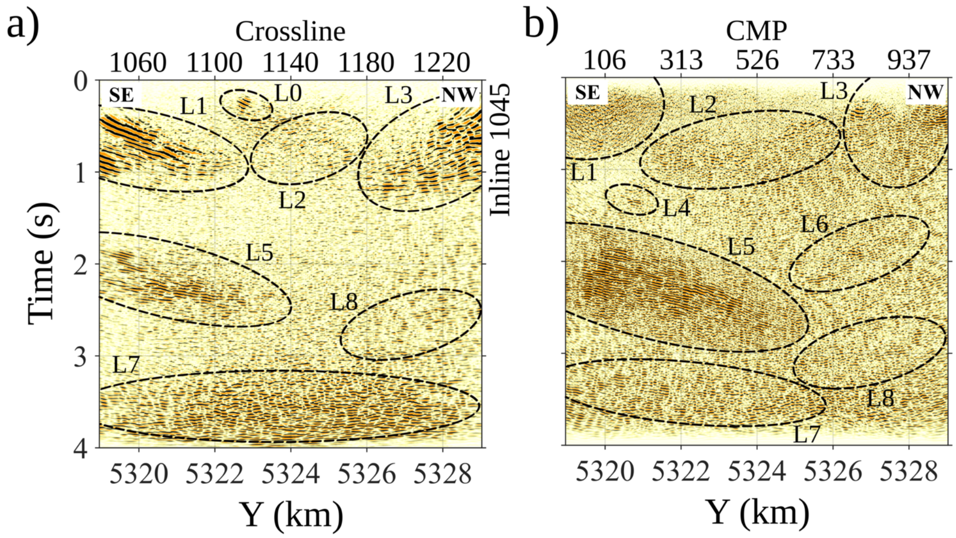

Figure 3.16: Comparing the swath 3D migration result along the inline 1045 (a) with the poststack Kirchhoff time migration of 2.5D MF stack section (b).

3.9 Conclusion

We have presented the application of four different seismic imaging algorithms on the Larder Lake crooked seismic reflection transect, which was acquired over a crystalline geological environment in the Superior Craton of Canada. Particularly, we examined the performance of the 2.5D multifocusing stacking method and compared its Kirchhoff time migrated image with the 2D phase-shift time migration of dip moveout corrected stack, 2D prestack Kirchhoff time migration, and the swath 3D poststack migration.

On a synthetic model, generated using the same real acquisition geometry used in the Larder Lake area, the 2.5D MF approach produces a true zero-offset wavefield by correcting the azimuthal-dependant normal and dip moveouts simultaneously. Additionally, the proposed method focused primary reflections at their correct poststack locations and estimated the inline and crossline dips from seismic data accurately, which can be used for structural interpretation.

On the field data, the 3D swath processing could not image steeply dipping reflections correctly, however, it delineated the extension of some of the subhorizontal reflections, particularly in the northern part of the Larder Lake structural basin (< 2 s). In comparison to the other results, the 2.5D MF method considerably improved the quality of the seismic section and yield a high-resolution section with a high S/N. The 2.5D MF method mapped the prominent steeply dipping reflection packages more coherently. In addition to the main feature at 2.5 s on the SE end, the 2.5D MF method focused new reflections at times less than 2 s with a high S/N, which were not constructed by the 2D DMO stack and 2D prestack migration workflows. Furthermore, the proposed method accurately extracted 3D structural information including inline and crossline dips. In the shallow zone less than 2 s, the inline dips were estimated to be to the south in the same trend directions as some clusters of short but strong flat-lying reflections, then these trends could be interpreted with greater confidence. This study clarified that the 2.5D multicasting method can be an effective alternative to the 2D conventional stacking (NMO+DMO+CDMO) and 2D prestack migration methods in processing crooked surveys.

3.10 Acknowledgements

This research was funded by the NSERC Canada First Research Excellence Fund (MERC-ME-2022-00). GeoThrust and Globe Claritas were used for 2D and 3D seismic data processing. We acknowledge GeoTomo for providing an academic license. The Seismic Unix open-source platform was used for an efficient implementation of the 2.5D MF imaging method. Visualization and interpretation in 3D were carried out with GOCAD. The SOFI3D open-source package was used to produce the synthetic data sets using the finite differences method. We thank Thomas Bohlen, Denise De Nil, Daniel Köhn, and Stefan Jetschny for developing the SOFI3D code. The authors acknowledge Absolute Imaging Inc. for the conventional and advanced processing of the seismic data and Bryona Fernandes for providing the geological map in the study area. The authors would like to acknowledge the comments provided by all editors, for their very insightful comments on the manuscript. This work was enabled in part by the facilities of the Shared Hierarchical Academic Research Computing Network (SHARCNET:www.sharcnet.ca) and Compute/Calcul Canada (www.computecanada.ca).

Appendix 3-A: Differential evolution

The differential evolution (DE) algorithm introduced by Storn and Price (1997), is a robust and reliable derivative-free global optimization method. The method is an evolutionary algorithm and optimizes a problem by improving a candidate solution iteratively. Differential evolution can solve multi-dimensional, non-linear, and non-differentiable continuous functions.

In the multifocusing wavefront analysis, the analytical form of the objective function is not determined as it depends on reflection amplitudes on the super common-midpoint gather. Therefore, the derivation of the objective function can not be computed to find the global maximum. Additionally, the cost function in the MF method is a multi-dimensional and non-linear function. Therefore, the DE method can be a smart choice to efficiently solve the MF searching problem for determining the MF unknown parameters.

The DE algorithm involves updating a population of candidate solutions iteratively using three steps: mutation, crossover, and selection (see Algorithm 1). First, an initial random population consists of NP vectors $\vec{m}_i$, $\forall i = 1, 2, .., N_P$, is generated with uniform distribution between the lower and upper boundaries (m_j^L, m_j^U) using the expression

$$m_{i,j,G} = m_j^L + rand_j.(m_j^U - m_j^L), \tag{3-A.1}$$

where $rand_j$ denotes a uniformly distributed value between $[0, 1]$, $G = 0$, and $m_{i,G}$ is a vector of MF unknown parameters with size of D. At each iteration, called a generation, a mutation operator generates new vectors by the combination of vectors randomly chosen from the current population by the following expresiom

$$v_{i,j,G+1} = m_{r_1,j,G} + F(m_{r_2,j,G} - m_{r_3,j,G}), \qquad r_1 \neq r_2 \neq r_3 \neq i \tag{3-A.2}$$

where $F \in [0, 2]$ is the scale factor of the mutation that controls the amplification of differential variation. The indexes $r_1, r_2, r_3 \in \{1, ..., N_P\}$ are chosen randomly and are different from index i. Next, for enhancing the diversity of the mutated parameter vectors, the crossover operator produces the trial vector by mixing the mutated vector and a predetermined target vector that can be obtained by

$$u_{i,j,G+1} = \begin{cases} v_{i,j,G+1}, & rand(j) \leq CR \quad or \quad j = randn(i), \\ m_{i,j,G}, & \text{otherwise}, \end{cases} \tag{3-A.3}$$

where $j = 1, 2, ..., D$; $CR \in [0, 1]$ is the crossover rate. $rand(j) \in [0, 1]$ is the j^{th} evaluation of a uniform random generator number and $randn(i) \in \{1, 2, ..., D\}$ is a randomly chosen index which ensures that $u_{i,G+1}$ gets at least one element from $v_{i,G+1}$; otherwise no new parent vector would be generated and the population would not update. Finally, in the selection step, the trial vector is accepted for the next generation which increase the value of the objective function; otherwise, the old value is retained. The selection operator is as follows

$$m_{i,G+1} = \begin{cases} u_{i,G+1}, & f(u_{i,G+1}) \geq f(m_{i,G}), \\ m_{i,G}, & \text{otherwise}. \end{cases} \tag{3-A.4}$$

Algorithm 1 Pseudo code for differential evolution (adapted after Storn and Price, 1997)

```
Determination of population size $N_P$, mutation scale factor $F$, and crossover rate $CR$;
Determination of the constraint range and the coherence function;
function DE(NP, CR, F, Range, Coherence Function)
    Set generation index;
    ($G \leftarrow 0$)
    $P_G \leftarrow$ random initialization of population for $N_P$ individuals in the defined range;
    ($P_G = \{m_{1,G}, m_{2,G}, ..., m_{N_P,G}\}$);
    $f_x \leftarrow$ fitness of each individual $m_{i,G}, \quad i = \{1, 2, ..., N_P\}$;
    while stopping criteria is not reached do
        for $i = 1$ until $N_P$ do
            choose 3 random different individuals $m_{r_1}, m_{r_2}, m_{r_3}$;
            for $j = 1$ until $D$ do
                $v_{i,j,G+1} \leftarrow m_{r_1,j,G} + F(m_{r_2,j,G} - m_{r_3,j,G})$;    ▷ Mutation
                if $r_i \in [0, 1] \leq CR$ then                                   ▷ Crossover
                    $u_{i,j,G+1} \leftarrow v_{i,j,G+1}$;
                else
                    $u_{i,j,G+1} \leftarrow m_{i,j,G}$;
                end if
            end for
            $f_u \leftarrow$ fitness of each individual $u_{i,G}, \quad i = \{1, 2, ..., N_P\}$;
            if $f(u_{i,G+1}) \geq f(m_{i,G})$ then                                ▷ Selection
                $m_{i,G+1} \leftarrow u_{i,G+1}$;
            else
                $m_{i,G+1} \leftarrow m_{i,G}$;
            end if
        end for
        Set generation index;
        ($G \leftarrow G + 1$)
    end while
end function
```

Chapter 4

3D generalized spherical multifocusing seismic imaging

Hossein Jodeiri Akbari Fam [1]*, Mostafa Naghizadeh [1], Öz Yilmaz [2], and Richard Smith [1]

[1] Mineral Exploration Research Centre, Harquail School of Earth Sciences, Goodman School of Mines, Laurentian University, Sudbury, Ontario, Canada.

[2] Anatolian Geophysical, Urla, Izmir, Turkey.

*Corresponding Author E-mail: hjodeiri@laurentian.ca

4.1 Abstract

We introduce a three-dimensional generalized spherical multifocusing (GSMF) algorithm to generate 3D stacked volume that is equivalent to a synthesized 3D zero-offset wavefield for crooked-line/3D seismic data with arbitrary recording geometry from areas with irregular topography, complex near-surface, and complex subsurface. The algorithm is based on a 3D extension of the spherical multifocusing method into the most general form. We develop a 3D operator for generalized spherical multifocusing with a closed-form implicit formulation that can be applied to seismic data with arbitrary spatial coordinates of sources and receivers. The extended method simultaneously corrects for elevation statics, non-hyperbolic moveout associated with reflections beneath complex overburden structures, and azimuth-dependent dip-moveout effects. The resulting GSMF stacked volume can then be time- or depth-migrated using a 3D zero-offset migration algorithm to obtain the 3D subsurface image. In addition, we parameterize the formulation dually generalized for both the optical domain and the effective medium. The optical domain and effective medium are auxiliary media with straight-ray geometry and constant velocity, which can approximate the actual subsurface model to account for heterogeneity either by shifting the reference time to project the problem into the optical image space or by adjusting the velocity of an effective overburden, respectively. The performance of the proposed method with the optical parameterization is tested using 3D synthetic data with both 3D and crooked-line surveys. The numerical tests have shown that the new approximation is significantly accurate for gently to highly curved interfaces beneath low to relatively high heterogeneous overburden with rugged topography, even at large offsets and at large midpoint separations. Additionally, the method is rigorously tested using a 3D real seismic data set acquired over a complex thrust-belt area with rugged terrain. Compared to the conventional 3D stacking, the new formulations yield high-resolution

and accurate seismic stacked volume from land seismic data collected with arbitrary 3D geometries.

4.2 Introduction

Three-dimensional (3D) seismic surveys have proven to be highly effective for imaging the subsurface since their introduction in the mid-1970s (Nestvold, 1996). In optimal circumstances, the 3D seismic method can provide a complete and accurate volumetric image of the subsurface (Eaton et al., 1997; Yilmaz, 2001; Biondi, 2006). Also, the greater information provided by 3D seismic reduces uncertainty in creating geological models (Yilmaz, 2001). Three-dimensional seismology has drastically improved our ability to detect and recover hydrocarbons. Meanwhile, this technology opened new horizons in other exploration disciplines such as minerals prospecting (Davies et al., 2004). One of the greatest advantages of a 3D seismic survey is a high-spatial resolution with accurate positioning of features in the image volumes (Yilmaz, 2001). These surveys can be used to estimate the 3D velocity field and can significantly improve the imaging quality and spatial frequency of data (Davies et al., 2004). Focusing seismic energy at the correct location and reducing spatial aliasing are other advantages of 3D surveys. In 3D seismic studies, the wavefield propagation direction can be determined accurately and out-of-plane reflections can be focused at the correct locations (Biondi, 2006). In addition, the 3D nature of diffractions could be correctly collapsed by 3D imaging methods (Biondi, 2006). Therefore, areas with complex 3D structures, such as geological settings with compressional tectonic fold systems and fault networks, can be potentially mapped with more detail (Freeman et al., 1990).

Three-dimensional prestack migration is needed to correctly image geological structures with 3D features. The complex subsurface geologic settings with significant lateral velocity heterogeneity are better resolved with prestack depth migration methods, compared with prestack/poststack time migration (Yilmaz, 2001). This is because depth imaging locates reflectors more accurately and resolves complicated raypaths to map steeply dipping layers and near-vertical faults. However, the high computational cost and the lack of an accurate velocity-depth model hamper utilizing this method. Irregular distribution of sources and receivers has a further negative effect on 3D prestack migration methods and therefore seismic data reconstruction methods are used to regularize the locations of data before its application (Biondi, 2006). Building an accurate velocity-depth model for migrating seismic data in the depth domain is a difficult process, especially in complex geology and noisy environments and it needs to be tied to geology (Vestrum et al., 2011). An alternative approach to the depth-domain imaging method is using the time-domain stacking and poststack migration methods. Overall, depth-imaging methods do not supersede time-imaging methods (Vestrum et al., 2011) because they require an accurate velocity-depth model and time enhanced gather for its input. In fact, these are two fundamentally different approaches and their characteristics make them complementary to each other. The processing methods in the time-domain can potentially produce more coherent and clear structural stacked sections and images, detailed stacking and root-mean-square (RMS) velocity fields, and enhanced seismic gathers. They also can provide interpreted horizons for building an accurate velocity model as a function of depth. However, they require accurate and generalized moveout operators. Hence, improving the quality of time-domain stacked sections and developing accurate and generalized moveout operators is the focus of this research.

Dense coverage will not necessarily result in accurate subsurface imaging unless static corrections are applied appropriately and velocity analysis is performed correctly. Therefore, we need an operator that can precisely approximate reflection and diffraction traveltimes within a common-cell gather by considering variable offset, azimuth, topography, and near-surface changes. The two main categories of high-resolution stacking algorithms are the common reflection surface (CRS) methods (Müller, 1999; Jäger et al., 2001) and multifocusing (MF) methods (Gelchinsky et al., 1999a,b). The CRS theory offers a relatively simple framework (algebra), which allows the method to be extended to three dimensions easily (Fomel and Kazinnik, 2009; Landa et al., 2009). The extension of the CRS method to three dimensions is straightforward (Fomel and Kazinnik, 2009) and has been published (Bergler et al., 2002; Müller, 2003). However, extending the multifocusing method to three dimensions is more difficult because the mathematics involved are more complex (Fomel and Kazinnik, 2009; Schwarz and Gajewski, 2017).

Landa et al. (2009) proposed the spherical MF method in three dimensions by adding one more parameter to the two-dimensional spherical MF formula. The spherical multifocusing was derived for a circular reflector with the assumption of straight rays (Landa et al., 2009). The 3D SMF method did not consider the variation of source and receiver elevations, and the recording surface is assumed to be flat. In all respects, the spherical MF method is robust, and its traveltime expression does not have any singularities as there are in the planar MF formulation. Also, the central ray can be either a normal ray or a paraxial ray (rays in the vicinity of a central ray) with finite offset. Therefore, this method can be directly applied to zero- and finite-offset data without any modification. Zero- and common-offset stack sections can be produced without additional cost. This method requires solving a quartic equation for each iteration in estimating wavefield parameters, which increases the computational cost. Later, Jodeiri Akbari Fam et al. (2021a) developed the 2.5D MF method to generate 2D zero-offset wavefields along crooked seismic surveys or 3D zero-offset wavefields volume. This method can be considered as a 3D extension for the planar multifocusing approach, which can explicitly correct 3D normal and azimuth-dependent dip moveouts simultaneously and accounts for midpoint scattering. However, it is accurate for quasi-hyperbolic reflections and its capability is limited in resolving non-hyperbolic diffractions and reflections. Hence, a non-hyperbolic higher-order moveout operator is required that could potentially improve stacked volume constructed from seismic data acquired over an area with rugged topography and strong heterogeneous overburden.

The formulation of 3D spherical multifocusing that can account for irregular acquisition surfaces has not yet been described in the geophysical literature. In this research, we expand a three-dimensional generalized spherical multifocusing seismic stacking method for a crooked-line/3D seismic data set acquired over an area with irregular topography. We use 3D GSMF as an abbreviation of the proposed method for convenience. In the following sections, we first review the relevant background. Then, we derive the traveltime formula for the 3D GSMF algorithm. Next, the performance of the proposed method is examined on synthetic and real data sets. Finally, we evaluate the efficiency and accuracy of the method and discuss the results.

4.3 Processing and imaging challenges of 3D seismic surveys

The quality of 3D seismic imaging algorithms can be deteriorated by 1) inherent natural geological factors such as near-surface heterogeneity, the ruggedness of topography, and complexity of subsurface geology, and 2) factors associated with survey geometry and acquisition design such as the midpoint distributions, fold coverage, and source-receiver azimuthal variations. Acquisition footprint refers to the distortion of the amplitude and phase of reflections encountered during processing resulting from the acquisition geometry and adversely impacts the results after steps such as 3D DMO correction (Yilmaz, 2001). Therefore, the applicability of each processing step can be directly tied to the survey acquisition parameters. A proper understanding and addressing of these issues are crucial for building an accurate and efficient seismic processing flow. Below, we discuss in detail a few of the potential seismic survey pitfalls that can adversely affect the imaging methods.

4.3.1 Irregular data coverage

The image quality might be degraded when spatial sampling is not acquired uniformly. Several potential pitfalls arising from the irregular 3D seismic acquisition have been identified (Biondi, 2006; Vestrum et al., 2011), which can be addressed by the novel generalized multifocuisng method proposed in this paper. For instance, irregular spatial sampling can distort seismic amplitudes and lead to coherent artifacts in the image (Biondi, 2006). Full 3D seismic data coverage is required to correctly collapse out-of-plane energies, accurately map the details of the subsurface features, and detect three-dimensional structures (Biondi, 2006; Vestrum et al., 2011). In order to fully sample 3D seismic waves, wide azimuth data with an even contribution of both near and far offsets are required to accurately image 3D subsurface structures (Cheraghi et al., 2012). However, acquiring 3D land seismic data with full coverage might be expensive and a low grid density in at least one dimension is often chosen in a 3D design, particularly in rugged topography. Besides, environmental and logistical restrictions prevent collecting high-density data, resulting in an irregular survey with inadequate coverage (Vestrum et al., 2011). Coarse and irregular spatial sampling results in an uneven distribution of source-receiver offsets and azimuths, which adversely affects the S/N of the recorded seismic data and might reduce the quality of the resulting image. For instance, velocity analysis and multiple-attenuation processing might fail if the data do not include far offsets (Yilmaz, 2001). Also, uneven fold coverage over an area leads to variations in the stacked amplitudes and increases the uncertainty of velocity analysis (Yilmaz, 2001). Overall, uneven fold, azimuth, and offset coverages violate the 3D wave sampling theorem (Vermeer, 1998). One can use larger cells to collect midpoints with broader azimuth and offset ranges. However, in areas with complex subsurface geology, this strategy would result in non-hyperbolic reflections, particularly for far-offset data. The conventional 3D processing flow (NMO+DMO) cannot accurately correct the non-hyperbolic moveout.

An irregular survey geometry also leads to significant midpoint scattering. In this case, the reflection traveltimes in a common-cell gather associated with a dipping interface with both inline and crossline dip components will deviate from a single hyperbolic moveout curve (Yilmaz, 2001). On the other hand, in a regular swath survey, the vast range of the source-receiver azimuths might lead to significant traveltime deviations from an ideal hyperbolic moveout trajectory even without midpoint scattering (Yilmaz, 2001). The effect of the broad azimuth range can be similar or greater than midpoint scattering impacts. The conventional stacking procedure using an operator with a hyperbolic behavior (NMO+DMO+Stack) only partially corrects these effects and causes amplitude smearing. Hence, we need a traveltime formula that is able to accurately describe the non-hyperbolic behavior and take into account the midpoint scattering and azimuth variation.

4.3.2 Elevation statics correction

Complex near-surface geology with rapid vertical variation and high lateral heterogeneity beneath rugged topography degrade the quality of collected data (Liner, 2016). Rugged terrain with significant variation in elevation of the topography causes considerable time shifts among traces (Chang et al., 2019b). Statics corrections play an important role in improving the quality of derived images. Elevation statics corrections is a standard processing step that is often applied to seismic data collected over irregular topography to correct the difference between the source and receiver elevations and transfer them to a flat/floating datum. Conventional source and receiver elevation statics corrections are carried out by performing traveltime tomography for near-surface velocity-depth modeling (Zhang and Toksöz, 1998). The tomography is a robust method that can address the statics problem – ranging from medium- to long-wavelengths – when near-surface complexity is present. This method requires picking first-break arrival times, which is a very time-consuming and expensive task. The performance of this algorithm depends on the accuracy of first-break picking and is not capable of resolving velocity reversals (Yilmaz et al., 2022).

For statics corrections, it is assumed that the raypaths are close to vertical incidence within the near-surface. This assumption is not always valid in areas with complicated near-surface structures, particularly for high-velocity consolidated heterogeneous medium. This might result in significant errors and could lead to an inaccurate elevation static correction, particularly for far-offset seismic data (Gurevich and Landa, 2002). In such a scenario, the time shifts resulting from the source-receiver elevation would be time variant for each trace (not static) and will depend on the emergence angle of reflection raypaths (Gurevich and Landa, 2002). Inaccurate statics also cause cumulative errors and an unstable velocity inversion process.

Land 3D seismic data acquisition within an area without restrictions, usually provide wide-azimuth data volume with low to moderate fold. Low fold or an inadequate near-surface coverage reduces the resolution of shallow sections leading to misties to the surface geology. In such cases, the refraction-static method cannot resolve the near-surface model due to low fold coverage. Improper refraction static correction leaves weathering effects poorly corrected, which results in cumulative errors, misfocusing, and mispositioning of reflections. Also, this prevents the correct application of the subsequent processes. For instance, subsequent velocity analysis introduces errors in reflection static corrections, which in turn could lead to low-resolution imaging results (Vestrum et al., 2011). Several mitigations can be deployed to increase the resolution of subsurface imaging. Tying 2D seismic lines across a 3D survey can be used as complementary data to provide high-resolution 2D coverage, particularly for the shallower depths (Vestrum et al., 2011). However, 2D seismic lines are confined to limited vertical planes and are not always available. Therefore, correcting the near-surface weathering effects requires a method that relies on reflection statics (Vestrum et al., 2011).

Dai and Cheadle (1995) extended the standard NMO method to correct the effect of source-receiver elevations. However, due to the unavailability of the emergence angle information in the conventional NMO process, this procedure requires an extra step to estimate the emergence angle. Several alternative advanced methods have been proposed, such as prestack depth migration of non-planar data (e.g. Wiggins, 1984; Al-Saleh et al., 2009) and the wave-equation datuming approach (e.g. Berryhill, 1984; Liu et al., 2011). However, those methods are computationally expensive and require a detailed velocity model in the depth domain. Acoustic and elastic full-wave inversions (FWI) (Liu and Zhang, 2014; Warner and Guasch, 2016; Liu and Zhang, 2017) are other alternatives for near-surface modeling, which can model lateral velocity variations with wavelengths shorter than those that can be resolved by traveltime tomography (Yilmaz et al., 2022). The FWI methods require extensive computation and are highly dependent on signal amplitudes and inversion parameters (Yilmaz, 2021; Yilmaz et al., 2022).

The determination of the emergence angle is an integral part of the multifocusing approach. Therefore, developing the spherical multifocusing to account for non-vertical raypaths for correcting source-receiver elevation effects in 3D cases is straightforward and has no additional cost (Gurevich and Landa, 2002; Landa et al., 2009). This method implicitly relies on reflection statics, and does not require first brack picking and a detailed near-surface velocity-depth model. Nevertheless, very short-wavelength near-surface velocity variations, which are within the range of residual statics, can not be modeled by any of the above methods. Applying residual statics corrections to land seismic data is an essential step and cannot be omitted (Yilmaz, 2021).

4.3.3 3D normal-moveout (NMO) and dip-moveout (DMO) corrections

The conventional 3D stacking method includes 3D normal- and dip-moveout corrections followed by the stacking process (NMO+DMO+Stacking), which transforms prestack seismic data into an equivalent zero-offset section (Biondi, 2006). In a 3D seismic survey over a dipping layer with both inline and crossline dip components, the midpoint scattering plus source-receiver azimuthal variation significantly deviates reflection traveltime from an ideal hyperboloid (a traveltime surface generated using the 3D NMO equation with a single velocity). Therefore, the conventional stacking using the 3D NMO operator could not approximate the moveout and will result in misalignments, which will attenuate high-frequency content and would result in a low-resolution stack section. In this case, the application of 3D DMO method for correcting the shot-receiver azimuth moveout (AMO) before stacking is necessary.

The 3D DMO corrects for the dip effect on stacking velocities and implicitly considers the effect of source-receiver azimuth on moveout velocities (Yilmaz, 2001). For 2D seismic surveys, all source-receiver pairs are along a 2D traverse and have the same azimuth. Therefore, all traces in a common-depth-point (CDP) gather – recorded for a dipping layer – can be dip moveout corrected using one stacking velocity. In other words, we just need to estimate the apparent dip of the layer along the profile for all traces. However, in a 3D case, each trace in a common-cell gather has a source-receiver azimuth. The stacking velocity of reflections from a dipping layer along each azimuth depends on the apparent dip along that azimuth. So, each trace in a common-cell gather needs to be corrected using different stacking velocities. In fact, the 3D DMO process corrects apparent dip effects (which contains effects of the true dip and the source-receiver azimuth) on moveout velocity along each source-receiver azimuth. Thus, the stacking velocity field estimated from the 3D DMO-corrected gathers is azimuth and dip independent. Accurate implementation of 3D DMO correction removes the reflection point dispersal and inline smearing caused by the azimuth variation (Yilmaz, 2001). In conventional processing of crooked-line seismic data, rather than applying 3D NMO and 3D DMO corrections, the 2D NMO plus 2D DMO corrections are usually followed by crossdip moveout (CDMO) analysis. The 2D DMO and CDMO methods corrects for the effect of dipping interfaces along the inline and the croosline directions, respectively. In this case, applying squintingly two dip moveout corrections along two distinct azimuths implicitly accounts for source-receiver azimuths.

Levin (1971) introduced the azimuth-dependent velocity analysis using a three-parameter traveltime equation for a dipping interface. In this method, traces are required to be subgrouped into three distinct azimuths. The velocity analysis can be performed along those azimuths independently. However, this might face challenges and lead to an unreliable stacking velocity field, since the land 3D data are often low fold, partitioning data into three subgroups with distinct azimuths limits the number of traces and offset range contributing to velocity analysis, which yields inaccurate estimates of stacking velocity field (Yilmaz, 2001).

In the conventional seismic processing methods, the 3D DMO correction increases the resolution of the stacked volume, however, this operator might impose amplitude and phase artifacts (Vermeer, 2002). Sequentially applying moveout corrections in the conventional processing flow generates a cumulative error (Biondi, 2006). In addition, the signal stretch effect (Yilmaz, 2001) resulting from the conventional moveout corrections has a considerable impact on the resolution of the stack section (Vermeer, 2002). The performance of 3D DMO is dramatically affected by survey geometry, for instance, applying 3D DMO for wide towed marine streamer data causes striped appearance as it does not address the midpoint scattering problem (Galbraith, 2001; Yilmaz, 2001). Hence, developing a non-hyperbolic higher-order 3D multifocusing approach could potentially improve zero-offset wavefield volume by simultaneously correcting for, in addition to elevation statics, normal moveout, azimuth-dependent dip moveout, and non-hyperbolic moveout associated with reflections beneath complex overburden structures.

4.4 Multifocusing methods

Over the past two decades, multifocusing and common reflection surface methods have been proposed to produce a high-resolution zero-offset simulation from multi-coverage seismic data. Recently, the multifocusing method has received wide attention due to its high accuracy in modeling diffractions and reflections from highly curved reflectors (Schwarz et al., 2014b). The multifocusing method is a sophisticated multi-parameter non-CMP-based stacking algorithm, which is derived based on the kinematics of wave propagation (Landa et al., 2009). The multifocusing stacking technology can significantly enhance the quality of seismic sections in complex geologic settings with a poor signal-to-noise ratio. Its formulation simulates reflection traveltime surface over the offset-midpoint domain and is categorized as a macro-model independent stacking approach (Gurevich and Landa, 2002; Belfer et al., 2008a; Schwarz et al., 2014b). In contrast to prestack depth migration methods, the multifocusing algorithm does not require any knowledge about the subsurface velocity-depth model, except for near-surface velocities (Gelchinsky et al., 1999a,b; Landa et al., 2009).

Several extensions of multifocusing method have been developed based on various scenarios and geometries, including planar and spherical. The planar multifocusing refers to the multifocusing moveouts depending on the focusing ratio constructed for the case of a planar dipping interface with constant-velocity overburden (Landa et al., 2009). The planar multifocusing methods, including 2D MF (Gelchinsky et al., 1999a), 2D IS-MF (Gurevich and Landa, 2002), and 2.5D MF (Jodeiri Akbari Fam et al., 2021a), were derived based on the spherical approximation (Gelchinsky and Keydar, 1999) of wavefronts and were constructed around a zero-offset ray and, in principle, are valid for short offsets. A quasi-hyperbolic approximation (Berkovitch et al., 2011) to actual traveltime curves/surfaces is one of the main limitations of the zero-offset 2D/2.5D MF methods, which reduces their accuracy (Landa et al., 2009; Jodeiri Akbari Fam et al., 2021a). They express reflection traveltime based on the kinematics of the central ray/plane and the moveout for a paraxial trace in the vicinity of the central point at source and receiver positions. In complex subsurface geology, strong lateral velocity variations and/or the presence of anisotropy can violate the spherical approximation of wavefronts and might cause the traveltimes of seismic events to become nonhyperbolic, and the zero-offset 2D MF operator approximation starts to be inaccurate, especially for large offsets (Berkovitch et al., 2011). Also, this might cause smearing of sharp discontinuities in the stack section (Gurevich and Landa, 2002).

Landa et al. (2009) proposed a non-hyperbolic higher-order traveltime for reflections from a circular/spherical reflector, called the spherical multifocusing method (2D/3D SMF), that significantly improved the accuracy of the MF method over curved events that were beneath layers with variable seismic velocity, which we term heterogeneous overburden. The spherical multifocusing theory was developed by Landa et al. (2009) to transfer the problem of the reflection traveltime for a spherical reflector into the problem of finding the tangency of an ellipse and a circle. Chang et al. (2019b) modified the SMF method to apply to 2D data acquired from irregular topography by considering non-zero elevations of sources and receivers. The new operator (IS-SMF) can correct moveout of curved reflection directly without prior elevation static corrections and is more robust over a wide range of source and receiver elevations. Also, it performs better on strongly curved interfaces compared to the conventional method, resulting in an increased resolution in the stack and time-migration sections.

4.4.1 Limitations of the 3D multifocusing methods

Elhaj et al. (2014) proposed an application of the 3D MF method for imaging and regularization of an irregular 3D seismic data set. However, they have not further expanded on the corresponding formulations of the 3D MF method. Jodeiri Akbari Fam et al. (2021a) developed the 2.5D MF method for processing crooked seismic lines which can be considered as a 3D extension for the planar multifocusing approach. This method explicitly corrects 3D normal, dip, and azimuth moveouts simultaneously and accounts for midpoint scattering. The 2.5D approach can approximate the 3D model of the wavefront, however, it assumes locally spherical wavefronts around the zero-offset central ray. Hence, developing a non-hyperbolic higher-order 3D MF approach could potentially improve stacked volume for highly curved reflectors beneath strong heterogeneous overburden.

In the 3D SMF method, the recording surface was assumed to be flat and its application is limited to seismic data acquired with a flat surface assumption. Hence, elevation statics corrections are required to compensate for the near-surface effects and to reference prestack data into a flat datum. Raypaths are typically assumed to be vertical in the conventional elevation statics correction methods. This assumption is mostly invalid and might lead to inaccurate static shifts for seismic data acquired over a severe irregular topography (Gurevich and Landa, 2002).

These issues can be addressed by extending the SMF method to a 3D generalized spherical multifocusing (3D GSMF) method. In order to develop this 3D GSMF method, we explicitly account for 3D spatial coordinates of the source and receiver including horizontal (x, y) coordinates and elevation. Table 4.1 summarises the advantages and shortcomings of the MF extensions. This table shows how the previous developments are inadequate to resolve important 3D processing challenges and thus it is necessary to develop a new methodology.

Table 4.1: The advantages and shortcomings of different MF-type methods.

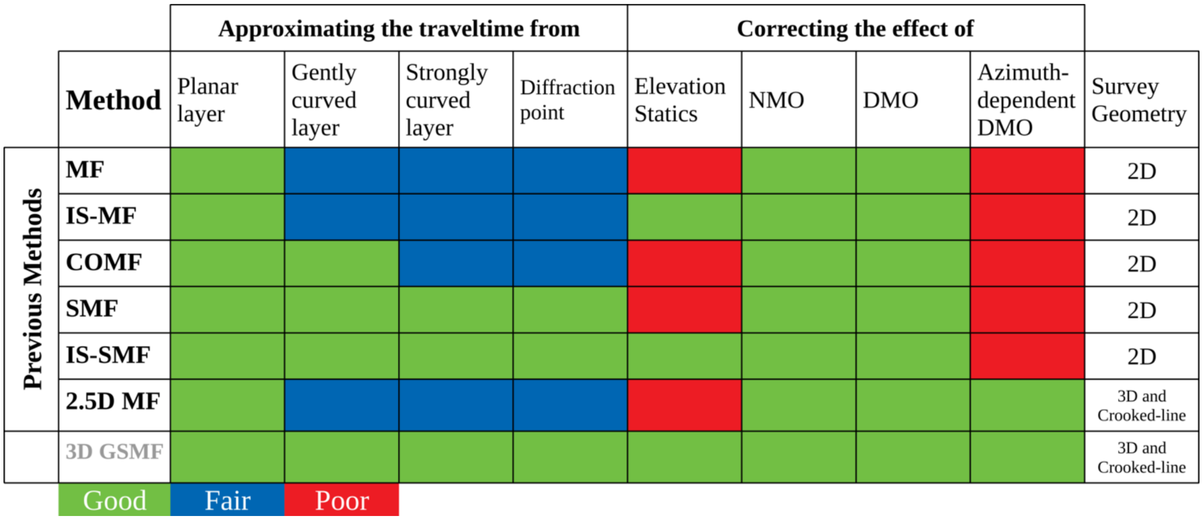

		Approximating the traveltime from				**Correcting the effect of**				
	Method	Planar layer	Gently curved layer	Strongly curved layer	Diffraction point	Elevation Statics	NMO	DMO	Azimuth-dependent DMO	Survey Geometry
Previous Methods	**MF**	🟩	🟦	🟦	🟦	🟥	🟩	🟩	🟥	2D
	IS-MF	🟩	🟦	🟦	🟦	🟩	🟩	🟩	🟥	2D
	COMF	🟩	🟩	🟦	🟦	🟥	🟩	🟩	🟥	2D
	SMF	🟩	🟩	🟩	🟩	🟥	🟩	🟩	🟥	2D
	IS-SMF	🟩	🟩	🟩	🟩	🟩	🟩	🟩	🟥	2D
	2.5D MF	🟩	🟦	🟦	🟦	🟥	🟩	🟩	🟩	3D and Crooked-line
	3D GSMF	🟩	🟩	🟩	🟩	🟩	🟩	🟩	🟩	3D and Crooked-line

🟩 Good 🟦 Fair 🟥 Poor

4.5 3D generalized spherical multifocusing method

In this section, we extend the 2D spherical multifocusing approach to deal with 3D seismic data by generalizing the multifocusing moveout correction with a new strategy for a spherical reflector below a crooked or 3D seismic survey and also account for irregular topography. In order to consider nonzero elevations and arbitrary horizontal spatial coordinates of sources and receivers, we employed transformation and projection operators to modify the SMF operator. This strategy allows us to develop the generalized version of the SMF to the most arbitrary 3D survey geometry.

The concept of deriving a traveltime formula by assuming a particular reflector geometry (Fomel and Kazinnik, 2009) was first introduced by Landa et al. (2009). They proposed a new multifocusing formulation for reflection traveltime assuming that the particular reflector geometry was spherical. This assumption, combined with assuming straight raypaths helps to derive a more accurate multi-parameter traveltime moveout expression without increasing the number of unknown wavefield parameters (Schwarz et al., 2014a). Here, we assumed a spherical reflector specified by one constant finite curvature parameter, applicable in all directions. Assuming such a reflector reduces the approximation parameter set from 8 to 4 in the 3D case (Landa et al., 2009). The geometry of most curved reflectors can be reasonably well approximated by a sphere. This assumption not only lets us exactly calculate the traveltime of reflections from strongly curved spherical reflectors and diffractions from scattering objects with very high curvatures but also helps to accurately estimate the traveltime of reflections from gently to highly curved non-spherical layers that can be approximately described with one curvature value (Landa et al., 2009). Various curvatures over a curved reflector, like folded structures with a combination of several anticlines and synclines, can be simulated by allowing the fitted curvature value to vary spatially. In fact, the new method decomposes and approximates a prestack seismic data cube from a complicated general curved interface into responses from a set of spheres at each common cell and time location, each with a different curvature value.

In order to achieve a uniform fold of coverage and even offset and azimuth distribution, one can adjust the size of each cell separately, which is called flexible binning (Yilmaz, 2001). The proposed method makes it possible to derive a reliable stacked section from flexible binned data. However, the flexible binning with larger dimensions causes another problem. Generally, the allocated midpoints into a cell may not coincide with the center of the cell. The distance between the midpoints and the center of the cell introduces an error in the moveout correction and leads to misfocusing of reflections and distortion of the stacked amplitudes. This effect has not been considered in the conventional moveout correction. One solution can be assigning the stacked trace to the center of the relevant midpoints rather than to the cell center. But this results in an unequal spacing of the stacked traces, especially in the crossline direction (Yilmaz, 2001). Taking into account the distance between the midpoints and the cell center when deriving the stacking operator is the most appropriate solution if the midpoints depart considerably from the cell center. Accounting for changes in the moveout with the azimuth is another issue arising from the processing of 3D seismic surveys. The azimuth-dependent moveout within a common-cell gather is critical when processing 3D land seismic data (Yilmaz, 2001), so will be incorporated here.

In order to account for the effect of heterogeneity on the traveltime moveout, an auxiliary medium with straight-ray geometry and constant velocity is considered (see Perroud et al., 1999). The auxiliary medium can synthesize (approximate) the actual subsurface model to account for heterogeneity either by shifting the reference time to project the problem into the optical domain or by adjusting the velocity of an effective overburden

(De Bazelaire, 1988; Höcht et al., 1999). Multi-parameter stacking methods can be categorized into two groups based on how they account for heterogeneity. One group assumes an effective auxiliary medium, like CRS and NMO, which approximates the inhomogeneous subsurface model with a medium of a constant effective velocity. The effective velocity is the adapted (shifted) velocity assigned to the effective auxiliary medium and replaced the actual velocity model. The other group, like MF and shifted NMO, uses concepts of geometrical optics, which accounts for heterogeneity by projecting the reflection traveltime problem into the optical domain (see Höcht et al., 1999). Based on assumptions of geometrical optics, the traveltime resulting from the bent reflection raypath traveling through a heterogeneous overburden can be approximated with a straight-ray geometry in a constant near-surface velocity, but with a different reflection point. In this approach, the replaced medium is achieved by changing the center of coordinates and described with shifted time and constant near-surface velocity. In other words, in the optical and effective-medium mechanisms, the heterogeneity effects are accounted for by shifting reference time and velocity, respectively (see Schwarz and Gajewski, 2017).

The accuracy of the effective medium operators is less affected by heterogeneity compared to the optical approaches. Whereas optical operators are stretch-free and are most suitable to describe reflection and diffraction traveltimes, particularly from highly curved reflectors (Schwarz et al., 2014a). The effective-medium-based stacking operators become inaccurate with increased curvature (Landa et al., 2009) and cause signal stretching after moveout correction because they vary as a function of the zero-offset time (Schwarz et al., 2015). But, this dependency allows determining the true reference traveltime (Schwarz and Gajewski, 2017). Landa et al. (2009) found that the spherical multifocusing might lose effectiveness when the overburden consists of a strong heterogeneity (Schwarz et al., 2014b). We follow Schwarz and Gajewski (2017) and transform the proposed operator from the optical (time-shifted domain) to the effective medium (velocity-shifted domain) or vice versa. Depending on the inherent character of the subsurface, one can employ one of those parameterizations. Shifting the reference time should accurately characterize diffractions and highly curved reflectors while shifting the constant velocity will accurately account for background velocity heterogeneities.

First, the original signal processing steps to attenuate the coherent/random noise and partially recover the amplitudes are applied. To have a correct representation of the zero-offset wavefield volume, recovering the diffraction response is important, which is likely to suffer from extensive filtering. Next, the midpoints are collected into 3D super common-cell gathers, which are gathers that comprise traces belonging to the nearby common-cell gathers within the limits of a certain span in the vicinity of the central (imaging) point. The optimal size of the 3D super cell can be estimated using Fresnel zone analysis (Hubral et al., 1993; Gurevich and Landa, 2002; Berkovitch et al., 2009). The next step is velocity or wavefield-attribute analysis using a 3D stacking operator. The optimal 3D super cell gathering can mostly solve the data coverage problem and can provide gathers with even fold, offset, and azimuth distributions. However, the super gathers might be comprised of reflections with broad midpoint scatter and reflection point dispersal. Also, the reflections might contain non-hyperbolic moveout, particularly far-offsets data. A robust operator that can account for normal, dip, and azimuth moveout effects simultaneously and account for nonhyperbolicity so as to fully resolve the moveout of near- to far-offsets data and estimate dip- and azimuth-independent stacking velocity field with high accuracy. In order to solve the problem associated with assuming vertical raypaths that is implicit in the conventional elevation statics corrections, we incorporated a reflection-based elevation statics corrections in the moveout operator by considering the nonzero elevations of source, receiver, and imaging point. Overall, we aim to derive such an operator that can address all the above-mentioned issues.

Figure 4.1a shows the ray geometry for a 3D survey setup over a 3D curved reflector with a general undulating structure. Here, we consider a locally spherical interface embedded in a constant velocity ($\hat{v}$) medium with irregular topography. A reflection ray (dashed blue ray) is generated by an arbitrarily located source (red asterisk), reflecting off the reflector interface, arriving back to the recording surface, and is captured by the receiver (blue triangle). In this figure, it is assumed that the inline, crossline, and depth directions correspond to the $x-$, $y-$, and $z-$axes, respectively. The imaging point $[X_0, Y_0, Z_0]$ is chosen arbitrarily (magenta square) on the irregular measurement surface, where the final stack trace will be assigned there. Note that the imaging point can be arbitrary and it is not essential to be aligned with the source and receiver. A sphere is fitted to the tangent to the reflector at the normal incident point (NIP, a point that the zero-offset normal ray emitting from the imaging point hits the reflector) to approximate the subsurface structure locally. The curvature and origin of the sphere are adjusted such that the sphere surface can produce the same reflection traveltime response as the measured trace (just one or all traces in the super gather) at that location.

The reflection ray can be simulated with a rotated spheroid (ellipsoid with two axes of equal length), where the source and receiver are the focal points of the spheroid. Hence, the problem of the reflection traveltime for spherical reflectors is turned into the problem of finding the tangency of the ellipsoid and the sphere. There are two methods that we can solve this problem, which allow generalizing application to three-dimensional subsurface geometries with rugged topography. One is directly deriving a closed-form solution for finding the tangency point of a rotated spheroid with a sphere. Another method is converting the 3D case into a 2D problem, then finding the tangency point of an ellipse and a circle using the derived solutions for Alhazens problem, finally converting back the solutions into the 3D space. The first approach leads to a very complicated and computationally expensive formula. The second approach is a straightforward strategy, which enables us to expand the spherical multifocusing method into the most general form. This strategy consists of two transformations and a projection of the coordinate system to convert the 3D to a 2D problem. The 3D GSMF method can be applied step by step as follows.

First, the origin of the global frame coordinate system (O) (Figure 4.1a) is transformed to the imaging point (Figure 4.1b). All coordinates in the new system (x, y, z) are determined with X, Y, and Z and the corresponding variable subscript. S, G, R, and NIP indicate the source, receiver, reflection point, and normal incident point, respectively.

$$\begin{array}{lll}
X_S = X_{Source} - X_0, & Y_S = Y_{Source} - Y_0, & Z_S = Z_{Source} - Z_0, \\
X_G = X_{Receiver} - X_0, & Y_G = Y_{Receiver} - Y_0, & Z_G = Z_{Receiver} - Z_0, \\
X_M = \dfrac{X_G + X_S}{2}, & Y_M = \dfrac{Y_G + Y_S}{2}, & Z_M = \dfrac{Z_G + Z_S}{2}, \\
H_X = \dfrac{X_G - X_S}{2}, & H_Y = \dfrac{Y_G - Y_S}{2}, & H_Z = \dfrac{Z_G - Z_S}{2}, \\
H = \sqrt{H_X^2 + H_Y^2 + H_Z^2}, & &
\end{array}$$

where M and H represent the midpoint and half-offset between the source and receiver pair.

Then, the center of the sphere (C) is retrieved from the spherical coordinates and expressed using wavefield attributes. In this case, the moveout operator depends on four wavefield attributes including the emergence angle $\hat{\hat{\beta}}$, the azimuthal angle $\hat{\hat{\phi}}$, radii of curvature of the normal $\hat{\hat{R}}_N$, and normal-incidence-point $\hat{\hat{R}}_{NIP}$ waves. The NIP wave represents a wave that emerges from a point source at a reflector. The normal wave (N) is a parallel wave emitted by different points at the reflector (as in the exploding reflector concept). The central ray (the green ray in Figure 4.1b) makes the angle of $\hat{\hat{\beta}}$ with respect to the vertical axis along the azimuthal angle of $\hat{\hat{\phi}}$. $\hat{\hat{\phi}}$ is the azimuthal angle of the horizontal projection of the central ray measured from the inline (x-axis). The four wavefield parameters involved in the 3D GSMF are estimated at the surface and provide distinct physical properties of the reflector with clear interpretation – the spatial position and the local curvature of the reflector. The emergence angle determines the reflector dip. The radius of curvature of the NIP wave is the propagation distance from the point source to the acquisition surface and describes the depth of the reflector. The radius of curvature of the N wave reflects the curvature of the reflector (Landa et al., 2009). $\hat{\hat{\square}}$ symbol is used to indicate the parameters that are required to be substituted according to chosen auxiliary medium. Therefore, the substitutions in the time-shift and velocity-shift mechanisms are

$$[\hat{\hat{v}}, \hat{\hat{t}}_0, \hat{\hat{\beta}}, \hat{\hat{\phi}}, \hat{\hat{R}}_{NIP}, \hat{\hat{R}}_N] = [v_0, t_{shift}, \beta, \phi, R_{NIP}, R_N] \; and$$
$$[\hat{\hat{v}}, \hat{\hat{t}}_0, \hat{\hat{\beta}}, \hat{\hat{\phi}}, \hat{\hat{R}}_{NIP}, \hat{\hat{R}}_N] = [v_{shift}, t_0, \beta^{eff}, \phi^{eff}, R^{eff}_{NIP}, R^{eff}_N],$$

respectively. The variable $\rho = R_{NIP}/R_N$ is a certain combination of the wavefield parameters that remain unchanged regardless of which auxiliary medium is employed. This allows us to replace R_N with its alternative R_{NIP}/ρ to reduce the number of parameters that are required to estimate when we exchange between the auxiliary medium mechanisms. In the optical domain, the mechanism that accounts for heterogeneity shifts the actual traveltime of the NIP wave (actual reference time t_0). In this mechanism, the geometry of the actual NIP wavefront recorded at the surface can be described accurately and the surface-based NIP wave attributes are actual (β, ϕ, R_{NIP}). However, the straight-ray assumption would fail at determining the actual traveltime of the NIP wave. In the velocity-shift mechanism, the constant overburden velocity $\hat{\hat{v}}$ is adjusted (v_{shift}) to adapt with the actual recorded zero-offset reference traveltime t_0. The velocity change perturbs the NIP wave attributes measured at the surface, including the actual curvature radius R_{NIP}, the emergence angle β, and the azimuthal angle ϕ. They represent effective properties (β^{eff}, ϕ^{eff}, R_{NIP}^{eff}) and no longer correspond to the actual surface measurements, due to the straight-ray assumption (Schwarz and Gajewski, 2017).

$$X_C = \frac{\hat{\hat{R}}_{NIP}}{\rho} \sin(\hat{\hat{\beta}}) \cos(\hat{\hat{\phi}}), \qquad Y_C = \frac{\hat{\hat{R}}_{NIP}}{\rho} \sin(\hat{\hat{\beta}}) \sin(\hat{\hat{\phi}}), \qquad Z_C = \frac{\hat{\hat{R}}_{NIP}}{\rho} \cos(\hat{\hat{\beta}}),$$
$$R_C = \frac{(1-\rho)\hat{\hat{R}}_{NIP}}{\rho}.$$

Second, all points are transformed into the new coordinate system (x', y', z') with the origin at the midpoint M of the source and receiver pair (Figure 4.1c). All coordinates in this system are determined with X', Y', and Z' and the corresponding variable subscript with a prime symbol.

$$X'_{C'} = X_C - X_M, \qquad Y'_{C'} = Y_C - Y_M, \qquad Z'_{C'} = Z_C - Z_M.$$

Third, a rotated spheroid is fitted to the pair of the source and receiver with the center at the origin M' and the focal points at the source and receiver coordinates (Figure 4.1d).

Fourth, a plane passing through the source (S'), the receiver(G'), the reflection point (R'), the center of the sphere (C'), and the spheroid (M') is fitted, which is shown in transparent light red in Figure 4.1e. Based on Snell's law, for a constant velocity model, the incident and reflected rays from a reflection point and the normal vector to the reflector are coplanar and reside in one plane. The intersections of the plane with the spheroid and sphere will be an ellipse and circle, respectively, which are shown with dashed pink lines.

This plane will have a hinge that is the line that connects the source and the receiver (the main axis of the spheroid in this figure). The plane rotates around the hinge changing its inclination until it passes through the center of the sphere. The spheroid is a 360-degrees rotation of a 2D ellipse along the axis that connects the source and the receiver. The radii of the semi-axes, perpendicular to the main axis, are equal (This is why we used the term "spheroid" instead of "ellipsoid"). Therefore, the intersections of the plane and the spheroid along at any inclination will be the same, and we do not need to estimate the inclination of the plane for each pair of source and receiver.

Fifth, all coordinates are projected from the 3D coordinate system into the 2D coordinate system of the inclined plane that intersects the center of the sphere ($x'' - z''$) shown in Figure 4.1f. The axis x'' is along the vector that connects the source to the receiver ($S'G'$). The axis z'' is orthogonal to the x'' within the plane. All coordinates in this system are determined with X'' and Z'' and corresponding variable subscript. A double prime symbol is added to all variables and the subscript n is used for normalized variable with respect to the radius of the circle R''_C ($R''_C = R'_C = R_C$). In order to find the vector z'' within the plane encompassing (S', R', G', M', and C'), we find the cross product of the vectors $\overrightarrow{M'G'}$ and $\overrightarrow{M'C'}$. The resulted vector y'' will be normal to the plane and all vectors that are situated in the plane. Then, the vector z'' will be cross product of the

x'' and y''.

$$\overrightarrow{M'G'} = [H_X, H_Y, H_Z], \qquad \overrightarrow{M'C'} = [X'_{C'}, Y'_{C'}, Z'_{C'}],$$

$$\hat{X}''_{unit} = \frac{\overrightarrow{M'G'}}{||(\overrightarrow{M'G'}||_2}, \qquad \hat{Y}''_{unit} = \frac{\hat{X}''_{unit} \times \overrightarrow{M'C'}}{||(\overrightarrow{M'C'}||_2}, \qquad \hat{Z}''_{unit} = \hat{X}''_{unit} \times \hat{Y}''_{unit},$$

$$X''_{C''} = \hat{X}''_{unit} \bullet \overrightarrow{M'C'}, \qquad Y''_{C''} = \hat{Y}''_{unit} \bullet \overrightarrow{M'C'}, \qquad Z''_{C''} = \hat{Z}''_{unit} \bullet \overrightarrow{M'C'},$$

$$\hat{\hat{v}}_n = \frac{\hat{\hat{v}}}{R''_C}, \qquad h_n = \frac{H}{R''_C},$$

$$if H \neq 0 \rightarrow \qquad X''_{C''n} = \frac{X''_{C''}}{R''_C}, \qquad Z''_{C''n} = \frac{Z''_{C''}}{R''_C},$$

$$if H = 0 \rightarrow \qquad X''_{C''n} = \frac{X'_{C'}}{R''_C}, \qquad Z''_{C''n} = \frac{Z'_{C'}}{R''_C}.$$

This step converts the 3D reflection modeling problem with irregular topography into a 2D case with a flat surface. Within this plane (Figure 4.1f), applying the 2D spherical moveout formula (see Appendix 4-A for more detail) provides the reflection moveout (Δt) as follow:

$$\Delta t = t - \hat{\hat{t}}_0 = \frac{2}{\hat{\hat{v}}_n} \sqrt{\frac{h_n^2 \; R''_{X''n} \; (Z''_{C''n} - R''_{Z''n})}{Z''_{C''n} \; R''_{X''n} - X''_{C''n} \; R''_{Z''n}}} - \frac{2 \; R''_{NIP_n}}{\hat{\hat{v}}_n},$$

or geometrically can be expressed by

$$\Delta t = t - \hat{\hat{t}}_0 = \frac{\sqrt{(-h_n - R''_{X''n})^2 + {R''_{Z''n}}^2}}{\hat{\hat{v}}_n} + \frac{\sqrt{(h_n - R''_{X''n})^2 + {R''_{Z''n}}^2}}{\hat{\hat{v}}_n} - \frac{2 \; R''_{NIP_n}}{\hat{\hat{v}}_n},$$

where h is the half-offset, $[R''_{X''n},\ R''_{Z''n}] = [X''_{C''n} + \cos(\theta),\ Z''_{C''n} + \sin(\theta)]$ is the coordinate of the reflection point (R''), and $R''_{NIP_n} = \sqrt{{X''_{C''n}}^2 + {Z''_{C''n}}^2} - 1$. $\theta = 2 \ \text{atan}(u)$ and u

can be determined by solving the quartic equation expressed as:

$$b_4\ u^4 + b_3\ u^3 + b_2\ u^2 + b_1\ u^1 + b_0 = 0,$$

where

$$\begin{aligned}
b_0 &= Z''_{C''n}\ (X''_{C''n} + 1),\\
b_1 &= 2\ h_n^2 - 2\ {X''_{C''n}}^2 + 2\ {Z''_{C''n}}^2 - 2\ X''_{C''n},\\
b_2 &= -6\ X''_{C''n}\ Z''_{C''n},\\
b_3 &= -2\ h_n^2 + 2\ {X''_{C''n}}^2 - 2\ {Z''_{C''n}}^2 - 2\ X''_{C''n},\\
b_4 &= Z''_{C''n}\ (X''_{C''n} - 1),
\end{aligned}$$

where $bi(i = 0 - 4)$ are the coefficient of the quartic equation. The quartic equation has four complex-valued solutions in general. Analytical and numeral solutions can be used to find the solutions (see, e.g. Burnside and Panton, 1892). The convex and concave spherical reflectors are the two most common cases, where there is a single real-valued solution in both cases. To satisfy Fermat's principle, we select the minimum value for the reflection traveltime.

Sixth, the coordinate of the reflection point (R'') is transformed back into the global frame in 3D space, called RP, using the unit vectors of $x'-$, $y'-$, and $z'-$axis and reverse of the transformation operators used in the first and second steps.

$$\begin{aligned}
RP_X &= R_C\ (\hat{X}'_{unit} \bullet \overrightarrow{R''_n}) + X_M + X_0,\\
RP_Y &= R_C\ (\hat{Y}'_{unit} \bullet \overrightarrow{R''_n}) + Y_M + Y_0,\\
RP_Z &= R_C\ (\hat{Z}'_{unit} \bullet \overrightarrow{R''_n}) + Z_M + Z_0,
\end{aligned}$$

where $\overrightarrow{R''_n} = [R''_{X''n}, 0, R''_{Z''n}]$ and

$$\begin{aligned}
\hat{X}'_{unit} &= \frac{[\hat{i} \bullet \hat{X}''_{unit}, \hat{i} \bullet \hat{Y}''_{unit}, \hat{i} \bullet \hat{Z}''_{unit}]}{||[\hat{i} \bullet \hat{X}''_{unit}, \hat{i} \bullet \hat{Y}''_{unit}, \hat{i} \bullet \hat{Z}''_{unit}]||_2}, \\
\hat{Y}'_{unit} &= \frac{[\hat{j} \bullet \hat{X}''_{unit}, \hat{j} \bullet \hat{Y}''_{unit}, \hat{j} \bullet \hat{Z}''_{unit}]}{||[\hat{j} \bullet \hat{X}''_{unit}, \hat{j} \bullet \hat{Y}''_{unit}, \hat{j} \bullet \hat{Z}''_{unit}]||_2}, \\
\hat{Z}'_{unit} &= \frac{[\hat{k} \bullet \hat{X}''_{unit}, \hat{k} \bullet \hat{Y}''_{unit}, \hat{k} \bullet \hat{Z}''_{unit}]}{||[\hat{k} \bullet \hat{X}''_{unit}, \hat{k} \bullet \hat{Y}''_{unit}, \hat{k} \bullet \hat{Z}''_{unit}]||_2}.
\end{aligned}$$

The derived formula enables us to calculate not only the reflection traveltime (t) but also the spatial coordinate of the reflection point (RP). Therefore, we can estimate the multifocusing parameters and focusing function (σ), as by-products. The formulation is derived for a homogeneous overburden, but it can be developed to the inhomogeneous model using the auxiliary medium theory mentioned above (Perroud et al., 1999; Jäger et al., 2001). We expressed the moveout formula for a general auxiliary medium of constant velocity $\hat{\hat{v}}$ with its respective reference time $\hat{\hat{t}}_0$. The proposed generalized moveout can account for heterogeneity using two different mechanisms including shifting time or shifting velocity, and it depends on the choice of $(\hat{\hat{t}}_0, \hat{\hat{v}})$. One can switch between two different representations, the operator in the optical projection or in the effective domain, by exchanging $(t_0, v_{shift}) \leftrightarrow (t_{shift}, v_0)$. In the wavefield attribute analysis using a global optimization algorithm, the (t_0, v_{shift}) substitutions used in the velocity-shift mechanism lead to effective wavefield parameters $[\hat{\hat{\beta}}, \hat{\hat{\phi}}, \hat{\hat{R}}_{NIP}] = [\beta^{eff}, \phi^{eff}, R^{eff}_{NIP}]$. While the (t_{shift}, v_0) substitutions used in the time-shift mechanism lead to actual wavefield parameters $[\hat{\hat{\beta}}, \hat{\hat{\phi}}, \hat{\hat{R}}_{NIP}] = [\beta, \phi, R_{NIP}]$. ρ remain unchanged regardless of which auxiliary medium is employed.

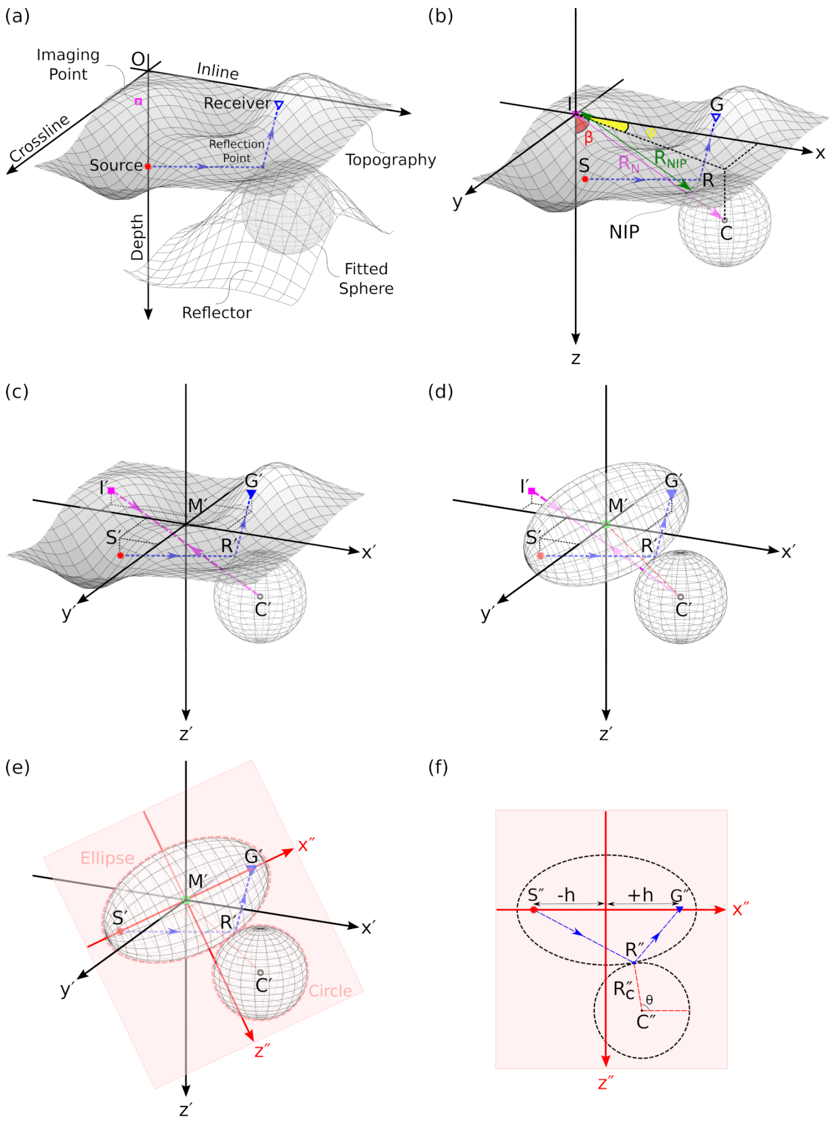

Figure 4.1: Ray scheme of the 3D generalized spherical multifocusing method. a) the ray (dashed blue line) geometry of a reflection from a curved interface, generated by a arbitrarily located pair of source and receiver sitting on an irregular topography. A sphere is fitted to the reflector to approximate the subsurface structure locally at the normal incident point. b) The wavefield attributes (β, ϕ, R_N, and R_{NIP}) in the coordinate system transformed from the origin of the global frame (O) (Figure 4.1a) to an arbitrarily chosen imaging point (magenta square in Figure 4.1a). c) The normal-incident-point ray (dashed magenta line) geometry in the coordinate system transformed into the origin at the midpoint of the source and receiver pair. d) The rotated spheroid fitted to the pair of the source and receiver with the center of origin and the focal points of the source and receiver pair. e) The plane passed through the source, receiver, reflection point, center of the sphere, and center of the spheroid. The intersections of the plane with spheroid and sphere are an ellipse and circle, respectively, which are shown with dashed pink lines. f) The ray scheme of the 3D generalized spherical multifocusing projected onto the fitted plane used for the 2D spherical multifocusing.

Modeling the traveltime of a reflection from a planar reflector and a diffraction from a point diffractor can be considered as special cases of the proposed method and can be achieved by substituting $R_N = \infty$ and $R_N = R_{NIP}$, respectively. The proposed approach is exact for plane dipping interfaces, spherical reflectors, and point diffractors with a homogeneous velocity background (Fomel and Kazinnik, 2009; Landa et al., 2009). Also, this method can accurately approximate reflection traveltime for a vast range of curvature and heterogeneity including gently to highly curved interfaces (flat reflector to point diffractor) beneath mild to relatively high heterogeneous overburden (Landa et al., 2009).

The 2D spherical MF method for flat and irregular surfaces are special cases of the proposed approach. In two-dimensional cases, the moveout operator depends on three wavefield attributes including the emergence angle β, radii of curvature of the normal R_N, and normal-incidence-point R_{NIP} waves (Landa et al., 2009). In three-dimensional surveys, the corresponding formulation depends on only an additional parameter (four attributes in total), the azimuthal angle ϕ between the inline and the vertical plane containing the central ray.

The proposed formulation is a dual moveout expression that can account for heterogeneity by two different mechanisms. A processor can select the auxiliary medium – either optical projected or effective replacement medium – by supplying the corresponding substitutions. The time-shifted 3D GSMF is better suited for mapping gently to strongly curved geometries with low to moderate overburden heterogeneity from prestack data into a zero-offset wavefield stacked section. While the velocity-shifted version of the 3D GSMF is suggested to use for mapping of subsurface with gently curved layers and moderate to relatively high heterogeneity. Note that depth domain imaging methods are superior in solving for the effect of strong lateral velocity changes, compared to time imaging approaches. We will test the performance of the proposed method only using the optical form of the 3D GSMF operator in the example sections.

4.6 Implementation

Here, we introduce a time processing sequence, which can significantly improve the accuracy of the stacking velocity field and subsurface stacked volume. The 3D seismic prestack data used as input to the 3D GSMF are defined in a 7D space including the recording time (t), the three-dimensional spatial coordinate of the source (X_S, Y_S, Z_S), and the three dimensional spatial coordinate of the receiver (G_S, G_S, G_S). In order to perform 3D binning, first, a regular grid is superimposed on the midpoints distribution. This grid includes cells with half the size of the receiver group interval in the inline direction and the receiver line spacing in the crossline direction. The seismic traces are then sorted into common-cell gathers. The imaging points are the center of the common-cells.

The multi-coverage stacking method, like multifcosuing, attempts to fully extract the information recorded in the prestack data. To that end, rather than applying the stacking step over single common-cell gathers, the proposed method can be applied over several nearby common-cell gathers. A super-cell consist of neighboring m inlines by n crosslines cells. The traces at the midpoint locations that fall within each super-cell constitute a super common-cell gather, which increases fold by a factor of $m \times n$. In other words, to build a super common-cell gather (super gather), a set of traces from neighboring cells are collected whose midpoints are in the vicinity of the imaging point and contain information about the same subsurface segments. The size of the super cell can be determined using Fresnel zone analysis.

The 3D super binning of traces makes fold coverage even, maintains adequate offset distribution with distinct azimuths, and allows the contribution of more traces in generating the stacked section, which in turn enables a more meaningful and reliable wavefield analysis and leads to more coherent focused reflection at the right location. Also, 3D super binning increases the statistical diversity of the information contributed in reconstructing the stacked trace assigned to the center of each cell (the imaging point or the central point). This assists to increase S/N significantly as super gathers compromise more traces.

Implementation of the 3D GSMF is technically challenging and requires determining four unknown parameters ($\hat{\hat{\beta}}$, $\hat{\hat{\phi}}$, $\hat{\hat{R}}_{NIP}$, and ρ) simultaneously. This is a data-driven method and does not require any knowledge of the subsurface model. A non-linear global optimization algorithm can be employed to determine the unknown 3D wavefield parameters through coherence analysis (Belfer et al., 2008a). In fact, the global optimization searching algorithm attempts to find a traveltime surface that optimally approximates the moveout of reflection recorded in a super gather by maximizing the coherence function (Yilmaz, 2001).

Estimating wavefield attributes using non-linear global optimization is the most computationally demanding part of multifocusing approaches. Also, the quality of the resulting stack volume highly depends on the accuracy of the estimated wavefront attributes (Xie and Gajewski, 2018). Therefore, selecting an efficient optimization method is a key factor. Here, we attempted to present a strategy that produces accurate zero-offset wavefield volumes while still being cost-effective. We examined the performance of several global optimization methods in terms of the accuracy of the determined wavefront parameters and the computational expenses. Among the evaluated optimization approaches, differential evolution (DE) (Storn and Price, 1997) outperformed and provided smoother attribute volumes and high-quality stacking sections. Discussing the performance of the tested global optimization algorithms is beyond the scope of this article. Overall, the DE method is a robust global optimization technique and has low sensitivity to the control parameters (Garabito and Cruz, 2019). Also, this method can be optimally adjusted to efficiently estimate parameters with high accuracy. Besides, the proposed processing workflow can be beneficial to the conflicting dip processing and maintain more features – especially diffractions – that would finally increase the image quality (Xie and Gajewski, 2018).

The attribute volumes are considered as by-products of multifocusing stacking process, which can be used for further processing steps, calculating a detailed dip- and azimuth-independent stacking velocity field, enhancing and regularizing prestack gathers, structural interpretation, wavefield separation, and NIP-wave tomography. These products are crucial inputs in prestack/poststack time/depth migrations (Xie, 2016).

The stacked and attributes volumes are required to be referenced to a datum surface, which defines the elevation of the surface that the final stack volume will be assigned and can be a flat ($Z_0 = constant$), floating ($Z_0 = f(X_0, Y_0)$), or actual topography surface. One can use the (x, y, z) coordinates of sources and receivers to build the topographic surface. Applying a smoothing filter on the topographic surface can smooth out rapid changes to generate the floating datum surface.

For an efficient implementation of the newly introduced 3D GSMF stacking method, we developed a package using the basic programming languages including C, C++, and Shell through the Seismic Unix platform (Stockwell Jr, 1999). We utilized the serial farming method to run the code in parallel on multiple processors. The Pagmo library (Biscani and Izzo, 2020) was incorporated into the package to estimate wavefield attributes accurately using various parallel optimization algorithms such as DE.

4.7 Synthetic Data Example

We generated synthetic numerical models to test the performance of the proposed method. The synthetic models include folded structures with a range of curvatures from low to high. Figure 4.2 shows the geometry of surveys planned for the synthetic data. We tested the proposed method on synthetic data generated for both 3D (Figure 4.2a) and crooked-line (Figure 4.2b) surveys. The red and blue dots are sources and receivers, and black squares (A, B, and C in both Figures 4.2a and 4.2b) are the location of selected super gathers. In the 3D survey, the transparent gray squares show the selected super cells each of which consists of three by three nearby cells. In the crooked-line configuration, the midpoints are darker for increasing offset and shown for the location of selected super cells each consisting of five nearby common cells. Here, the solid slalom black line is the processing line that is generated by fitting a low-order polynomial to the midpoints using a regression method.

Figure 4.3 shows three different synthetic velocity models beneath a topography surface with elevations ranging from -200 to 250 m. The models include a single sphere reflector with a constant curvature (Figure 4.3a), a single antiform-synform reflector with positive and negative curvatures (Figure 4.3b), and a model of multiple gently curved reflectors with various curvatures (Figure 4.3c). Also, a vertically strong heterogeneity (1500 - 4500 m/s) has been incorporated into the antiform-synform model (Figure 4.3b) to investigate the accuracy of the method in dealing with the inhomogeneous subsurface. We utilized the SOFI3D software (Bohlen, 2002) to numerically simulate seismic synthetic data.

For each model, we examined the applicability and accuracy of the proposed method for both 3D (Figure 4.2a) and crooked-line (Figure 4.2b) surveys. We quantitatively analyzed the accuracy of the new formula regarding traveltime approximations and compared its results with the reference models. Figure 4.4 and 4.5 depict the estimated 3D GSMF traveltime of reflection surfaces versus offset and common-midpoint number.

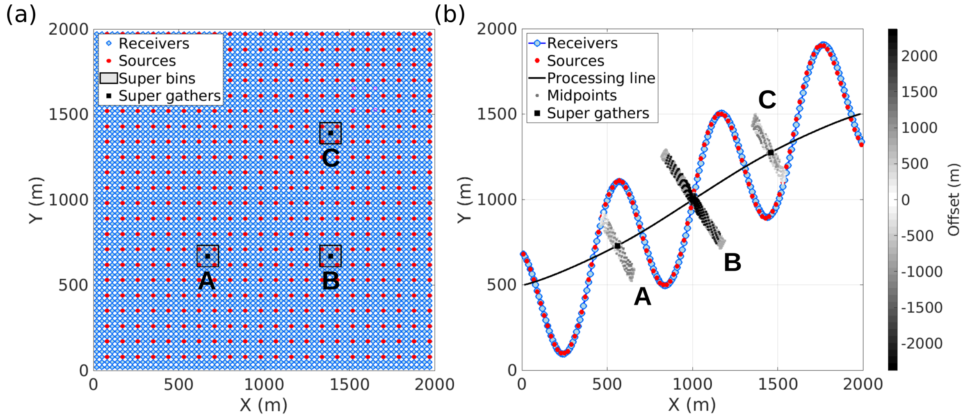

Figure 4.2: The geometry of surveys for synthetic data examination includes a) a 3D survey and b) a crooked-line survey. Sources and receivers are shown with the red and blue dots. The selected super gathers are shown with black squares. In figure (a), the transparent gray squares show the selected super cells each of which consists of three by three nearby cells. In figure (b), the solid slalom black line is the processing line, and midpoints (darker for greater offset) are shown for the selected super cells. In the crooked-line survey, each super cell consists of five nearby common cells.

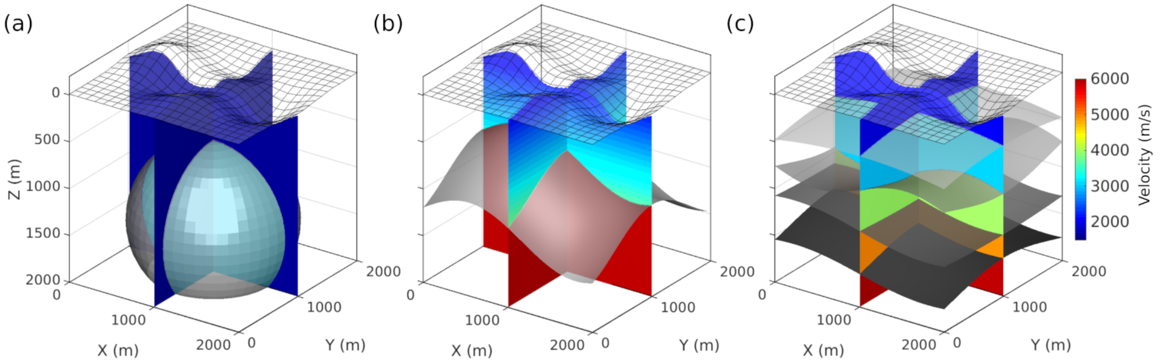

Figure 4.3: 3D synthetic velocity models beneath a topography surface with elevations ranging from -200 to 250 m, a) single sphere reflector, b) single antiform-synform reflector with vertical gradient background velocity, and c) multiple curved reflectors with various curvatures.

They are coloured by their differences with respect to the exact traveltime simulated using the finite-difference algorithm. Figures 4.4a and 4.4b show the results for the single sphere reflector (Figure 4.3a) with the 3D and crooked-line surveys at the two locations labeled A on Figures 4.2a and 4.2b respectively. Figures 4.4c and 4.4d depict the results for the single antiform-synform reflector (Figure 4.3b) with the 3D and crooked-line surveys at the two locations labeled B in 4.2. Figure 4.5 shows the results for each reflector of the multiple curved-layers model (Figure 4.3c). In this figure, each row from top to bottom corresponds to each reflector in order. The graphs in the first column (Figures 4.5a, 4.5c, 4.5e, and 4.5g) are the results for the data acquired using the 3D survey (Figure 4.2a) and the graphs in the second column (Figures 4.5b, 4.5d, 4.5f, and 4.5h) are the results for the data collected using the crooked-line survey (Figure 4.2b) at the two locations labeled C in 4.2. The reflections from each reflector are identified by analyzing the dip-independent stacking velocity spectrum. The unknown 3D GSMF wavefield parameters were estimated using the differential evolution global optimization algorithm, not least-square fitting methods, while the latter approach can reduce RMSE considerably. Overall, the values of the root-mean-square error (RMSE) demonstrate that the proposed method was able to approximate traveltime with high accuracy for reflectors with various curvatures and media with various heterogeneity, even in the presence of topography and regardless of the survey geometry.

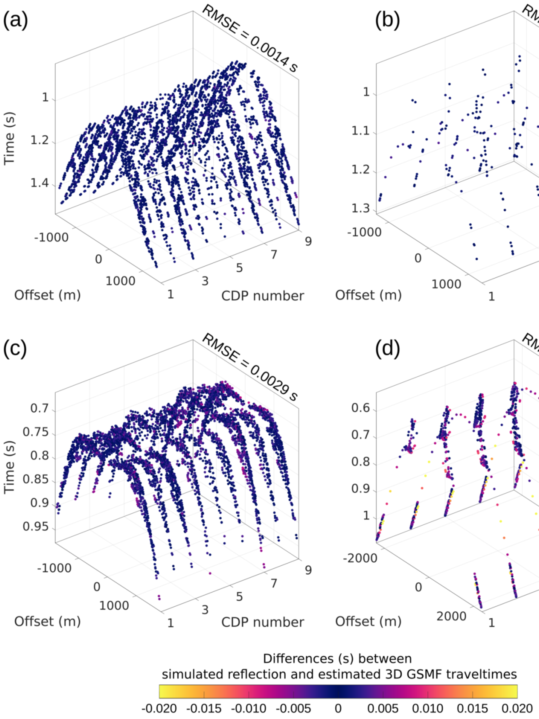

Figure 4.4: The traveltime of reflection surfaces estimated using the 3D GSMF method and coloured by its differences with respect to the exact traveltime simulated using the finite-difference algorithm. a) and b) show the results for the single sphere reflector (Figure 4.3a) with the 3D and crooked-line surveys at location A, respectively. c) and d) depicts the results for the single antiform-synform reflector (Figure 4.3b) with the 3D and crooked-line surveys at location B, respectively.

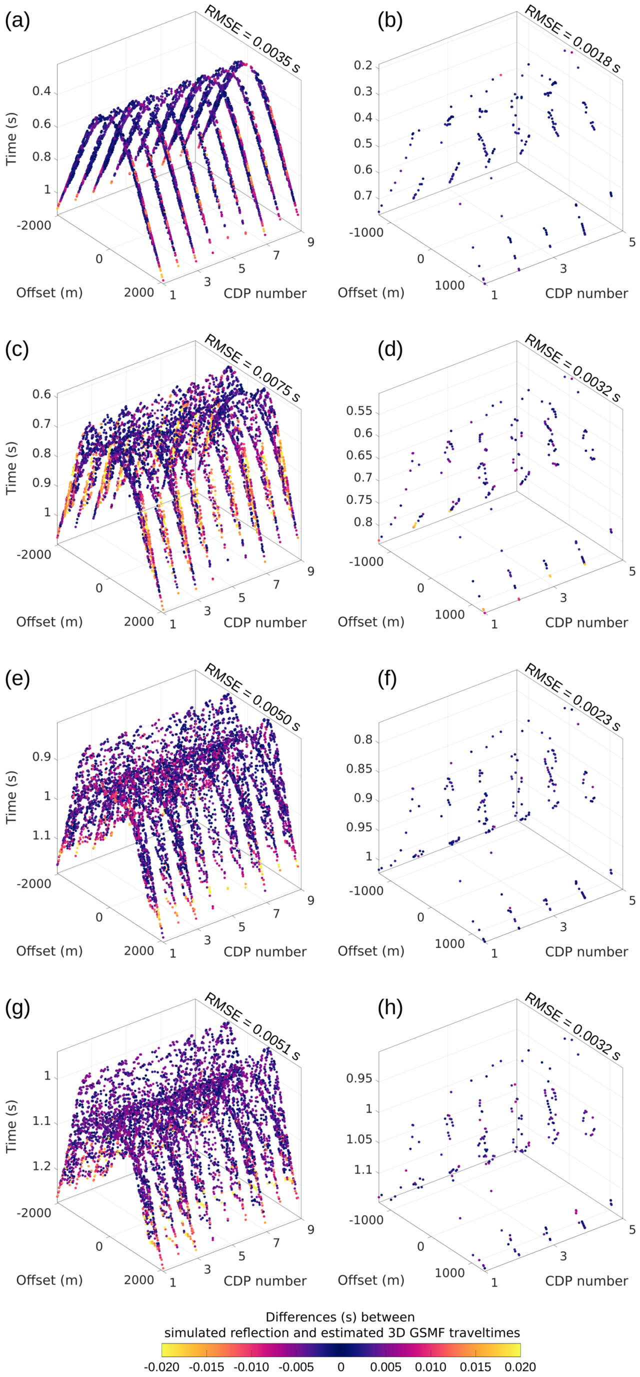

Figure 4.5: The traveltime of reflection surfaces estimated using the 3D GSMF method and coloured by its differences with respect to the exact traveltime simulated using the finite-difference algorithm for the model of multiple curved layers (Figure 4.3c). a), c), e), and g) show the results for the first, second, third, and fourth reflectors acquired with the 3D survey (Figure 4.2a) at location C, respectively. Figures b), d), f), and h) are for the first, second, third, and fourth reflectors collected using the crooked-line survey (Figure 4.2b) at location C, respectively.

We also used the 3D SEG C3WA benchmark synthetic velocity model (Aminzadeh et al., 1997) to test the performance of the introduced method. The velocity model is shown in Figure 4.6, which consists of an irregular-shaped salt body with several scattering objects and diffracting edges beneath a sedimentary overburden. This model includes several features that can generate higher-order traveltime moveouts. Also, the presence of a high-velocity salt body with a rough body caused a significant velocity heterogeneity, which made the reflections from the reflectors beneath it strongly non-hyperbolic. We added a topography surface with elevations ranging up to 400 m. Then, numerically simulate seismic synthetic seismograms using the finite difference method. Note that, we simulated the reflection wavefield to add time shifts associated with variation of the source and receiver elevations. We did not add them as static bulk shifts for all samples of each trace, which might impose errors resulting from the violation of the assumption of nearly vertical raypaths within the near-surface. After initial signal processing, the data was sorted into common-cell gathers. Next, three nearby common-cell gathers along the inline and crossline directions have been composed to build super common-cell gathers. To illustrate the results, we selected a super-cell with the center located at $[x = 4020, y = 5000]$ m, above the diffracting edges of the salt body with inhomogeneous overburden.

Figures 4.7 compares the results of applying the conventional and the 3D GSMF corrections on the synthetic super gather generated for the 3D SEG C3WA benchmark model. In this paper, the conventional processing sequence includes source-receiver elevation statics, normal, and dip moveout corrections. Here, for NMO correction, we used the stacking velocity field calculated from the exact synthetic velocity model. Figures 4.7a shows the original super gather that was sorted based on the trace number and shown for only positive offsets. Visible undulations along reflections are caused by the acquisition pattern and topography. Figures 4.7b and 4.7d are the conventionally processed and the

3D GSMF corrected gathers, respectively. Figures 4.7c and 4.7e are the stack traces of the conventionally- and the 3D GSMF-corrected gathers. The amplitudes of stack traces are preserved and are comparable. Figure 4.7f is the cropped 3D SEG C3WA velocity model with inline and crossline located at $y = 5000$ m and $x = 4020$ m. R1 indicates the reflection from a localy flat reflector with $R_N \to \infty$ and D1 indicates the diffration from the edge of the salt body where $R_N \to R_{NIP}$.

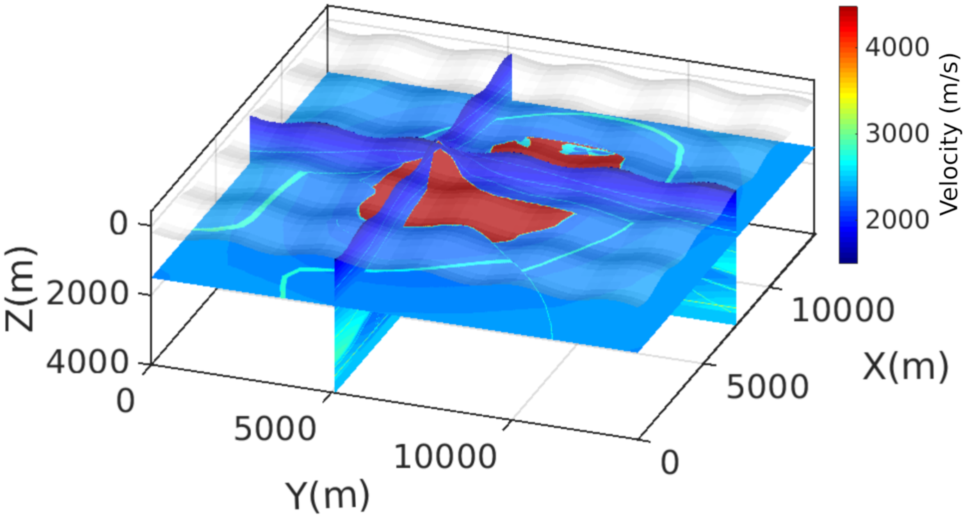

Figure 4.6: The 3D SEG C3WA benchmark synthetic velocity model with a topography surface. The elevation of topography is ranging up to 400 m (from -200 to 200 m).

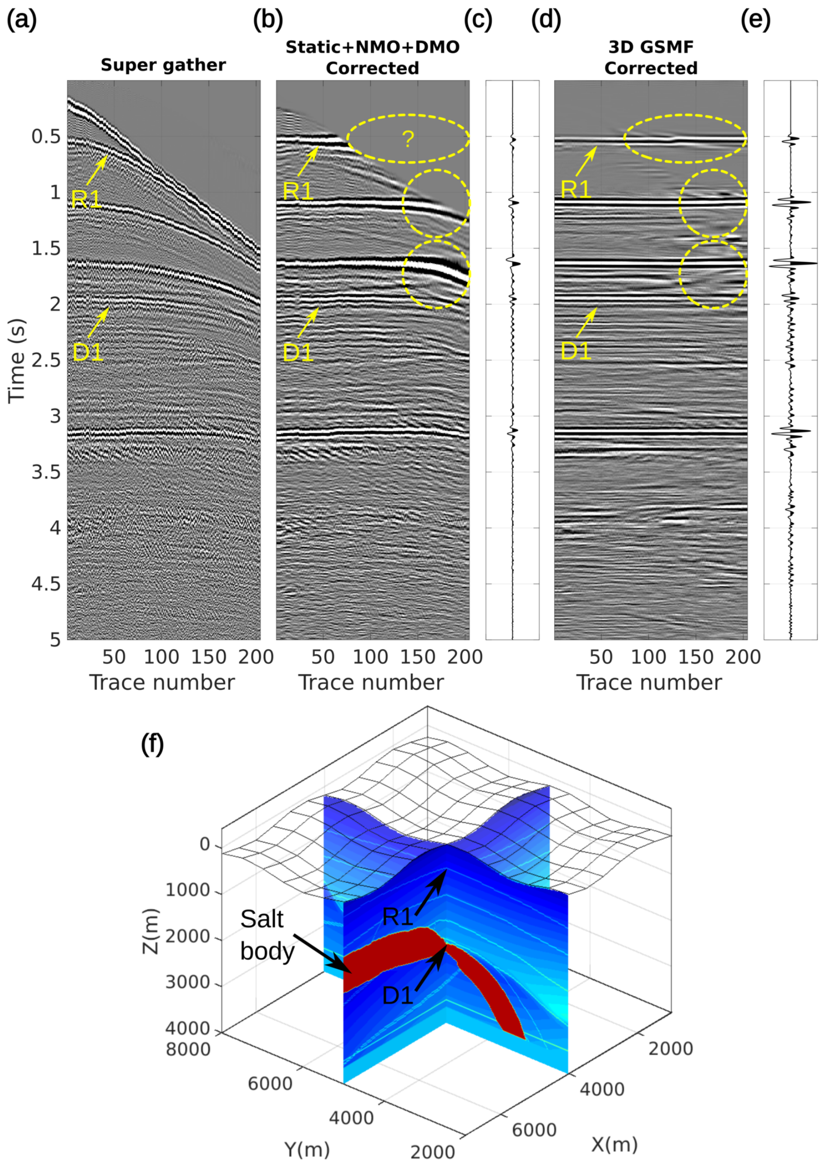

Figure 4.7: Results of applying b) the conventional corrections (source-receiver elevation statics + normal moveout + dip moveout corrections) and d) the 3D GSMF method on the synthetic super gather (a) located at $[x = 4020, y = 5000]$ m for the 3D SEG C3WA benchmark synthetic velocity model (Figure 4.4). c) and e) are the stack traces of the conventionally processed and the 3D GSMF corrected gathers. f) Cropped 3D SEG C3WA velocity model with inline and crossline located at $y = 5000$ m and $x = 4020$ m; the selected super-cell gather (a) recorded above the diffracting edges of the salt body with inhomogeneous overburden. A quarter of the topography surface was not plotted to see the subsurface model easily and point out some features. R1 indicates the reflection from a localy flat reflector with $R_N \to \infty$ and D1 indicates the diffration from the edge of the salt body where $R_N \to R_{NIP}$. Reflectors from beneath the salt body produced non-hyperbolic reflections.

Overall this result reveals that the proposed method accurately corrected all of the source-receiver elevation statics, normal, and dip moveout effects simultaneously (not sequentially), even in the presence of strong heterogeneity and variations of source and receiver elevations. The reflections have aligned across all of the near and far offsets and midpoint separations. This demonstrates that the 3D GSMF method is accurate in a large range of offsets and midpoints. The flatness and temporal location of events in the corrected gather (Figure 4.7d) gives us enough confidence about the accuracy of the proposed operator. The deviations along the reflection traveltimes in the super common-cell gather after conventional corrections are mostly the results of the time shifts associated with the source-receiver azimuth dependency of stacking velocities and nonhyperbolicity of higher-order events.

Also, the 3D GSMF method prevents the stretching problem (compare the signals marked with dashed yellow circles in Figures 4.7b and 4.7d) allowing to use of full-offset data (see the data marked with dashed yellow ellipses in Figures 4.7b and 4.7d), leading to an increased vertical resolution in stacked sections. However, the NMO correction caused wavelet stretching for shallow and long-offset reflections that cannot be mitigated by any of the subsequent corrections and need to be muted (see the muted part indicated with a question mark in Figure 4.7b). Comparing the stacked traces demonstrates that the 3D GSMF stacking method produces reflection data (Figure 4.7e) with sharper and a less deformed wavelet, higher vertical resolution, and a greater S/N than the conventional stacking method (Figure 4.7c).

Analysis of the velocity spectrum and wavefield attributes (by comparing the radius of normal (R_N) and normal-incident-point wave curvatures (R_{NIP})) allowed us to distinguish one of the diffraction events, which is shown by the yellow arrow (D1). Comparing this event (in Figures 4.7a, 4.7b, 4.7d) indicates the non-hyperbolic and higher-order behavior of the diffraction traveltimes. The 3D GSMF method enabled us to recognize and accurately simulate these events. Reflectors from beneath the salt body produced non-hyperbolic reflections. The 3D GSMF was also able to correct the non-hyperbolic moveout associated with reflections beneath the complex salt body.

4.8 Real Data Example

We examined the proposed approach on an extremely noisy 3D seismic dataset acquired over a thrust belt setting with irregular topography and complex overburden. In this area, the near-surface includes both lateral velocity variations and vertical velocity gradients. In addition, overthrust tectonism has led to imbricate structures, which makes seismic imaging a challenging task (Yilmaz, 2021). The survey spanned an area of approximately 200 km^2 at 12.4×16.2 km in size. A diagonal recording geometry was used to collect data, where source lines in the northerly direction are diagonal to the receiver lines (inline) in the northwest-southeast direction. The survey has been conducted using 9,108 seismic dynamite shots at an interval of 60 m with charge depths ranging from 4 to 10 m. In each shot, 10 receiver lines at 250-m separation, each includes 216 receiver groups at an interval of 40 m, record seismic signals. Source-receiver elevations vary between 105 and 249 m (Figure 4.10a).

The processing sequence is listed in Table 4.2. As a first step, we assigned survey geometry, transformed, and rotated the survey orientation such that the inline and crossline directions aligned along with E-W and N-S, respectively. Figure 4.8 shows the transformed and rotated survey geometry. Then, we estimate a 3D grid-based near-surface velocity-depth model using 3D nonlinear traveltime tomography. This step can plausibly resolve long- and relatively short-wavelengths lateral and vertical velocity variations within the near-surface. Next, shot-receiver tomostatics corrections are calculated (Figure 4.9a) and applied. Figure 4.9a shows how considerable and essential source-receiver elevation static shifts are in this dataset (ranging from -70 to +20 ms). The tomostatics corrections shift the sources and receivers vertically from the real topography down to the intermediate datum surface using the near-surface velocities and then vertically shift up to the floating datum surface using the replacement velocity (Yilmaz, 2021). The floating datum surface (Figure 4.10c) is generated from the topographic surface (Figure 4.10b) – built from coordinates of sources and receivers (Figure 4.10a) and then smoothed to remove rapid changes. The processes marked with an asterisk are necessary steps in the conventional processing sequence. In conventional processing, we shall continue subsequent data analysis and processing steps, including velocity analysis and stacking processes, on the seismic data referenced to the floating datum. While the 3D GSMF stacking method can be applied to the data with/without prior source-receiver elevation static corrections.

Signal processing is the next step, which includes geometric spreading correction, time-variant spectral whitening. After geometric spreading correction and time-variant spectral whitening, bottom tapering of amplitudes were applied to avoid undesirable effects. A bandpass filter has been used to attenuate any processing-induced noise outside the recoverable signal bandwidth. Then, field records have been time-windowed to 0-1.5 s, which includes the main reflections. Also, in order to challenge the performance of the proposed method, we reduced the fold coverage by limiting the offset range up to 1200 m. Figure 4.8a, an example shot is shown using a black plus sign, and its active receivers after limiting offset are shown in cyan. Figure 4.11 shows a field record before and after the application of the signal processing sequence.

The processed seismic shot gathers are then sorted into common-cell gathers. The di-

Table 4.2: The processing sequence of the real seismic data set

Process	**Parameter**
Assigning the Geometry	
Transformation-Rotation the Geometry	
* 3D Near-Surface Modeling	
* Shot-Receiver Tomostatics Corrections	replacement velocity of 2400 m/s
Signal Processing	
- Geometric Spreading Correction	scaling function $t^{1.4}$
- Time-Variant Spectral Whitening	signal bandwidth of 8-84 Hz
- Bandpass Filter	8-12-72-84 Hz
Time Windowing	0-1.5 s
Offset Limiting	[-1.2 +1.2] km
Binning	
Area Bounding	x=[2.5 9.5] and y=[7.0 14.0] km
Velocity Analysis/Attributes Search	
NMO+DMO/3D GSMF Correction	
Residual Statics Corrections	
Stacking	
Shifting Bandwidth to Lower Frequencies	4,8-72,84 Hz
Automatic Gain Control	250 sample window

mension of each cell is 20 m × 20 m in the inline and crossline directions, respectively. The fold map for the common-cell gathers is shown in Figure 4.8b. Common-cell gathers have been used to apply subsequent conventional processing steps. The dataset was bounded to an area with a size of 7 km × 7 km, covering the main and challenging geological features. This area is shown using a solid black square in Figure 4.8b and 4.8c. We estimated the 3D stacking velocity field by performing stacking velocity analysis using an image-based workflow. Then, we applied NMO corrections to the common-cell gathers using the 3D stacking velocity field. The estimated stacking velocity field (V_{stk}) is shown in Figure 4.12f.

Super common-cell gathers, consisting of nearby seven inlines by seven crosslines cells, have been used to increase the fold and improve the S/N in the multifocusing stacking method. Figure 4.8c shows the fold map for the super common-cell gathers. Comparing

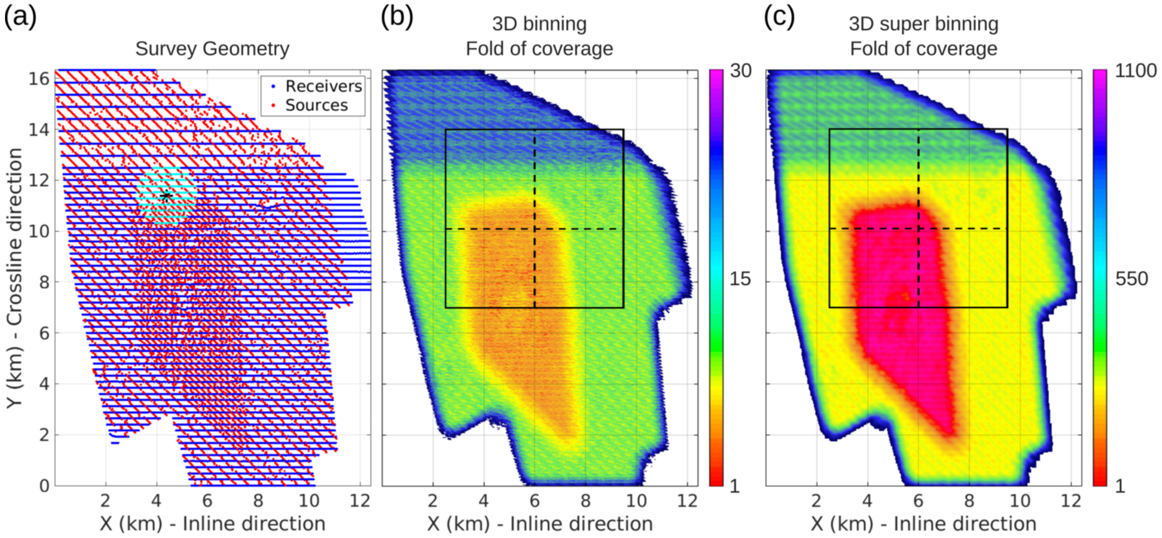

Figure 4.8: a) Survey geometry, sources and receivers are shown with red and blue dots, respectively. An example shot is shown using a black plus sign, and its active receivers (after limiting offset) are shown in cyan. b) The fold map used in conventional processing, and c) the super cell fold map used in the multifocusing processing. In figures (b) and (c), solid black square shows the selected area for the experiment, and dashed lines show the selected inline and crossline at y=10.1 km and x=6.0 km, respectively.

the fold maps for the 3D binned seismic data used in the conventional (Figure 4.8b) and the 3D GSMF methods (Figure 4.8c) demonstrates that performing the 3D super binning increases the fold by a factor of 36 and makes the fold coverage even. Also, the 3D super binning can maintain adequate offset distribution with distinct azimuths.

We estimated the 3D GSMF unknown parameters using the nonlinear differential evolution global optimization algorithm by maximizing the semblance function. Figure 4.12a-d display the volumes of the estimated wavefield attributes including R_{NIP}, R_N, β, and ϕ, respectively. Figure 4.12e shows the coherence cube – the values of the semblance function maximized in the global optimization searching of the 3D GSMF parameters. The derived 3D stacking velocity field in conventional processing (Figure 4.12f) was used as a constraint in the attributes estimation process to define a searching corridor. In Figure 4.12, the cubes are sliced at the time of 1300 ms and along the inline and crossline located at y=10.1 km and x=6.0 km, respectively. The selected inline and crossline are also shown in Figures 4.8b and 4.8c using dashed black lines. The attribute volumes can be used for calculating a detailed dip- and azimuth-independent stacking velocity field. Also, the geological significance can be drawn from the attributes panel. The inline attribute sections clearly show an anticline structure. The diffraction can also be identified using the criterion of $R_N = R_{NIP}$.

We applied 3D GSMF corrections to the super common-cell gathers using the estimated 3D wavefield attributes. This step requires a floating datum surface to reference stacked traces to the imaging points (X_0, Y_0, Z_0) chosen on the datum. We used the same floating datum (Figure 4.10c) used in the tomography and conventional stacking. Short-wavelength reflection traveltime deviations might be still left in the corrected gathers after moveout corrections. Residual statics corrections are required to account for these fluctuations (kinks). We estimated and applied 3D surface-consistent residual statics shifts using the 3D stack-power optimization method. Figure 4.9b shows the residual statics shifts for the conventional processing. Eventually, the corrected traces are stacked and post-processed using a bandpass filter and automatic gain control.

We derived two stack volumes including the 3D conventional (Tomostatics + NMO + DMO) and 3D GSMF stack volumes. Also, we tested both strategies including the application of the 3D GSMF stacking method on the super common-cell gathers with/without prior source-receiver elevation static corrections. The results of both strategies were almost the same in this case, where the offset and midpoint apertures allowed sufficiently

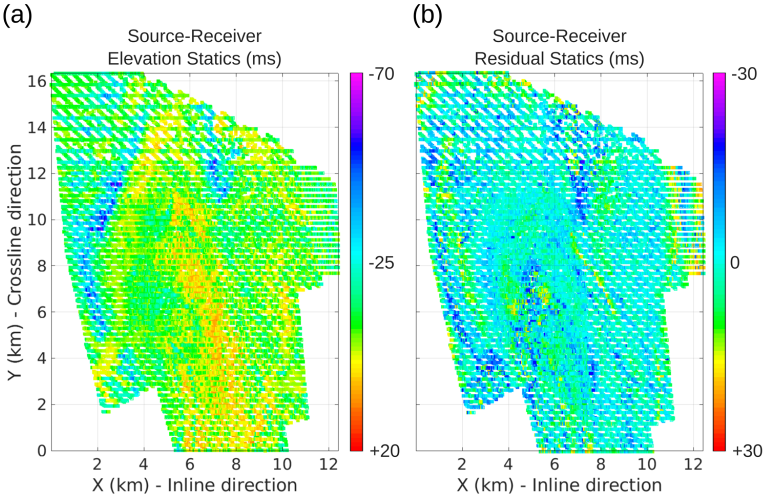

Figure 4.9: The source-receiver a) elevation and b) residual statics

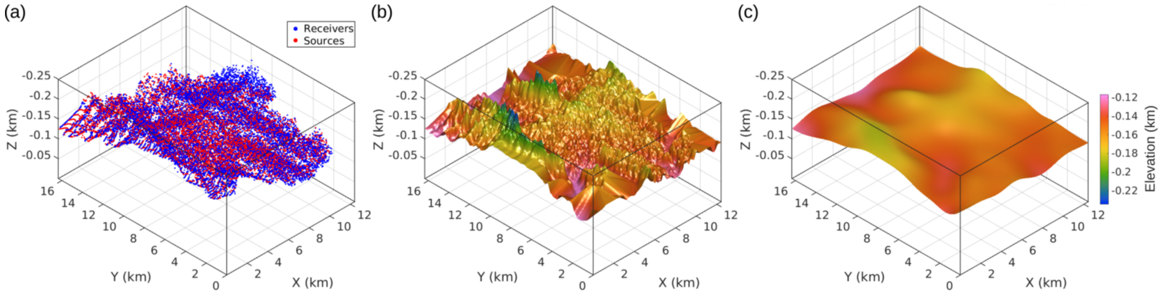

Figure 4.10: a) 3D survey geometry for showing source-receiver elevation distribution, b) the topography surface generated by fitting a surface to the source and receiver distribution, c) the floating datum generated by smoothing the topography surface

enough fold coverage. Trace spacings in the inline and crossline directions are both 20 m. Improvements achieved by the 3D GSMF approach compared to the conventional 3D processing method are well illustrated in Figures 4.13 and 4.14. Figure 4.13 displays the stack sections along the selected inline and crossline located at y=10.1 km and x=6.0 km from the 3D stacked volumes, respectively. Figures 4.13a and 4.13c shows the conventional and the 3D GSMF stacks along the selected inline and crossline and Figures 4.13b and 4.13d shows them along the selected crossline, respectively. The time slices at 600, 800, and 1300 ms from the 3D stacked volumes are shown in Figure 4.14 in columns

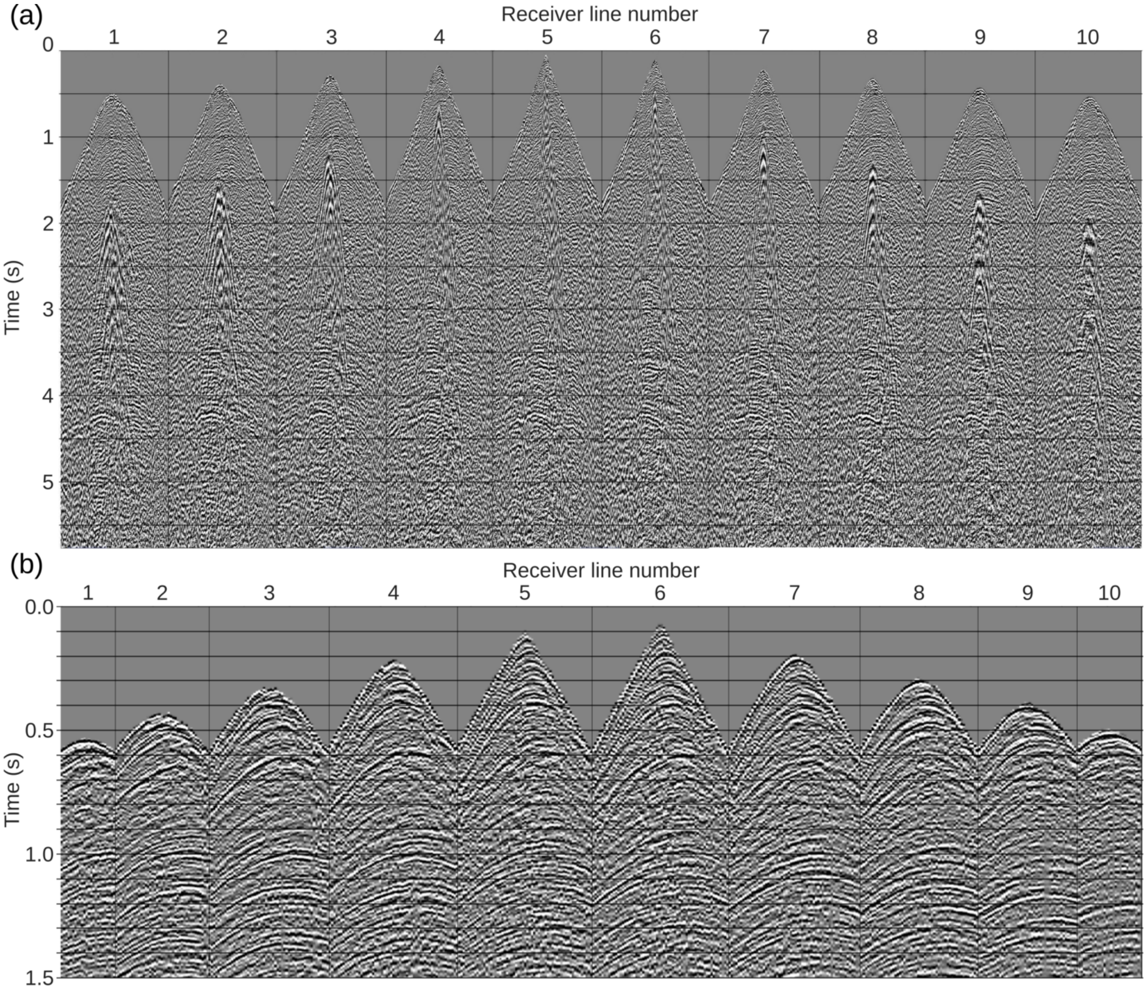

Figure 4.11: An example of the field record before (a) and after (b) signal processing and static corrections.

from left to right. In this figure, the first row is for conventional processing and the second row is for the 3D GSMF method. The results of applying the 3D GSMF method indicate that the proposed method was able to map the complex imbricate structure and the thrust faults. Comparing the results demonstrate that the 3D GSMF method significantly improved the quality of stacked sections, increased the vertical and hori-

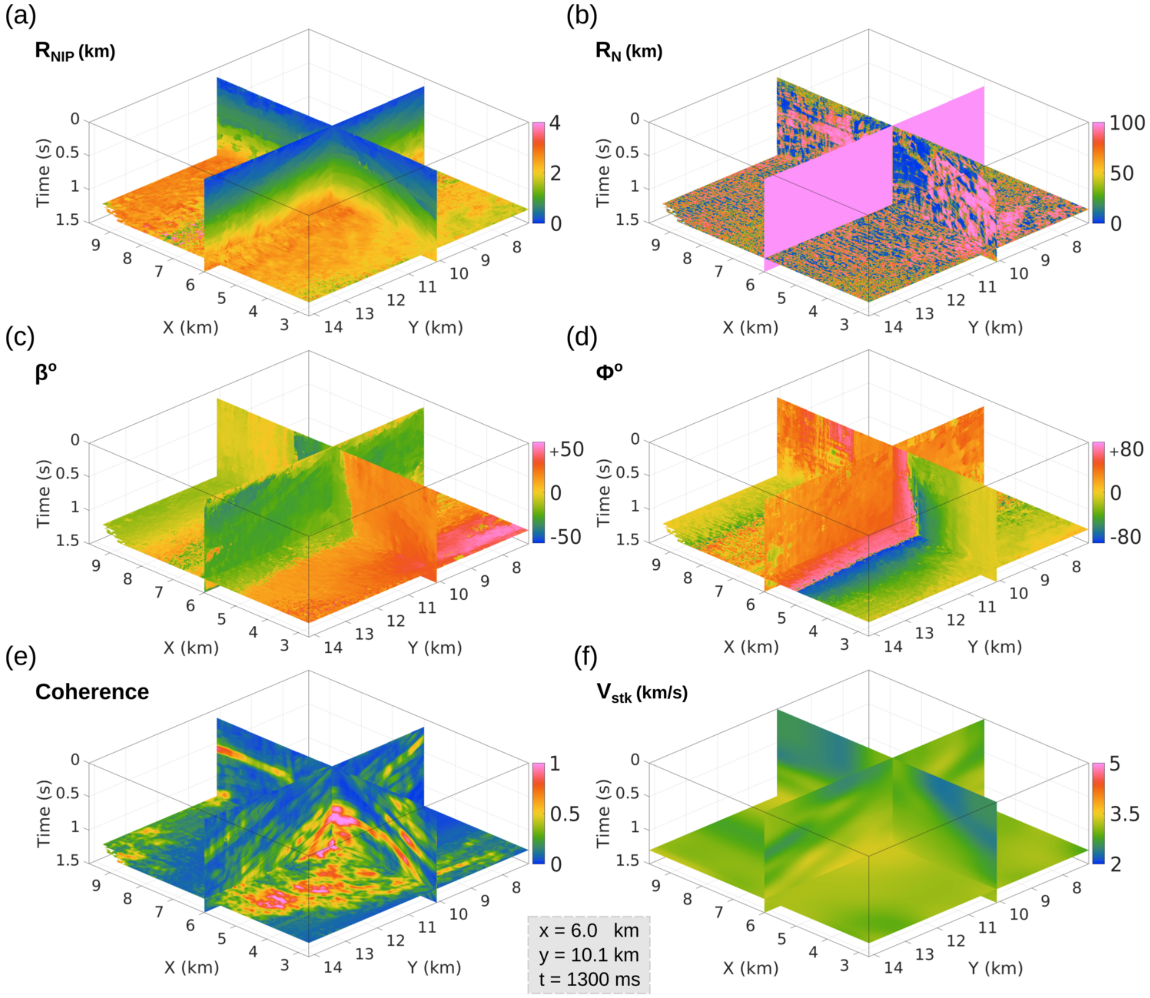

Figure 4.12: The cubes of wavefield attributes including R_{NIP} (a), R_N (b), β (c), and ϕ (d), which are estimated using the differential evolution algorithm for the 3D GSMF method. e) The coherence cube as the values of the semblance maximized in the global optimization process for searching the 3D GSMF parameters. f) The stacking velocity field used in conventional stacking, which was estimated using conventional velocity analysis. The cubes are sliced at the time of 1300 ms and along the inline and crossline located at y=10.1 km and x=6.0 km, respectively.

zontal resolutions, and increased the S/N. Also, the proposed method provided valuable wavefield attributes, which introduces great improvements for structural interpretations and many other applications.

4.9 Discussion

The 3D GSMF approach is well suited for stacking 3D seismic data to produce a true zero-offset wavefield by mapping both reflections and diffractions with high accuracy from prestack to poststack domain. We presented a closed-form solution for a spherical interface, which is valid for reflector curvatures, ranging from the diffraction limit

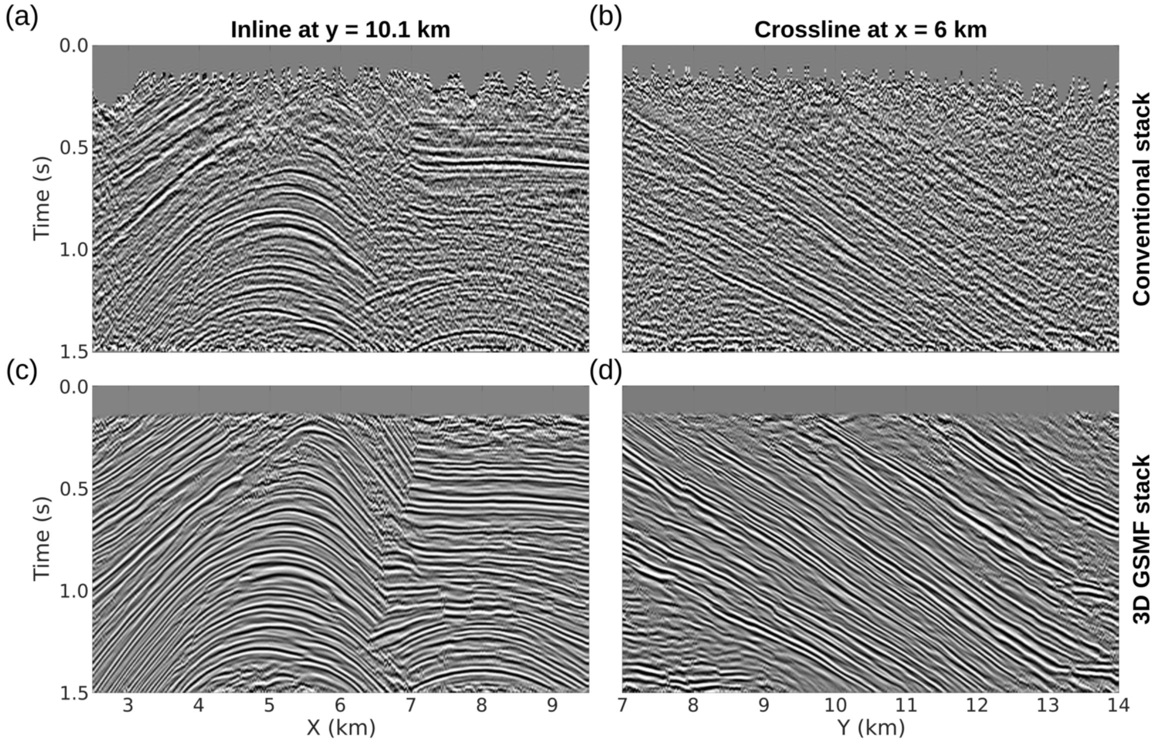

Figure 4.13: a-b) The conventional stack sections along the inline and crossline located at y=10.1 km and x=6.0 km, respectively. c-d) The 3D GSMF stack sections along the inline and crossline located at y=10.1 km and x=6.0 km, respectively.

$(R_N \rightarrow R_{NIP})$ to the planar interface $(R_N \rightarrow \infty)$, for low to relatively high heterogeneous velocities in the subsurface with smooth to rugged topography. We parameterized the formulation using two auxiliary medium mechanisms, which allows considering heterogeneity either by shifting the constant velocity of an effective overburden or by shifting the reference time in the vicinity of the reference ray in an optical domain. Shifting the reference time should accurately characterize diffractions and highly curved reflectors, while shifting the constant velocity will accurately account for background velocity heterogeneities. The proposed method can be applied directly for 3D seismic data collected over an irregular surface – where the vertical and horizontal coordinates of the sources, receivers, and imaging points can be different – without the need for prior elevation static corrections. Practically, due to fewer unknown wavefield attributes (only four) compared

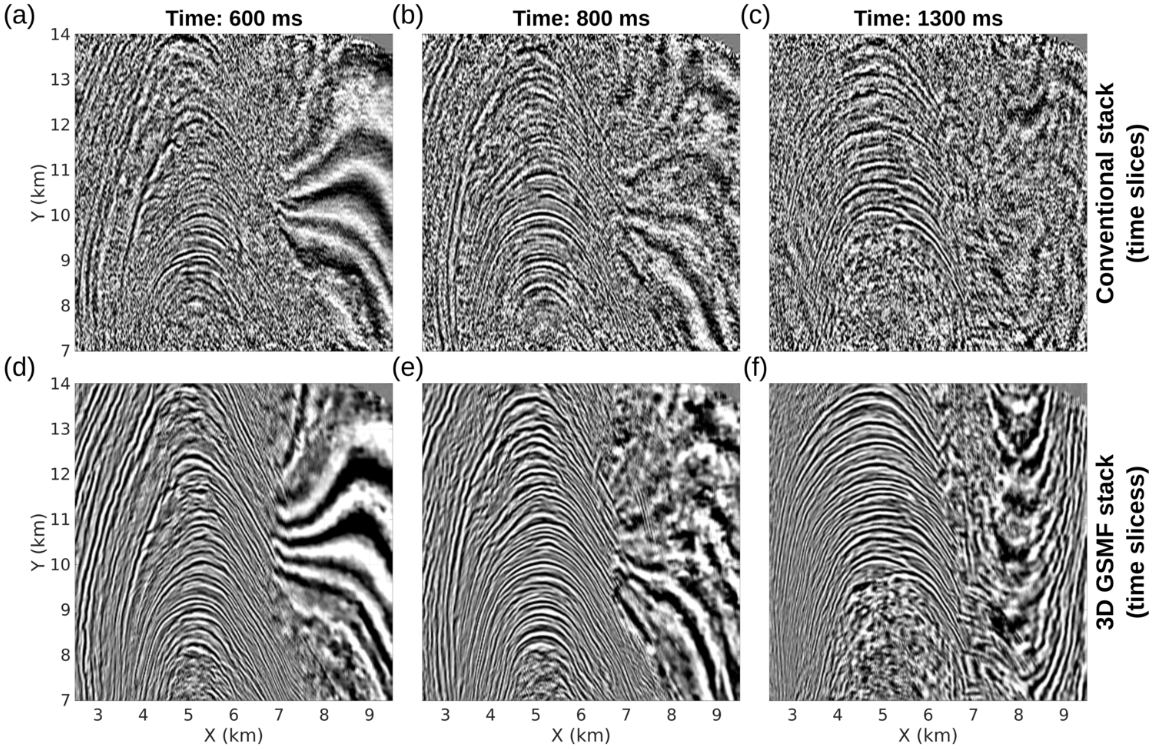

Figure 4.14: a-c) The time slices of the conventional stack cube at the times of 600, 800, and 1300 ms, respectively. d-f) The time slices of the 3D GSMF stack cube at the times of 600, 800, and 1300 ms, respectively.

to other 3D multiparameter stacking operators with eight parameters, the application of the global optimization algorithm in searching the attributes can be more stable and computationally less demanding.

Most of the 3D seismic imaging methods assume regular and adequate sampling (Biondi, 2006). However, the proposed approach can resolve the issues arising from irregular and inadequate spatial sampling of the data. Also, the application of the 3D GSMF on vertical seismic profiling (VSP) data is straightforward. 3D diffraction imaging is another useful application of the proposed method. One can produce a diffractivity volume by substituting $R_N = R_{NIP}$, which can be used for the identification of geologic discontinuities, detecting local heterogeneities, and a reliable interpretation of non-smoothed subsurface features. The estimated wavefield attribute volumes have several valuable applications. One of the main potential applications is deriving detailed dip- and azimuth-independent stacking velocity field. Also, attribute cubes could be used for prestack data enhancement and regularization. In addition to reflection traveltime and wavefield attributes, the spatial coordinates of the reflection point can be determined directly from the solutions. The reflection point coordinates and wavefield attributes provide useful information and could be a great help in structural interpretation.

Comparing the 2.5D MF with the 3D GSMF methods can help to determine which method would be suitable to use according to their accuracy, capability, and computational cost. The 2.5D multifocusing method (Jodeiri Akbari Fam and Naghizadeh, 2020; Jodeiri Akbari Fam et al., 2021a) offers 3D planar multifocusing moveout correction and 3D modeling of the wavefront. This approach assumes locally spherical wavefronts around the zero-offset central ray, which are valid for quasi-hyperbolic approximation and short to mid offsets. Hence, developing a non-hyperbolic higher-order 3D MF approach was considered. We derived a 3D multi-parameter moveout formula based on the higher-order assumption of locally circular wavefronts and by assuming an analytical reflector geometry and a constant velocity overburden. Assuming an analytical reflector geometry allows deriving moveout approximations without increasing the number of degrees of freedom (Schwarz and Gajewski, 2017). The 3D GSMF utilizes the same set of kinematic attributes used in the 2.5D multifocusing but in a different formulation, which allows more accurate moveout modeling in a large range of offsets and midpoints. The derivation was performed for a homogeneous overburden with constant velocity but can be applied to the inhomogeneous case using the concept of an auxiliary medium (Gurevich and Landa, 2002). The 3D GSMF method can achieve better results than the 2.5D MF method for highly curved reflectors beneath strong heterogeneous overburden, but it has a high computational cost. While both methods depend on four wavefield attributes, the 3D GSMF method requires solving a quartic equation. Also, irregular topographies are considered in the 3D method which makes it a more sophisticated method, while the 2.5D method can only be applied to seismic data with a flat datum.

The version more general algorithm would be to assume an elliptical reflector with arbitrary orientation and three distinct curvatures along the semi-axes. However, a sphere with a finite constant curvature can locally simulate the shape of a vast range of geometry and model their structures with relatively high accuracy in 3D space. Also, a planar reflector and a point diffractor are special cases of the sphere, and most subsurface reflectors have attributes somewhere between these two extreme cases. These are our reasons behind choosing the sphere as the subsurface reflector geometry. The 3D GSMF method can exactly determine the reflection traveltime moveout from a single-curvature curved reflector — as well as a dipping layer — under a homogeneous overburden. Also, the proposed method can accurately simulate the reflection traveltime moveout for any curved reflector that can be approximated using a single curvature.

One of the disadvantages of the closed-form implicit solution for the reflection traveltime from a circular reflector is solving a quartic equation, which makes this algorithm computationally expensive. However, it can be more accurate in the case of strongly curved layers and point diffractions compared to classic standard multifocusing methods. Approximating subsurface reflector geometry with only one curvature is the other limitation of the proposed method (only one curvature is allowed to model the subsurface reflector locally). Also, large velocity variations can deviate reflection propagation paths (the blue ray in Figure 4.1) from the plane that contains the source, receiver, and reflection point (the transparent red plane in Figure 4.1e). Then, the reflection propagation paths are no longer lied on a plane and lie on more complicated surfaces (Biondi, 2006). We assumed that the source, receiver, reflection point, and center of the sphere are coplanar. Therefore, large velocity variations might impose an error in the traveltime and the wavefield attributes estimations. In practice, this does not seem to be a problem, as illustrated by our synthetic and real examples.

Spherical multifocusing theory provides the fundamental basis for developing a moveout expression for different geometrical shapes, such as general three-dimensional ellipsoids (Landa et al., 2009). Deriving a multifocusing traveltime expression for an ellipsoid with three radii of curvature and arbitrary orientation can offer a more realistic and accurate moveout operator for a full range of three-dimensional reflector curvatures but increases the number of wavefield parameters. Computationally, the determination of the 3D GSMF parameter is more efficient than estimating more unknown parameters for general ellipsoids. Deriving a formulation of an elliptical multifocusing is underway and will be published in the near future. The elliptical multifocusing method aims to find the tangency point between two ellipsoids including an ellipsoid fitted to the source-and-receiver pair and a local ellipsoid with arbitrary orientation, size, and location fitted to the reflector.

The optical representation of the proposed method was tested on synthetic data with various curvatures ranging from low (gently curved interfaces) to high (spherical reflector or point diffractors) (see Figures 4.3 and 4.6). Also, different heterogeneities were incorporated to models. A strong vertical gradient velocity (1500-4500 m/s) was assigned to the synthetic model shown in Figure 4.3b. The presence of a high-velocity salt body with a rough body in the 3D SEG C3WA benchmark synthetic data (Figure 4.6) caused a significant velocity heterogeneity, and not only produced high-order diffractions but also made the reflections from the reflectors beneath it strongly nonhyperbolic. Numerical tests have shown that the new approximation is significantly accurate for highly curved reflectors with relatively strong heterogeneity at large offsets or at large midpoint separations. Application of the new method on the real seismic data provided a more focused zero-offset wavefield volume with improved resolution compared to the conventional results. The 3D GSMF method enabled us to obtain a 3D stacked cube and visualize the subsurface more accurately.

4.10 Conclusion

We proposed a novel multifocusing stacking method by extending the spherical multifocusing method into the most general form in three dimensions, called the 3D generalized spherical multifocusing (GSMF) algorithm. Our algorithm transforms multi-coverage prestack seismic data into a synthesized 3D zero-offset wavefield volume. The introduced method account for the elevation and spatial coordinate of all source and receiver positions, so can be applied for crooked-line/3D seismic data collected with arbitrary recording geometry from areas with irregular topography. The extended method simultaneously corrects for elevation statics, non-hyperbolic moveout associated with reflections beneath complex overburden structures, and azimuth-dependent dip-moveout effects. We evaluated the performance of the new method in the optical form on different 3D complex synthetic models generated with both 3D and crooked-line surveys. The numerical tests have demonstrated that the new formulation is significantly accurate for a range of low to relatively high heterogeneity, variations of source and receiver elevations, and a broad range of offsets and midpoint separations. Application of the proposed approach on the generic synthetic model revealed that the new stacking formula is stretch free and can accurately simulate reflections and diffractions traveltime over a vast range of curvatures – ranging from the diffraction limit ($R_N \rightarrow R_{NIP}$) to the planar interface ($R_N \rightarrow \infty$) – even for seismic data with rugged topography and from beneath a strong inhomogeneous overburden with an irregular salt body. The differences and root-mean-square errors (RMSE) of reflection surfaces estimated using the 3D GSMF method were calculated with respect to the exact traveltime simulated using the finite-difference algorithm for synthetic models. Quantitative analysis revealed that the new operator was able to simulate the wavefield with high accuracy (with mean RMSEs of 0.0025 s and 0.0042 s for the crooked-line and 3D surveys, respectively) and accurately corrected the source-receiver elevation statics, normal, and dip moveout effects simultaneously (not sequentially). In the example of a super common-cell gather produced for the 3D SEG C3WA benchmark model, the reflections were aligned across all of the near and far offsets and midpoint separations, and the flatness and temporal location of events in the corrected gather showed the effectiveness of the proposed method. Application of the 3D GSMF method on the 3D low-fold seismic data acquired over a complex trust-belt area with rugged topography and noisy data environment yielded a high-resolution and more focused zero-wavefield stacked volume compared to the conventional 3D stacking method. Also, the experiments demonstrated that the new formulation was accurate for surveys that varied in elevation by 400 and 450 m in the synthetic examples and 144 m in the field example. The estimated attribute volumes were used for visualizing the subsurface quantitatively and for structural interpretation. The attributes panel clearly showed an anticline structure and determined the curvatures and dips of reflections. Compared to the conventional processing, the proposed approach significantly improved the quality of the 3D stacked volume with enhanced S/N and more coherent reflections (particularly in shallow zones).

4.11 Acknowledgements

This research was funded by the NSERC Canada First Research Excellence Fund (MERC-ME-2022-00). GeoThrust software was used for 2D and 3D seismic data processing. We acknowledge GeoTomo for providing an academic license. We appreciate Dr. Benjamin Schwartz and Dr. Ivan Abakumov for constructive discussions. SOFI3D open-source software was used to produce seismic synthetic data sets using the finite differences method. We thank Thomas Bohlen, Denise De Nil, Daniel Köhn, and Stefan Jetschny for developing the SOFI3D code. The authors would like to acknowledge the comments provided by all editors, for their very insightful comments on the manuscript. This work was enabled in part by the facilities of the Shared Hierarchical Academic Research Computing Network (SHARCNET:www.sharcnet.ca) and Compute/Calcul Canada (www.computecanada.ca).

Appendix 4-A: Traveltime on a circular/spherical reflector

The analysis of reflection phenomena on a circular reflector has been discussed in several disciplines such as Alhazens problem in mathematics, collision detection in robotics, reflection from a spherical mirror in geometrical optics, and the circular billiard problem. A fourth-order algebraic equation has been derived to model reflection from a circular reflector (Neumann, 1998; Drexler and Gander, 1998). Analytical solutions of the equation are also provided that generally include four complex responses. We presented an implicit formulation for 3D generalized spherical multifocusing which is based on the closed-form solution to the 2D reflection problem. Simply, we derive the proposed 3D method based on the solution for finding the tangency point of an ellipse and a circle.

Consider the ray geometry for the 2D reflection problem from the source $s = [-h, 0]$ to the receiver $g = [+h, 0]$ with the half-offset h and in a constant velocity v_0. The equation of the fitted ellipse to the source-receiver pair as the focal points is given by

$$\mathcal{E} = \sqrt{(x - x_s)^2 + (z - z_s)^2} + \sqrt{(x - x_g)^2 + (z - z_g)^2} - v_0 t \rightarrow$$

$$\mathcal{E} = \sqrt{(x + h)^2 + z^2} + \sqrt{(x - h)^2 + z^2} - v_0 t. \tag{4-A.1}$$

The circular reflector with the center of $c = [x_c, x_z]$ and radius of r_c can be expressed by

$$\mathcal{C} = (x - x_c)^2 + (z - z_c)^2 - r_c^2. \tag{4-A.2}$$

The tangency condition in Euclidean space is expressed as follows (Zill et al., 2011);

$$||\nabla\mathcal{E}\times\nabla\mathcal{C}||_2 = ||det(\begin{bmatrix} i & k \\ \partial\mathcal{E}/\partial x & \partial\mathcal{E}/\partial z \\ \partial\mathcal{C}/\partial x & \partial\mathcal{C}/\partial z \end{bmatrix})||_2 = 0, \tag{4-A.3}$$

where $\nabla = \partial/\partial x + \partial/\partial z$. The equation 4-A.3 indicates that the ellipsoid and the sphere are tangent to each other if their gradients are parallel, in other words, the L2-norm of their cross product needs to be equal to zero. The traveltime (t) can be determined by inserting partial derivations of 4-A.1 and 4-A.2 into 4-A.3:

$$t = \frac{2}{v_0}\sqrt{\frac{h^2\ x\ (z_c - z)}{z_c\ x - x_c\ z}}. \tag{4-A.4}$$

The circle can be expressed in the parametric form by $x = x_c + r_c \cos\theta$ and $z = z_c + r_c \sin\theta$. Substituting $\theta = 2\arctan u \rightarrow u = \tan\theta/2$, $\sin\theta = \frac{2\tan\theta/2}{1+\tan^2\theta/2}$, and $\cos\theta = \frac{1-\tan^2\theta/2}{1+\tan^2\theta/2}$ gives:

$$x = x_c + r_c\ \frac{1-u^2}{1+u^2},\quad z = z_c + r_c\ \frac{2\ u}{1+u^2}. \tag{4-A.5}$$

Inserting 4-A.4 and 4-A.5 in 4-A.1 lead to

$$\frac{Q(u)}{2\ h^2\ u(u-1)(u+1)} = 0, \tag{4-A.6}$$

where

$$\begin{aligned}
&Q(u) = b_4\ u^4 + b_3\ u^3 + b_2\ u^2 + b_1\ u^1 + b_0 = 0,\\
&b_0 = z_c\ (x_c + r_c),\\
&b_1 = 2\ h^2 - 2\ {x_c}^2 + 2\ {z_c}^2 - 2\ r_c\ x_c,\\
&b_2 = -6\ x_c\ z_c,\\
&b_3 = -2\ h^2 + 2\ {x_c}^2 - 2\ {z_c}^2 - 2\ r_c\ x_c,\\
&b_4 = z_c\ (x_c - r_c),
\end{aligned}$$

In 4-A.6, $u = 0$ and $u = \pm 1$ correspond to a vertical and a horizontal tangents and are only possible when $z_c = 0$ and $x_c = 0$, respectively. Hence, solving $Q(u)$ can provide all solutions to 4-A.6. By substituting the solutions in 4-A.5 the reflection point can be determined. Then, substituting the reflection point coordinate in 4-A.4 gives the reflection traveltime t.

Chapter 5

Concluding statements

5.1 Summary and Conclusions

Three-dimensional (3D) seismic surveys can: 1) provide reliable and accurate subsurface images of complex 3D structures; 2) focus seismic energy at the correct location; and 3) reduce spatial aliasing. However, low fold coverage reduces the resolution of the resulting images. Two-dimensional (2D) seismic surveys can lead to a high-resolution image if the geology is also 2D and the traverse is perpendicular to strike but often this is not the case. Furthermore, the surveys are also conducted along a crooked line traverse due to poor access in rugged terrains, logistical reasons, and environmental restrictions. The crookedness of line traverses, irregular topography, and complex subsurface geology with steeply dipping and curved interfaces could adversely affect the signal-to-noise ratio (S/N) of the data. The crooked-line geometry violates the assumption of a straight-line survey that is a basic principle behind the 2D multifocusing (MF) method and leads to crossline spread of midpoints. Additionally, the crooked-line geometry can give rise to potential pitfalls and artifacts such as deformation of reflections and considerable time- and offset-variant time shifts. All these factors lead to difficulties in imaging and velocity-depth model estimation.

I introduced two methods that can generate a stacked section that is equivalent to a synthesized zero-offset wavefield for crooked-line/3D seismic data with arbitrary recording geometry from areas with a complicated near-surface and a complex subsurface. The traveltime equation in these methods achieves better signal alignment before stacking for transforming multicoverage prestack data into an accurate poststack zero-offset wavefield. The first method uses a 2.5D multifocusing (2.5D MF) reflection traveltime equation, which explicitly takes into account the midpoint dispersion and crossdip effects. The 2.5D MF formulation is based on an extension of the planar MF method into three dimensions with a flat datum. This method does not consider the variation of source and receiver elevations, and the recording surface is assumed to be flat. The new formulation simultaneously corrects for 3D normal and azimuth-dependent dip moveouts (or inline and crossline dip moveouts in the context of crooked-line seismic data processing). A simultaneous correction is significantly more accurate than removing these effects sequentially. The method is accurate for quasi-hyperbolic reflections and its capability is limited in resolving non-hyperbolic diffractions and reflections. The second method is a three-dimensional generalized spherical multifocusing (3D GSMF) algorithm, which is based on a 3D extension of the spherical MF method into the most general form with irregular topography. I developed a non-hyperbolic higher-order moveout operator with a closed-form implicit formulation that can be applied to seismic data with arbitrary spatial coordinates of sources and receivers. The second method simultaneously corrects for elevation statics, non-hyperbolic moveout associated with reflections beneath complex overburden structures, and azimuth-dependent dip-moveout effects. The algorithms can accurately extract 3D structural information and remove anomalous dip-dependent velocities, which enable us to produce more accurate and high-resolution seismic images. This would allow for maximally resolved data-driven reconstructions of the complex subsurface structure. Both proposed methods can be applied to generate either a 2D stacked section along the crooked traverse or a 3D stacked volume. The resulting stacked seismic section can then be time- or depth-migrated using a 2D/3D zero-offset migration algorithm to obtain the 2D/3D subsurface image.

The developed kinematic expressions of the traveltime stacking surface for each proposed method depend on a set of four unknown parameters measured at each image point and time location. The main practical problem of the multifocusing implementation is the simultaneous determination of the optimal wavefield parameters. Determining global optimal parameters is a crucial step, particularly for complex structures and low-fold data. Wavefield analysis is required to estimate the wavefield attributes, which is a nonlinear multi-dimensional global optimization problem. Searching optimal attributes can be performed automatically using a multidimensional nonlinear global optimization method based on a coherency objective function. I incorporated a numerical approach by adapting the very fast simulated annealing (VFSA) and differential evolution (DE) algorithms to estimate optimal attributes and improve the accuracy and resolution of the generated results. The convergence behavior, computational cost, and accuracy of both optimization algorithms were evaluated on synthetic data for searching for the optimal solution of the wavefield attributes. The stacking velocity field derived from conventional stacking velocity analysis is used to determine the lower and upper bound constraints of the search range for the radius of curvature of normal incidence point wave (R_{NIP}). The results showed that the both algorithms are well-suited to determine the wavefield attributes within a reasonable number of iterations. The use of the stacking velocity field as a priori information to constrain for R_{NIP} leads to noticeable improvements in the estimation of the wavefront parameters and speeds up the convergence. Comparing the effectiveness and efficiency of both optimization methods demonstrates that the VFSA method is computationally cost-effective, however, the DE algorithm is more accurate than the VFSA algorithm. The DE can find optimal parameters with good precision and accuracy, and fine-tuning the parameters for DE algorithms can reduce the running time. The VFSA method can reach the global maximum faster than DE, but it is accompanied by uncertainty.

I investigated the accuracy of the 2.5D MF formulation by testing it on different 3D synthetic models containing various 3D dipping and curved interfaces and heterogeneous overburdens with crooked-line surveys. Numerical tests show that the 2.5D MF traveltime formula yields more accurate time shifts and better-flattened stretch-free reflections before stacking and can accurately focus the primary reflections at their poststack correct locations. The results showed that the 2.5D MF method extracts structural information with good accuracy even for layers with dips over 40°.

Also, I tested the 2.5D MF method on two real data sets with crooked-line surveys. Applying the proposed approach to one 2D crooked-line data set collected in a thrust-belt area with subsurface complexity led to a high-resolution seismic stacked section with a significant quality improvement compared to the conventional methods. The generalized cross dip moveout analysis and conventional normal moveout stacking algorithm were both applied to generate conventional stacked sections for comparison purposes. Steeply dipping reflections were better focused and were mapped with high clarity compared to the conventional methods. Also, this algorithm brought new reflections into focus that did not appear in the conventional results. The 2.5D MF method enhanced the vertical resolution and S/N of the stack section compared to both conventional stacking algorithms.

I also presented the application of the 2.5D MF method on the Larder-Lake crooked 2D seismic reflection transect, which was acquired over a crystalline geological environment in the Superior Craton of Canada. I compared the Kirchhoff time migrated image of the 2.5D MF stack with the 2D phase-shift time migration of dip moveout corrected stack, 2D prestack Kirchhoff time migration, and the swath 3D poststack migration. Compared to the results of other methods mentioned above, applying the 2.5D MF stacking algorithm improved the quality of the structural stack considerably and yield a more reliable subsurface section with a high resolution. The 3D swath processing could not image steeply dipping reflections correctly, however, it delineated the extension of some of the subhorizontal reflections, particularly in the Larder Lake structural basin. The 2.5D MF method mapped the prominent steeply dipping reflection packages more coherently. In addition to the main feature, the 2.5D MF method focused new reflections with a high S/N, which were not constructed by the 2D DMO stack and 2D prestack migration workflows. Furthermore, the proposed method accurately extracted 3D structural information including inline and crossline dips. This study clarified that the 2.5D multifocusing method can be an effective alternative to the 2D conventional stacking (NMO+DMO+CDMO) and 2D prestack migration methods in processing crooked surveys. The swath 3D imaging result convinced us to test the 2.5D MF or 3D GSMF approach to produce a volumetric stack in further research.

I evaluated the performance of the 3D GSMF method parameterized in optical auxiliary medium on different 3D complex synthetic models generated with both 3D and crooked-line surveys. The numerical tests demonstrated that the new formulation is accurate for a range of low to relatively high heterogeneity, variations of source and receiver elevations, and a broad range of offsets and midpoint separations. Quantitative analysis revealed that the new operator was able to simulate the wavefield with high accuracy (with mean RMS errors of 2.5 and 4.2 ms for the crooked-line and 3D synthetic surveys, respectively) and accurately corrected the source-receiver elevation statics, normal, and dip moveout effects simultaneously (not sequentially). Application of the proposed approach on the 3D SEG C3WA benchmark synthetic velocity model depicted that the new stacking formula is stretch free. In this example, the reflections were aligned across all of the near and far offsets and midpoint separations, and the flatness and temporal location of events in the corrected gather showed the effectiveness of the proposed method. The result also showed that the proposed method can accurately simulate reflections and diffractions traveltime over a vast range of curvatures – ranging from the diffraction limit ($R_N \rightarrow R_{NIP}$) to the planar interface ($R_N \rightarrow \infty$) – even for seismic data with rugged topography and from beneath a strong inhomogeneous overburden with an irregular salt body. The differences and RMS errors of reflection surfaces estimated using the 3D GSMF method were calculated with respect to the exact traveltime simulated using the finite-difference algorithm for synthetic models.

Application of the 3D GSMF method on the 3D low-fold seismic data acquired over a complex trust-belt area with rugged topography and a noisy data environment yielded a high-resolution and more focused zero-wavefield stacked volume compared to the conventional 3D stacking method. Also, the experiments demonstrated that the new formulation was accurate for surveys that varied in elevation by 450 m in the synthetic examples and 144 m in the field example. The estimated attribute volumes were used for visualizing the subsurface and for structural interpretation. Compared to the conventional processing, the proposed approach significantly improved the quality of the 3D stacked volume with enhanced S/N and more coherent reflections (particularly in shallow zones).

Comparing the application of the two newly developed methods on crooked-line synthetic seismic data from a single sphere reflector showed that the 3D GSMF operator simulated the reflection traveltime surface almost two times better than the 2.5D MF formula (with

RMS errors of 1.0 and 1.97 ms for the 3D GSMF and 2.5D MF methods, respectively), even in the presence of a severe elevation variation. The reason behind this can be attributed to the fact that the 2.5D MF formula is derived for a locally planar interface and is a quasi-hyperbolic moveout operator, whereas the 3D GSMF is developed for a locally spherical reflector and is a non-hyperbolic operator.

Comparing the 2.5D MF with the 3D GSMF methods can help to determine which method would be suitable to use according to their accuracy, applicability, and computational cost. The 2.5D multifocusing method (Jodeiri Akbari Fam and Naghizadeh, 2020; Jodeiri Akbari Fam et al., 2021a) offers 3D planar multifocusing moveout correction and 3D modeling of the wavefront. This approach assumes a locally spherical wavefront around the zero-offset central ray, which is valid for a quasi-hyperbolic approximation and short to mid offsets. The 3D multi-parameter moveout formula is based on the higher-order assumption of locally circular wavefronts and is assuming an analytical reflector geometry and a constant velocity overburden. Assuming an analytical reflector geometry allows deriving moveout approximations without increasing the number of degrees of freedom. The 3D GSMF utilizes the same set of kinematic attributes that are used in the 2.5D multifocusing but in a different formulation, which allows more accurate moveout modeling in a large range of offsets and midpoints. The 3D GSMF method can achieve better results than the 2.5D MF method for highly curved reflectors beneath strong heterogeneous overburden, but it has a high computational cost. While both methods depend on four wavefield attributes, the 3D GSMF method requires solving a quartic equation. Also, irregular topographies are considered in the 3D method which makes it a more sophisticated method, while the 2.5D method can only be applied to seismic data after elevation statics corrections and reference data to a flat datum.

The Larder Lake transect mostly includes planar dipping interfaces, where both 2.5D

MF and 3D GSMF methods might lead to similar results, except to the part beneath a strong heterogeneous overburden and the near-surface that includes tight folding. Hence, testing the 3D GSMF algorithm on Larder Lake data would not be a suitable case study to examine its performance and show the strength of the proposed method. Also, the application of the 3D GSMF method on crooked-line seismic data to generate a 2D stacked section or a 3D stacked volume can be considered its secondary application. Therefore, we first attempted to test the 3D GSMF method on the 3D data set, rather than crooked-line seismic data, to realize the main potential application of the proposed method.

Generally, our research on multifocusing made noticeable improvements in imaging complex structures. We opened new horizons in the processing of crooked seismic lines by developing new theoretical methods for applying 2.5D and 3D multifocusing methods, which can be considered as innovative contributions of the current thesis. The new theoretical frameworks could address the longstanding challenges in the processing of crooked-line seismic data acquired in hard-rock environments. The proposed methods can be utilized to generate a very detailed and high-resolution stacked section with a high signal-to-noise ratio for comprehensive interpretation of seismic data acquired by a survey using a crooked line or a sparse irregular 3D seismic survey from a geologically complex area with rugged topography and heterogeneous overburden. Developing the advanced multifocusing seismic stacking package aims to use the potential of the new, robust, and coherent MF algorithms efficiently in generating high-resolution seismic sections from Metal Earths data making the section easier to interpret and less ambiguous.

5.2 Future works

The current research focused on deriving mathematical concepts, developing the theoretical background, and testing the performance of the introduced algorithms on challenging seismic data sets. Future work should focus on exploiting the potential of multifocusing algorithms to maximally resolve data-driven reconstructions of the solid earth. The 2.5D MF method can be applied to 2D crooked-line or 3D seismic data to produce a 3D stacked volume. The 3D GSMF method can be used to produce 2D straight/slalom stacked sections from 2D crooked-line seismic data. These can be other important applications of proposed methods that are required to be tested in the future. A possible future work is applying the 2.5D MF and 3D GSMF methods to Larder Lake or other Metal Earth crooked-line traverses to produce 3D stacked volume.

I suggest examining the performance of reflection-based elevation statics corrections applied by the 3D GSMF method on the seismic data with severe horizontal heterogeneity. In addition to generating a high-resolution zero-offset wavefield, the proposed methods have a wide range of applications in further imaging processes and quantitative structural interpretation. For instance, wavefield attributes can be used for multiple attenuations and wavefield separation of converted waves. The input seismic data for prestack migration requires to be regularly sampled spatially and enhanced. As another application, the noisy prestack super common-midpoint gathers with non-hyperbolic reflections and irregular acquisitions can be moveout corrected, enhanced, and regularized using the proposed formulations. As future research, we could work on adapting the 3D GSMF method to generate 3D diffraction volume, which would be crucial for prospecting geological discontinuities, local heterogeneities of mineral deposits, and networks of fractures in reservoirs. Furthermore, the introduced methods can be modified to improve images obtained using vertical seismic profiling. The 3D GSMF method can be also adapted to localize passive seismic events in earthquake seismology by deriving a dual formulation expressed in the time- and velocity-shifted auxiliary media for the moveout of a point diffractor in the shot gather.

In addition to the applications mentioned above, the generalized spherical multifocusing theory importantly provides the fundamental basis for developing a moveout expression for different geometrical shapes, such as general three-dimensional ellipsoids. A more general algorithm would assume an elliptical reflector with arbitrary orientation and three distinct curvatures along the semi-axes. Deriving a multifocusing traveltime expression for an ellipsoid with three radii of curvature and arbitrary orientation can offer a more realistic and accurate moveout operator for a full range of three-dimensional reflector curvatures but increases the number of wavefield parameters, which in turn increases the computational cost and might reduce the accuracy of simultaneous estimation of optimal parameters. Deriving a formulation of an elliptical multifocusing is underway and will be published in the near future.

5.3 Summary of the key achievements

5.3.1 Peer-reviewed journal publications and under review manuscripts

A research paper was published and two manuscripts were submited in international Q1 and Q2 academic journals as follows:

- Jodeiri, H., Naghizadeh, M., and Ö. Yilmaz, 2021, 2.5D multifocusing imaging of crooked-line seismic surveys: Geophysics, 86, no. 6, 1–67, doi: 10.1190/geo2020-0660.1.

- This article was nominated by the Geophysics editors and highlighted in ”Geophysics Bright Spots” in The Leading Edge, 41, no. 1, 62.

- Jodeiri, H., Naghizadeh, M., and Ö. Yilmaz, 3D generalized spherical multifocusing seismic imaging: Geophysics. (**Under review**)

- Jodeiri, H., Naghizadeh, M., and Ö. Yilmaz, High-resolution 2.5D multifocusing imaging of crooked seismic profile in a crystalline rock environment: results from the Larder Lake area, Ontario, Canada: Geophysical prospecting. (**Under review**)

5.3.2 Conference publications

- Jodeiri, H., Naghizadeh, M., and Ö. Yilmaz, 2021, Application of 2.5D multifocusing seismic imaging in a crystalline rock environment: Results from Larder Lake area, Ontario, Canada: First International Meeting for Applied Geoscience & Energy, Extended Abstracts, 2639–2643, doi: 10.1190/segam2021-3594582.1.

- Jodeiri, H. and M. Naghizadeh, 2020, 2.5D multi-focusing imaging of crooked-line seismic surveys: 82nd Conference and Exhibition, EAGE, Extended Abstracts, 1–5, doi: 10.3997/2214-4609.202011662.

- Jodeiri, H. and M. Naghizadeh, 2020, High-resolution multi-focusing seismic imaging of Metal Earth’s Larder Lake transect: Prospectors & Developers Association of Canada International Convention.

- Jodeiri, H. and M. Naghizadeh, 2019, Multi-focusing stacking using the very fast simulated annealing global optimization algorithm: GeoConvention, Extended Abstracts.

- Jodeiri, H. and M. Naghizadeh, 2019, Multi-Focusing stacking technique: A robust method of improving subsurface seismic imaging: Prospectors & Developers Association of Canada International Convention.

5.3.3 Developed software packages

The code packages that were developed in *Matlab* and using C and C++ in Seismic Unix software framework are listed as follows:

- 3D GSMF stacking and wavefield analysis using differential evolution algorithm
- 2.5D MF stacking and wavefield analysis using differential evolution and simulated annealing algorithms
- 2D MF stacking and wavefield analysis using differential evolution algorithm
- 3D and crooked-line seismic data binning
- Super common-midpoint/common-cell gather enhancement by removing nonhyperbolicity of reflections and partial stacking using new formulations
- 2D/3D synthetic velocity model building and crooked-line/2D/3D survey designing pack for generating synthetic seismic data using finite difference algorithm

For efficient implementation of the proposed processing flows, the packaged C and C++ codes were executed and parallelized using a serial farming technique by Shell scripting.

5.3.4 Funding statement

My Ph.D. research proposal was supported by NSERC Canada First Research Excellence Fund through the Metal Earth project. In addition, several other sources in Canada and the United States were awarded to my developmental work such as the Society of Exploration Geophysics (SEG) Scholarships and Ontario Graduate Scholarship, which is jointly funded by the Ontario Government and Laurentian University. The list of granted scholarships are as follows:

- SEG/Chevron scholarship by Society of Exploration Geophysics award in 2021,
- SEG scholarship by Society of Exploration Geophysics award in 2020,
- Ontario Graduate Scholarship jointly by the Government of Ontario and Laurentian University in 2020,
- Summer fellowship by Laurentian University in 2020,
- Trillium Foundation scholarship by Parya in 2020,
- SEG scholarship by Society of Exploration Geophysics award in 2019,
- CSEG scholarship by Canadian Society of Exploration Geophysics foundation award in 2018,
- Differential tuition fee waiver scholarship for international students by Laurentian University, 2018 – 2022.

Bibliography

Abakumov, I. (2016). *Systematic analysis of double-square-root-based stacking operators.* PhD thesis, University of Hamburg.

Ahmadi, O., Juhlin, C., Ask, M., and Lund, B. (2015). Revealing the deeper structure of the end-glacial parvie fault system in northern Sweden by seismic reflection profiling. *Solid Earth*, 6(2):621–632.

Ahmed, K. A., Schwarz, B., and Gajewski, D. (2015). Application of the 3D common-reflection-surface stack workflow in a crystalline rock environment. *Geophysical Prospecting*, 63(Hard Rock Seismic imaging):990–998.

Al-Saleh, S., Margrave, G., and Gray, S. (2009). Direct downward continuation from topography using explicit wavefield extrapolation. *Geophysics*, 74(6):S105–S112.

Alkhalifah, T. and Tsvankin, I. (1995). Velocity analysis for transversely isotropic media. *Geophysics*, 60(5):1550–1566.

Aminzadeh, F., Jean, B., and Kunz, T. (1997). *3D salt and overthrust models.* Society of Exploration Geophysicists.

Ayer, J. A., Amelin, Y., Corfu, F., Kamo, S., Ketchum, J., Kwok, K., and Trowell, N. (2002). Evolution of the southern Abitibi greenstone belt based on U–Pb geochronology: autochthonous volcanic construction followed by plutonism, regional deformation and sedimentation. *Precambrian Research*, 115(1):63–95.

Ayer, J. A., Thurston, P. C., Bateman, R., Dub, B., Gibson, H. L., Hamilton, M. A., Hathway, B., Hocker, S. M., Houl, M. G., Hudak, G., Ispolatov, V. O., Lafrance, B., Lesher, C. M., MacDonald, P. J., Ploquin, A. S., Piercey, S. J., Reed, L. E., and Thompson, P. H. (2005). *Overview of results from the Greenstone Architecture Project: Discover Abitibi Initiative*. Ontario Geological Survey.

Bécel, A., Shillington, D. J., Nedimović, M. R., Webb, S. C., and Kuehn, H. (2015). Origin of dipping structures in fast-spreading oceanic lower crust offshore Alaska imaged by multichannel seismic data. *Earth and Planetary Science Letters*, 424:26–37.

Beckel, R. A. and Juhlin, C. (2019). The cross-dip correction as a tool to improve imaging of crooked-line seismic data: a case study from the post-glacial Burtrask fault, Sweden. *Solid Earth*, 10(2):581–598.

Belfer, I., Berkovitch, A., and Sydykov, K. (2008a). Multifocusing: A new method of multifold seismic data processing. *CSEG Recorder April*, pages 30–32.

Belfer, I., Nekrasova, L., Nevidimova, A., Korabelnikov, A., Kulikova, A., and Berkovitch, A. (2008b). A revised interpretation of the Russkoye field, Western Siberia, using multifocusing technology. *first break*, 26(4).

Bergler, S., Hubral, P., Marchetti, P., Cristini, A., and Cardone, G. (2002). 3D common-reflection-surface stack and kinematic wavefield attributes. *The Leading Edge*, 21(10):1010–1015.

Berkovitch, A., Belfer, I., Hassin, Y., and Landa, E. (2009). Diffraction imaging by multifocusing. *Geophysics*, 74(6):WCA75–WCA81.

Berkovitch, A., Belfer, I., and Landa, E. (2008). Multifocusing as a method of improving subsurface imaging. *The Leading Edge*, 27(2):250–256.

Berkovitch, A., Deev, K., and Landa, E. (2011). How non-hyperbolic multifocusing improves depth imaging. *First Break*, 29(9):103–111.

Berkovitch, A., Deev, K., and Landa, E. (2012a). Multifocusing-based multiple attenuation. *The Leading Edge*, 31(10):1146–1154.

Berkovitch, A., Deev, K., Rauch-Davies, M., and Landa, E. (2012b). Non-hyperbolic multifocusing improves depth imaging. In *11th Simposio Bolivariano-Exploracion Petrolera en las Cuencas Subandinas*, pages CP–330. European Association of Geoscientists & Engineers.

Berkovitch, A., Eppelbaum, L., Scharff, N., and Guberman, E. (2004). Integration of advanced seismic multifocusing technology with potential field analysis. *66th Conference and Exhibition, EAGE, Extended Abstracts.*

Berkovitch, A., Gelchinsky, B., and Keydar, S. (1994). Basic formulae for multifocusing stack. In *56th EAEG Meeting*, pages CP–47. European Association of Geoscientists & Engineers.

Berkovitch, A., Keydar, S., Landa, E., and Trachtman, P. (1998). Multifocusing in practice. In *SEG Technical Program Expanded Abstracts 1998*, pages 1748–1751. Society of Exploration Geophysicists.

Berryhill, J. R. (1984). Wave-equation datuming before stack. In *SEG Technical Program Expanded Abstracts 1984*, pages 397–399. Society of Exploration Geophysicists.

Biondi, B. L. (2006). *3D seismic imaging.* Society of Exploration Geophysicists.

Biscani, F. and Izzo, D. (2020). A parallel global multiobjective framework for optimization: pagmo. *Journal of Open Source Software*, 5(53):2338.

Bohlen, T. (2002). Parallel 3D viscoelastic finite difference seismic modelling. *Computers & Geosciences*, 28(8):887–899.

Borghi, P., Curia, D., Alayón, M., Veeken, P., Lescano, I., and Justo, D. (2017). Sierra de Reyes 3D seismic survey (onshore Argentina): depth imaging complex geology by applying multi-focusing, kirchhoff, beam and RTM workflows. *First Break*, 35(12):67–76.

Bräunig, L., Buske, S., Malehmir, A., Bäckström, E., Schön, M., and Marsden, P. (2020). Seismic depth imaging of iron-oxide deposits and their host rocks in the Ludvika mining area of central Sweden. *Geophysical Prospecting*, 68(1-Cost-Effective and Innovative Mineral Exploration Solutions):24–43.

Burnside, W. S. and Panton, A. W. (1892). *The theory of equations: with an introduction to the theory of binary algebraic forms*. Hodges, Figgis.

Buzlukov, V. and Landa, E. (2013). Imaging improvement by prestack signal enhancement. *Geophysical Prospecting*, 61(6):1150–1158.

Castle, R. J. (1994). A theory of normal moveout. *Geophysics*, 59(6):983–999.

Causse, E. (2002). Seismic traveltime approximations with high accuracy at all offsets. In *64th EAGE Conference & Exhibition*, pages CP–5. European Association of Geoscientists & Engineers.

Causse, E., Haugen, G. U., and Rommel, B. E. (2001). Large-offset approximation to seismic reflection traveltimes. *Geophysical Prospecting*, 48(4):763–778.

Červenỳ, V., Klimeš, L., and Pšenčík, I. (1984). Paraxial ray approximations in the computation of seismic wavefields in inhomogeneous media. *Geophysical Journal International*, 79(1):89–104.

Chang, D., Hu, T., and Zhang, C. (2019a). Application of spherical multifocusing technology for multiple attenuation on irregular topography. In *The 13th SEGJ International Symposium, Tokyo, Japan, 12-14 November 2018*, pages 100–103. Society of Exploration Geophysicists and Society of Exploration.

Chang, D., Zhang, C., Hu, T., and Wang, D. (2019b). Spherical multifocusing method for irregular topography. *Geophysics*, 84(4):V233–V243.

Cheraghi, S., Malehmir, A., and Bellefleur, G. (2012). 3D imaging challenges in steeply dipping mining structures: New lights on acquisition geometry and processing from the Brunswick no. 6 seismic data, Canada. *Geophysics*, 77(5):WC109–WC122.

Cheraghi, S., Naghizadeh, M., Snyder, D., Haugaard, R., and Gemmell, T. (2020). High-resolution seismic imaging of crooked two-dimensional profiles in greenstone belts of the Canadian shield: results from the Swayze area, Ontario, Canada. *Geophysical Prospecting*, 68(1-Cost-Effective and Innovative Mineral Exploration Solutions):62–81.

Curia, D., Borghi, P., Noble, J., Berkovitch, A., Justo, D., and Alayón, M. (2017). The impact of multifocusing in the processing of land 3D seismic data in a fold and thrust belt setting: Ranquil Norte Block, Neuquén Basin, Argentina. *The Leading Edge*, 36(9):770–774.

Curia, D., Veeken, P., Zunino, J., Deev, K., and Pelman, D. (2012). Multifocusing seismic processing to improve poor response areas below basalt layers, Canadon Asfalto basin, Argentina. *74th Conference and Exhibition, EAGE incorporating EUROPEC, Extended Abstracts*, pages CP–293.

Dai, N. and Cheadle, S. (1995). Two-parameter NMO processes from surface. *GeoConvention Conference, Calgary, Canada*, pages 135–136.

Davies, R. J., Stewart, S. A., Cartwright, J. A., Lappin, M., Johnston, R., Fraser, S. I., and Brown, A. R. (2004). 3D seismic technology: are we realising its full potential? *Geological Society, London, Memoirs*, 29(1):1–10.

De Bazelaire, E. (1988). Normal moveout revisited: Inhomogeneous media and curved interfaces. *Geophysics*, 53(2):143–157.

Dörrie, H. (2013). *100 great problems of elementary mathematics*. Courier Corporation.

Drexler, M. and Gander, M. J. (1998). Circular billiard. *SIAM review*, 40(2):315–323.

Du Bois, L., Levato, L., Besnard, J., Escher, A., Marchant, R., Olivier, R., Ouwehand, M., Sellami, S., Steck, A., and Wagner, J. (1990). Pseudo-3D study using crooked line processing from the Swiss Alpine Western profileline 2 (Val D'Anniviers-Valais). *Tectonophysics*, 173(1-4):31–42.

Eaton, D., Milkereit, B., Adam, E., and Gubins, A. (1997). 3D seismic exploration. In *Proceedings of Exploration*, volume 97, pages 65–78.

Elhaj, N., Rutherford, S., Gish, D., Rauch-Davies, M., Pelman, D., and Deev, K. (2014). Multi-focusing imaging and regularization of an irregular 3D dataset in an urban environment. *first break*, 32(6):83–86.

Fomel, S. and Kazinnik, R. (2009). Non-hyperbolic common reflection surface: 79th annual international meeting. In *SEG, Expanded Abstracts*, pages 3620–3623.

Fomel, S. and Kazinnik, R. (2013). Non-hyperbolic common reflection surface. *Geophysical Prospecting*, 61(1):21–27.

Fossen, H. (2016). *Structural geology.* Cambridge University Press.

Freeman, B., Yielding, G., and Badley, M. (1990). Fault correlation during seismic interpretation. *First Break*, 8(3).

Frieman, B. M., Kuiper, Y. D., Kelly, N. M., Monecke, T., and Kylander-Clark, A. (2017). Constraints on the geodynamic evolution of the Southern Superior province: U-Pb LA-ICP-MS analysis of detrital zircon in successor basins of the Archean Abitibi and Pontiac subprovinces of Ontario and Quebec, Canada. *Precambrian Research*, 292:398–416.

Galbraith, M. (2001). 3D seismic surveys – past, present and future. *Recorder*, 26(06).

Gao, D. and Di, H. (2015). Extreme curvature and extreme flexure analysis for fracture characterization from 3D seismic data: New analytical algorithms and geologic implications. *Geophysics*, 80:IM11–IM20.

Garabito, G. and Cruz, J. C. R. (2019). Application of very fast simulated annealing and differential evolution in the search for FO-CRS wavefield attributes. *Geophysics*, 84(5):O81–O92.

Gelchinsky, B. (1992). Homeomorphical imaging method of analyzing the structure of a medium. US Patent 5,103,429.

Gelchinsky, B., Berkovitch, A., and Keydar, S. (1999a). Multifocusing homeomorphic imaging: Part 1. basic concepts and formulas. *Journal of Applied Geophysics*, 42(3-4):229–242.

Gelchinsky, B., Berkovitch, A., and Keydar, S. (1999b). Multifocusing homeomorphic imaging: Part 2. multifold data set and multifocusing. *Journal of Applied Geophysics*, 42(3-4):243–260.

Gelchinsky, B. and Keydar, S. (1999). Homeomorphic imaging approach – theory and practice. *Journal of Applied Geophysics*, 42(3-4):169–228.

Gurevich, B., Keydar, S., and Landa, E. (2002). Multifocusing imaging over an irregular topography. *Geophysics*, 67:639–643.

Gurevich, B. and Landa, E. (2002). Multifocusing imaging with controlled reflection-point dispersal. *Geophysics*, 67(5):1586–1592.

Hale, D. (1984). Dip-moveout by fourier transform. *Geophysics*, 49(6):741–757.

Hedin, P., Almqvist, B., Berthet, T., Juhlin, C., Buske, S., Simon, H., Giese, R., Krauß, F., Rosberg, J.-E., and Alm, P.-G. (2016). 3D reflection seismic imaging at the 2.5 km deep COSC-1 scientific borehole, central Scandinavian Caledonides. *Tectonophysics*, 689:40–55.

Heilmann, Z. (2007). *CRS-stack-based seismic reflection imaging for land data in time and depth domains*. PhD thesis, Karlsruhe Institute of Technology.

Hewitt, D. F. (1949). Township of Skead, district of Timiskaming, Ontario. *Ontario Department of Mines, Annual Report*.

Hewitt, D. F. (1951). Geology of Skead township, Larder Lake area. *Ontario Department of Mines, Annual Report*.

Hewitt, D. F. (1963). The Timiskaming series of the Kirkland Lake area. *The Canadian Mineralogist*, 7(3):497–523.

Hloušek, F., Malinowski, M., Bräunig, L., Buske, S., Malehmir, A., Markovic, M., Sito, L., Marsden, P., and Bäckström, E. (2021). 3D reflection seismic imaging of the iron-oxide deposits in the Ludvika mining area (Sweden) using a focusing pre-stack depth migration approach. *Solid Earth Discussions*, pages 1–24.

Höcht, G. (2002). *Traveltime approximations for 2D and 3D media and kinematic wavefield attributes*. PhD thesis, University of Karlsruhe.

Höcht, G., De Bazelaire, E., Majer, P., and Hubral, P. (1999). Seismics and optics: hyperbolae and curvatures. *Journal of Applied Geophysics*, 42(3-4):261–281.

Hubral, P. (1983). Computing true amplitude reflections in a laterally inhomogeneous earth. *Geophysics*, 48(8):1051–1062.

Hubral, P. (1999). *Special Issue Macro-model independent seismic reflection imaging*. Elsevier.

Hubral, P., Schleicher, J., Tygel, M., and Hanitzsch, C. (1993). Determination of fresnel zones from traveltime measurements. *Geophysics*, 58(5):703–712.

Jackson, S. L., Fyon, J. A., and Corfu, F. (1994). Review of Archean supracrustal assemblages of the southern Abitibi greenstone belt in Ontario, Canada: products of microplate interaction within a large-scale plate-tectonic setting. *Precambrian Research*, 65(1-4):183–205.

Jackson, S. L., Fyon, J. A., and Thurston, P. C. (1991). The Western Abitibi subprovince in Ontario. *Geology of Ontario*, 4(Part 1):405–482.

Jäger, R., Mann, J., Höcht, G., and Hubral, P. (2001). Common-reflection-surface stack: Image and attributes. *Geophysics*, 66(1):97–109.

Jodeiri Akbari Fam, H. and Naghizadeh, M. (2019). Multi-focusing stacking using the very fast simulated annealing global optimization algorithm. *GeoConvention Conference, Calgary, Canada.*

Jodeiri Akbari Fam, H. and Naghizadeh, M. (2020). 2.5D multi-focusing imaging of crooked-line seismic surveys. In *82nd EAGE Annual Conference & Exhibition*, volume 2020, pages 1–5. European Association of Geoscientists & Engineers.

Jodeiri Akbari Fam, H., Naghizadeh, M., and Yilmaz, Ö. (2021a). 2.5D multifocusing imaging of crooked-line seismic surveys. *Geophysics*, 86(6):S355–S369.

Jodeiri Akbari Fam, H., Naghizadeh, M., and Yilmaz, Ö. (2021b). Application of 2.5D multifocusing seismic imaging in a crystalline rock environment: Results from Larder Lake area, Ontario, Canada. In *First International Meeting for Applied Geoscience & Energy*, pages 2639–2643. Society of Exploration Geophysicists.

Juhlin, C. (1995). Imaging of fracture zones in the Finnsjön area, central Sweden, using the seismic reflection method. *Geophysics*, 60(1):66–75.

Juhlin, C. and Lund, B. (2011). Reflection seismic studies over the end-glacial burträsk fault, skellefteå, Sweden. *Solid Earth*, 2(1):9–16.

Kim, J., Moon, W. M., Percival, J. A., and West, F. G. (1992). Seismic imaging of shallow reflectors in the eastern kapuskasing structural zone, with correction of crossdip attitudes. *Geophysical Research Letters*, 19(20):2035–2038.

Kim, J. S., Lee, S. J., Seo, Y. S., and Ju, H. T. (2014). Enhancement of seismic stacking energy with crossdip correction for crooked survey lines. *The Journal of Engineering Geology*, 24:171–178.

Landa, E. (2007). *Beyond conventional seismic imaging*. EAGE publications.

Landa, E., Gurevich, B., Keydar, S., and Trachtman, P. (1999). Application of multifocusing method for subsurface imaging. *Journal of Applied Geophysics*, 42(3-4):283–300.

Landa, E., Keydar, S., and Moser, T. J. (2009). Multifocusing revisited-inhomogeneous media and curved interfaces. *Geophysical Prospecting*, 58(6):925–938.

Landa, E., Rauch-Davies, M., Berkovitch, A., Pelman, D., and Deev, K. (2013). Using multi-focusing 3D diffraction imaging to predict fracture corridors/swarms in the Bazhenov formation. *75th Conference and Exhibition, EAGE incorporating SPE EUROPEC, Extended Abstracts.*

Larner, K. L., Gibson, B. R., Chambers, R., and Wiggins, R. A. (1979). Simultaneous estimation of residual static and crossdip corrections. *Geophysics*, 44(7):1175–1192.

Levin, F. K. (1971). Apparent velocity from dipping interface reflections. *Geophysics*, 36(3):510–516.

Liner, C. L. (2016). *Elements of 3D seismology.* Society of Exploration Geophysicists.

Liu, W., Zhao, B., Zhou, H.-w., He, Z., Liu, H., and Du, Z. (2011). Wave-equation global datuming based on the double square root operator. *Geophysics*, 76(3):U35–U43.

Liu, Z. and Zhang, J. (2014). Pseudo 2D elastic full waveform inversion for near surface imaging. In *SEG Technical Program Expanded Abstracts 2014*, pages 1017–1021. Society of Exploration Geophysicists.

Liu, Z. and Zhang, J. (2017). Joint traveltime and waveform envelope inversion for near-surface imaging. *Pure and Applied Geophysics*, 174(3):1269–1289.

Lundberg, E. and Juhlin, C. (2011). High resolution reflection seismic imaging of the Ullared deformation zone, southern Sweden. *Precambrian Research*, 190(1-4):25–34.

Malehmir, A. and Bellefleur, G. (2016). Pros and cons of 2D crooked seismic profiles for deep mineral exploration – a comparison with 3D surveys in geologically complex mining environment. In *EAGE/DGG Workshop on Deep Mineral Exploration*, volume 2016, pages 1–5. European Association of Geoscientists & Engineers.

Malehmir, A., Dahlin, P., Lundberg, E., Juhlin, C., Sjöström, H., and Högdahl, K. (2011). Reflection seismic investigations in the Dannemora area, central Sweden: Insights into the geometry of polyphase deformation zones and magnetite-skarn deposits. *Journal of Geophysical Research: Solid Earth*, 116(B11).

Malehmir, A., Durrheim, R., Bellefleur, G., Urosevic, M., Juhlin, C., White, D. J., Milkereit, B., and Campbell, G. (2012). Seismic methods in mineral exploration and mine planning: A general overview of past and present case histories and a look into the future. *Geophysics*, 77(5):WC173–WC190.

Malehmir, A., Schmelzbach, C., Bongajum, E., Bellefleur, G., Juhlin, C., and Tryggvason, A. (2009). 3D constraints on a possible deep $>$ 2.5 km massive sulphide mineralization from 2D crooked-line seismic reflection data in the Kristineberg mining area, northern Sweden. *Tectonophysics*, 479(3-4):223–240.

Mancuso, C. and Naghizadeh, M. (2021). Generalized cross dip moveout correction of crooked 2D seismic surveys. *Geophysics*, 86:1–61.

Mann, J. (2002). *Extensions and applications of the common reflection surface stack method*. Logos-Verlag.

Mann, J. and Duveneck, E. (2004). Event-consistent smoothing in generalized high-density velocity analysis. In *SEG Technical Program Expanded Abstracts 2004*, pages 2176–2179. Society of Exploration Geophysicists.

Marfurt, K. J. and Kirlin, R. L. (2000). 3D broad-band estimates of reflector dip and amplitude. *Geophysics*, 65:304–320.

Martin, G. S., Wiley, R., and Marfurt, K. J. (2006). Marmousi2: An elastic upgrade for marmousi. *The Leading Edge*, 25(2):156–166.

May, B. T. and Straley, D. K. (1979). Higher-order moveout spectra. *Geophysics*, 44(7):1193–1207.

Mayne, W. H. (1962). Common reflection point horizontal data stacking techniques. *Geophysics*, 27(6):927–938.

Milkereit, B., Berrer, E., King, A. R., Watts, A. H., Roberts, B., Adam, E., Eaton, D. W., Wu, J., and Salisbury, M. H. (2000). Development of 3D seismic exploration technology for deep nickel-copper depositsa case history from the Sudbury basin, Canada. *Geophysics*, 65(6):1890–1899.

Mooney, W. D. (2021). The moho discontinuity. In Alderton, D. and Elias, S. A., editors, *Encyclopedia of Geology (Second Edition)*, pages 732–743. Academic Press, Oxford, second edition edition.

Müller, N. A. (2003). The 3D common-reflection-surface stack – Theory and application. Master's thesis, Karlsruhe Institute of Technology.

Müller, T. (1999). *The common reflection surface stack method: Seismic imaging without knowledge of the velocity model*. Der Andere Verlag.

Naghizadeh, M., Smith, R. S., Sherlock, R., Rubingh, K., Lafrance, B., Ayer, J. A., Cheraghi, S., Snyder, D. B., Vergne, J., Mordret, A., et al. (2021). Active and passive seismic imaging of the central Abitibi greenstone belt, Larder Lake, Ontario. *Earth and Space Science Open Archive ESSOAr*.

Naghizadeh, M., Snyder, D., Cheraghi, S., Foster, S., Cilensek, S., Floreani, E., and Mackie, J. (2019). Acquisition and processing of wider bandwidth seismic data in crystalline crust: progress with the Metal Earth project. *Minerals*, 9(3):145.

Nedimović, M. R. and West, G. F. (2003a). Crooked-line 2D seismic reflection imaging in crystalline terrains: Part 1, data processing. *Geophysics*, 68(1):274–285.

Nedimović, M. R. and West, G. F. (2003b). Crooked-line 2D seismic reflection imaging in crystalline terrains: Part 2, migration. *Geophysics*, 68(1):286–296.

Nestvold, E. (1996). The impact of 3D seismic data on exploration, field development, and production. *SG 42: Applications of 3-D Seismic Data to Exploration and Production*, 3:1–7.

Neumann, P. M. (1998). Reflections on reflection in a spherical mirror. *The American Mathematical Monthly*, 105(6):523–528.

Panea, I. and Bugheanu, D. (2017). Analysis of crooked-line 2D seismic reflection data recorded in areas with complex surface and subsurface conditions. *Exploration Geophysics*, 48(4):493–503.

Peloquin, A. S., Piercey, S. J., and Hamilton, M. A. (2008). The Ben Nevis volcanic complex, Ontario, Canada: part of the late volcanic phase of the Blake River group, Abitibi subprovince. *Economic Geology*, 103(6):1219–1241.

Perroud, H., Hubral, P., and Höcht, G. (1999). Common-reflection-point stacking in laterally inhomogeneous media. *Geophysical Prospecting*, 47(1):1–24.

Poulsen, K. H. (2017). The Larder Lake-Cadillac break and its gold districts. *in Reviews in Economic Geology*, 19:133–167.

Rodriguez-Tablante, J., Tryggvason, A., Malehmir, A., Juhlin, C., and Palm, H. (2007). Cross-profile acquisition and cross-dip analysis for extracting 3D information from 2D surveys, a case study from the Western Skellefte district, Northern Sweden. *Journal of Applied Geophysics*, 63(1):1–12.

Salisbury, M. H., Harvey, C. W., Matthews, L., Eaton, D., and Milkereit, B. (2003). The acoustic properties of ores and host rocks in hardrock terranes. *Hardrock seismic exploration: SEG*, pages 9–19.

Schleicher, J., Hubral, P., Tygel, M., and Jaya, M. S. (1997). Minimum apertures and fresnel zones in migration and demigration. *Geophysics*, 62(1):183–194.

Schleicher, J., Tygel, M., and Hubral, P. (2007). *Seismic true-amplitude imaging*. Society of Exploration Geophysicists.

Schmelzbach, C., Juhlin, C., Carbonell, R., and Simancas, J. F. (2007). Prestack and poststack migration of crooked-line seismic reflection data: a case study from the South Portuguese zone fold belt, Southwestern Iberia. *Geophysics*, 72(2):B9–B18.

Schoepp, A., Labonte, S., and Landa, E. (2014). Multifocusing 3D diffraction imaging for dectection of fractured zones in mudstone reservoirs. In *Unconventional Resources Technology Conference, Denver, Colorado, 25-27 August 2014*, pages 695–701. Society of Exploration Geophysicists, American Association of Petroleum.

Schoepp, A., Labonté, S., and Landa, E. (2015). Multifocusing 3D diffraction imaging for detection of fractured zones in mudstone reservoirs: Case history. *Interpretation*, 3(1):SF31–SF42.

Schwarz, B. and Gajewski, D. (2017). A generalized view on normal moveout. *Geophysics*, 82:V335–V349.

Schwarz, B., Vanelle, C., and Gajewski, D. (2014a). Auxiliary media – A generalized view on stacking. In *76th EAGE Conference and Exhibition 2014*, volume 2014, pages 1–5. European Association of Geoscientists & Engineers.

Schwarz, B., Vanelle, C., and Gajewski, D. (2015). Shifted hyperbola revisited – The two faces of NMO. In *77th EAGE Conference and Exhibition 2015*, volume 2015, pages CP–451. European Association of Geoscientists & Engineers.

Schwarz, B., Vanelle, C., Gajewski, D., and Kashtan, B. (2014b). Curvatures and inhomogeneities: An improved common-reflection-surface approach. *Geophysics*, 79(5):S231–S240.

Singh, S. P., Agnihotri, N., Dhiman, P., and Ghosh, G. (2010). Crooked line seismic survey in thrust-belt and mountainous area of mizoram, north east India: A case study. In *Biennial International Conference & Exposition on Petroleum Geophysics*, pages 125–128.

Stockwell Jr, J. W. (1999). The cwp/su: seismic un∗x package. *Computers & Geosciences*, 25(4):415–419.

Storn, R. and Price, K. (1997). Differential evolution – a simple and efficient heuristic for global optimization over continuous spaces. *Journal of global optimization*, 11(4):341–359.

Taner, M., Treitel, S., Al-Chalabi, M., and Fomel, S. (2007). An offset dependent NMO velocity model. In *69th EAGE Conference and Exhibition incorporating SPE EUROPEC 2007*, pages CP–27. European Association of Geoscientists & Engineers.

Taner, M. T. and Koehler, F. (1969). Velocity spectradigital computer derivation applications of velocity functions. *Geophysics*, 34(6):859–881.

Thomson, J. E. (1943). *Geology of McGarry and McVittie Townships, Larder Lake area.* Department of Mines.

Thomson, J. E. (1946). The Keewatin-Timiskaming unconformity in the Kirkland Lake district. Royal Society of Canada.

Vermeer, G. J. (1998). 3D symmetric sampling. *Geophysics*, 63(5):1629–1647.

Vermeer, G. J. (2002). *3D seismic survey design*. Society of Exploration Geophysicists.

Versteeg, R. (1994). The marmousi experience: Velocity model determination on a synthetic complex data set. *The Leading Edge*, 13(9):927–936.

Vestrum, R., Dolgov, V., Wittman, G., Csontos, L., and Gittins, J. (2011). 3D seismic imaging over two structurally complex surveys in the foothills of Pakistan. *First Break*, 29:61.

Warner, M. and Guasch, L. (2016). Adaptive waveform inversion: Theory. *Geophysics*, 81(6):R429–R445.

Wiggins, J. (1984). Kirchhoff integral extrapolation and migration of nonplanar data. *Geophysics*, 49(8):1239–1248.

Wu, J. (1996). Potential pitfalls of crooked-line seismic reflection surveys. *Geophysics*, 61(1):277–281.

Wu, J., Milkereit, B., and Boerner, D. E. (1995). Seismic imaging of the enigmatic Sudbury structure. *Journal of Geophysical Research: Solid Earth*, 100(B3):4117–4130.

Xie, Y. (2016). Automatic estimation of the 3D CRS attributes by a metaheuristic-based optimization. In *78th EAGE Conference and Exhibition 2016*, volume 2016, pages 1–5. European Association of Geoscientists & Engineers.

Xie, Y. and Gajewski, D. (2018). 3D wavefront attribute determination and conflicting dip processing. *Geophysics*, 83(6):V325–V343.

Yilmaz, Ö. (2001). *Seismic data analysis: Processing, inversion, and interpretation of seismic data*. Society of Exploration Geophysicists.

Yilmaz, Ö. (2021). *Land seismic case studies for near-surface modeling and subsurface imaging*. Society of Exploration Geophysicists.

Yilmaz, Ö., Gao, K., Delic, M., Xia, J., Huang, L., Jodeiri, H., and Pugin, A. (2022). A reality check on full-wave inversion applied to land seismic data for near-surface modeling. *The Leading Edge*, 41(1):40–46.

Zhang, J. and Toksöz, M. N. (1998). Nonlinear refraction traveltime tomography. *Geophysics*, 63(5):1726–1737.

Zill, D., Wright, W. S., and Cullen, M. R. (2011). *Advanced engineering mathematics*. Jones & Bartlett Learning.